



HAL
open science

Mechanical behavior and durability of earth concrete : an experimental and numerical study

Hassan Fardoun

► **To cite this version:**

Hassan Fardoun. Mechanical behavior and durability of earth concrete : an experimental and numerical study. Mechanics [physics]. Université de Bordeaux, 2022. English. NNT : 2022BORD0120 . tel-04368458

HAL Id: tel-04368458

<https://theses.hal.science/tel-04368458>

Submitted on 1 Jan 2024

HAL is a multi-disciplinary open access archive for the deposit and dissemination of scientific research documents, whether they are published or not. The documents may come from teaching and research institutions in France or abroad, or from public or private research centers.

L'archive ouverte pluridisciplinaire **HAL**, est destinée au dépôt et à la diffusion de documents scientifiques de niveau recherche, publiés ou non, émanant des établissements d'enseignement et de recherche français ou étrangers, des laboratoires publics ou privés.

THÈSE PRÉSENTÉE
POUR OBTENIR LE GRADE DE

DOCTEUR DE L'UNIVERSITÉ DE BORDEAUX

ÉCOLE DOCTORALE : Sciences Physiques et de l'Ingénieur
SPÉCIALITÉ: Mécanique

par Hassan Fardoun

**Mechanical behavior and durability of earth concrete: an
experimental and numerical study**

Sous la direction de : Prof. Nadia SAIYOURI
Co-encadrement : Dr. Jacqueline Saliba

Soutenue le 30 Mars 2022

Membres du jury :

M. GRONDIN, Frédéric	Ecole Centrale de Nantes	Rapporteur
M. DARQUENNES, Aveline	INSA Rennes	Rapporteuse
M. ZENTAR, Rachid	IMT Lille Douai	Examineur
Mme. SAIYOURI, Nadia	Université de Bordeaux	Directrice
Mme. SALIBA, Jacqueline	Université de Bordeaux	Co-encadrement

LIST OF PUBLICATIONS

Journal articles

- H. Fardoun, J. Saliba, N. Saiyouri Evolution of acoustic emission activity throughout fine recycled earth concrete under compressive tests, Theoretical and applied fracture mechanics, 119 (2022) 103365 <https://doi.org/10.1016/j.tafmec.2022.103365>
- H. Fardoun, J. Saliba, N. Saiyouri, Earth concrete at wet and dry curing conditions, submitted.
- H. Fardoun, J. Saliba, N. Saiyouri, Earth concrete under cyclic loadings: stress strain curves and acoustic emission damage assessment, submitted.
- H. Fardoun, J. Saliba, N. Saiyouri, Effect long-term deformations on strength development of fine recycled earth concrete, submitted.

Conference papers

- H. Fardoun, J. Saliba, N. Saiyouri, Long-terms deformations of earth concrete, First International RILEM Conference on Earthen Construction, Paris
- H. Fardoun, J. Saliba, N. Saiyouri, Monitoring the size effect behavior of earth concrete incorporating recycled sand, submitted.
- H. Fardoun, J. Saliba, N. Saiyouri, Monitoring the effect of age and drying on the fracture behavior of earth concrete, Academic Journal of Civil Engineering. 39 (1) (2021) 1-4.
- H. Fardoun, Evaluating the drying effect on the behavior of earth concrete using acoustic emission technique, Academic Journal of Civil Engineering. 38 (2) (2021) 163–166.
- H. Fardoun, J. Saliba, N. Saiyouri, An attempt to estimate the fulfillment of Kaiser Effect in earth concrete mixtures, Academic Journal of Civil Engineering. 39 (1) (2021) 116-119.
- H. Fardoun, J. Saliba, N. Saiyouri, Finite Element Modeling of the Mechanical Behavior of Earth Concrete, Academic Journal of Civil Engineering. 38 (1) (2020) 117-120.

TITRE : Comportement mécanique et durabilité des bétons de terre : étude expérimentale et numérique

Résumé: Ces dernières années, de nombreux efforts ont été réalisés dans le domaine de la construction pour remplacer le béton traditionnel par des matériaux alternatifs. Par exemple, les constructions réalisées à partir de la terre crue sont intéressantes considérant leurs meilleures propriétés thermiques et acoustiques par rapport à un béton ordinaire. L'objectif de la production de ce béton est de réduire la consommation de ciment et donc la production de CO₂, de fournir des solutions pour éviter l'épuisement des ressources naturelles comme les granulats et de réduire la consommation d'énergie dans le processus de production. Ces dernières années, plusieurs études ont été réalisées afin de développer des méthodes plus communes et faciles à appliquer dans le domaine de la construction, ce qui a conduit à la désignation de béton de terre. Ce béton est constitué d'argile traitée par de faibles quantités d'un ou de plusieurs liants hydrauliques et peut être coulé comme un béton ordinaire. De plus, de nombreux efforts ont été réalisés dans le domaine de la construction pour remplacer l'agrégat naturel par des agrégats recyclés pour éviter l'épuisement des ressources naturelles. Dans un premier temps, les effets de l'argile et du sable recyclé sur le comportement mécanique sous sollicitations monotones du béton de terre a été étudié. Des essais de compression ont été réalisés à différents âges et différentes conditions de cure et suivis simultanément avec les techniques de traitement d'images et d'émission acoustique. Des essais de flexion ont été aussi réalisés. Les résultats ont montré la perte des propriétés mécaniques à cause du remplacement du sable naturel par du sable recyclé et en augmentant le pourcentage d'argile. De plus, les résultats ont montré comment l'argile contribue au développement de la résistance après une courte période de séchage (14 jours) et à la perte de résistance après une longue période de séchage (90 jours) en raison de la formation de fissures induites par le retrait. Cette perte des propriétés mécaniques était plus importante dans les mélanges avec du sable recyclé. Afin de mieux comprendre l'effet du séchage sur le comportement à la rupture, le retrait de dessiccation a été mesuré en parallèle avec la perte de masse. Dans un second temps, le comportement mécanique sous sollicitations cycliques du béton de terre a été étudié et suivi simultanément avec les techniques de traitement d'images et d'émission acoustique. Une assez bonne corrélation concernant l'évolution de l'endommagement a été révélée entre les deux techniques. Les déformations à long terme (retrait endogène, retrait de séchage, fluage endogène et fluage de séchage) ont été aussi mesurées afin d'évaluer les propriétés résiduelles mécaniques à long terme. Les résultats ont révélé que le retrait endogène diminue tandis que le fluage endogène, le retrait et le fluage de séchage augmentent lorsque le sable naturel est remplacé par du sable recyclé. Des simulations numériques aux éléments-finis ont été réalisées aussi en utilisant le modèle d'endommagement isotrope de Fichant afin de reproduire le comportement à la rupture de ces matériaux. Des simulations des déformations différées du béton de terre ont été aussi réalisées.

Mots clés: Béton de terre, sable recyclé, argile, endommagement, émission acoustique, corrélation d'images, durabilité

TITLE: Mechanical behavior and durability of earth concrete: an experimental and numerical study

Abstract: In recent years, many efforts have been made in the field of construction to replace traditional concrete with alternative construction materials. Constructions made from raw earth are interesting considering their better thermal and acoustic properties compared to ordinary concrete. Earth materials possess advantages in terms of CO₂ emissions and energy consumption. In addition, they are of low cost and available. A step beyond other earth materials, earth concrete is designed to be pourable. On the other side, efforts have been made also to replace natural sand (NS) by recycled sand (RS) to avoid resource depletion. This thesis aims to assess the effect of clay and RS on the mechanical properties and durability of earth concrete. Compressive tests were carried out at different ages and at different curing conditions and monitored in parallel with acoustic emission (AE) and digital image correlation (DIC) techniques. Flexural tests were performed as well. The results revealed degradation in the mechanical properties and fracture energy as recycled sand replaces natural sand and with the increase of clay content. However, an improvement in the fracture toughness was reported in presence of RS and higher clay content at later wet curing ages. At drying conditions, the results showed how clay contributes to strength development after a short period of drying (14 days) and to strength loss after long period of drying (90 days) due to the formation of shrinkage induced cracking. Such loss was more significant in the recycled sand-clay mixtures. To better understand this behavior, shrinkage was measured in parallel with mass loss. In addition, ultrasonic tests were conducted. Furthermore, earth concrete mixtures were subjected to cyclic loadings and monitored also by AE and DIC. A good correlation between both investigations was revealed. The results permitted to state that Kaiser Effect is not necessarily affected crack width development. Long-term deformation tests were carried out (autogenous shrinkage, drying shrinkage, basic creep and drying creep) on NS and RS mixtures in order to evaluate the long-term residual mechanical properties. The results revealed that when RS replaces NS, autogenous shrinkage decreases while basic creep, drying shrinkage, drying creep increases. Regarding numerical modelling, numerical simulations with finite elements were performed using Fichant's isotropic damage model to reproduce the failure behavior of these materials. In addition, simulations for the mass loss and shrinkage were carried out to eventually assess the hygro-mechanical behavior of earth concrete.

Key words: Earth concrete, recycled sand, clay, damage, image correlation, acoustic emission, durability

Table of contents

Chapter 1 Mixture design and evolution of earth concrete fracture behavior with age	6
1.1 Mechanical strength of earth materials	6
1.1.1 Particle size distribution	6
1.1.2 Effect of stabilization on strength	8
1.1.3 Phenomenological models.....	10
1.1.4 Summary of key points	10
1.2 Recycled sand (RS).....	11
1.2.1 Saturation degree.....	12
1.2.2 RA incorporating earth materials: the effect on mechanical strength.....	13
1.2.3 Summary of key points	14
1.3 Monitoring by means of acoustic emission (AE)	14
1.3.1 Hits, amplitude, AE energy and events	15
1.3.2 AE energy –fracture energy	17
1.3.3 Crack classification	18
1.4 Monitoring by digital image correlation (DIC)	19
1.5 Experimental program	21
1.5.1 Materials.....	21
1.5.2 Preliminary tests and mix design	24
1.5.3 Experimental procedure	25
1.6 Results	27
1.6.1 Mechanical properties	27
1.6.2 Correlation of stress and AE activity	29
1.6.3 AE energy – fracture energy	31
1.6.4 Correlation between DIC and AE events localization maps	32
1.6.5 Warning sign of potential failure of earth concrete mixtures.....	35
Conclusions	39
Chapter 2 Hygric properties and damage monitoring of earth concrete mixtures at different curing conditions	43
2.1 Drying	43
2.1.1 Migration of water and air.....	44
2.1.2 Approaches to model drying	45

2.1.3 Convection	47
2.2 Drying shrinkage.....	47
2.2.1 Clay content and plasticity index	47
2.2.2 Clay minerology.....	48
2.2.3 Density	49
2.2.4 Soil structure	49
2.2.5 Water content	50
2.2.6 Rate of desiccation	50
2.2.7 Modeling of drying shrinkage	52
2.3 Capillary suction effect.....	54
2.3.1 Surface tension and contact angle	54
2.3.2 Young-Laplace equation	55
2.3.3 Kelvin equation	55
2.3.4 Capillary rise	56
2.3.5 Effect of clay content	57
2.3.6 Effect of temperature (T) and relative humidity (RH)	57
2.4 Carbonation.....	59
2.5 Experimental program	60
2.5.1 Materials and mix design	60
2.5.2 Experimental procedure	60
2.6 Results.....	64
2.6.1 Mechanical properties	64
2.6.2 Ultrasonic pulse velocity tests.....	66
2.6.3 AE analysis.....	68
2.6.4 Capillary rise	73
2.6.5 Carbonation	74
2.6.6 Sorption isotherms.....	74
2.6.7 Shrinkage tests.....	77
2.6.8 Modeling of drying shrinkage	79
Conclusions	80

Chapter 3 Part A. Earth concrete under cyclic loadings: Stress-strain curves and acoustic emission damage assessment	82
3.1 Quasi-brittle materials under cyclic loadings	82
3.2 AE damage assessment	84
3.2.1 Kaiser Effect.....	84
3.2.2 Damage assessment.....	87
3.2.3 Shortcomings.....	87
3.3 Experimental program	88
3.3.1 Materials, preliminary test and mix design	88
3.3.2 Test procedure	88
3.4 Results	89
3.4.1 Stress-strain curves.....	89
3.5 Damage assessment by means of AE	91
3.5.1 Load ratio (LR) – Kaiser Effect	91
3.5.2 Calm ratio.....	93
3.5.3 Damage classification	94
3.6 Kaiser Effect by means of DIC.....	95
Conclusions	99
Chapter 3 Part B. Hygro-mechanical modeling of natural and recycled earth concrete mixtures.....	101
3.7 Damage mechanics	101
3.7.1 Damage variable concept	101
3.7.2 Uniaxial damage: the classical theory	102
3.7.3 Mazars isotropic damage model.....	105
3.7.4 The unilateral effect	106
3.7.5 Plasticity.....	107
3.7.6 Localizing problem	107
3.7.7 Fichant isotropic damage model	108
3.7.8 Spatial variability	109
3.8 Application on earth concrete	110
3.8.1 Elastic and fracture parameters	110
3.8.2 Application on earth concrete at macroscale.....	110

3.9 Results	111
3.9.1 Monotonic curves	111
3.9.2 Damage field as function of stress level	112
3.10 Shrinkage induced cracking	115
Conclusions	115
Chapter 4 Long-term deformations of earth concrete	119
4.1 Shrinkage	120
4.1.1 Capillary pressure:	120
4.1.2 Disjoining pressure:	121
4.1.3 Surface tension:	121
4.1.4 Interlayer water theory:	121
4.1.5 Dominant mechanism	121
4.1.6 Elastic or viscoelastic response	122
4.2 Creep	122
4.2.1 Creep mechanisms in soils	122
4.2.2 Creep mechanisms in concrete	123
4.2.3 Drying creep as structural effect	124
4.3 Effect of recycled concrete aggregate (RCA) on long-term deformations... 124	
4.3.1 Effect of RCA on total shrinkage and total deformations	125
4.3.2 Effect of RCA on autogenous shrinkage and basic creep	127
4.3.3 Effect of aggregate size on shrinkage and creep	127
4.3.4 Effect of temperature (T) and relative humidity (RH)	128
4.4 Experimental program	130
4.4.1 Materials	130
4.4.2 Experimental procedure	130
4.5 Results	132
4.5.1 Long-term deformations	132
4.5.2 Shrinkage	132
4.5.3 Creep	133
4.5.4 Strength development due to long-term deformations	136
4.5.5 Reference specimens	137

4.5.6 AS specimens	137
4.5.7 BC specimens	137
4.5.8 DS specimens	138
4.5.9 DC specimens.....	138
4.6 Acoustic emission (AE) analysis	139
4.6.1 Distribution of AE hits	139
Conclusions.....	141

List of figures

Figure 1.1: Lower and upper limits for particle size distribution for rammed earth (Maniatidis & Walker, 2003).....	7
Figure 1.2: Effect of clay-silt on the compressive strength and young modulus (Wu et al., 2013).7	7
Figure 1.3: Effect of lime percentage on the compressive strength of montmorillonite (a) (left), and Kaolinite (b) (right) (Bell, 1996).....	8
Figure 1.4: Effect of lime on the compressive strength (a) and Atterberg limits of kaolinite (b) (Kavak & Baykal, 2012)	9
Figure 1.5: Effect of cement content on the stress-strain deformations of soil for (Estabragh et al., 2018) (a) and (Sariosseiri & Muhunthan, 2009) (b).....	9
Figure 1.6: Correlation between the compressive strength and w/c ratio (Horpibulsuk et al., 2006) (a) and porosity to cement ratio (Ma et al., 2016) (b)	10
Figure 1.7: Recycled aggregate saturation degree situation when added to a mixture	12
Figure 1.8: Effect of soil substitution by RCA on the compressive strength (a) and global porosity (Kanema el al., 2016) (b)	13
Figure 1.9: Effect of RCA replacement in rammed earth (Arrigoni et al., 2018) (a) and clay soils stabilization by RCA (Kianimehr et al., 2019) (b) on the compressive strength	14
Figure 1.10: Schematic representation of an AE signal	15
Figure 1.11: Correlation between stress and cumulative number of AE hits (a) and amplitude and cumulative energy (Kouta, 2020) (b)	16
Figure 1.12: Localization of AE events at different stress levels.....	16
Figure 1.13: Correlation between stress and AE hits of NAC (a) and RAC (b) (Watanabe el al., 2007).....	17
Figure 1.14: Correlation between fracture energy and AE energy of earth concrete mixtures with different fibers content and length (Kouta, 2020) (a) and recycled tire rubber-filled concrete mixtures (Han et al., 2018) (b)	17
Figure 1.15: Crack classification based on RA and AF	18
Figure 1.16: Crack classification based on AF and RA in NAC (left) and RAC (right) under compression loading (Watanabe et al., 2007)	19

Figure 1.17: Strain fields (ϵ_{xx}) of earth concrete mixture under compression at different stress levels (Kouta, 2020)	21
Figure 1.18: Particle size distribution of each component (a) and each clay-sand mixture (b)	22
Figure 1.19: Surface of RS after being sprayed with phenolphthalein (a) and X-ray diffraction pattern of RS (b)	22
Figure 1.20: Determination of SSD point of RS based on the porous drying theory	23
Figure 1.21: Piezoelectric sensors' position	26
Figure 1.22: Cameras and lights for DIC as a part of the compressive test setup and stress-strain curves obtained with different methods (b)	27
Figure 1.23: Stress-strain curves of each mixture at different curing ages	27
Figure 1.24: Evolution of the compressive strength of the different mixtures with age (a) Change in strength development with respect to the previous strength and age (b)	28
Figure 1.25: Determination of fracture energy (Nakamura et al., 2018) (a) (left) and fracture energy of each mixture at different curing ages (b) (right)	29
Figure 1.26: Correlation between stress and AE activity of the different mixture at different curing ages	31
Figure 1.27: Correlation between AE energy and fracture energy	32
Figure 1.28 : Strain fields (ϵ_{xx}) and the transition of AE events throughout the five phases of the fracture process at the different curing ages	35
Figure 1.29: The criteria behind the adopted line and RA-AF diagrams of the four mixtures at 90 days	36
Figure 1.30: AE hits and AE energy of each mixture as function of different phases	39
Figure 2.1: Effect of clay content and plasticity index on the volumetric shrinkage strain (Albrecht and Benson, 2001)	48
Figure 2.2: Autogenous and total shrinkage of different earth concrete mixtures (Chinh Ngo, 2017)	48
Figure 2.3: Volumetric shrinkage strain (%) as function of density (Albrecht and Benson, 2001)	49
Figure 2.4: Time required to start cracking as function of soil thickness of close packing and loose packing soils (Corte & Higashi, 1960)	49
Figure 2.5: Volumetric shrinkage strain as function of water content relative to optimum water content (%) (Albrecht & Benson, 2001)	50
Figure 2.6: Effect of geometry on drying rate (Carette et al., 2020)	51
Figure 2.7: Displacement field (along x-axis) of mortar specimens at RH of 73% (left) and 40% (right) (Gao et al., 2021)	51
Figure 2.8: Drying cracks development until 48 hours (Trabelsi et al., 2012)	52
Figure 2.9 : Water meniscus	55
Figure 2.10: Soil-water retention curves for two rammed earth mixtures (A and B) (Jacquin et al., 2008) (a) and of two mixtures (b) (Beckett & Augarde, 2012)	57

Figure 2.11: Air humidity and suction effect as function of compressive strength (MPa) (Dierks and Ziegert, 2002)	58
Figure 2.12: Modulus of elasticity and compressive strength as function of suction (and RH) (Bruno, 2016)	58
Figure 2.13: Effect of stabilization (Bruno, 2016)	59
Figure 2.14: Compressive strength ratio at sealed and drying conditions of sand mixture (a) and loam-sand mixture (b) (Ho et al., 2017).....	59
Figure 2.15: Ultrasonic pulse velocity test (calibration and measurement) (Ngo, 2017)	61
Figure 2.16: Molds with metal studs and shrinkage tests device	62
Figure 2.17: Capillary rise test procedure	62
Figure 2.18: Different forms of isotherm curves.....	63
Figure 2.19: Specimens in the climate chamber	64
Figure 2.20: Stress-strain curves of all mixtures at the age of 14, 28 and 90 days	65
Figure 2.21: (a) compressive strength, (b) flexural strength, (c) fracture energy and (d) pre-peak slope of each mixture	66
Figure 2.22: : (a) UPV at sealed and drying conditions in function of age; (b) Correlation between the pre-peak slope and modulus of elasticity at RH=90%	68
Figure 2.23: Correlation between stress and AE activity represented by distribution of AE hits and AE energy	70
Figure 2.24: Localization of AE events (dimensions in meters) of NS30/70 at RH=90% and RH=50% with respect to different phases.....	71
Figure 2.25: Strain evolution (ϵ_{xx}) of each mixture at 28 days at RH=90% and RH=50% at different stress levels.....	72
Figure 2.26: Correlation of cumulative AE hits (%) (a) and AE energy (aJ) (b) with peak frequency of each mixture at dry curing condition	73
Figure 2.27: Mass gain and coefficient of absorption of each mixture due to capillary rise	74
Figure 2.28: Carbonation at 120 days. From right to left: NS30/70, RS20/80, RS30/70 and RS40/60 where the upper and lower row correspond to the specimens at wet and drying curing conditions, respectively.....	74
Figure 2.29: Equilibrium moisture content curves (sorption isotherms)	75
Figure 2.30: Fitting curves based on the least square method for all the mixtures	76
Figure 2.31: Mass loss, autogenous shrinkage and total shrinkage of different mixtures	78
Figure 2.32: Geometry and boundary conditions for prisms (a) and cubes (b).....	78
Figure 2.33: Reproduction of mass loss curves for prisms (a) and cubes (b)	79
Figure 2.34: The evolution of internal RH in prisms (a) and cubes (b)	79
Figure 2.35: Simulation of drying shrinkage of prisms (left) and cubes (right)	80
Figure 3.1: A typical response of masonry subjected to cyclic compression loadings (Mojsilović, 2020).....	83
Figure 3.2: Key features of earth concrete under cyclic loadings:	83

Figure 3.3: Cumulative number of AE hits versus stress in case of (a) zero AE activity and (b) AE activity at low stress level (Lavrov, 2003)	85
Figure 3.4: AE hit rate versus stress of the two reloading cycles (Yoshikawa & Mogi, 1989; Yoshikawa, & Mogi, 1981).....	85
Figure 3.5: Damage classification based on the two ratios	87
Figure 3.6: Stress-strain curves of RS20/80-50 obtained with different methods	89
Figure 3.7: Stress-strain curves of the different mixtures	89
Figure 3.8: Residual strains at RH=90% and RH=50% (a) and the secant slope of each mixture (b)	91
Figure 3.9: Onset of AE in NS30/70 at each cycle	92
Figure 3.10: Correlation of stress and cumulative number of signal strength as function of time of NS30/70.....	92
Figure 3.11: Load ratios of each mixture at RH=90% and RH=50%	93
Figure 3.12: Calm ratios of each mixture at RH=90% and RH=50%	94
Figure 3.13: Load-Calm diagrams of each mixture	95
Figure 3.14: Evolution of strain (ϵ_{xx}) of each mixture at both curing conditions	97
Figure 3.15: Attempt to verify Kaiser Effect	98
Figure 3.16: CMOD at different stress levels in RS20/80-50 and RS40/60-50.....	98
Figure 3.17: Definition of damage	101
Figure 3.18: Element of damaged material subjected to tensile force F	102
Figure 3.19: Complete response of the damaged material	104
Figure 3.20: The damage theory: stress-strain for uniaxial loading.....	106
Figure 3.21: Boundary conditions	111
Figure 3.22: Comparison between the experimental and numerical stress-strain curves	112
Figure 3.23: Damage field of each mixture at different curing condition.....	115
Figure 3.24: Shrinkage induced cracking on NS30/70 and RS30/70.....	115
Figure 4.1: time-dependent strains with time (a) strain versus time under creep test (b) (Neville et al., 1983).....	120
Figure 4.2: Effect of RCA replacement on shrinkage and creep evolution with age (Domingo-Cabo et al., 2009)	125
Figure 4.3: Specific creep from left to right of NAC and RAC (Geng et al., 2019).....	125
Figure 4.4: From left to right: SEM of (a) NAC and (b) RAC (Geng et al., 2019)	126
Figure 4.5: Effect of RCA on autogenous and drying shrinkage (a) (left) (Mao et al., 2021) and Effect of RCA on basic creep (Fan et al., 2020) (b) (right).....	127
Figure 4.6: The free shrinkage strains of different specimens at different environment conditions (from left to right: Environments A, B and C).....	129
Figure 4.7: Effect of RH on creep rate	130
Figure 4.8: Autogenous shrinkage, drying shrinkage, basic creep and drying creep tests.....	131
Figure 4.9: AE sensors positions.....	131

Figure 4.10: Mass loss (a) and autogenous shrinkage and total shrinkage of cylinders (NS and RS) and prisms (NS-P and RS-P) (b)	132
Figure 4.11: Drying shrinkage as function of RH and temperature (a) and Drying shrinkage as function of mass loss	133
Figure 4.12: Basic creep strains of NS and RS mixtures (a) and basic creep strain per stress (b)	134
Figure 4.13: Evaluation of drying creep for NS and RS	135
Figure 4.14: Stress-strain curves of each specimen	136
Figure 4.15: Compressive strength of each mixture	136
Figure 4.16: Young's modulus of each mixture	137
Figure 4.17: Correlation between the stress-strain curves and distribution of AE hits.....	141

List of Tables

Table 1.1: The three characteristics of a speckle pattern	20
Table 1.2: Properties of clay	21
Table 1.3: Cement components.....	23
Table 1.4: Water parameters' values	24
Table 1.5: Mix design of preliminary tests	25
Table 1.6: Slump, compressive strength and flexural strength at different pre-saturation degrees of RS30/70.....	25
Table 1.7: Mix design of the four mixtures.....	25
Table 2.1: Mix design of the four mixtures.....	60
Table 2.2: Density values of each mixture	67
Table 2.3: Poisson's ratio at different curing ages.....	68
Table 2.4: Porosity of each mixture	76
Table 2.5: Least square method for NS30/70.....	76
Table 2.6: Parameters used for simulation	79
Table 2.7: Granger's approach parameters	80
Table 3.1: Mix design of each mix.....	88
Table 3.2: Elastic and fracture parameters of each mixture	110
Table 3.3: Effect of standard deviation of E and f_t on damage filed	113
Table 4.1: Mix design of each mixture	130

General Introduction

Raw earth or soil has been used as a construction material for thousands of years. The construction by earthen materials may date back 10,000 years. It has taken different forms e.g. wattle and daub, cob, rammed earth, earth bricks, compressed earth blocks (CEB)... It is of low cost, limits energy consumption, reusable (Soudani et al., 2016) and plays a significant role in terms of moisture buffering and temperature control (Alassaad et al., 2021). Thus, improving sustainability of earth concrete can reduce the negative impact of current consumption on future society. Earth concrete, in addition to the mentioned benefits, is designed in this study to be pourable.

The physical and chemical breakdown of earth's rocks – the process known as weathering-accounts for soil formation (Török and Dransfield, 2018). Soils comprise a range of particle sizes. Often, they are defined as clays and non-clays. Clays are of a size less than 2 μm or 5 μm . The non-clays are silt of a size between 2 μm (or 5 μm) and 20 μm or 50 μm , sand of a size between 20 μm (or 50 μm) and 2 mm, gravel between 2 mm and 20 mm and stones of a size larger than 20 mm. A soil can be extracted from a certain area or can be 'engineered-mixed soil or artificial' where its components are chosen from different sources.

The presence of different grain sizes has a great influence in earth materials. This is due to the fact that the response and shapes of each particle size is different. Clays, the small flat grains, will not respond to pressure in the same way as sands, the coarse (coarser than clay) rounded grains, do. Furthermore, clays, generally, behave in a plastic manner while sands act in a fragile way. Thus, the more the amount of clays is, the greater the tendency of the material to deform in a plastic way. On the other hand, the more large particles are presented in the mix, the more rigid will be the behavior of the sample (Avrami et al., 2008). In addition, fine particles (clay and silt) affect the mechanical behavior also as they have filling effect. Therefore, as a new material of low strength, an investigation on the mechanical performance of earth concrete is required.

Clay minerals are an integral part of an earthen building material. Clays' surfaces have an effect on water molecules when they are bonded to them. When water moves inside and outside the structure, it leads to a change in the dimension of a clay particle. This phenomenon occurs mainly in swelling clays (or smectites).

Clays are generally classified into two groups: swelling clays (or smectites) and non-swelling clays. Swelling clays can be dioctahedral smectite such as beidellite, montmorillonite, and nontronite or trioctahedral smectite such as saponite and vermiculite. Non-swelling clays comprise no charge clays such as kaolinites or high charge ones such as micas and illite. Thus, for earth construction, the swelling clays are less suitable as they exhibit large dimensional changes with moisture content. Nevertheless, regardless of type of clay, the material will still be sensitive to water and therefore the assessment of the effect of drying is of high importance.

Structures are subjected to different loadings and temperature and humidity variations during their life time. These loads cause long-term deformations (or known also as time-dependent deformations) which are of high importance in earth concrete due particularly to the latter's fine particles, principally clay. These deformations are the autogenous shrinkage, drying shrinkage, basic creep and drying creep. Autogenous shrinkage is the time-dependent strain of non-loaded specimen at sealed conditions (exchanging no water with the environment). The reduction in volume here is due to chemical shrinkage and self-desiccation. Drying shrinkage is the time-dependent strain difference between a non-loaded specimen at drying conditions (exchanging water with the environment) and autogenous shrinkage. The reduction in volume here is due to the water migration to the outside the specimen due to the relative humidity (RH) gradients. Basic creep is the time-dependent strain difference between a loaded specimen at sealed conditions from one side and the autogenous shrinkage and elastic (instantaneous) strain from other side. The sum of basic creep strain and the two shrinkage ones in addition to the instantaneous strain results generally in a total deformation less than that obtained, at simultaneous drying, from a loaded drying specimen (true strain or total strain). This difference is known as drying creep or Picket's effect. Each of these deformations has its effect on the mechanical properties i.e. compressive strength, Young's modulus, tensile strength... Such properties, due to the resulted deformations, may increase or decrease.

During the production process, the particle size of the generated recycled aggregate varies. The obtained coarse Recycled Concrete Aggregates (RCA) are accompanied with large amount of fine RCA or recycled sand (RS) (<4mm). It is estimated that RS accounts for 50% after the crushing of Construction Demolition Waste (CDW). In addition, CDW represents one third of all waste generated in Europe (Ramaroson et al., 2018). The Netherlands which is believed to have an outstanding CDW management system, its approach is simply crushing and considering the outcome as base in road construction (Zhang et al., 2019). RS is getting applied in road construction in addition to cementitious renderings and masonry mortars, filling material and soil stabilization (cement replacement). Based on the fact that a continuous increase of the amount of CDW is expected in the coming years and that the road construction market will eventually slow down and recede, an alternative market of RS or recycled aggregate in general is required. The porous state and possible internal cracking and eventually the high water absorption of RS in addition to lack of standards have made RS limited to laboratory tests and restricted at concrete sites. Knowing that earth concrete is already of low strength and sensitive to drying, the consideration of RS as an earth concrete component may thus do not prevent taking it into account as an alternative market. In addition, RS is a porous material and clay is of fine particles. This may make the latter capable of filling the pores in the former.

Despite the high amount of studies, the current knowledge and understanding of earth concrete properties and design procedures are still insufficient. This lack of experience in designing and building with earth can cause several problems related to moisture sensitivity, shrinkage and cracking. This thesis aims to assess mechanical properties and durability of earth concrete

incorporating RS. Natural sand (NS) earth concrete mixture and other RS earth concrete mixtures of different amounts of clay were prepared. Experimental and numerical studies are carried out and the output is presented in this 4-chapter-thesis.

Chapter 1 aims to assess the mechanical properties at different curing ages of the different mixtures. First of all, a state of art is presented. It states the mix designs adopted for earthen mixtures and the factors influencing the mechanical properties of earth materials. In addition, the effect of natural aggregate replacement by recycled aggregate on mechanical properties are discussed after highlighting the different possible options of saturation degrees of recycled aggregate. A preliminary test on the effect of RS saturation degree on workability and strength is conducted. Eventually, the mixtures are prepared, casted in cubic specimens and subjected to uniaxial compressive tests at 14, 28 and 90 days. The compressive tests are monitored in parallel with acoustic emission (AE) and digital image correlation (DIC) techniques for a better understanding of the fracture process.

Chapter 2 comprises experimental and numerical investigations. It is aimed experimentally to assess the effect of drying on the mechanical properties of earth concrete from one side and to better understand numerically the process of water migration in the different mixtures due to relative humidity gradients. Regarding the experimental work, cubic specimens are conserved at dry conditions. Compressive tests monitored in parallel with AE and DIC techniques are carried out and correlation with those at wet conditions in the first chapter takes place. To better understand the results, mass loss, autogenous shrinkage and drying shrinkage tests are carried out. Furthermore, specimens at wet and dry conditions are assessed with ultrasound. Regarding modeling, finite element analysis of water transfer and drying shrinkage using the software Castem is performed.

Chapter 3 is constituted of two parts. Part A is experimental while part B is numerical. Experimentally, specimens are subjected to cyclic compressive loadings at wet and dried conditions. Stress-strain curves are assessed in terms of their residual strength, secant modulus and the forms of unloading - loading curves. Moreover, an AE-based method is considered to quantify the progressive damage in earth concrete in parallel to damage assessment carried out by DIC. In chapter 3 part B, a numerical hygro-mechanical assessment is carried out to examine the shrinkage-induced cracking.

Chapter 4 concerns the long-term deformations. NS and RS earth concrete mixtures are put outdoors to examine their vulnerability to autogenous shrinkage, drying shrinkage, basic creep and drying creep. Moreover, all the specimens after a period of two months of durability tests are subjected to compressive tests to evaluate the residual properties.

<u>Chapter 1 Mixture design and evolution of earth concrete fracture behavior with age</u>	6
<u>1.1 Mechanical strength of earth materials</u>	6
<u>1.1.1 Particle size distribution</u>	6
<u>1.1.2 Effect of stabilization on strength</u>	8
<u>1.1.3 Phenomenological models</u>	10
<u>1.1.4 Summary of key points</u>	10
<u>1.2 Recycled sand (RS)</u>	11
<u>1.2.1 Saturation degree</u>	12
<u>1.2.2 RA incorporating earth materials: the effect on mechanical strength</u>	13
<u>1.2.3 Summary of key points</u>	14
<u>1.3 Monitoring by means of acoustic emission (AE)</u>	14
<u>1.3.1 Hits, amplitude, AE energy and events</u>	15
<u>1.3.2 AE energy –fracture energy</u>	17
<u>1.3.3 Crack classification</u>	18
<u>1.4 Monitoring by digital image correlation (DIC)</u>	19
<u>1.5 Experimental program</u>	21
<u>1.5.1 Materials</u>	21
<u>1.5.2 Preliminary tests and mix design</u>	24
<u>1.5.3 Experimental procedure</u>	25
<u>1.6 Results</u>	27
<u>1.6.1 Mechanical properties</u>	27
<u>1.6.2 Correlation of stress and AE activity</u>	29
<u>1.6.3 AE energy – fracture energy</u>	31
<u>1.6.4 Correlation between DIC and AE events localization maps</u>	32
<u>1.6.5 Warning sign of potential failure of earth concrete mixtures</u>	35
<u>Conclusions</u>	39

Chapter 1 Mixture design and evolution of earth concrete fracture behavior with age

As a new material of low strength, the examination of earth concrete's mechanical behavior is a must. In this chapter, it is aimed to assess how the mechanical properties of earth concrete are influenced by the percentage of clay from one side and by the replacement of natural sand (NS) by recycled sand (RS) from other side. Our screening in past research on the assessment of the effect of recycled aggregate by AE under compressive loadings has found few articles. Therefore, in addition to the basic assessment of the mechanical properties of different earth concrete mixtures, this chapter aims to analyze the evolution of AE activity throughout earth concrete mixtures under compressive loadings.

1.1 Mechanical strength of earth materials

1.1.1 Particle size distribution

Earth construction has been in service for thousands of years. It has taken different forms such as wattle and daub, cob, rammed earth, earth bricks, compressed earth blocks (CEB)... It is of low cost, limits energy consumption, reusable and plays a significant role in terms of moisture buffering and temperature control. Beyond these advantages, earth concrete is designed to be pourable .

The particle size distribution of earth materials has been always an area of interest for researchers and it is agreed that each material form possesses its own range of particle size. For rammed earth, the 1990s and early 2000s considered 20-35% of fine particles (clay and silt) and 70-80% of sand and gravel (2 to 20 mm) as shown in figure 1.1. On the other side, more than 50% of clay-silt was considered for compressed earth blocks in the mid-2000s. Years back, Miccoli et al. (2014) adopted 36%, 51%, 57% and 82% of fine particles for rammed earth, earth mortar, earth block and cob, respectively. Recently, Arrigoni et al. [6] considered a rammed earth of 86% fine particles. The available knowledge and current understanding of earth concrete properties and design procedure are still insufficient.

Particle size distribution influences different properties such as strength, Young's modulus, fracture energy and shrinkage. Higher sand content may increase strength and Young's modulus due to solid skeleton these particles possess. On the other side, they may reduce the fracture energy. In fact, clays tend to slide on one another, while sand grains tend to push into one another in a rigid manner, and they eventually break at points of contact where stress is concentrated. Clays, in general, will behave in a plastic manner, while sands will behave in a fragile manner. Regarding shrinkage, clay particles, being fine, contribute to shrinkage increase.

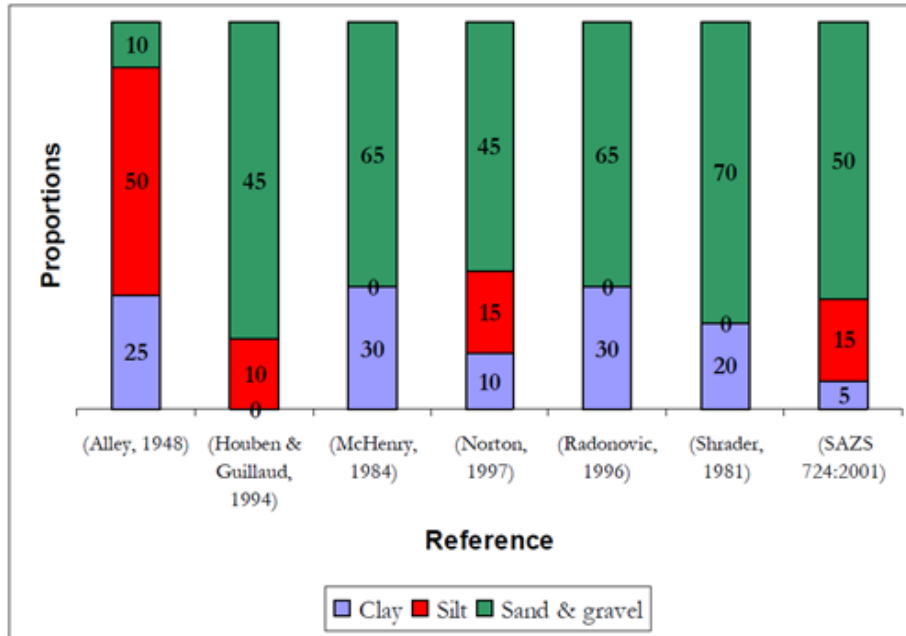


Figure 1.1: Lower and upper limits for particle size distribution for rammed earth (Maniatidis & Walker, 2003)

Wu et al. (2013) casted four earth mixtures comprising natural soil (clay-silt of 88.6% and sand of 11.4%) in addition to a coarser fraction (sand of 74.7% and gravel 25.3%). These four mixtures had a coarse sandy fraction ranging from 60% to 45% and fine clayey-silty fraction ranging from 40% to 55%. Unconfined compression tests were carried out on the four obtained bricks. Regarding strength and stiffness, the results in figure 1.2 showed that a clay-silt fraction of almost 50% is acceptable. Fine particles are of great compactness. The study of Wu (Wu et al., 2013) means that clay does not lose their compaction role when added to an extent less than 50%.

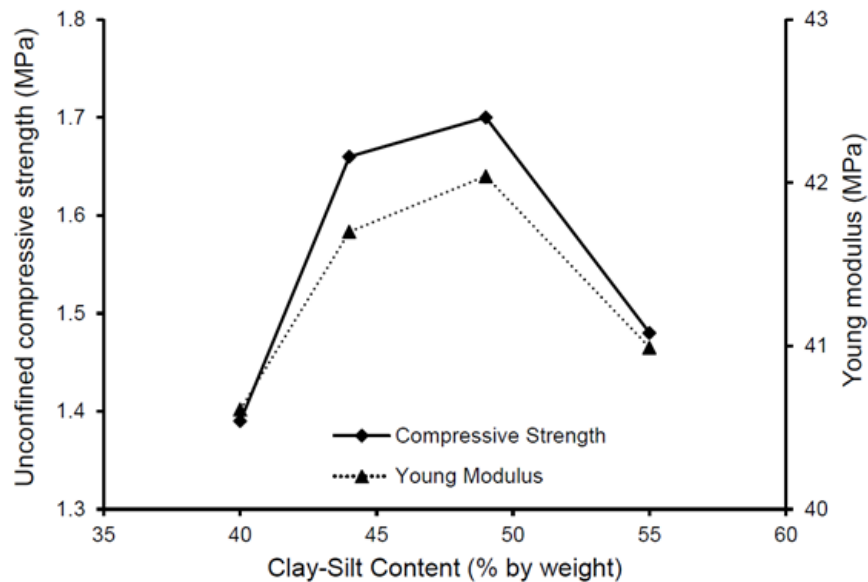


Figure 1.2: Effect of clay-silt on the compressive strength and young modulus (Wu et al., 2013)

1.1.2 Effect of stabilization on strength

The chemical stabilization of raw earth materials is a common and very old practice. It is adopted for the purpose of improving the performance of soil. Ancient stabilizations took different forms such as the adding of tree resins, casein from milk, cactus juice and many others (Houben and Guillaud, 1994).

Each stabilizer has its own boundary of influence and thus a combination of different stabilizers aiming for improvements at different levels is a common practice. Due to the fact that the main weaknesses of earth materials are the vulnerability to water and the low strength, lime and Portland cement are of the most adopted binders.

The lime's effect on compressive strength up to 28 days seems to be influenced by clay type. Figure 1.3 (a) shows basically that the optimum lime content in case of montmorillonite is 4% and that a lower or higher percentage reduces the compressive strength. In case of kaolinite, it is found that after certain lime content, the compressive strength slightly fluctuates. As shown in figures 1.3 (b) and 1.4 (a), the optimum lime content is almost 2% (with still a bit of increase at 28 days at 4%) according to Bell (Bell, 1996) and 4% according to Kavak and Baykal (Kavak and Baykal, 2012). Eventually, it seems that 4% of lime seems acceptable to different types of clay regarding compressive strength. For long-term strength, the pozzolanic reactions due to the addition of lime enhance the cohesion and the increase of long term strength (Ngo et al., 2020).

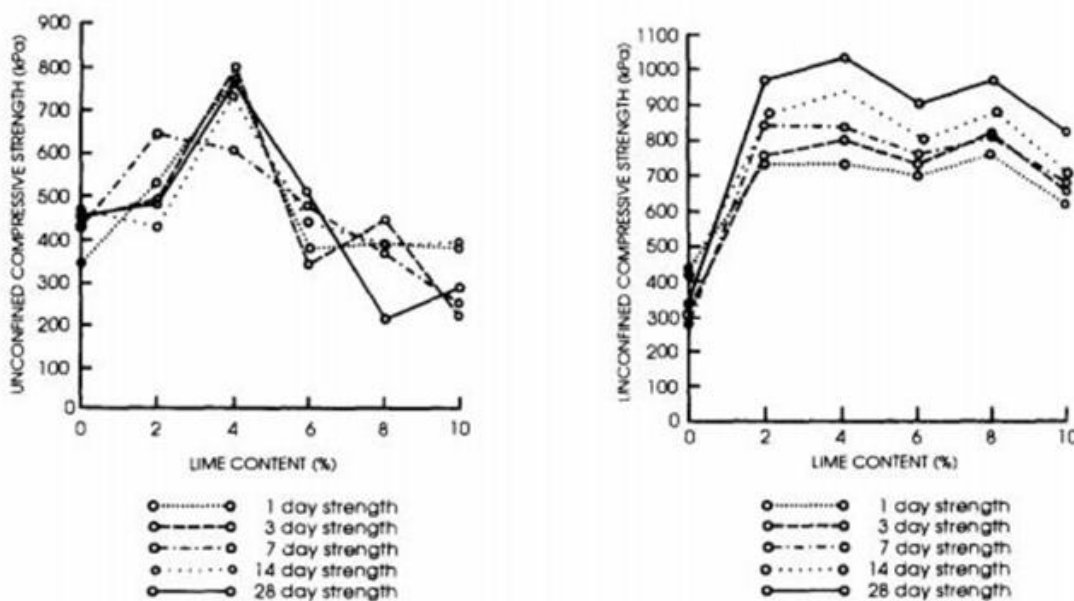


Figure 1.3: Effect of lime percentage on the compressive strength of montmorillonite (a) (left), and Kaolinite (b) (right) (Bell, 1996)

It is important to note that the treatment of clay by lime has been adopted also to improve soil workability, increase the plastic limits (plastic index (PI) = liquid limit – plastic limit) and to reduce the volume changes (Bell, 1996 ; Lemaire et al., 2013 ; Chinh Ngo, 2018). Nevertheless, it seems, according to figure 1.4 (b), that when lime is added to the non-swelling clay kaolinite, the plastic index is barely changed. Indeed, the lowest liquid limit was reported at 0 % of lime content.

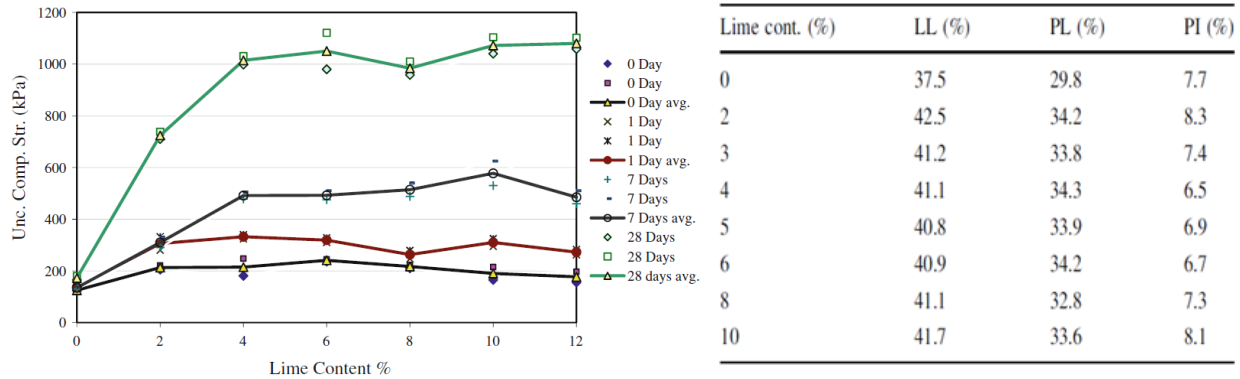


Figure 1.4: Effect of lime on the compressive strength (a) and Atterberg limits of kaolinite (b) (Kavak & Baykal, 2012)

Regarding cement, figure 1.5 shows the stress-strain curves of two different soils with different percentage of cement content (Estabragh et al., 2018; Sariosseiri & Muhunthan, 2009). It can be stated that the compressive strength and pre-peak slope increases with cement content. This can be attributed to the hydration reactions.

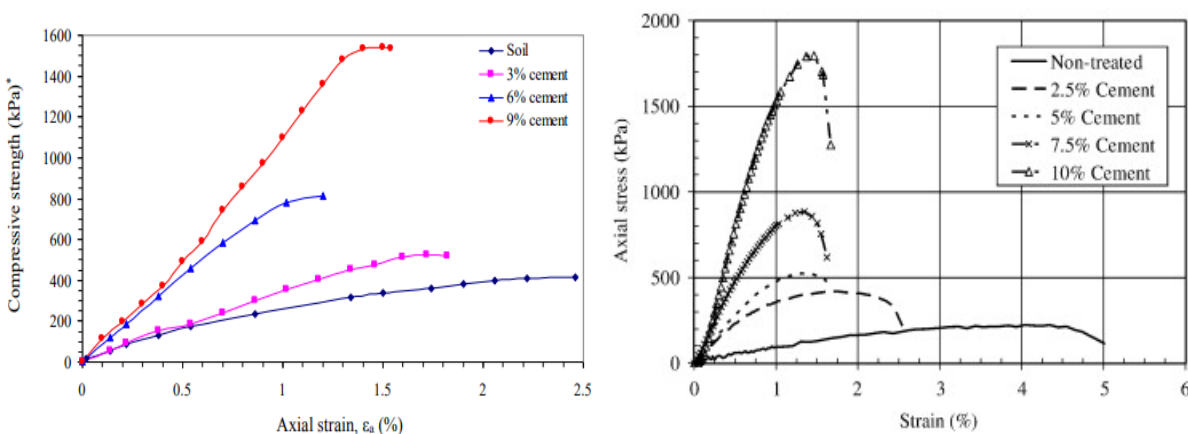


Figure 1.5: Effect of cement content on the stress-strain deformations of soil for (Estabragh et al., 2018) (a) and (Sariosseiri & Muhunthan, 2009) (b)

1.1.3 Phenomenological models

Earth is influenced by the particle size distribution and stabilization. The latter comprises mainly lime and cement where the former is linked mostly to non-swelling clays. To better recognize the mechanisms behind strength development of cement stabilized earth, researchers have assessed the influence of different variables by proposing phenomenological models.

Strength increases with cement content. In addition to this factor, initial water content is a significant parameter. Eventually, models correlating the compressive strength to initial water to cement ratio (w/c) have been proposed. Figure 1.6 (a) shows the unconfined compressive strength as function of soil w/c ratio. It can be seen that the higher compressive strength was reported as w/c ratio decreases. However, the effect of age is not taken into account. Furthermore, earth properties in these two parameters are ignored. To overcome these limitations, Lorenzo and Bergado (2006, 2004) proposed models by taking into account the void ratio, specific gravity and unit weight. In addition, the authors address a relationship between the parameters of stabilized earth after some days of curing as function of cement content and curing age.

Ma et al. (2016) proposed different equations for different curing ages. In his work, the unconfined compressive strength was correlated to porosity to cement ratio (n_i/C) where the porosity is based on water content, unit weight and specific gravity. Figure 1.6 (b) shows how strength decreases with porosity.

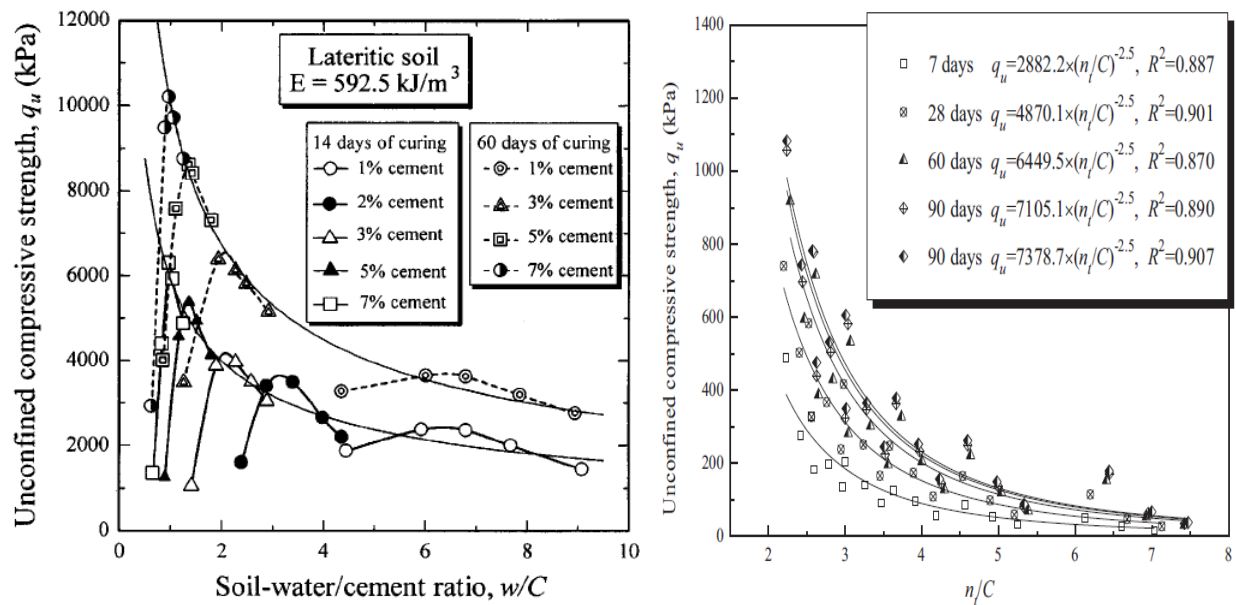


Figure 1.6: Correlation between the compressive strength and w/c ratio (Horpibulsuk et al., 2006) (a) and porosity to cement ratio (Ma et al., 2016) (b)

1.1.4 Summary of key points

In the previous sections, the following has been stated:

- Fine particles contribute to strength as long as they don't overpass the threshold. Each material would have its own boundary size limits of particles.
- The strength increases with cement content and decreases with porosity.
- A 4% of lime seems applicable to different clay type in terms of strength. In terms of volume changes, the addition of lime content to kaolinite clay would not reveal important changes.
- The strength decreases with water content and accordingly decreases with water to cement ratio.

1.2 Recycled sand (RS)

During the production process, the particle size of the generated recycled aggregate varies. The obtained coarse recycled concrete aggregates (RCA) are accompanied with large amount of fine RCA. In the following study the term recycled sand (RS) is mainly used instead of fine recycled aggregate. It is estimated that RS accounts for 50% after the crushing of construction and demolition wastes (CDW). In addition, it possesses one third of all waste generated in Europe (Ramaroson et al., 2018). Therefore, the use of RS would be an ecological turning point in the field of construction.

RS has been considered in three main practices: (1) in the fabrication of Portland clinker being considered as alternative raw material (2) in the production of cement, it has successfully replaced the limestone filler, (3) as a filler in concrete (Le & Bui, 2020). The incorporation RS in concrete has been limited. This is due to the fact that RS possesses undesirable properties.

RS is of high internal cracking, porosity and eventually high water absorption capacity (more than coarse RCA). In addition, while the natural aggregate concrete (NAC) possesses one interfacial transition zone (ITZ) which is between the sand and the matrix, the RAC may be of three ITZs. Knowing that RCA is of natural aggregate and old cement mortar, the three ITZ may be: (1) between the natural aggregate (NA) and old cement matrix, (2) NA and new matrix and (3) new matrix and old cement matrix. Furthermore, RS possesses great amount of sulfur compound.

The main and principal limitation of recycled aggregate (RA) is the higher water absorption (WA) capacity of its porous and cracked attached mortar. It is expressed as follows:

$$\%WA = (M_{SSD} - M_{OD}) * 100 / M_{OD} \quad (1-1)$$

where WA is the water absorption, M_{SSD} is the saturated surface dry mass and M_{OD} is the oven dry mass. It may be worth to mention that SSD is defined as the condition of an aggregate in which the surface of the particles is dry while the inner part is saturated.

1.2.1 Saturation degree

The WA has to be known. It is the key to predict the effective water needed for a mixture. In other words, as RA absorbs water basically according to its water absorption capacity, this should be taken into account so it does not affect the water required to other components in the mixture (clay and cement) and workability. RA is added to a mixture in one of the following situations (figure 1.7):

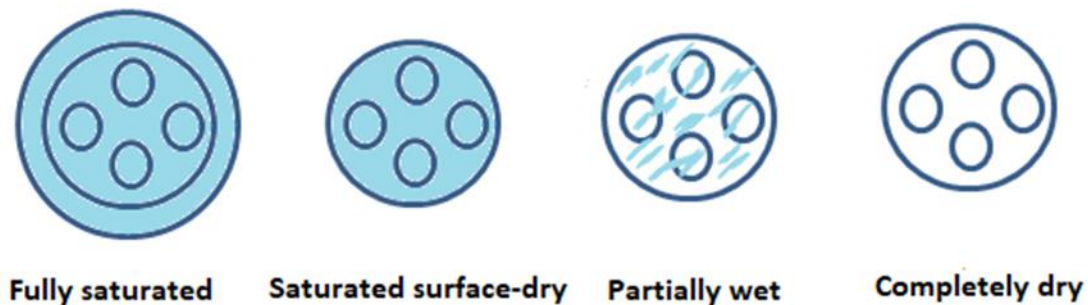


Figure 1.7: Recycled aggregate saturation degree situation when added to a mixture

1.1.2.1 Effect of saturation degree on strength

In case that NA and RA are of similar or comparative WA so that there is no need to the addition of water, a degradation in the mechanical properties may not be the outcome (Adams et al., 2016). Nevertheless, RS is more likely to be of high water absorption so that in addition to superplasticizers, more water is likely to be added to the mixture.

Due to its high water absorption, RS or generally RCA if added to a mixture in the dry state, they act like a sponge. Their water absorption potential absorbs the water added to the mix (or the local water) and thus a slump loss would be reported. Eventually, as a result of slump loss, a higher strength is revealed in the RCA mixtures. Poon et al. (2004) and Zhang et al. (2019) reported this aspect. To avoid slump loss, pre-saturation or the addition of water during the mixing process has to be considered. On the other side, the saturation degree weakens the ITZ of the mixture. Eventually, preliminary tests are very often carried out. A pre-saturation at 80% is adopted very often.

It may be worth to note certain points that have been addressed concerning the saturation of RA. Knowing that concrete production time requires two hours (more or less as transportation is taken into account) or that laboratory mixtures are mixed for few minutes, and that RA during this time is not able to absorb all the quantity of added water, this justifies why some researchers in lab studies tend to pre-saturate aggregate based on short time pre-saturation (3 min, 5 min...) (García-González et al., 2014). In other words, if water was added to saturate the recycled aggregate (RA), however, the latter was not able to absorb all the quantity in a given time, this will increase the water content and thus affects the water to cement ratio. Furthermore, it has been stated that 24 hours (usually the period stated by standards) is not enough time to reach

saturation and fill all pores and not enough for density calculation. For instance, Schouenborg et al. (2004) stated that the WA can double after one year.

1.2.2 RA incorporating earth materials: the effect on mechanical strength

The effect of addition of RA into earth materials is not frequently assessed. Kanema et al., (2016) assessed the effect soil substitution by recycled RCA on the mechanical properties of earth concrete mixtures. Such substitution ranged between 20% and 57% (RA/skeleton ratio). The results of compressive strength and global porosity are presented in figure 1.8 (note that the mixtures were prepared industrially at site and manually at laboratory). The results show an increase in the compressive strength with RCA.

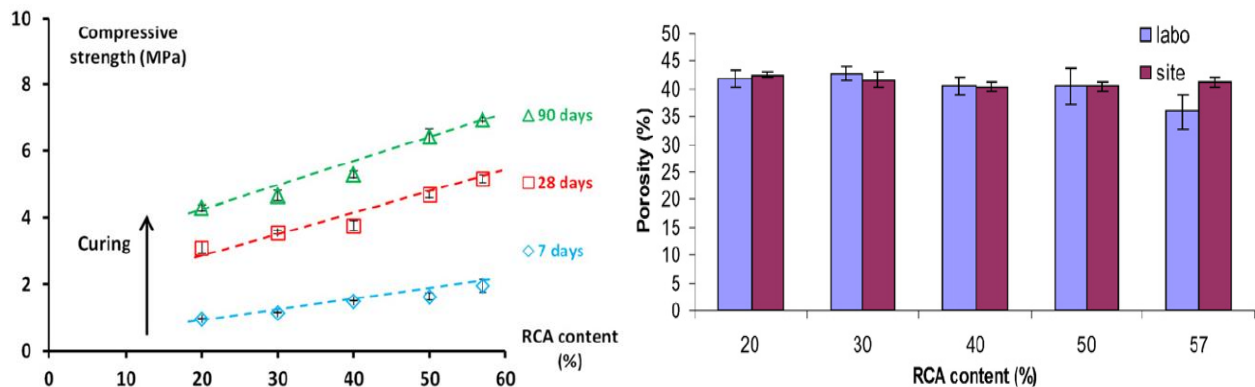


Figure 1.8: Effect of soil substitution by RCA on the compressive strength (a) and global porosity (Kanema et al., 2016) (b)

It can be deduced from the results of porosity that both components, the soil and RCA, are of comparative water absorption capacities. This confirms with what has been stated in 1.1.1.1 that a similar WA between NA and RA has not to be necessarily followed by degradation in strength.

Figure 1.9 (a) shows the effect of crushed limestone and engineered soil substitution by RCA (Arrigoni et al., 2018). Knowing that the optimum water content increases in both soils with RCA, the results show a clear decrease in strength in the crushed limestone and no clear trend in engineered soils. The author attributed the latter to a possible effect of particles size distribution. On the other hand, figure 1.9 (b) shows the effect soil stabilization by RCA (instead of cement). The results show an increase in strength up to 28 days. The authors attributed this to friction, pozzolanic reactions and unhydrated cement on the old attached mortar.

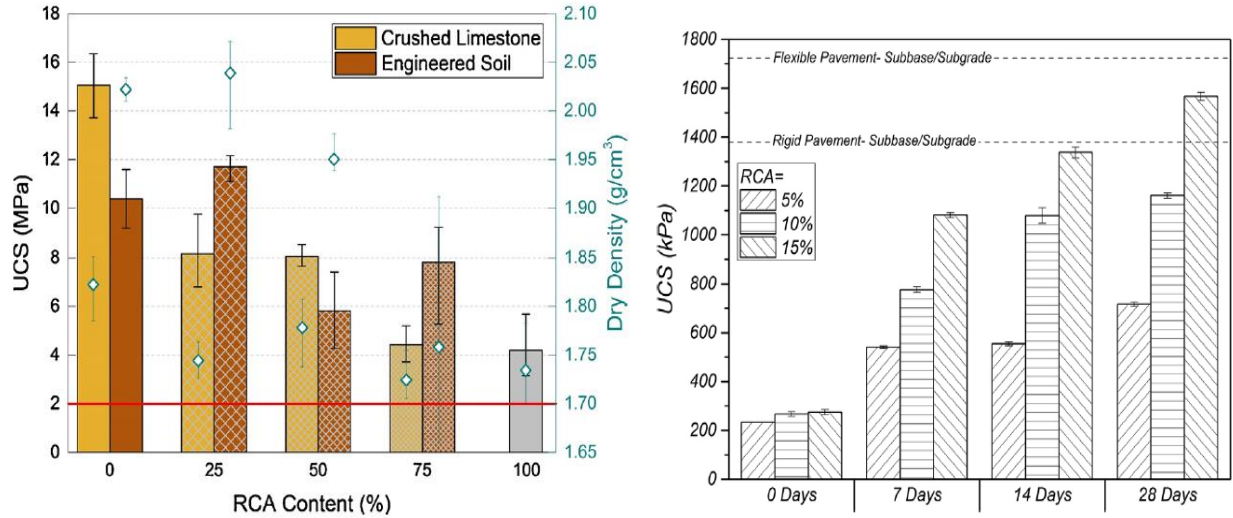


Figure 1.9: Effect of RCA replacement in rammed earth (Arrigoni et al., 2018) (a) and clay soils stabilization by RCA (Kianimehr et al., 2019) (b) on the compressive strength

1.2.3 Summary of key points

- RS is most likely to be of high water absorption capacity.
- If RS is added to a mixture in a dry state (or as received state) without adding water it would absorb, a slump loss and eventually a virtual strength increase will be reported. To avoid slump loss, pre-saturation or the addition of extra water can take place.
- Preliminary tests are to be carried out.
- Taking into account what has been stated in part 1.1.2 about the effect of water content and porosity on strength of earth materials; it is worth to state again that RS is generally of high porosity and thus it demands more water than NS.

1.3 Monitoring by means of acoustic emission (AE)

AE is the study of elastic waves generated by a material subjected to external stresses. When concrete is exposed to external mechanical loading, these waves are mainly of friction and micro-cracking sources. Once the elastic wave is generated, it travels throughout the material to be detected at the end by piezoelectric sensors placed at the surface (Beattie, 2013). The elastic wave is modified during its propagation according to its acoustic path in the material's structure. The piezoelectric sensor transforms the acoustic wave into an electrical signal to be analyzed by the examiner. Analysis is carried out based on the output parameters such as amplitude, AE absolute energy, counts, frequency... These parameters and others are often used to classify the cracking mode or fracture mechanisms and to assess damage. A sharp increase in counts or energy, for instance, most probably designates the formation of a macrocrack; signals possessing high frequencies can be indications of microcracks initiation while those of a few KHz are probably

detected just before failure (Wu et al., 2019), a lower b-value corresponds to more development in cracks (Sagasta et al., 2018)...Figure 1.10 shows a schematic representation of an AE signal.

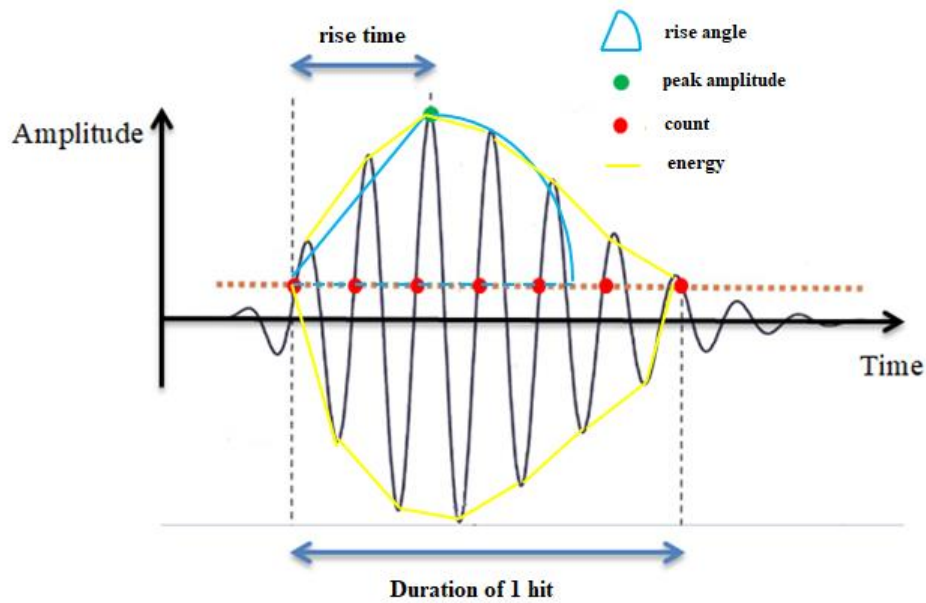


Figure 1.10: Schematic representation of an AE signal

1.3.1 Hits, amplitude, AE energy and events

Figure 1.11 shows the monitoring of an earth concrete mixture (30% clay and 70% NS) under uniaxial compression loading by AE throughout the entire fracture process. The author divided the fracture process based on the AE activity into four phases. Kouta (2020) attributed the remarkable signals in phase 1 to the unevenness in the specimen surface, to the damage at the corners and to the stress concentration at the support levels. The author reported a very little increase in hits and almost zero energy in phase two that corresponds to the non-linear phase before the peak. Regarding the rapid increase in hits, amplitude levels and energy in phase 3, this is a reflection of the formation of macrocracks. Finally, phase 4 was reflected by stabilization in AE activity.

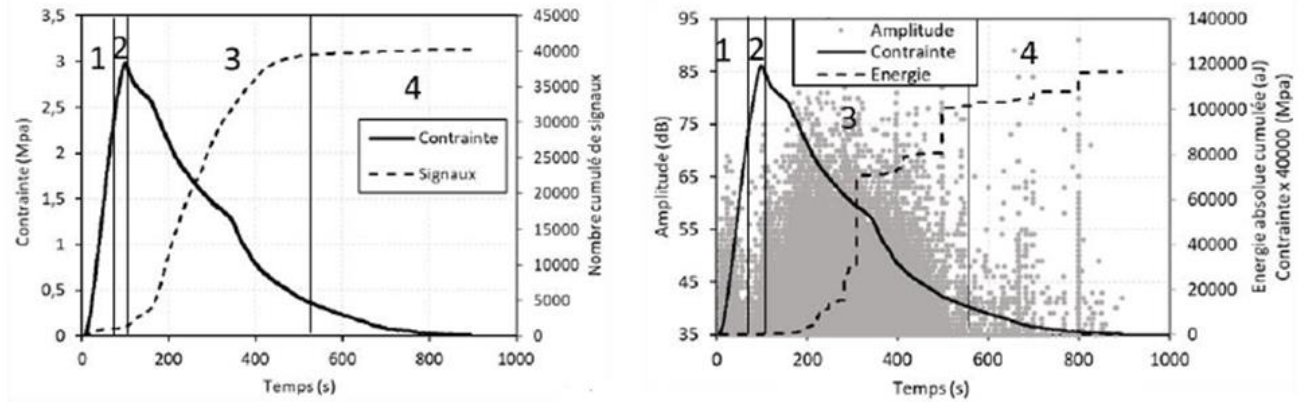


Figure 1.11: Correlation between stress and cumulative number of AE hits (a) and amplitude and cumulative energy (Kouta, 2020) (b)

The author assessed the localization of AE events -which signifies the capture of a signal by multiple sensors- at different stress levels as shown in figure 1.12. The author attributed the general low number of AE events to the of the material. In addition, the localization of AE events at top and bottom of the specimen has been attributed to the metallic plate contact with the specimen upon loading.

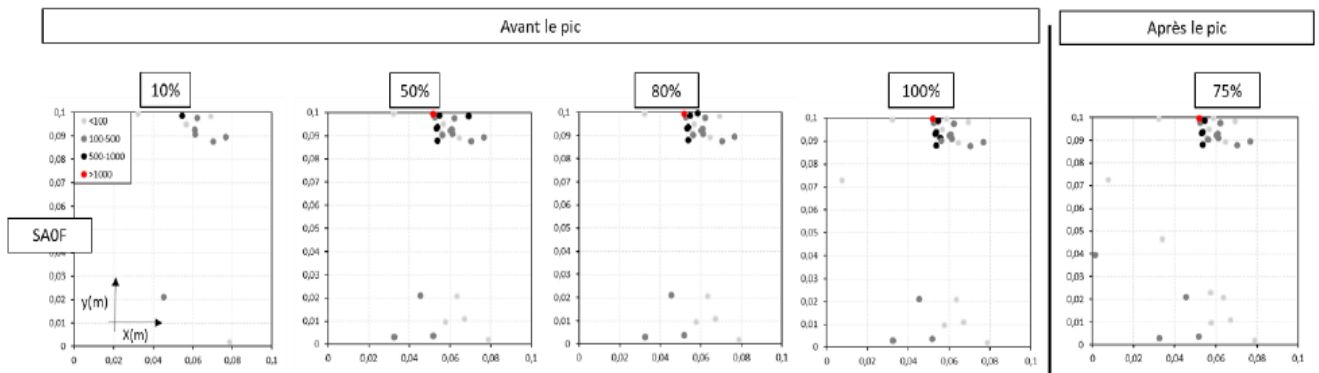


Figure 1.12: Localization of AE events at different stress levels.

When searching for past studies, it can be noticed that research on monitoring recycled aggregate mixtures' fracture behavior by means of AE is not widely spread. Particularly, under uniaxial compression, limited papers have been found. Figure 1.13 shows the correlation between stress and AE hits of natural aggregate concrete (NAC) or as it is named in the study (N) and recycled aggregate concrete (RAC) or as its named in the study (RV-0) (Watanabe et al., 2007). Though both mixtures reached similar maximum stress level, it can be noticed that AE activity started earlier in the RV-0 mixture. According to the Watanabe et al. (2007), such aspect means the ineffectiveness to improve the nucleation of microcracking in concrete made with recycled aggregate.

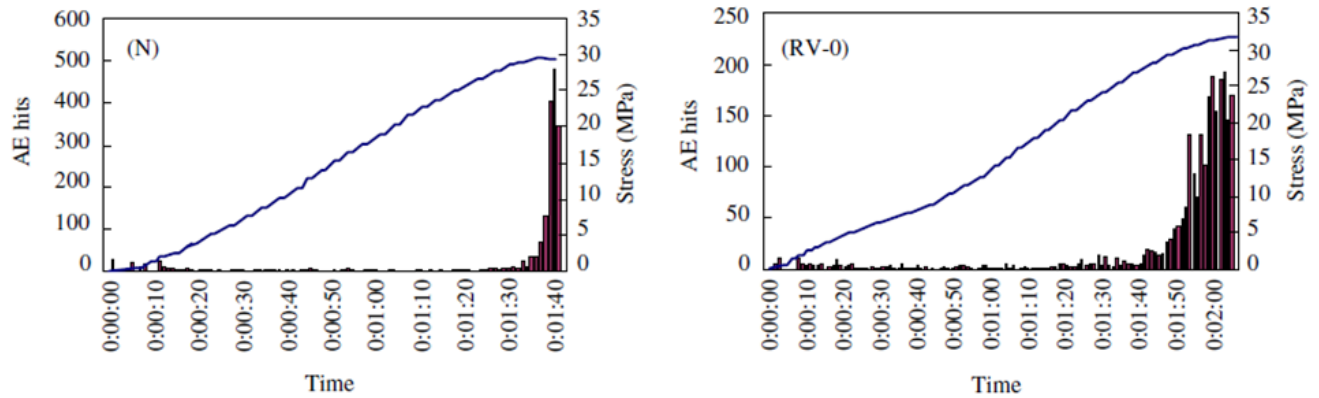


Figure 1.13: Correlation between stress and AE hits of NAC (a) and RAC (b) (Watanabe et al., 2007)

1.3.2 AE energy –fracture energy

AE energy is one of the AE parameters whose physical meaning can be correlated to the physical energy or fracture energy. The true energy is directly proportional to the area under the AE wave. For earth concrete mixtures, AE energy-fracture energy correlation was found for beams under flexion. Kouta (2020) correlated the AE energy to the flexural fracture energy of earth concrete mixture without fibers and others with fibers of different lengths and amounts. As shown in figure 1.14 (a) (left), it can be stated the two parameters are proportional. Similarly, Han et al. (2018) correlated the AE energy to the flexural fracture energy as shown in figure 1.14 (b). The mixtures differed in crumb rubber or waste tire amount to form recycled tire-rubber concrete mixtures. The amount ranged from 0% to 15%. Proportionality between the two parameters has been reported. However, for each study, it can be stated that different equations have been yielded.

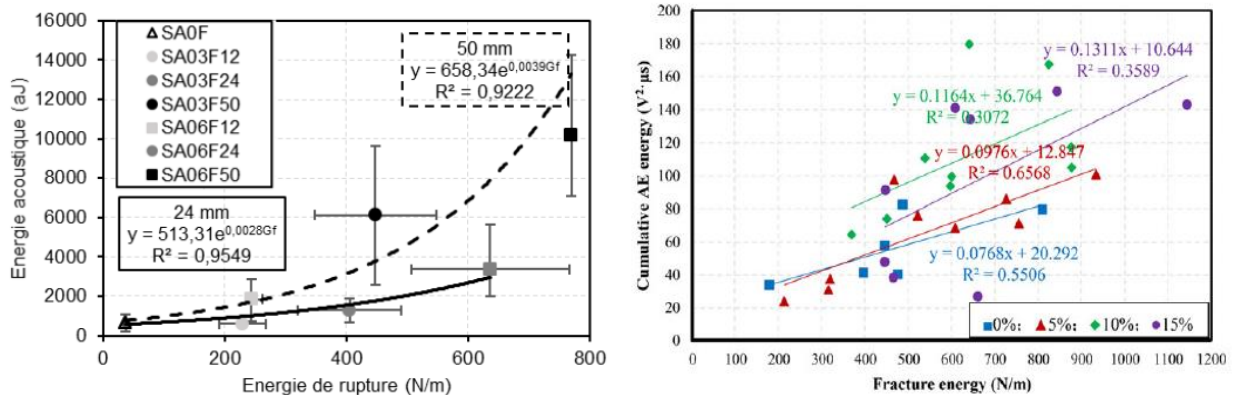


Figure 1.14: Correlation between fracture energy and AE energy of earth concrete mixtures with different fibers content and length (Kouta, 2020) (a) and recycled tire rubber-filled concrete mixtures (Han et al., 2018) (b)

1.3.3 Crack classification

Compressive failure is a much more complex phenomenon than tensile failure. The compressive failure behavior is related to the formation, propagation and coalescence of several microcracks. Furthermore, the volumetric observation of cracks in compression is different from that in tension. Theoretically speaking, vertical cracks are to be formed when concrete is under compressive external loading. Under such stresses, dilation takes place and thus lateral tensile failure occurs. Nevertheless, perfectly vertical microcracks would not be formed as the external compressive load induces a complex system of stresses. (Fardoun et al., 2020; Sagar et al., 2018). The loading plates restrict the specimen to expand laterally and accordingly a triaxial confined region is generated. Eventually, failure can be due to the effect of tension and shear.

Tensile cracks and shear cracks are the two common crack forms in concrete. By means of AE, it is possible to distinguish the two types by the two parameters rise angle (RA) and average frequency (AF) where:

$$RA = \frac{\text{rise time}}{\text{amplitude}} \quad (1-2)$$

$$AF = \frac{\text{counts}}{\text{duration}} \quad (1-3)$$

Figure 1.15 clarifies how the type of crack is reflected on the AE signal. It is generally believed that AE signal of shear crack has high RA value and low AF value, and AE signal of tensile crack has high AF value and low RA value.

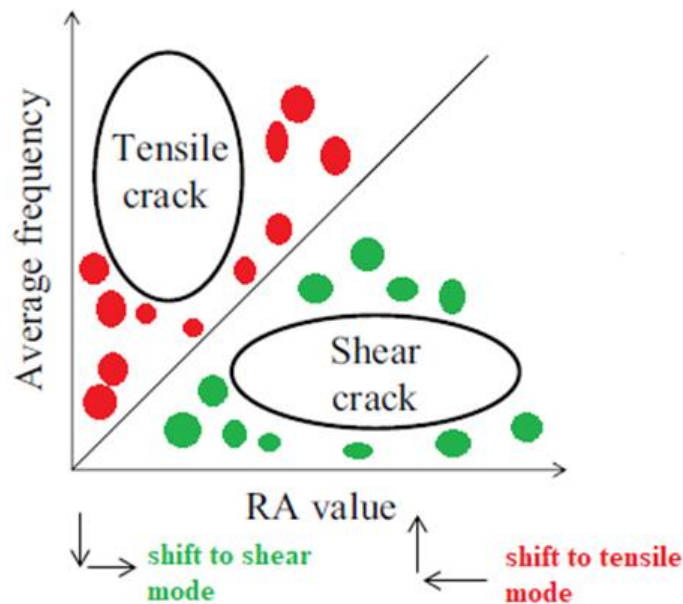


Figure 1.15: Crack classification based on RA and AF

However, there is no accurate classification standard for the two types of cracks. The RA and AF value ratios (RA/AF) were set to 10:1 in tensile tests of concrete (Ohtsu et al., 2007), 10:1 in recycled concrete subjected to monotonic loading (Watanabe et al., 2007), 1:30 in concrete beams under 4 point bending tests (Aggelis, 2011) and 1:80000 in reinforced concrete beams under 4 point bending tests (Aldahdooh & Muhamad Bunnori, 2013)...

Watanabe et al. (2007) assessed the types of cracks formed in NAC and RAC under compression loadings by means of the two AE parameters as shown in figure 1.16. The authors examined the type of crack until the maximum stress in three phases (1/3 of maximum stress of each phase). The results show that in NAC both types of cracks were formed in phase 1 and phase 3 while only tensile cracks were presented in phase 2. On the other side, shear and tensile cracks were formed in the three phases of RAC. The author stated that this reflect a lower quality of adhesion with the RCA.

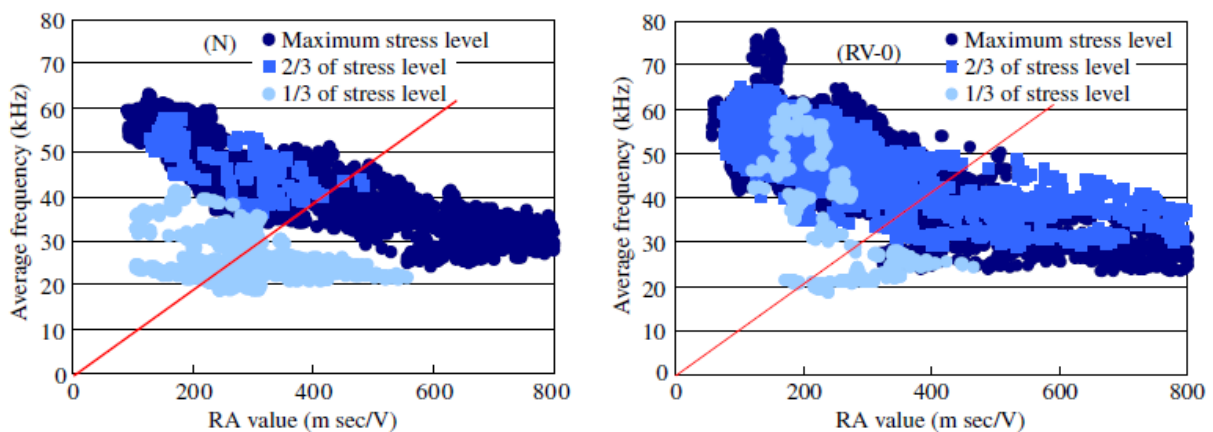


Figure 1.16: Crack classification based on AF and RA in NAC (left) and RAC (right) under compression loading (Watanabe et al., 2007)

1.4 Monitoring by digital image correlation (DIC)

When working with DIC, the field of view (FoV) of the camera has to match with the structure size. This is basically easy to achieve when working in a laboratory while complicated if a large structure is under assessment. If the structure or what being assessed is too large for the FoV, the camera then has to be re-positioned so that the distance increases and the FoV would be able to capture the object. Consequently, the camera spatial resolution decreases (Poozesh et al., 2020). After setting the camera's final position, the calibration of the DIC system is required to make accurate measurements (Ozbek et al., 2010).

DIC tracks points on the specimen's surfaces which are unique from one another. More particularly, it works by tracking group of neighboring pixels which are called subsets. The latter is user-defined. It should be large enough to provide unique speckle information for all subsets throughout the surface while remaining small enough to deliver a good spatial resolution. Classic correlation is as follows (where C is the correlation function, x and y are the pixel coordinates of

the reference image, u and v are the displacement (or the movement of the subset), n is the subset size, I and I^* represent the image before and after motion, respectively and the last term ($x + u + i, y + v + j$) corresponds to the pixel values after motion):

$$C(x, y, u, v) = \sum_{i, j = -n/2}^{n/2} (I(x + i, y + j) - I^*(x + u + i, y + v + j))^2 \quad (1-4)$$

The specimen has to be prepared by the application of a speckle pattern on its surface. To achieve uniqueness in information, the adopted pattern should be non-repetitive (random), isotropic (directionally independent) and in high contrast. Table 1.1 clarifies this. White dots on black ones or black dots on white ones meet the requirements. It is worth to note that a uniform dot size is important.

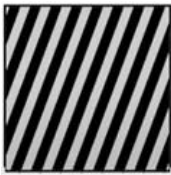
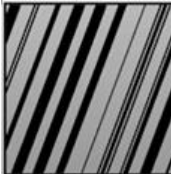
	Non-repetitive	Isotropic	High contrast
	✗	✗	✓
	✓	✗	✓
	✓	✓	✗
	✓	✓	✓

Table 1.1: The three characteristics of a speckle pattern

Illumination is considered to ensure high quality images (Pan et al., 2012). When DIC assessment is conducted in a laboratory, switching off lights to have a dark environment in the presence of another illumination source as LED flashlights (Ozbek et al., 2010) has proven its effectiveness. Illumination acts mostly to improve the third requirement of a speckle pattern as mentioned above: the image contrast.

DIC captures the strain and displacement at the surface. Figure 1.17 shows the strain fields (ϵ_{xx}) of an earth concrete mixture under uniaxial compression (Kouta, 2020). The damage increases with stress level.

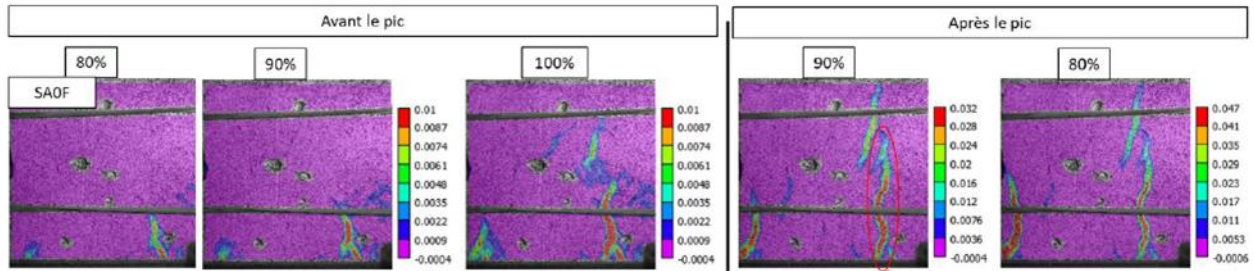


Figure 1.17: Strain fields (ϵ_{xx}) of earth concrete mixture under compression at different stress levels (Kouta, 2020)

1.5 Experimental program

1.5.1 Materials

1.1.2.2 Soil

The work considers four mixtures. A mixture that comprises an artificial soil with 30 % of clay and 70% of NS –NS30/70- and three others constituted of RS and 20%, 30% and 40% of clay named respectively: RS20/80, RS30/70 and RS40/60. The particle size distribution curves of the three components in addition to the four clay-sand mixtures are shown in figure 1.18. Sieving was adopted for particles of diameter greater than 0.08 mm (Standard AFNOR, 1995) while sedimentation was considered for the finer ones (NF (French Standards), 1992).

A non-swelling clay Kaolinite is used. Tests display a liquid limit and a plastic limit of 52.84% and 32.81%, respectively in addition to 0.5% water content as presented in table 1.2. The clay is classified according to the Unified Soil Classification System (USCS) as slightly plastic clay with a plasticity index I_p equal to 20.

Water content (%)	Liquid limit (%)	Plastic limit (%)
0.5%	52.84%	32.81%

Table 1.2: Properties of clay

The used NS is classified as a poorly graded sand with a small methylene blue value indicating that the sand is insensitive to water (Uniformity coefficient $C_u = 3.35$, and curvature coefficient $C_c = 0.58$). On the other side, RS is classified as a well graded sand with a methylene blue value

of 0.15 (sandy) (Uniformity coefficient $C_u = 13$, and curvature coefficient $C_c = 1.2$). RS was brought from a platform located in Merignac (a municipality in the south-west of France).

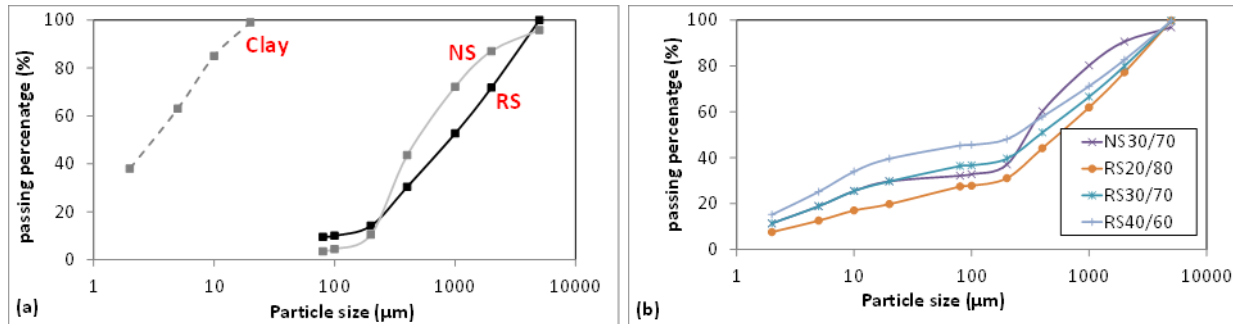


Figure 1.18: Particle size distribution of each component (a) and each clay-sand mixture (b)

The carbonation of RS was investigated by spraying an acid-base indicator (phenolphthalein) on the surface (figure 1.19 (a)). In fact, the hydrated products of the cement paste react with the carbon dioxide present in the atmosphere which reduces the pH of the pore solution. The results show that RS is highly carbonated with a PH lower than 9 except at some small areas.

The mineralogy of RS has been also studied using the X-ray diffraction (XRD) analysis (Smith et al., 2001). XRD patterns were obtained using a PANalytical PW3020 Bragg-Brentano θ - 2θ geometry diffractometer equipped with a secondary monochromator over an angular range $2\theta=3^\circ$ - 80° . Figure 1.19 (b) shows the XRD patterns where the obtained peaks were identified using an embedded database under EVA processing software. The diffractogram illustrates that the main minerals present in RS are: calcite, quartz and albite.

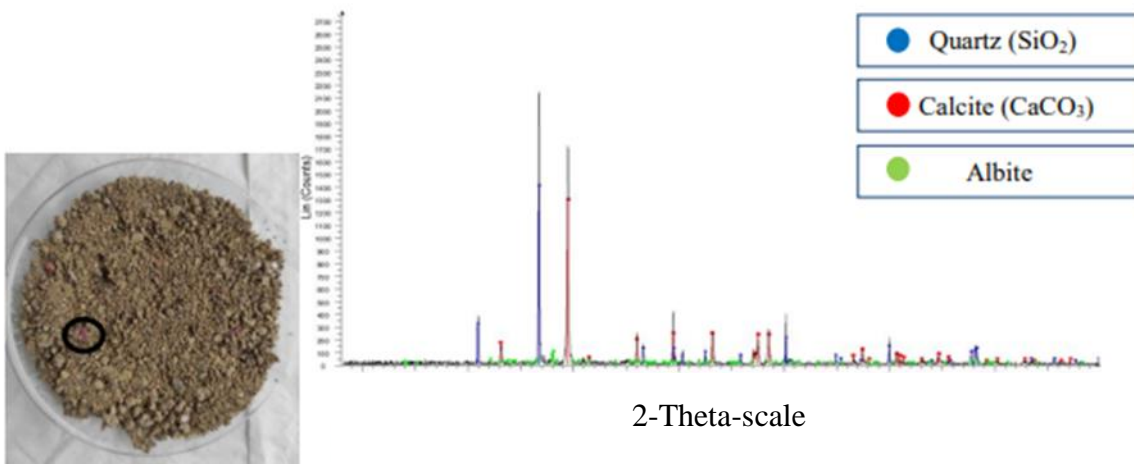


Figure 1.19: Surface of RS after being sprayed with phenolphthalein (a) and X-ray diffraction pattern of RS (b)

1.1.2.3 Water absorption

As stated, the knowledge of the water absorption (WA) capacity of RS is mandatory. The latter was determined based on the theory of the drying porous media (Quattrone et al., 2016). The drying taking place of fully saturated aggregate is expected to be of constant rate of evaporation. When the evaporation of exterior water ends, that of the pores starts and thus evaporation rate changes from constant into a decreasing one. At this transition point, the SSD is considered. The evaporation rate (R) can be determined by the following equation:

$$R = \left(-\frac{S}{A}\right) \left(\frac{dX}{dt}\right) \quad (1-5)$$

where S is the mass of dried solid (kg), A the area exposed to drying (m²), X the water content and t time. The test was done on five RS samples and three NS samples. NS and RS reported a water absorption value of $WA_{NS} = 1.02\%$ and $WA_{RS} = 14.6\%$, respectively. Figure 1.20 shows the rate of evaporation-water content curve of one of the RS samples that revealed a water absorption value of 13.63% (the standard deviation is 5.54).

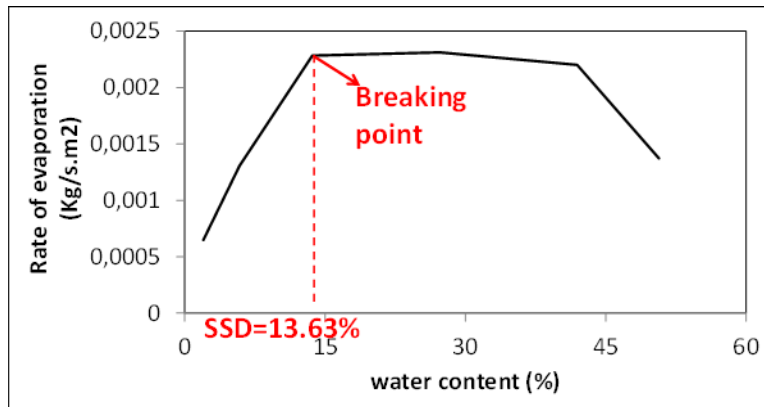


Figure 1.20: Determination of SSD point of RS based on the porous drying theory

1.1.2.4 Stabilizers

Cement is considered in the mixtures. A value of 9 % of dry solid mass was added. Table 1.3 shows its composition. Though this percentage is considered high, it is worth to note that it has been adopted in recent studies (Arrigoni et al., 2018). Furthermore, as going to be presented in the next section, the saturation degree trials done on RS30/70 –with 9% of cement- barely exceeds a compressive strength more than 2 MPa (which is the minimum compressive strength of rammed earth (Arrigoni et al., 2018).

Main components	C ₃ S	C ₂ S	C ₄ AF	C ₃ A	SO ₂ ,NA ₂ O, S ⁻
%	65	12	6	12	>5

Table 1.3: Cement components

1.1.2.5 Superplasticizers

Superplasticizers are being adopted to achieve workable mixtures. In the following work, Tempo 10 is used.

1.5.2 Preliminary tests and mix design

Preliminary tests were realized for the mixture with 30% clay and 70% RS (RS30/70). The considered pre-saturation degrees of RS are 50%, 80% and 100%. Pre-saturation takes place 24 hours before mixing (NAM, 2016). The effective water (w_{eff}) was considered as the total water (w_T) minus the water required for RS (w_{RS}) and that required for clay (w_{cl}) (as expressed in equations below).

$$w_{eff} = w_T - (w_{RS} + w_{cl}) \quad (1-6)$$

$$w_{RS} = w_{pre} - w_{c-RS} = (w_{sat} * \frac{(wa)_{RS}}{100} * RS) - \frac{w_{cRS}}{100} * RS \quad (1-7)$$

$$w_{cL} = W_{ll-cl} - W_{c-cl} = (\frac{w_{ll}}{100} * C) - (\frac{w_{cCL}}{100} * C) \quad (1-8)$$

Where:

w_{pre} is the water added for pre saturation

C is clay amount

w_{sat} is the saturation degree of RS

$(wa)_{RS}$ is the calculated water absorption of RS

w_{cRS} is the water content of RS

w_{ll} is the liquid limit of clay

w_{cCL} is the water content of clay

Note that for determining the water content of a certain component, 3 samples were taken from different positions of the bag as most probably each position differs in water content: from the top, middle and bottom of the bag. Table 1.4 presents the parameters' values and table 1.5 presents the mix designs. W_{cNS} and $(wa)_{NS}$ are the water content and water absorption of NS.

w_{ll}	w_{cCL}	wa_{RS}	w_{cRS}	wa_{NS}	w_{cNS}
52.84%	0.5%	14.6%	2.58%	1.02%	0.05%

Table 1.4: Water parameters' values

Components (kg/m ³)	Clay (C)	Sand (S)	Cement	w_{eff}	Superplasticizers
50%-SAT	366	855	110	214	1.32
80%-SAT	366	855	110	177	1.32

100%-SAT	366	855	110	152	1.32
----------	-----	-----	-----	-----	------

Table 1.5: Mix design of preliminary tests

Slump tests in addition to compression and flexural tests were carried out at the age of 7 and 28 days for mixtures with different pre-saturation degrees of RS30/70. The results are displayed in table 1.6. The overall goal of those preliminary tests is to verify to what extent the pre-saturation degree may affect the workability and the mechanical properties.

Property	50%-SAT (STD)	80%-SAT (STD)	100%-SAT (STD)
Slump	6.8	7.5	7.8
Compression strength at 7 days (MPa)	1.91 (± 0.12)	1.65 (± 0.14)	1.64 (± 0.14)
Compression strength at 28 days (MPa)	2.84 (± 0.11)	2.18 (± 0.07)	2.15 (± 0.15)
Flexural strength at 7 days (MPa)	0.75 (± 0.03)	0.64 (± 0.038)	0.63 (± 0.046)
Flexural strength at 28 days (MPa)	0.89 (± 0.05)	0.89 (± 0.03)	0.75 (± 0.03)

Table 1.6: Slump, compressive strength and flexural strength at different pre-saturation degrees of RS30/70

Table 1.6 shows that slump values decrease with lower degrees of pre-saturation. However, the differences in slump did not exceed 1 cm between mixtures. A slight decrease in the compressive and flexural strengths has been observed as the pre-saturation rate increases. The difference of strengths between the 80%-SAT and 100%-SAT is less remarkable compared to those between 50%-SAT and 80%-SAT. It is believed that the interfacial transition zone (ITZ) is influenced by the saturation states of RS. Zhao et al. (2015) revealed finer ITZs when RS are introduced in their dry state compared to those introduced in their saturated state.

The choice in this study was more governed by slump values. Aiming to workability not less than 7 cm, 80% pre-saturation was carried out 24 hours prior to mixing.

The mix designs of the four mixtures following the procedure above are presented in table 1.7.

Components (kg/m^3)	Clay (C)	Sand (S)	Cement	W_{eff}	Superplasticizers
NS30/70	440	1026	132	140	1.32
RS20/80	271	1084	122	167	1.32
RS30/70	366	855	110	177	1.32
RS40/60	460	690	103	187	1.32

Table 1.7: Mix design of the four mixtures

1.5.3 Experimental procedure

1.1.2.6 Compressive tests

10x10x10 cm³ cubes were casted for all mixtures. Demolding was done 3 days after casting and cured at a relative humidity (RH) of 90%. Compressive tests were carried out at the age of 14, 28

and 90 days after casting. An electro-mechanical machine with a capacity of 100 kN was used. The loading rate was modified at two different positions in the post-peak regions (80% and 30% of peak stress) to reduce the experiment time. The adopted loading rate values were 0.5 mm/min, 1.5 mm/min and 4.5 mm/min.

1.1.2.7 Acoustic emission (AE)

The AEWIN acquisition system with a data analysis and storage system was used. 8 R15 piezoelectric sensors were placed on two opposite sides of the specimens using a thin layer of silicone to ensure a good coupling and signal capture. The detected signals were amplified with a 40 dB differential amplifier. The detection threshold was set at 33 dB to avoid the effect of possible noise development. The 8 piezoelectric sensors position allows to cover the whole surface and to localize damage in 3D with better precision. Figure 1.21 shows the sensor's positions.

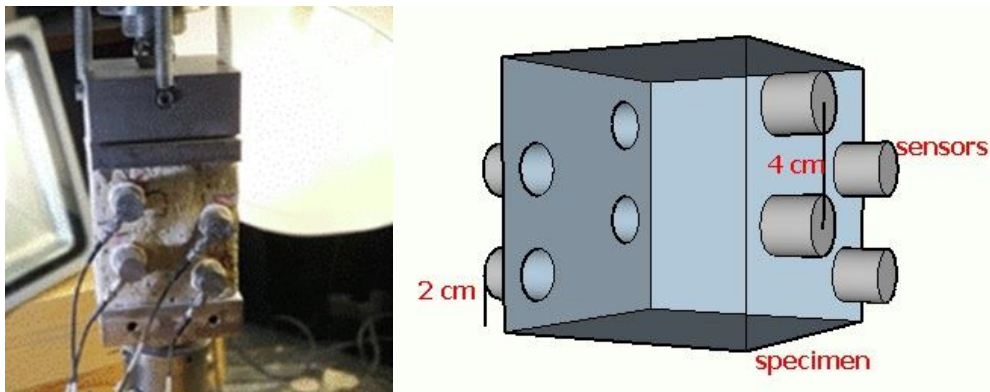


Figure 1.21: Piezoelectric sensors' position

1.1.2.8 Digital image correlation (DIC)

Image treatment processing was performed using the commercial VIC 2D software with a resolution of 0.05 mm per pixel. The specimen's surface was sprayed by a white speckle followed by a black one prior to testing. The cameras' resolution was of 2452x2056 pixels. Two lamps at each side were set to enhance brightness.

1.1.2.9 Strain measurement

Figure 1.22 (a) shows the cameras and lights used in DIC as a part of the compressive test setup in addition to markers placed at the loading plates and press. Figure 1.22 (b) shows the stress-strain curves obtained from different approaches. For the DIC method, the strains of the whole surface were exported directly from DIC. For the two other methods, the strain was derived based on the marker tracking according to the loading plate and the press displacement using the camera. It can be noticed that VIC 2D software was not able to capture the strain in the post peak region. In fact, the consideration of a two dimensional (2D) processing requires the specimen to

be flat, planer to the imaging center and at a constant distance perpendicular to the visual sensor during the whole experiment which was not achieved after the peak. It can be noticed that the slope value of the linear phase is more important with DIC approach and basically it is more representative of the real strain of the material. Nevertheless, aiming to deliver an integral work as possible and being interested in the fracture behavior, in the following chapter, the full stress-strain curves are presented based on the loading plate method.

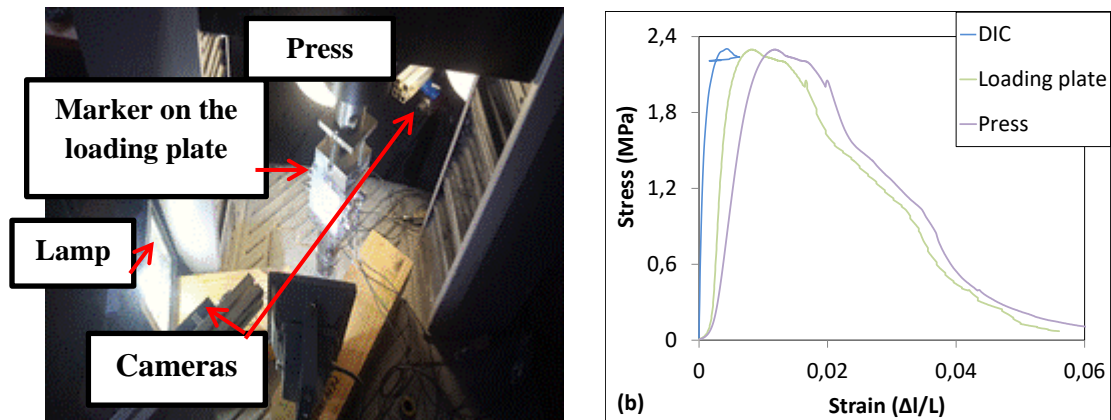


Figure 1.22: Cameras and lights for DIC as a part of the compressive test setup and stress-strain curves obtained with different methods (b)

1.6 Results

1.6.1 Mechanical properties

Figure 1.23 shows the stress-strain curves of the different mixtures obtained at the age of 14, 28 and 90 days. The local increase of stress captured at certain points in the post peak region can be attributed to the change in loading rate as mentioned earlier.

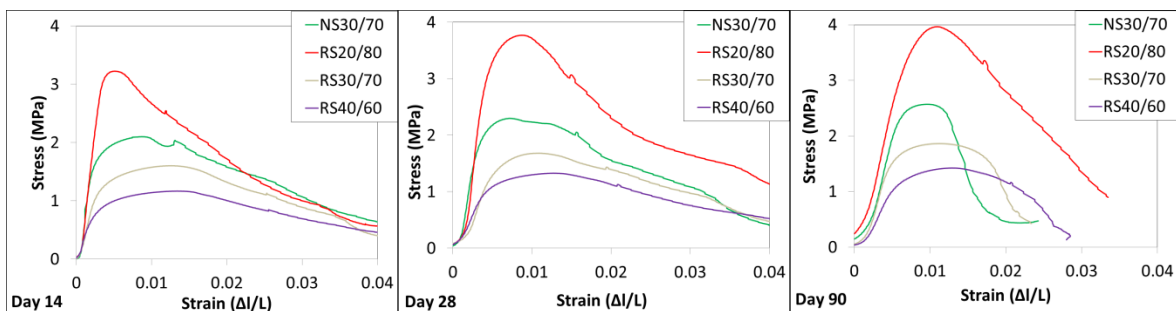


Figure 1.23: Stress-strain curves of each mixture at different curing ages

Based on those curves different parameters were calculated. Figure 1.24 (a) shows the evolution of the compressive strength with age for the different mixtures. RS20/80 reported the highest compressive strength. It can be noticed that this mixture exhibited the highest variability in

strength. This can be attributed to the high RS amount that accordingly possesses an important solid skeleton and heterogeneity.

The compressive strength decreases as RS replaces NS. This degradation in strength can be attributed to the fact that more water was required to compensate the loss in workability due to the high water absorption of RS. In addition, the bad state –presence of cracks and pores- in RS might have weakened the mixture’s mechanical properties (Wang et al., 2020). In the same way, high clay content requires more water and thus a decrease in strength was revealed as the percentage of clay increases. As the compressive strength decreases with clay content, this may give a sign that clay inclusion above 20% in earth concrete make them loose their filler effect that is known to contribute positively to strength (Avrami et al., 2008).

The compressive strength increases with age for the different mixtures. Figure 1.24 (b) shows the change in strength development with respect to the previous compressive strength and age. Equation 1-9 clarifies the calculation of the strength development where CS_2 and CS_1 represent the second and previous compressive strengths, respectively.

$$\text{strength development (\%)} = (CS_2 - CS_1) \times 100 / CS_1 \quad (1-9)$$

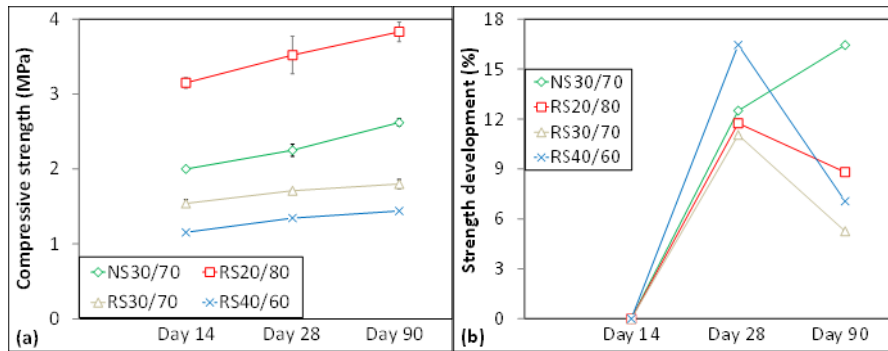


Figure 1.24: Evolution of the compressive strength of the different mixtures with age (a) Change in strength development with respect to the previous strength and age (b)

An important increase in strength has been observed between 14 and 28 days for the different mixtures (12% for RS30/70 to 17% for RS40/60). At the age of 90 days, the NS mixture NS30/70 reported a ‘positive’ strength development. In other words, its increase in strength from day 28 to day 90 was higher from that obtained between 14 and 28 days. Nevertheless, this aspect was not reflected in RS mixtures. Indeed, the effect of RS (or recycled aggregate) on the long-term concrete strength has been controversial. González-Fonteboa, & Martínez-Abella (2005), Yang et al. (2008) and others reported higher increase in recycled aggregate concrete strength at advanced ages while recently Meng et al. (2021) stated a higher strength development in natural aggregate concrete. Ulloa et al. (2013) reported both trends in his work. While the better enhancement in strength in natural aggregate concrete is being assigned to the general known defects of recycled aggregate, the higher level of strength improvement in recycled aggregate concrete has been

attributed specifically to the cementing action of unhydrated cement paste on aggregates' surfaces in addition to carbonation.

Many efforts have done on crack localization behavior in tension. Such localization has been modeled by a stress-crack width relationship based on the tensile fracture energy. On the other side, it was alleged that fracture zone under compressive tests is not accurately determined. In the following study, the fracture energy is considered as the post peak area under the load-displacement curves until a residual strain of 20% of peak stress as shown in figure 1.25 (a) (Nakamura et al., 2018). This plastic energy is believed to be independent of specimen size and geometry. Figure 1.25 (b) shows the change in fracture energy for the different mixtures as function of the curing age. At the age of 90 days, the fracture energy exhibited its lowest value pointing out that earth concrete behaves in a more brittle way with curing age. RS20/80 - the mixture with the highest sand content and strength- exhibited the highest fracture energy followed by NS30/70 and then RS30/70 and RS40/60 following the same trend as the compressive strength.

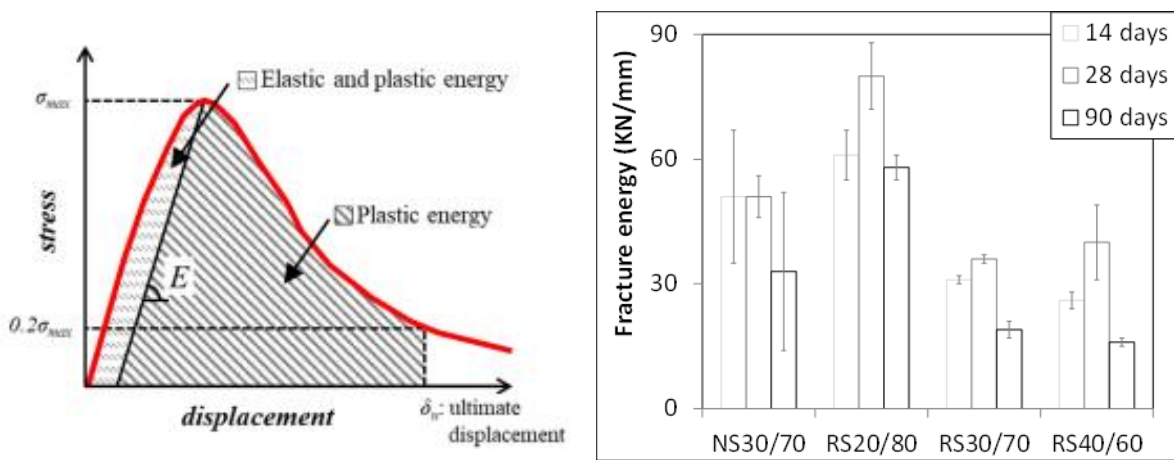


Figure 1.25: Determination of fracture energy (Nakamura et al., 2018) (a) (left) and fracture energy of each mixture at different curing ages (b) (right)

1.6.2 Correlation of stress and AE activity

Figure 1.26 shows the correlation between stress and AE activity represented by the amplitude and the cumulated number of AE hits for the four mixtures at the age of 14, 28 and 90 days. The number of AE hits as function of time in all drawings is presented in a way to take the full y-axis of the figure so the change in the slope is clearer. This way permits to better correlate the stress to AE activity. Only in this section, phase 3 is treated as one part and when necessary phase 4 is divided.

a) Phase 1: Compaction phase

The AE activity in this phase is remarkable. A compaction process may have taken place until a limited stress level. During this compaction phase, there is no formation of new cracks. The AEs

recorded are mainly due to pre-existing cracks' and pores' closure at initial loadings. Other source of AE activity might be linked to the friction with plates and stress concentration.

b) Phase 2: Linear phase

Very often, this phase is considered elastic. However, earth concrete exhibits inelastic strains during this phase. Yet by means of AE technique that reflected this stage by low AE activity, it can be stated that the linear phase evidences limited and few cracks' development.

c) Phase 3: stable growth and unstable growth of cracks

At different occasions, the AE activity during phase 3 is of increasing tendency (NS3070 at 14 days and 28 days). The shift into a higher AE activity indicates that the degree of damage is higher and that the rate of damage is increasing. Eventually, this phase can be composed of two parts (according to chapter 2 as going to be shown, the first part may be called the phase of stable growth of cracks and the second part may be called the phase of unstable growth of cracks).

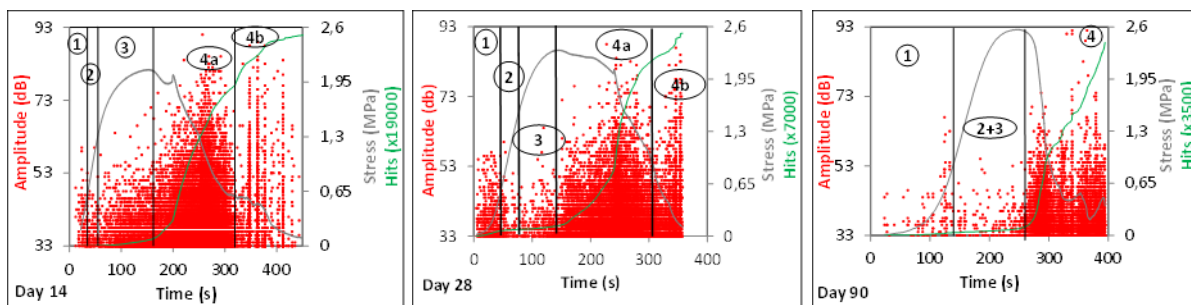
At curing age of 14 and 28, the AE activity in NS30/70 during this stage is higher than RS30/70 and all other mixtures though it is of not highest strength. In fact, the possible lower ITZ properties of RS mixtures due to the fact that it is porous and due to the pre-saturation took place for RS (Zhao et al., 2015) may be behind the lower AE activity in RS mixtures.

Eventually, it can be noticed that the pre-peak AE activity of each mixture decreases with age reaching its lowest count at 90 days. This can be attributed to the increase in strength with age.

d) The post peak phase

The softening phase is the phase where the material breaks down. Macrocracks are formed. Their formations are reflected by a sharp increase in the number of AE hits and levels of amplitude to decrease after that at different occasions declaring the stable propagation of cracks (phase 4b). At a curing age of 90 days, a delay in macrocrack formation can be noticed particularly for NS30/70 and RS20/80 pointing out to a more brittle behavior. Based on the stress-strain curves in figure 1.23 and the correlation between stress and AE curves in figure 1.26, it can be noticed that RS30/70 is more ductile than NS30/70 from one side and RS4/60 more than RS20/80 from other side. Thus, the replacement of NS by RS and the increase in clay content enhances the fracture toughness –which is the ability to resist brittle failure- of earth concrete.

NS30/70



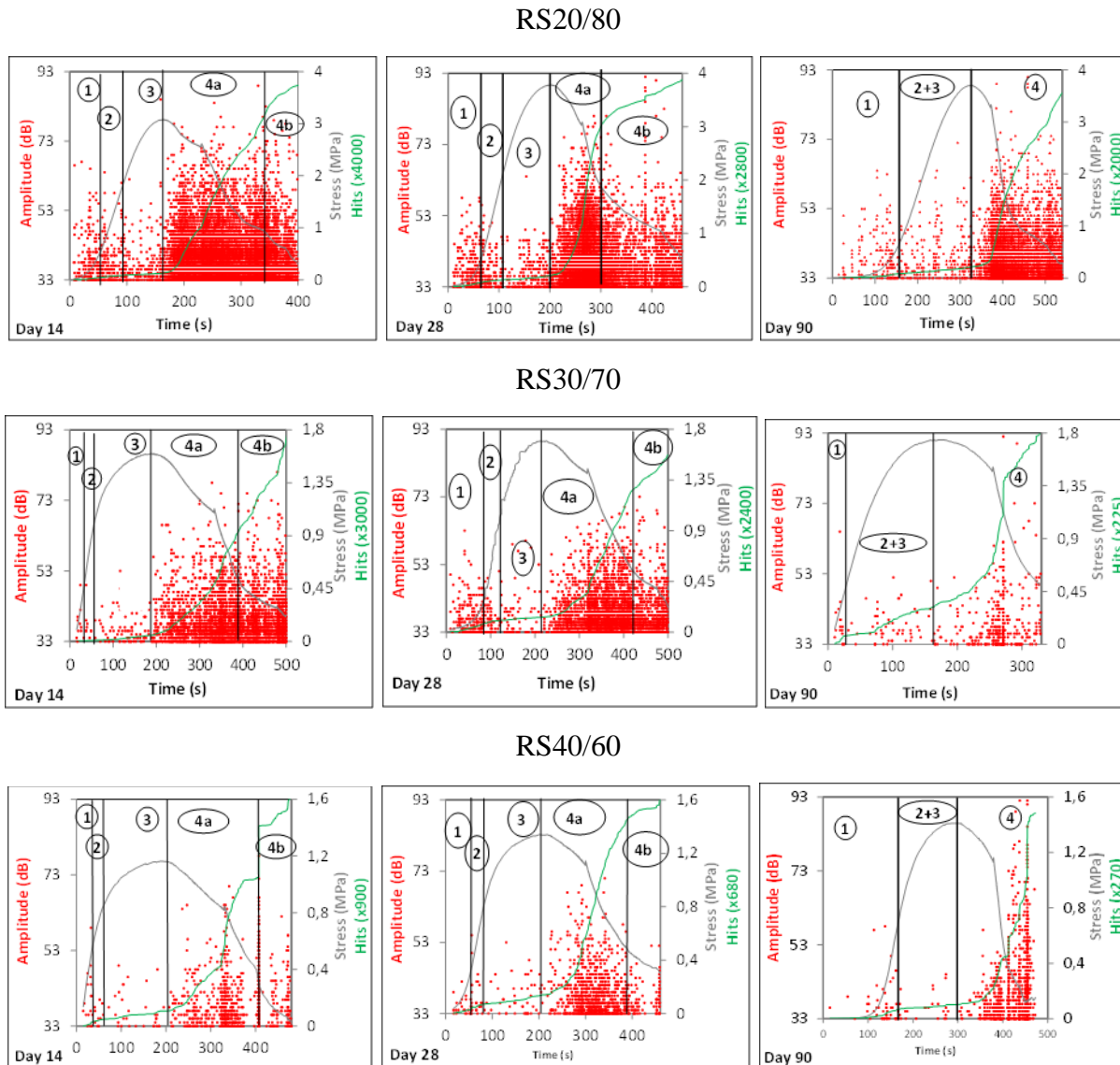


Figure 1.26: Correlation between stress and AE activity of the different mixture at different curing ages

1.6.3 AE energy – fracture energy

It is aimed from this section to verify whether proportionality exists between AE energy and fracture energy for the different mixtures with age. As stated before, the latter has been considered as the post-peak area under the load-displacement curves until 20% of peak stress.

Figure 1.27 shows the AE energy and the considered fracture energy of each mixture at different curing ages. NS30/70 reported highest AE energy though it is not of highest fracture energy. Thus the correlation between AE energy and fracture energy is unsuccessful. This may confirms with highest AE hits in NS30/70 at day 14 and day 28 as stated the previously and that NS30/70 is of better ITZ properties.

The generated AE energy increased with the fracture energy at different occasions. The fracture energy at 14 and 28 days of NS30/70 and RS30/70 were of significant differences confirming with the differences in the AE energy. These great differences in AE energy between NS30/70 and RS30/70 confirm that RS mixture (RS30/70) is weaker as it has original defects. A lower AE energy in RS30/70 compared to NS30/70 reflects the lower ITZ properties, pre-saturation and the possible internal damage in the former that have led to lower strength.

At 90 days, RS30/70 and RS40/60 exhibited very close fracture energy and AE energy values. Moreover, NS30/70 and RS20/80 reported decrease at 90 days. This decrease in the AE energy can be attributed to the higher degree of brittleness experienced by these two mixtures at 90 days. A remarkable change in AE energy may be considered as an indicator to a change in the fracture behavior of the material.

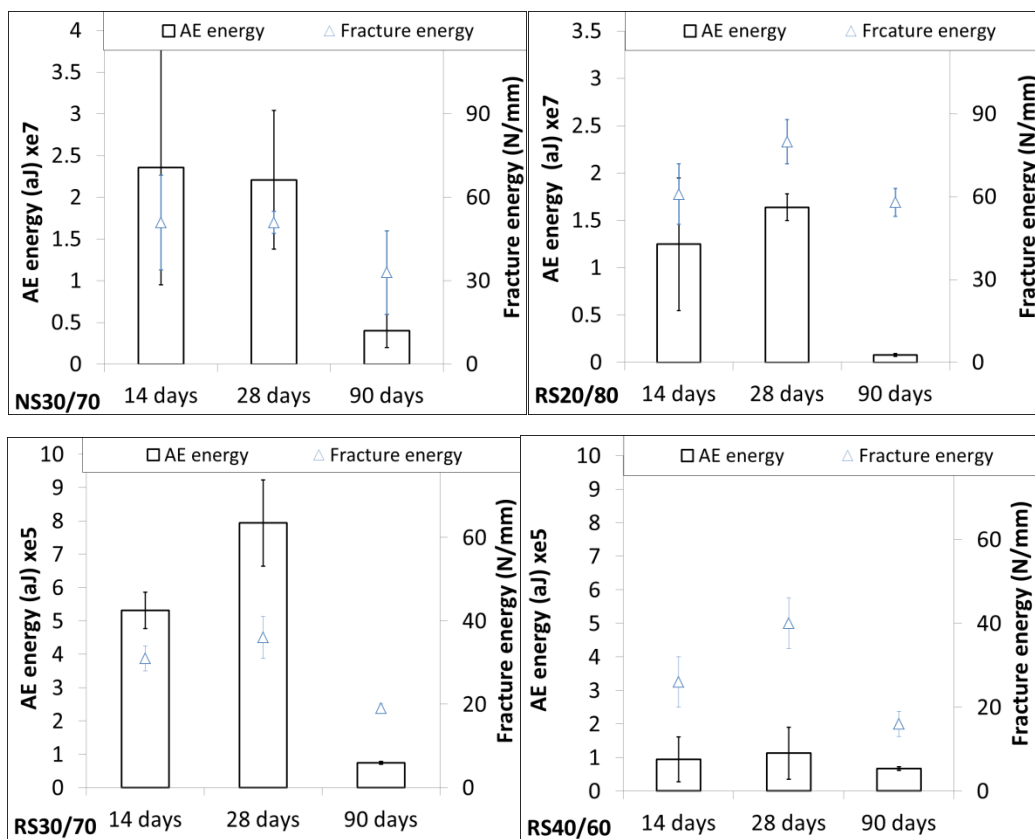


Figure 1.27: Correlation between AE energy and fracture energy

1.6.4 Correlation between DIC and AE events localization maps

An AE event located in 3D refers to the capture of a signal by at least 4 sensors. AE events are signs of cracks' formation. Figure 1.28 shows the localization of AE events for the different mixtures at different curing ages is displayed. The phases are designated as function of stress level as follows for all mixtures: (1) compaction phase (0-20%), (2) linear phase (21-45%), (3a) stable growth –of cracks- (46-79%), (3b) unstable growth (80-99%) and (4) the softening phase

(100-180%) (more explanation is presented in chapter 2) . It is worth to note that attenuation is higher with the increase of clay content in RS mixtures which may be responsible of the decrease of detected AE events. In addition, it shows the evolution of strain field in x-direction (ϵ_{xx}) for specimens at 28 days at peak stress in addition to final failure mode.

Regarding DIC, it can be noticed that damage is more severe in RS30/70 than NS30/70 and in mixtures of higher clay content than RS20/80. Regarding final failure, similarity is basically reported. Theoretically speaking, vertical cracks are to be formed when concrete is subjected to compressive loading. Nevertheless, perfectly vertical microcracks would not be formed as the loading plates restrict the specimen to expand laterally and accordingly a triaxial confined region is generated. Eventually, failure can be due to the effect of tension and shear.

At each curing age, NS30/70 exhibited few AE events in the compaction phase. However, RS20/80 revealed multiple events in this phase at all curing ages and similarly RS30/70 did at 28 days. As stated before, the compaction phase is characterized by closure of cracks and pores rather than the formation of new cracks. As RS is known to possess original defects, a remarkable number of AE events can be expected in RS mixtures during the compaction phase.

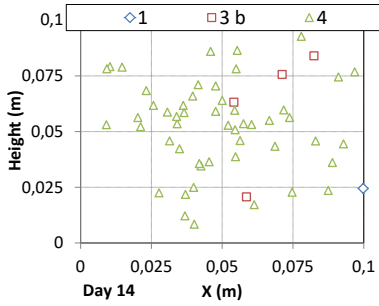
During the linear phase, NS30/70 did not show any single event at the curing ages of 14, 28 and 90 days. Nevertheless, RS20/80 exhibited multiple events in this phase at all curing ages. Furthermore, events were reported in phase 3a in RS20/80 contrary to NS30/70. This may indicate that the RS mixture is more vulnerable to damage at lower stress levels. During the 3b phase, NS30/70 reported multiple events at 14 days to generate only one at 28 and 90 days. This decrease in the number of AE events may be attributed to the increase in strength with age. The overall number of softening events decreases at 90 days. This can be attributed to the less ductile behavior evidenced by the materials in addition to speed change (Sagar et al., 2018).

The events of the softening phase can be noticed at different locations in NS30/70. However, the most gathering of events are basically detected in the middle of the specimen. This is due to the final failure mode as presented. To the contrary, it can be noticed at multiple occasions - particularly at 90 days- that AE events at early loading levels were basically closer to the loading plates which are due to specimen-loading plate contact.

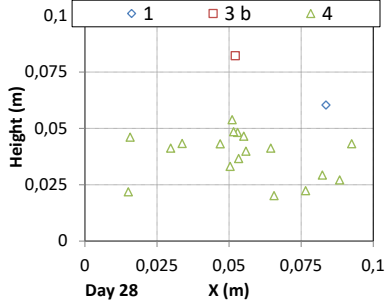
Multiple events have been captured at the top right of RS20/80 specimen at 28 days. To better understand this, the energy map (in aJ) of events is presented. It shows that these events are of considerable absolute energy (as highlighted in a circle). The verification with the DIC and cameras' photos showed the presence of a macrocrack at this region. Thus, the applicable correlation between AE events and the generated macrocrack in compression test can be attributed to the consecutive generation (and in a short time) of the five events (of considerable energy) at the top right for RS20/80 at the age of 28 days. It might be worth to note that the cameras and AE sensors correspond to adjacent specimen sides. Nevertheless, the complete detachment of the specimen sides and the sensors ensures the link between the AE events and the macrocrack.

NS30/70

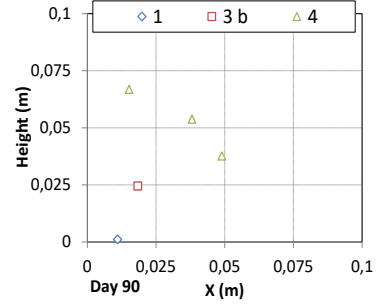
DAY 14



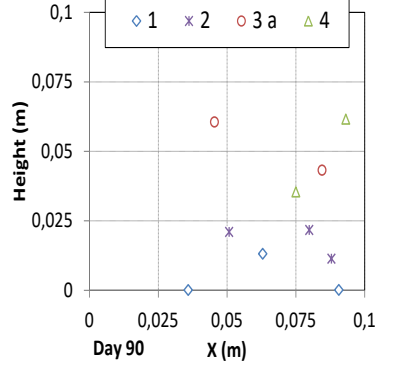
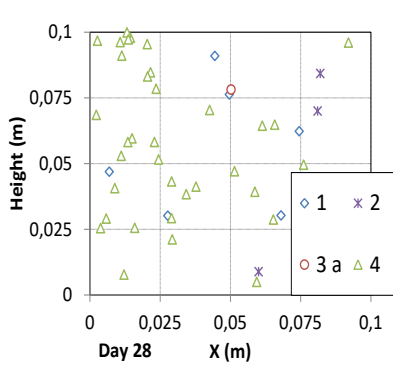
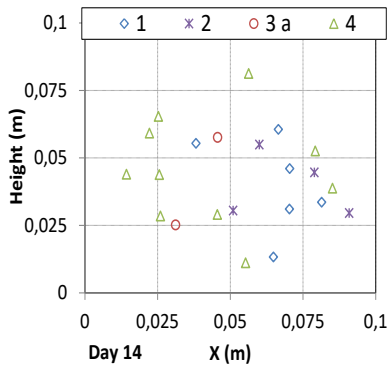
DAY 28



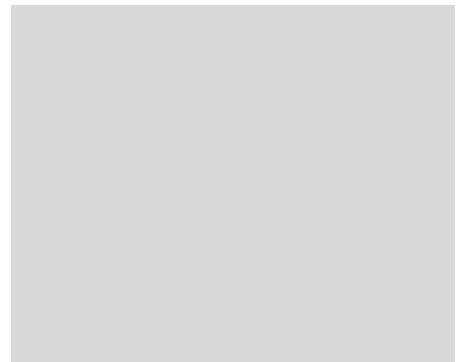
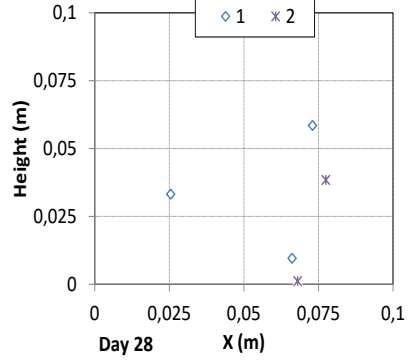
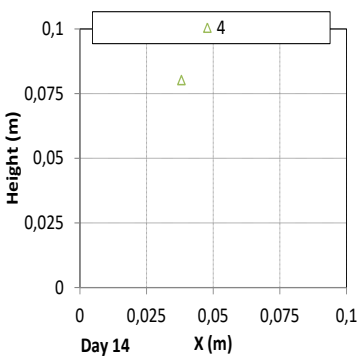
DAY 90



RS20/80



RS30/70



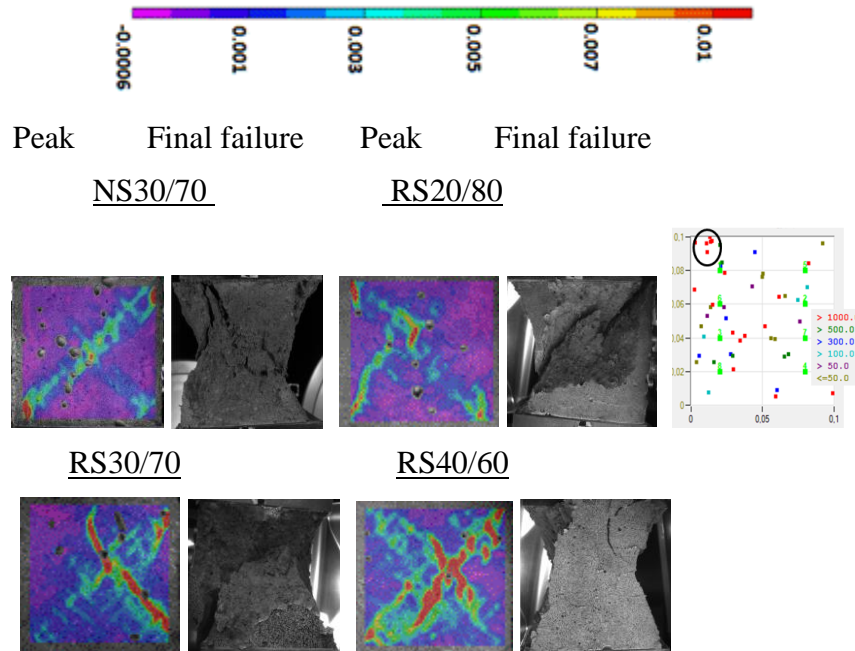


Figure 1.28 : Strain fields (ϵ_{xx}) and the transition of AE events throughout the five phases of the fracture process at the different curing ages

1.6.5 Warning sign of potential failure of earth concrete mixtures

By means of DIC or the normal photos presented in the previous section, the differentiating of types of cracks of cubes under compression is not a usual task. Nevertheless, the classification of tensile and shear cracks based on the relationship between RA is widely accepted. RA and AF were used to monitor damage evolution from tensile micro-cracks to brittle macro-cracks and failure modes of various concrete structures. A straight line is used to classify AE signals generated during the failure of specimens. This line depends on the material and type of loading and consequently different RA-AF ratios can be found in the literature. However, AE characteristics of earth concrete have not been studied in controlled laboratory and thus there is a lack of such information.

Some studies adopted cluster analysis to better distinguish shear cracks from tensile cracks. Ohno and Ohtsu (2010) may be the first who compared the results of concrete using SiGMA and parameter analysis and then verified the precision of RA-AF ratios. A recent attempt to achieve better precisions was carried out based on statistical analysis of dominant frequency characteristics of AE waveforms.

The approach carried out in this study to locate the RA-AF line basically was inspired by the criteria adopted by study in 2011 (Aggelis, 2011). The author assumed for the assessment of steel fiber-reinforced concrete damage that AE activity before the formation of the major crack is mainly of tensile type due to matrix cracking. After the major crack, due to the friction between the fibers and the surrounding concrete matrix, the AE events were considered of shear type.

Accordingly, figure 1.29 shows correlation between stress level and RA (figure 1.29a) and AF (figure 1.29b) as function of time for NS30/70. After the peak stress or major crack, RA of values more than 1 were highly reported contrary to the linear and non-linear phases before peak stress. On the other side, hits of AF less than 167 KHz were highly generated starting from the peak. Eventually, the ratio 1:167 or 3:500 was adopted as presented in figure 1.29 below.

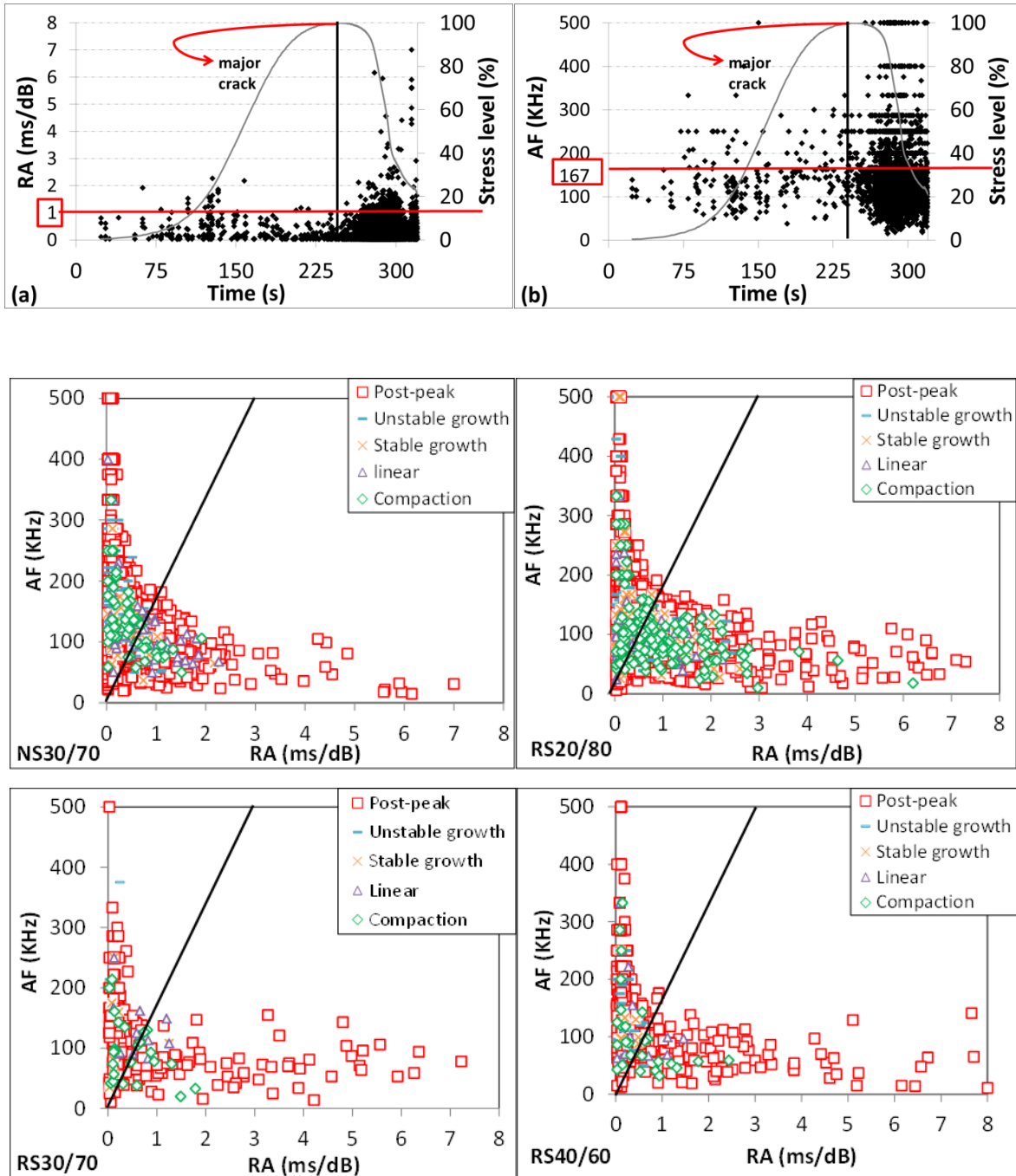


Figure 1.29: The criteria behind the adopted line and RA-AF diagrams of the four mixtures at 90 days

Figure 1.30 shows, based on figure 1.29, the tensile AE hits and AE energy from one side and the shear AE hits and AE energy from other side of each mixture for the four pre-peak phases. The results show that during the compaction phase, both hits are present. RS20/80, the mixture with highest RS content, generated the most of AE hits in this phase confirming with the results of the previous section. Past research reported low AE energy levels during this phase attributing it to the fact of no formation of new cracks (Xie et al., 2020). The important AE shear levels exhibited particularly in NS30/70 during the compaction phase here –with respect to softening phase- may be due to probable crushing and flatness irregularities with the loading plate.

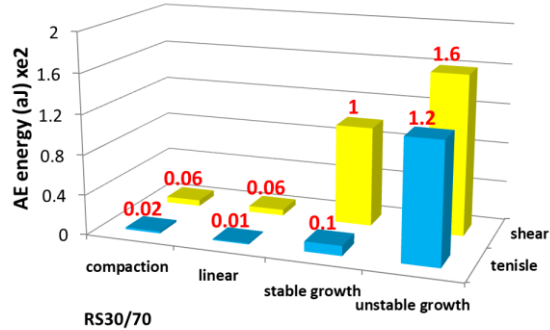
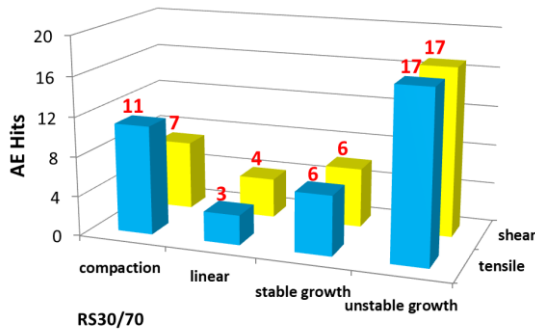
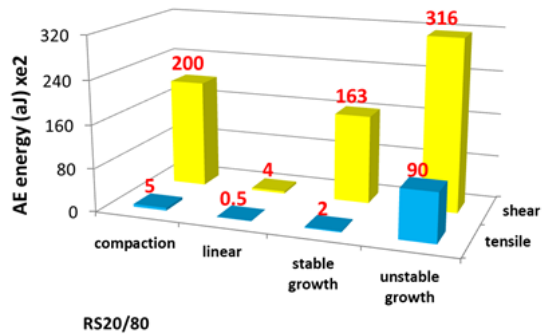
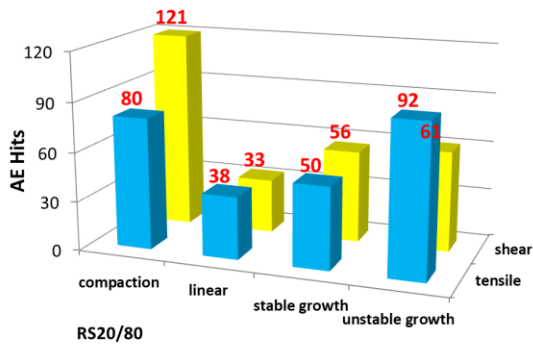
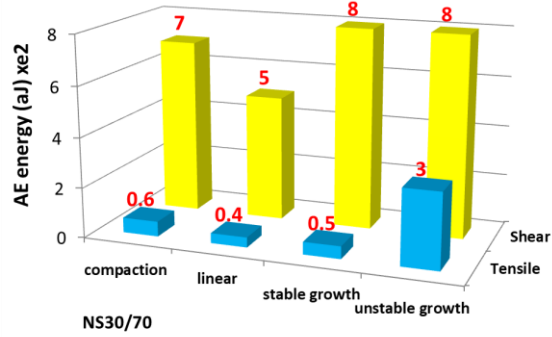
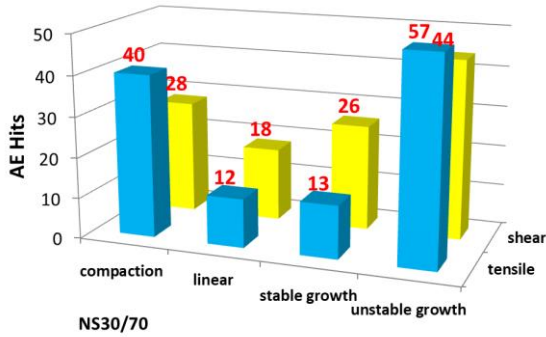
In the two subsequent stages that correspond to the initiation and propagation of microcracks, both shear and tensile hits are presented but still the shear ones are dominant. This was accompanied by mostly higher shear AE energy. In fact, the cracking behavior during tensile cracking and shear cracking is different (Du et al., 2020). The tensile cracks are mainly intergranular crack that basically propagate along the internal microstructure surface while shear failure comprises both intergranular cracks and transgranular cracks. Generally speaking, the energy released by transgranular cracks is of higher energy. Thus, under similar conditions, more AE energy can be expected in shear failure than tensile failure.

The hits continue to generate until reaching the phase that comes before the peak. Unlike the previous stages, the shear hits are not dominant anymore. The rate of tensile cracks increases. This reflects the higher degree of dilation experienced by the earth concrete specimens under uniaxial compression loading during this phase. It is worth to mention that the tensile strength of earth materials is very low. In terms of energy, the shear AE energy is higher than the tensile AE energy as expected.

It can be noticed that the number of AE hits of RS20/80 during these pre-peak phases at 90 days reported the highest compared to other mixtures. This contradicts with the outcome at 14 and 28 days where NS30/70 generated the largest number of hits at these ages. This may be attributed to the higher strength development experienced by NS30/70 as already demonstrated in figure 6 (b). On the other side, despite the higher AE hits of RS20/80 in the linear phase that represent crack initiation, the released AE energy was less than that of NS30/70 (400 aJ for RS20/80 and 500 aJ for NS30/70). This can indicate that NS30/70 requires more energy to form a crack than RS20/80 and thus declaring a better ITZ property in the former. This ensures the analysis carried out previously.

Eventually, the primary goal from AE analysis is to provide beneficial information to engineers so that they are able to prevent the failure of a structure. In real structures, the degree of damage depends on the phase it's going through. Structures outside are mainly in the linear and non-linear phases (Wu et al., 2019). As stress level increases, the material goes through different phases. The non-linear phase is what matters most and particularly the unstable growth phase as it comes directly before the peak.

According to the results, the shift into higher tensile energy can be a sign of a shift from the stable growth phase to the unstable growth phase. It can be noticed that the AE tensile energy increases in the unstable growth phase while it was of insignificant values in the previous three stages. Therefore, the shift into high tensile energy in earth concrete may be a sign of potential coming failure.



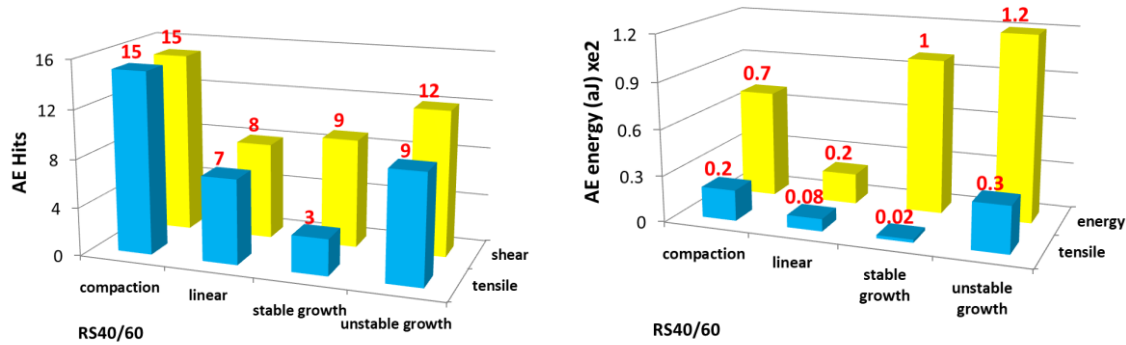


Figure 1.30: AE hits and AE energy of each mixture as function of different phases

Conclusions

The fracture behavior of earth concrete mixtures prepared with natural sand or recycled sand with different amount of clay was assessed under uniaxial compression by means of AE technique in addition to DIC technique. The conclusions are as follows:

- The compressive strength decreases when RS replaces NS and with clay content which can be attributed mainly to the both components –RS and clay- requirements for water. The same trend was revealed for fracture energy. In addition, the NS mixture exhibits higher percentage of strength development at long term than RS mixtures. However, the fracture toughness of earth concrete increases with RS and clay.
- Higher AE activity was reported in the pre-peak phase of NS30/70 at 14 and 28 days which may indicate lower ITZ properties in the RS mixtures. Moreover, an unsuccessful correlation has been observed between AE energy and fracture energy at 14 and 28 days with higher AE energy in NS30/70 which may ensure that NS30/70 if of better ITZ properties. The brittleness experienced by NS30/70 and RS20/80 at 90 days was reflected by a decrease in AE energy.
- The Correlation between AE and DIC for specimens under flexion is considered a basic task and to our knowledge it is always successful. However, the attempts to correlate them for compressive tests have never been clear. The following study revealed that the correlation between AE events and DIC under compressive loadings seems applicable in case of consecutive high energized AE events generation.
- The fracture process has been distinguished by different phases as follows: compaction, linear, stable growth –of cracks-, stable growth and softening. RS mixtures generate more AE events in the compaction phase than NS mixture due to the pre-existing pores and cracks. In addition, RS mixtures exhibited AE events at earlier stress levels which may indicate an earlier initiation of cracks. All phases reported higher shear AE hits and shear AE energy except the unstable growth phase which directly comes before the peak

reported higher tensile AE hits and remarkable increase in AE energy and thus it can be considered as a future potential failure. Furthermore, shear cracks are dominant in the post-peak region of earth concrete mixtures and thus they are more responsible for the final collapse.

Chapter 2 Hygric properties and damage monitoring of earth concrete mixtures at different curing conditions43

2.1 Drying 43

2.1.1 Migration of water and air..... 44

2.1.2 Approaches to model drying 45

2.1.3 Convection 47

2.2 Drying shrinkage..... 47

2.2.1 Clay content and plasticity index 47

2.2.2 Clay mineralogy..... 48

2.2.3 Density 49

2.2.4 Soil structure 49

2.2.5 Water content 50

2.2.6 Rate of desiccation 50

2.2.7 Modeling of drying shrinkage..... 52

2.3 Capillary suction effect 54

2.3.1 Surface tension and contact angle 54

2.3.2 Young-Laplace equation 55

2.3.3 Kelvin equation 55

2.3.4 Capillary rise 56

2.3.5 Effect of clay content 57

2.3.6 Effect of temperature (T) and relative humidity (RH) 57

2.4 Carbonation..... 59

2.5 Experimental program 60

2.5.1 Materials and mix design 60

2.5.2 Experimental procedure 60

2.6 Results..... 64

2.6.1 Mechanical properties 64

2.6.2 Ultrasonic pulse velocity tests..... 66

2.6.3 AE analysis..... 68

2.6.4 Capillary rise 73

2.6.5 Carbonation 74

2.6.6 Sorption isotherms..... 74

2.6.7 Shrinkage tests	77
2.6.8 Modeling of drying shrinkage	79
Conclusions	80

Chapter 2 Hygric properties and damage monitoring of earth concrete mixtures at different curing conditions

Durable construction materials are those who maintain over long-period of time their properties mainly against environment conditions. The previous chapter assessed the compressive strength and fracture behavior of earth concrete mixtures at wet conditions at different curing ages. It is aimed in this chapter to assess the effect of curing conditions on mechanical properties and fracture behavior of earth concrete mixtures. In fact, as a result of water transfer from inside to outside the specimen, the compressive strength of a concrete or earth material may increase due to capillary suction effect or decrease due shrinkage induced cracking. These phenomena are known to be important in earth materials due to the latter sensitivity to drying. Furthermore, the replacement of natural sand (NS) by recycled sand (RS), the porous material, increases its vulnerability to drying. The mixtures during uniaxial compression tests are monitored in parallel with acoustic emission (AE) and digital image correlation (DIC). Moreover, specimens are assessed by ultrasonic pulse velocity (UPV) test at different curing conditions. For a better interpretation, mass loss, shrinkage and capillary rise are also conducted.

2.1 Drying

The factor initiating drying is the relative humidity gradient between concrete and the environment outside. Consequently, water moves outwardly. This process affects the surface zone of civil engineering structures. Besides, it is often accompanied by chemical reactions that occur in non-saturated conditions, such as the penetration of chloride ions or carbonation. Moreover, a change in moisture induces deformations. These deformations, in their turn, can lead to structure damage when restrained. Concrete is affected by the presence of moisture and the knowledge of its distribution is of substantial practical importance. Based on these facts, it is important to understand drying and the mechanisms of transfer. It is believed that different phenomena (less or more coupled) are involved. Permeability and diffusion are considered predominant modes.

Permeability is the flow rate of a gas or fluid through concrete under pressure gradient. It is affected mainly by porosity and pore structure. Generally, the higher the porosity is, the higher the permeability is. Concerning pore structure, it depends on four aspects:

- Pore size distribution: fluid will pass easier in the case of large pores.
- Tortuosity: it is a measure of the degree of zigzag of a pore.
- Connectivity of pores: Even if porosity is high, permeability can be low due to low connectivity.
- Pore shape: irregular shape can be an obstacle to flow.

Diffusivity, on the other hand, is the measure of the ability for a chemical to move in concrete. This transfer occurs from an area of higher concentration to an area of a lower one. Diffusion has

two situations: steady state flow (Fick's first law) and non-steady state flow (Fick's second law) (Wang, 2014).

2.1.1 Migration of water and air

The migration process occurs mainly by four coupled mechanisms (Oshita & Tanabe, 2000 ; Mainguy et al., 2001). They are as follows:

- The transfer of liquid water: its driving mechanism is the pressure gradient governed by the permeability of the porous network. This movement can be described using Darcy's law:

$$v_l = -\frac{K}{\eta_l} k_{rl} \nabla p_l \quad (2-1)$$

where v_l ($m.s^{-1}$) represents the filtration speed of liquid water, K (m^2) corresponds to the intrinsic permeability of the material, k_{rl} is the relative permeability of liquid water, η_l (Pa.s) symbolizes the dynamic viscosity of the saturated liquid (water) and p_l the pressure of saturated liquid (Pa).

- The transport of moisture under the vapor phase, its driving mechanism is the concentration gradient governed by the diffusivity of the water vapor. This movement can be described using Fick's first law:

$$\Phi_{diff} = -D_{diff} \nabla C_{v,l} \quad (2-2)$$

where $C_{v,l}$ ($kg.m^{-3}$) is the concentration of free water vapor, D_{diff} ($m^2. s^{-1}$) is the diffusivity of water vapor and Φ_{diff} ($kg.m^{-2}. s^{-1}$) is the flow of free water vapor.

- The transport of dry air, its driving mechanism is the pressure gradient governed by the permeability of the porous network. This movement can be described using Darcy's law :

$$v_a = -\frac{K}{\eta_a} k_{ra} \nabla p_a \quad (2-3)$$

where v_a ($m.s^{-1}$) represents the speed of dry air liquid water, k_{ra} is the relative permeability of liquid water, η_a (Pa.s) symbolizes the dynamic viscosity of dry air and p_a the pressure of dry air (Pa).

- Convective transport of water under vapor phase essentially. The water vapor is driven by the migration of dry air, if it takes place.

$$\Phi_{conv} = C_{v,l} v_a \quad (2-4)$$

where Φ_{conv} is the flow of water vapor due to convection.

According to the aforementioned equations, drying can be modelled based on the mass conservation equations of water and gas:

$$\left\{ \begin{array}{l} \frac{\partial(\Phi\rho_l S_l)}{\partial t} = -\nabla(\Phi S_l v_l) - \mu_{l \rightarrow v} \\ \frac{\partial[\Phi\rho_v(1 - S_l)]}{\partial t} = -\nabla(\Phi(1 - S_l)\rho_v v_v) + \mu_{l \rightarrow v} \\ \frac{\partial[\Phi\rho_a(1 - S_l)]}{\partial t} = -\nabla(\Phi(1 - S_l)\rho_v v_v) \end{array} \right\} \quad (2-5)$$

Where Φ represents porosity, S_l is the saturation degree, ρ_i is the density of the fluid (1 for liquid water, v for vapor and a for dry air), v_i corresponds to fluid speed and μ the rate of volume vaporization.

2.1.2 Approaches to model drying

As presented before, several mechanisms are responsible for the departure of water and air outside earth concrete. Three approaches have been adopted to modelling drying. They are as follows:

- The multi-phasic approach describes the transfer of both phases: liquid and gas. Transfers are governed by permeation and diffusion equations and hence, three factors are taken into account: liquid water, water in the form of steam and dry air. Adopting this approach allows the consideration of the physical process of each component and reveals the dominant mode of transfer. On the other hand, it is complicated. Each new law of transfer implies the identification of new parameters (Baroghel-Bouny et al., 1999).

- A simplified approach. It takes into account only the transfer of liquid water by permeation as expressed below (Soleilhet et al., 2017):

$$\frac{\partial S_l}{\partial p_c} \frac{\partial p_c}{\partial t} = \text{div} \left(k_{rl}(S_l) \frac{K}{\mu \emptyset} \text{grad}(p_c) \right) \quad (2-6)$$

where k_{rl} is the relative humidity parameters and the others are similar to equation (2-5).

- The resolution of a global non-linear diffusion equation is another simplified approach. It involves a water transfer coefficient that is a function of relative humidity or the specific water content. In our study, we are going to consider this approach. Besides the complexity of the first approach, the approach is able to accurately calculate the evolution in time and distribution of

moisture content within the material (Bažant & Najjar, 1972; Mensi et al., 1988; Benboudjema, 2002). The equation is similar to Fick's second law:

$$\frac{\partial C}{\partial t} = \nabla[D_{eq}(C)\nabla C] \text{ ou } \frac{\partial C}{\partial h} \frac{\partial h}{\partial t} = \nabla[D_{eq}(h)\nabla h] \quad (2-7)$$

where D_{eq} is the equivalent diffusion coefficient of water; $\partial C/\partial h$ is the moisture capacity (the slope isotherm of adsorption curve).

When drying takes place during a relative humidity not less than 50% and at ambient temperature, the consideration of the mass balance equation of liquid water only (equation 2-6) is applicable. This natural drying permits to consider that the transfer of gas is negligible and that the deformation speed of the solid skeleton, diffusion and convection are also negligible. This, therefore, allows us to consider equation 2-6.

The saturation degree is expressed as follows:

$$S_l = \frac{w\rho_s}{\emptyset\rho_l} \quad (2-8)$$

where w , ρ_s , \emptyset and ρ_l are the water content, the apparent density of the material, porosity and liquid (water) density.

The capillary pressure (p_c) is the difference between the gas pressure (p_g) and the liquid water pressure (p_l). The p_g is considered to be constant and equal to the atmospheric pressure. Thus, the relationship between the capillary forces and relative humidity, according to Kelvin's equation, can be expressed as follows:

$$p_c = \frac{-\rho_l RT}{M_w} \ln(RH) \quad (2-9)$$

where R is the gas constant ($8.314 \text{ J} \cdot \text{K}^{-1} \cdot \text{mol}^{-1}$) and T is the temperature (K) and M_w is the molecular mass of water ($\text{kg} \cdot \text{mol}^{-1}$) and p_c is in J/m^3 or Pa.

The relative humidity characterizes the equilibrium between the liquid water and the steam; the degree of saturation characterizes the liquid water content of the material. The relationship between these two quantities is established by the sorption or adsorption isotherm of the material. Such phenomena represent the evolution of the water content as function of relative humidity.

The relationship between water permeability and saturation degree in addition to the degree of saturation with relative humidity are expressed according to Mualem relationship and Van Genuchten equation:

$$k_{rl}(S_l) = \sqrt{S_l} \left[1 - (1 - S_l^{\frac{1}{A}}) \right]^q \quad (2-10)$$

$$S_l(p_c) = \left[1 + B \ln(hr)^{\frac{1}{1-A}} \right]^{-A} \quad (2-11)$$

$$S_l(p_c) = \left[1 + \left(\frac{P_c}{B} \right)^{\frac{1}{1-A}} \right]^{-A} \quad (2-12)$$

Equation 2-12 is based on equation 2-9. Concerning the parameters, q generally ranges from 2 to 4 and A and B are fitting parameters to be determined from the sorption-desorption curves.

2.1.3 Convection

By considering the thermal transfer by convection, the temperature is replaced by water content:

$$q = h(C_e + C) \quad (2-13)$$

where C_e is the external water content at the surface of convection and C is the water content at the surface of convection.

The convection process can be as non-linear as function of capillary pressure p_c .

$$h_{pc} = h_0(\alpha + \beta \cdot P_c) \quad (2-14)$$

Previous work stated that α and β are constant values where $\alpha = 5.68E-9$ and $\beta=1.74E-17$ (Reviron, 2009).

2.2 Drying shrinkage

Drying causes volume changes or shrinkage. The later may get restrained leading to the development of internal tensile stresses. If these stresses exceed the tensile strength of soil, microcracks are generated which may lead to strength loss. In earth concrete, the restrictions may be due to soil heterogeneity, in particular the fine-grained soils (clay), and to non-uniform water distribution. In the case of earth concrete load bearing walls, the external restraint (frictional boundary condition) may be also responsible for shrinkage induced cracking. Such cracks are known as boundary cracks (Levatti et al., 2019). In addition, at the microscopic level, the different constituents of cement paste (C-S-H, portmandite...) do not deform identically. In the following paragraphs, the factors contributing to such phenomenon are stated.

2.2.1 Clay content and plasticity index

Soils with higher clay content have a greater affinity to water. Thus, it is believed that drying and shrinkage increases with clay content in addition to plasticity index. Figure 2.1 shows the

volumetric shrinkage strain (%) as function of (a) clay content and (b) plasticity index. Regardless of the type of soils that are represented by different shapes, it can be seen that such strain increases with both parameters.

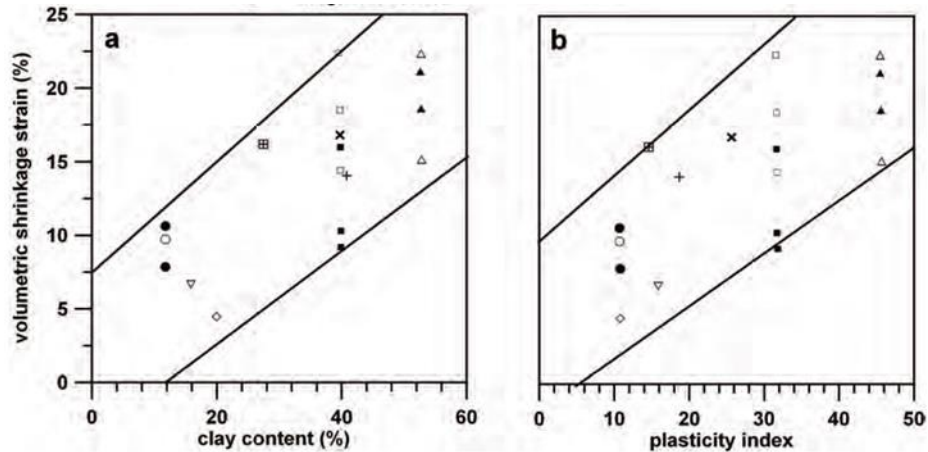


Figure 2.1: Effect of clay content and plasticity index on the volumetric shrinkage strain (Albrecht and Benson, 2001)

Figure 2.2 shows the autogenous shrinkage (at sealed conditions) and total shrinkage (total shrinkage = drying shrinkage + autogenous shrinkage). It can be seen that the mixture 40A0F (40% of clay in addition to 0% of fibers) is of shrinkage more than 20A0F and 0A0F (Chinh Ngo, 2017).

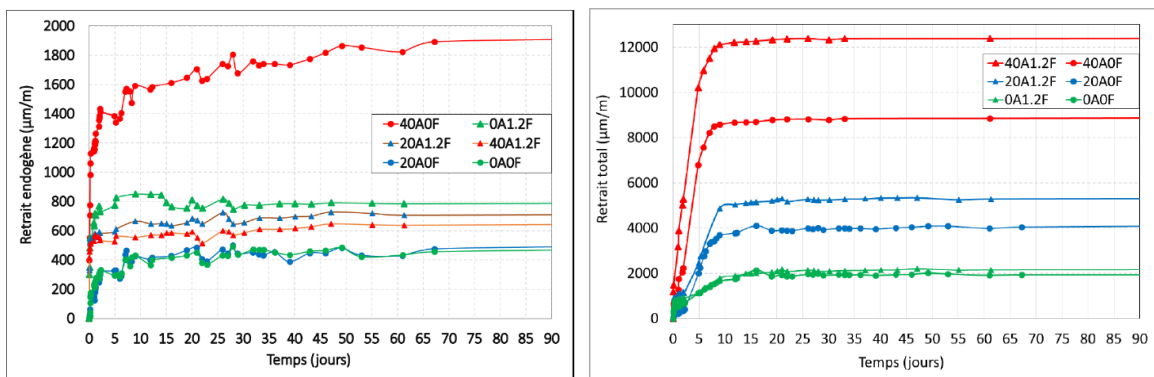


Figure 2.2: Autogenous and total shrinkage of different earth concrete mixtures (Chinh Ngo, 2017)

2.2.2 Clay mineralogy

The two basic units of clay minerals are silica tetrahedron and alumina octahedron. They form respectively, silica sheet and alumina sheet. Different structures of the stacked combinations of the basic sheet structures with different types of bonding between the sheets result in different types of clay minerals. The three main clay minerals are: Kaolinite, montmorillonite and illite. It is known that soils that include swelling clays such as montmorillonite are more vulnerable to

shrinkage cracking than non-swelling clay such as Kaolinite (The clay mineralogy intersects with the plasticity index mentioned above) (Fardoun, 2021; Fardoun et al., 2021).

2.2.3 Density

According to Albrecht and Benson (2001), the density of soils influences their cracking behavior. Figure 2.3 shows the volumetric shrinkage strain (%) as function of dry unit weight. According to the results, the strain decreases with density.

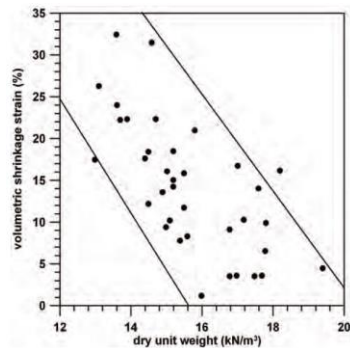


Figure 2.3: Volumetric shrinkage strain (%) as function of density (Albrecht and Benson, 2001)

2.2.4 Soil structure

It has been said that soil structure affects the cracking pattern. Fang (1997) stated that a flocculated structure if got exposed to desiccation would exhibit different cracking pattern (and larger) than dispersed structure.

A past study assessed the impact of soil thickness on the time required to start cracking (days) for close packing soil (denser soils) and loose packing soil (Corte & Higashi, 1960). A linear relation was revealed for close packing soil while a saturation curve type was exhibited in the loose one (figure 2.4). Thus, generally speaking, the loose packing is more susceptible to cracking.

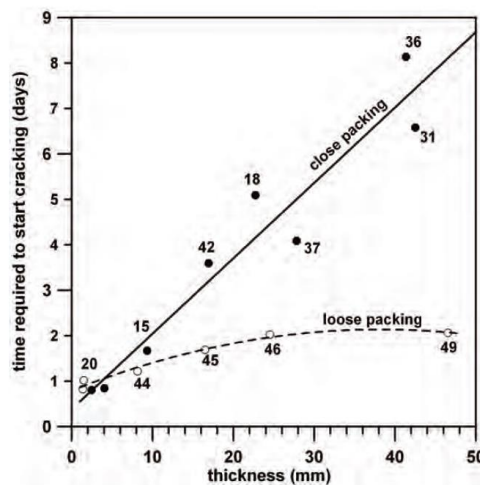


Figure 2.4: Time required to start cracking as function of soil thickness of close packing and loose packing soils (Corte & Higashi, 1960)

2.2.5 Water content

The theory of Haines (Haines, 1923) states that the specimens compacted at their optimum water content exhibit the lowest volume changes among specimens compacted at different water content because they have least volume of water and the most volume of soil particles per unit volume of soil. Figure 2.5 shows the volumetric shrinkage strain as function of water content to relative optimum water content (%) (Albrecht and Benson, 2001). The results revealed that the deviation from the optimum water content causes increase in shrinkage strains.

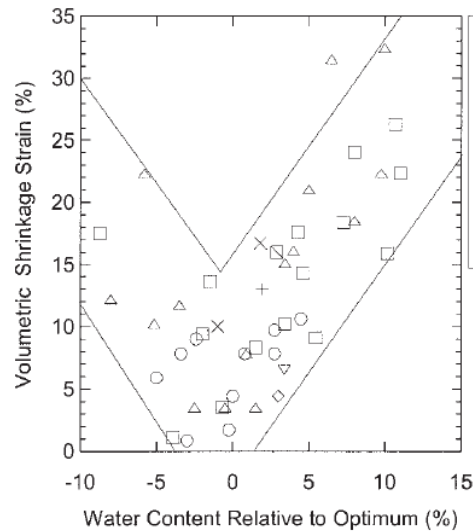


Figure 2.5: Volumetric shrinkage strain as function of water content relative to optimum water content (%) (Albrecht & Benson, 2001)

2.2.6 Rate of desiccation

The rate of desiccation of two specimens of similar thickness at different weathering conditions (relative humidity and temperature) is different. Similarly, two specimens at the same weathering conditions but of different thicknesses will have different rate of desiccation. Such rate influences the rate of cracks formation. Figure 2.6 shows the effect specimen size and geometry on the mass loss (Carette et al., 2020). The red sides are the sides subjected to drying. It can be seen that G1, the specimen of longest drying path, is of lower drying rate.

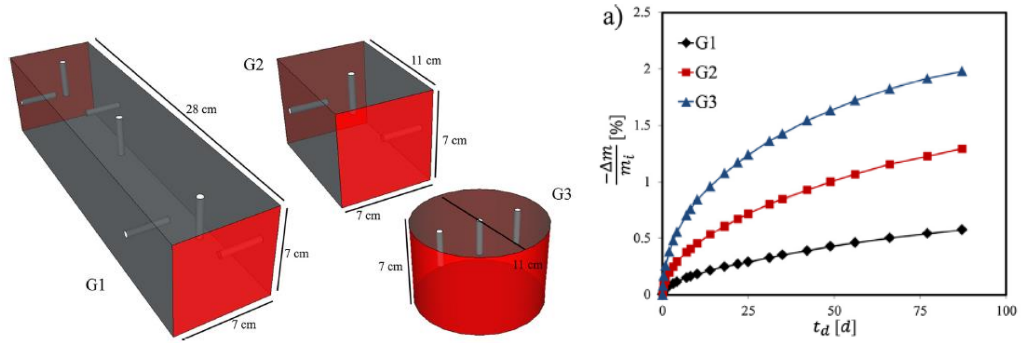


Figure 2.6: Effect of geometry on drying rate (Carette et al., 2020)

Temperature and relative humidity (RH) define the weathering condition. Figure 2.7 shows the displacement fields (along x-axis) of mortar specimens conserved for 60 days at different RHs conditions (Gao et al., 2021). The assessment was carried out by means of DIC. Larger displacements were found at a lower RH.

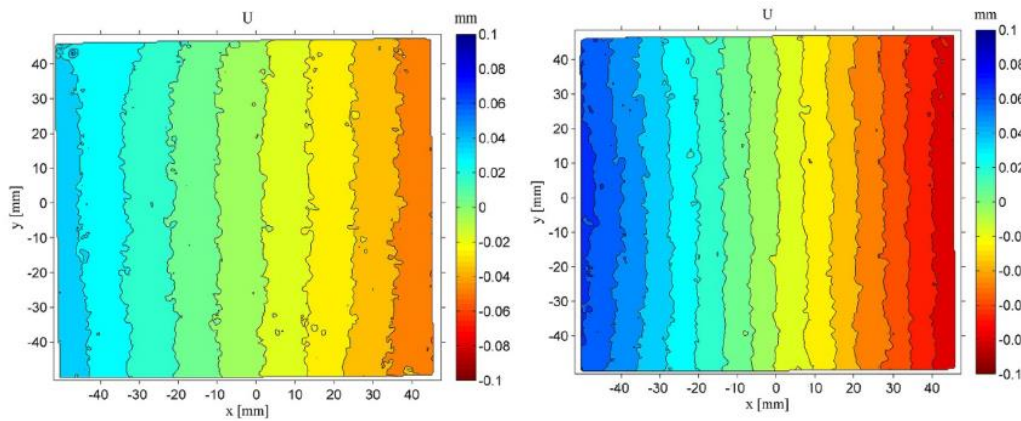


Figure 2.7: Displacement field (along x-axis) of mortar specimens at RH of 73% (left) and 40% (right) (Gao et al., 2021)

Figure 2.8 shows the development of cracks with time in clayey soils. The initiation, propagation and coalescence of drying cracks can be seen as time passes throughout two days of drying (Trabelsi et al., 2012).

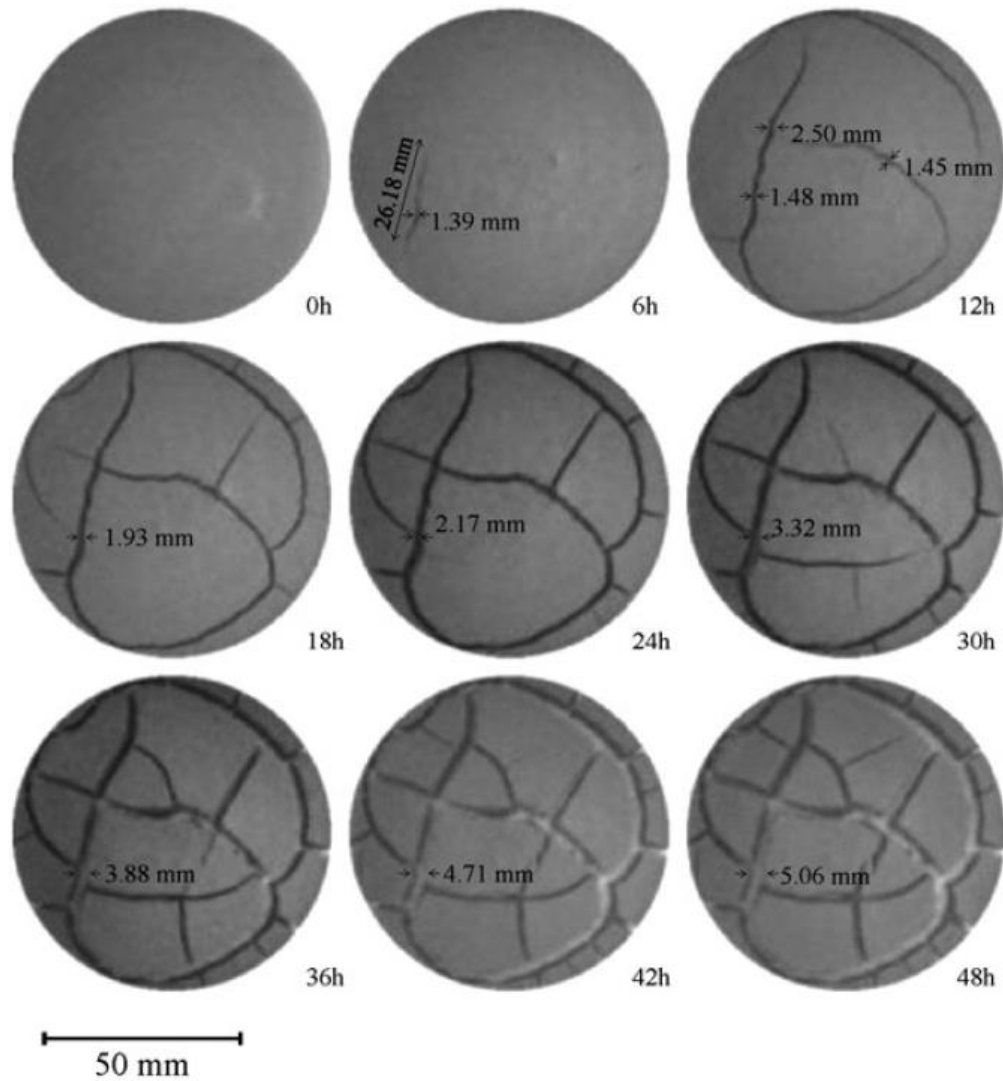


Figure 2.8: Drying cracks development until 48 hours (Trabelsi et al., 2012)

2.2.7 Modeling of drying shrinkage

Simplified approach

These were adopted by many researchers to model drying shrinkage. They have been expressed in terms of relative humidity (Wittmann & Roelfstra, 1980) or water content (Thelandersson et al., 1988; Granger et al., 1997). Granger's expression considering a viscoelastic material is:

$$\epsilon_{rd} = -K \frac{\Delta P_s}{P_s} \quad (2-15)$$

where $\frac{\Delta P_s}{P_s}$ is the mass loss and K is the coefficient of proportionality expressed as follows:

$$K = k\rho_c \quad (2-16)$$

where ρ_c is the density of concrete and k is a fitting parameter.

Poromechanics

The deformation of a porous saturated body can be described using Biot's approach (Biot, 1941).

$$\varepsilon = b\left(\frac{1 - 2\nu}{E}\right)p \quad (2-17)$$

where b is the biot coefficient of value between the porosity and 1, ν poisson's ratio, E modulus of elasticity and p water pressure.

Bishop (1959) extended Biot's approach to partial saturated porous material. The concept of two fluids at different pressure has been introduced: water pressure and gas pressure. Hence, the average pore pressure is expressed as follows:

$$p = S_w p_w + (1 - S_w) p_g \quad (2-18)$$

where S_w , p_w and p_g are saturation degree of liquid water, water pressure and gas pressure. Not considering the gas pressure and adopting $p_c = p_g - p_w$ reduces the average pore pressure into $p = -S_w p_c$ where p_c can be determined from the Kelvin-Laplace equation. Schrefler approach, according to the literature, is similar and it is represented as follows:

$$\varepsilon = b\left(\frac{1 - 2\nu}{E}\right)(-S_w p_c) \quad (2-19)$$

Coussy et al. (2004) introduced the concept of equivalent pore pressure (π). It replaced the averaged pressure presented by Bishop. The equivalent pore pressure takes into account the interface energy (U) where $\pi = U - p$.

Finally, the equation expressing the volumetric change can be written as follows:

$$\varepsilon = b\left(\frac{1 - 2\nu}{E}\right)(-S_w p_c + U) \quad (2-20)$$

Vlahinić et al. (2009) assumed that the partially saturated media or pores are fully saturated with water, while drying affects only the bulk modulus of the effective solid. The authors hence reported, in other words, that during drying, the bulk modulus of the solids changes and it is expressed in terms of the water saturation degree. The formulation is expressed as follows:

$$\varepsilon = b \left(\frac{1}{K_b} - \frac{1}{\bar{K}(S_w)} \right) (-S_w p_c) \quad (2-21)$$

where K_b and \bar{K} are the drained bulk modulus of the porous body and the effective bulk modulus, respectively.

2.3 Capillary suction effect

As a result of drying, the increase in strength occurs due to the increase in capillary pressure (suction effect) which leads to stiffening effect (Yurtdas et al., 2004). Soil gains strength by combined action of cohesion and friction (Van Damme & Houben, 2018). Mainly the capillary forces, in addition to ionic correlation forces and Van der Waals, are the sources of cohesion. The increase in capillary pressure links more the gaps between the clay particles themselves (the soil's smallest fraction) or the clays with other grains. This increases friction contributing as well to strength.

2.3.1 Surface tension and contact angle

Surface tension is a property which expresses the requirements to change the surface area of a sample (Atkins & De Paula, 2006). Water is of high surface tension. The surface tension of water can be expressed as follows:

$$\gamma_{lv} = 0.1171 - 0.0001516T \quad (2-22)$$

where T (in Kelvin) is the absolute temperature.

The contact angle requires the presence of three phases to be formed. In unsaturated soils, the contact angle is the angle between a line tangent to the air-water interface and the water-solid interface (Atkins and De Paula, 2006). It is formed due to the balance of forces between the liquid-vapor (γ_{lv}) solid-vapor (γ_{sv}) and solid-liquid (γ_{sl}) surface tensions. It is then as follows:

$$\cos(\theta_{slv}) = \frac{\gamma_{sv} - \gamma_{sl}}{\gamma_{lv}} \quad (2-23)$$

where θ_{slv} is the contact angle between a solid and a liquid in the presence of a vapor. Figure 2.9 verifies this. The curved surface shown is known as meniscus.

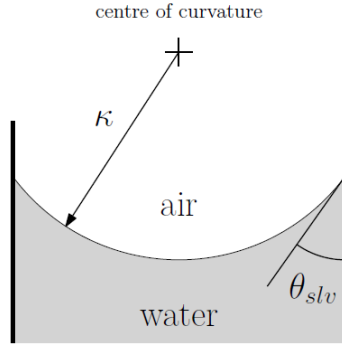


Figure 2.9 : Water meniscus

2.3.2 Young-Laplace equation

Young-Laplace equation is expressed based on the pressure below the curved surface (p_i) and the pressure above the curved surface (p_0).

$$p_0 - p_i = -\frac{2\gamma_{lv}\cos(\theta_{slv})}{k} \quad (2-24)$$

For an air-water interface, the previous equation can then be written as follows:

$$u_{air} - u_{water} = -\frac{2\gamma_{lv}\cos(\theta_{slv})}{k} \quad (2-25)$$

For air at atmospheric pressure, the water pressure defines the equation. This is basically a manifestation of capillary suction.

2.3.3 Kelvin equation

As water is consumed, air volume increases. In fact, the liquid phase is not pure water but it is water that contains dissolved air (Gens, 2010). Similarly, the phase above the curved surface is air containing water vapor. The relative humidity (RH) is related to the relative vapor pressure of the vapor of the liquid in the gas phase (the phase above the curved surface).

The chemical potential, at equilibrium, of a liquid (μ_l) and its vapor (μ_v) are equal (Beckett, 2011). The potential of liquid changes or vapour changes are expressed as $d\mu_l = V_{m1} \times dP$ and $d\mu_v = V_{mv} \times dP$, respectively where V_m and dP are the molar volume and the increase in pressure.

Assuming now that the vapor behaves as a perfect gas so that $P \times V = n \times R \times T$ where P and V are the pressure of gas and the volume respectively, R is the universal gas (8.314 J/molK) and n is the number of moles, so:

$$d\mu_v = -\frac{RTdP}{p} \ln(RH) \quad (2-26)$$

The equilibrium is translated as follows:

$$Vm_l dP_l = -\frac{RTdP_v}{p} \ln(RH) \quad (2-27)$$

The following modifications can be made if the increase in liquid and vapor pressures is small:

$$\int_{p^*}^{p^*+\Delta P_l} Vm_l dP_l = RT \int_{p^*}^p \frac{dP_v}{P_v} \quad (2-28)$$

where p^* is the saturated vapor pressure of the liquid above the surface and in equilibrium with no external effects. This can be simplified as:

$$\ln \frac{p}{p^*} = -\frac{Vm_l}{RT} \Delta P_l \quad (2-29)$$

The term $\frac{p}{p^*}$ may be expressed as the RH value. If the change in the liquid pressure is $\Delta P_l = -\frac{2\gamma_{lv}}{k}$ (by adopting a zero contact angle), then:

$$-\frac{2\gamma_{lv}}{k} = \frac{RT}{Vm_l} \ln(RH) \quad (2-30)$$

To make the equation like the one in the literature, the equation is then expressed as follows:

$$-\frac{2\gamma}{k} = \frac{RT}{V_m} \ln(RH) \quad (2-31)$$

2.3.4 Capillary rise

The phenomenon of capillary rise is associated with the drop in water pressure below a concave meniscus (the meniscus in figure 2.9). For a tube of radius (r_{tube}) in a free reservoir of liquid, the formation of a meniscus (due to the contact angles) causes the water column to rise up until the water pressure at the surface level is equilibrated.

As the procedure adopted previously, by assuming a contact angle of zero, the radius of the meniscus k is equal to the capillary tube radius (r_{tube}). Then equation 2-31 is re-written as:

$$-\frac{2\gamma_{lv}}{r_{tube}} = \frac{RT}{V_m} \ln(RH) \quad (2-32)$$

Another form of Kelvin equation is obtained and it can be expressed as follows:

$$\Psi_{cap} = -\frac{RT}{V_m} \ln(RH) \quad (2-33)$$

where Ψ_{cap} is the capillary pressure.

2.3.5 Effect of clay content

Jacquín et al. (2008) assessed the water retention properties of two earth materials (rammed earth). Based on a reference soil consisting of 74% of sand, 16% of silt and 10% of clay, modifications were done to obtain mix A of 10% extra sand and mix B of 10% extra clay. The two mixtures were compacted in layers at a water content of 10% to reach eventually a dry density of 2050 kg/m³. Figure 2.10 (a) shows that for the same suction, mix A –the coarser mixture- is of lower water contents than mix B (the finer mixture). Or in other words, at the same water content, the finer mixture is of higher suction.

Beckett & Augarde (2012) carried out a similar assessment on a mixture of 50% sand, 10 % gravel and 40% clay (mix 5:1:4) and another mixture of 70% sand, 10% gravel and 20% clay (mix 7:1:2). Both mixtures are of the same amount of gravel but of different clay and sand mixtures. The results in figure 2.10 (b) show that the finer mixture (mix 5:4:1) exhibits at the same suction a higher water content. Both studies indicate that suction effect is proportional to particle size distribution. The finer the particle, the more it undergoes suction. Therefore, the capillary suction is influenced by the percentage of fine particles and clay.

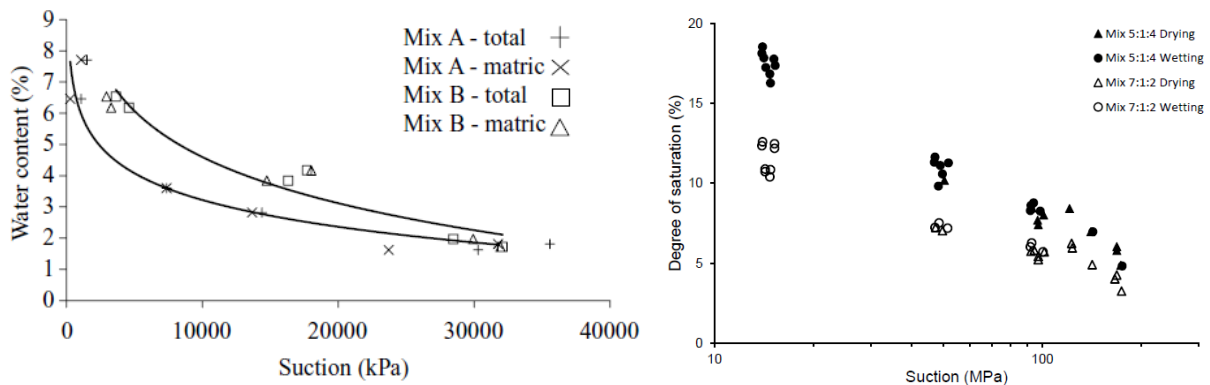


Figure 2.10: Soil-water retention curves for two rammed earth mixtures (A and B) (Jacquín et al., 2008) (a) and of two mixtures (b) (Beckett & Augarde, 2012)

2.3.6 Effect of temperature (T) and relative humidity (RH)

Dierks & Ziegert (2002) showed that the compressive strength decreases with the increase of air humidity. The results are presented in figure 2.11. The suction values were derived from RH values at constant temperature. In his assessment, a compressive strength of almost 2 MPa was reported at RH=95%. Such strength increased to almost 6 MPa at RH=5%. Respectively, this was accompanied by an increase in suction from 7 MPa to 405 MPa.

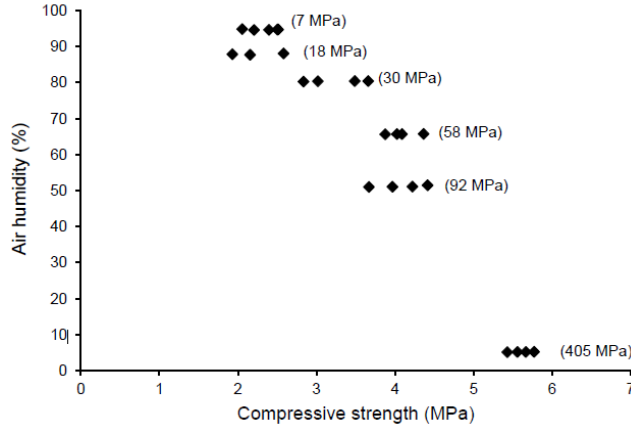


Figure 2.11: Air humidity and suction effect as function of compressive strength (MPa) (Dierks and Ziegert, 2002)

Bruno (2016) assessed the modulus of elasticity and compressive strength of unstabilised earth samples at RH of 95, 77, 62, 44, 25% and a constant temperature of 25°C. At each RH, the compaction pressure was adopted at 25 MPa, 50 MPa and 100 MPa. According to the results in figure 2.12, both properties increase as suction increases from 7 MPa to 112 MPa but then tend to stabilize as suction increases further. Bruno (2016) found the results in agreement with the idealized capillarity model of Fisher (Fisher, 1926) that states that the stabilizing effect formed by a water meniscus at the contact between two identical spheres grows with suction to shift after that towards a constant asymptote.

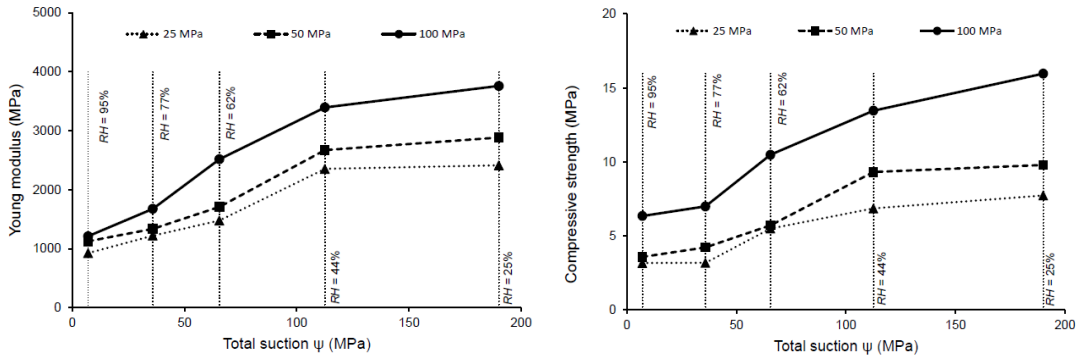


Figure 2.12: Modulus of elasticity and compressive strength as function of suction (and RH) (Bruno, 2016)

Figure 2.13 shows the effect of three different types of stabilization on the compressive strength and modulus of elasticity (compared to the previous stabilized mixtures). The results showed lower values with stabilization. The author stated that this is probably because the inter-particle bonding produced by capillarity is overridden by that produced by chemical stabilization.

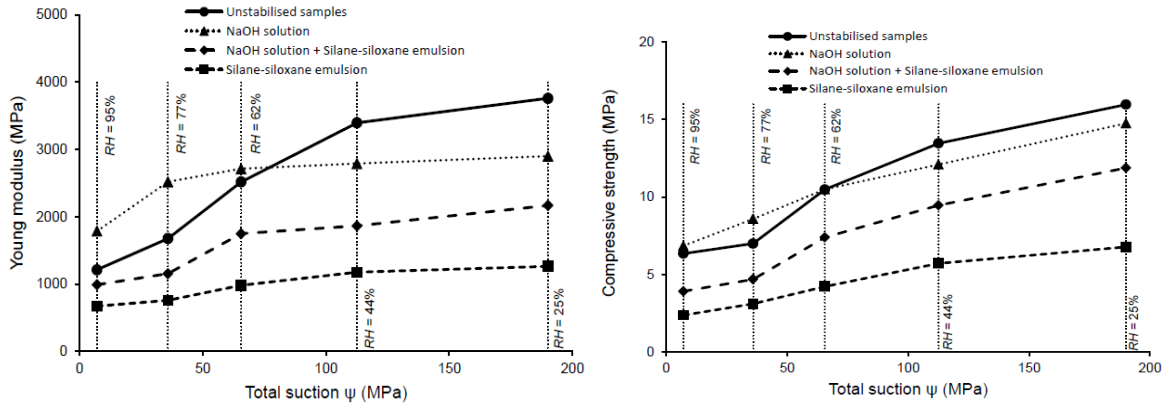


Figure 2.13: Effect of stabilization (Bruno, 2016)

Ho et al. (2017) assessed the effect of curing conditions on strength development of sand mixture and sand-loam mixture that exhibits high pozzolanic reactions (figure 2.14 (a) and (b)). The results in figure 2.14 showed that the strength increases until the age of 28 days. At sealed condition, the strength of the sand mixture after that stayed almost constant while for sand-load mixture, it increased. The author attributed this to pozzolanic reactions. The strength at drying condition was higher than that at sealed condition. The author attributed this to the decrease in water content.

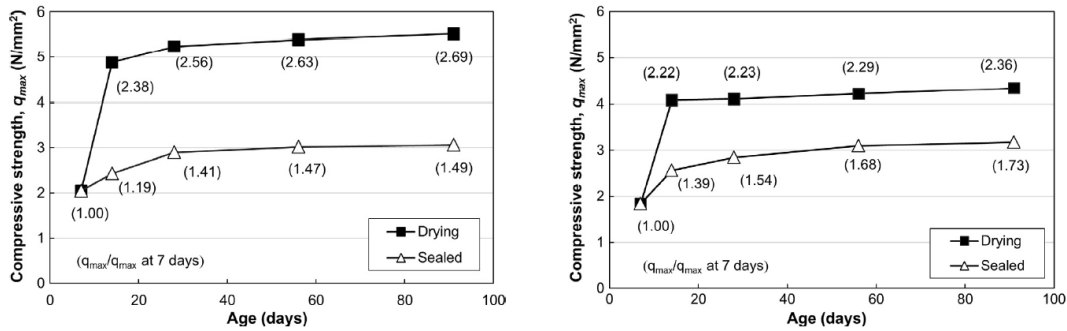


Figure 2.14: Compressive strength ratio at sealed and drying conditions of sand mixture (a) and loam-sand mixture (b) (Ho et al., 2017)

2.4 Carbonation

Carbonation is a process where carbon dioxide (CO_2) in ambient air penetrates cementitious materials and reacts with cement hydrates (Ho et al., 2017). This process is believed to have negative and positive effects on concrete. From one side, the reaction between the two components leads to reduction in pH and consequently increasing the possibility of carbonation-induced corrosion of embedded steel. Thus, carbonation is detrimental to reinforced concrete (Xian et al., 2022). On the other side, concrete strength at short and long term and durability (resistance to freeze-thaw deterioration, ettringite sulfate attack, acid attack, efflorescence formation and chloride permeation) can be improved (Ho et al., 2017; Xian et al., 2022).

2.5 Experimental program

2.5.1 Materials and mix design

The four mixtures considered in chapter 1 are adopted in this chapter. 30% of Kaolinite clay is mixed with 70% of NS. In addition, 20%, 30% and 40% of this clay are mixed with relative amount of RS. RS was pre-saturated at 80% 24 hours before mixing. 9% of cement of the dry solid components mass of each mixture was considered. Moreover, water was added to eventually reach a workability of 7 to 10 cm. Table 2.1 shows again the mix design of each mixture.

Components (kg/m ³)	Clay (C)	Sand (S)	Cement	W_{eff}	Superplasticizers
NS30/70	440	1026	132	140	1.32
RS20/80	271	1084	110	167	1.32
RS30/70	366	855	110	177	1.32
RS40/60	460	690	103	187	1.32

Table 2.1: Mix design of the four mixtures

2.5.2 Experimental procedure

As in chapter 1, the electro-mechanical machine with a capacity of 100 kN was used. The loading rate was modified at two different positions in the post-peak regions (80% and 30% of peak stress) to reduce the experiment time. The adopted loading rate values were 0.5 mm/min, 1.5 mm/min and 4.5 mm/min. In the following chapter, additional compressive tests were carried out at day 14, day 28 and day 90 at RH=50%. These tests were monitored also in parallel with acoustic emission (AE) and digital image correlation (DIC) techniques.

Additional tests have been also conducted:

- Flexural test:

Prism specimens were casted in 4x4x16 cm³ molds (3 specimens for each mixture). The loading rate was calibrated at 0.5 kN/s. The flexural tests took place at 28 days for specimens at RH=90% and RH=50%.

- Ultrasonic Pulse Velocity (UPV) test

The ultrasonic technique is a non-destructive method which allows the calculation of propagation velocity of ultrasonic waves based on the measurement of their propagation time in specimens of known traveled distance. The determined velocity can be related to the mechanical properties of concrete, to its quality (defects, cracks, voids, etc.) and to its dynamic modulus of elasticity.

The system consists of a PUNDIT (Portable Ultrasonic Non-destructive Digital Indicating Tester) pulse generator and two sensors. The generator sends out an electrical pulse which is converted into a longitudinal pressure wave by the emitter so that it can propagate through the material. The

receiver converts them into an electrical pulse that is returned to the generator as a time signal. The system thus displays the time difference between the transmission and reception of the signal with an accuracy of $0.1 \mu\text{s}$ (for the device used in our tests). Calibration is performed before a material assessment. The coupling between the sensors and the concrete is done with grease. Several factors can influence this measurement such as the coupling, the type of sensor, the measurement conditions and the water content of the material tested. The use of face-to-face sensors (direct configuration) makes it possible to generate longitudinal waves and to trace the characteristics of a linear and isotropic elastic material. Figure 2.15 better clarifies the test procedure.



Figure 2.15: Ultrasonic pulse velocity test (calibration and measurement) (Ngo, 2017)

- Mass loss and shrinkage

Shrinkage tests were carried out on prismatic specimens of dimensions $4 \times 4 \times 16 \text{ cm}^3$ fitted with metal studs at their ends. Specimens were kept after casting in covered molds for 24 hours to avoid drying. After 24 hours, specimens were removed from the mold and shrinkage measurements were carried out in an air-conditioned room at a temperature of $20^\circ\text{C} (\pm 2^\circ\text{C})$ and a RH of $50\% (\pm 5\%)$. Longitudinal strain measurement was performed using LVDT sensors with an accuracy of $3 \mu\text{m}$. For the measurement of the total shrinkage, the ends of specimens were covered with an adhesive aluminum foil which allows identical lateral drying on all four sides of the specimen. For autogenous shrinkage, specimens were completely covered to prevent drying. The mass loss was measured simultaneously on specimens of the same dimensions stored under the same drying conditions. Figure 2.16 shows the metallic molds and shrinkage tests device.



Figure 2.16: Molds with metal studs and shrinkage tests device

- Capillary rise

The capillary rise tests were carried out after 120 days of drying. The bottom side of each specimen is submerged in 2 mm of water. A cover is positioned during the test to prevent air movement around the samples. The mass of the specimens is measured periodically. Figure 2.17 better clarifies the procedure.



Figure 2.17: Capillary rise test procedure

- Carbonation

Earth concrete mixtures in the following study don't include steel. Thus, it would be beneficial to assess carbonation of the four mixtures at wet and drying curing conditions. After 120 days of casting, specimens at wet and dry conditions were cut in the middle and sprayed with an acid-base indicator (phenolphthalein) on the surface. It is aimed to capture any differences between earth concrete mixtures at RH=90% and RH=50% in addition to any differences regarding sand type.

- Sorption isotherm

The performance of earthen materials is usually linked with their hygro-thermal properties (hygric and thermal properties) that are characterized by thermal conductivity, heat capacity, water vapor permeability and sorption isotherms. The latter is a hygroscopic parameter. Hygroscopic materials such as earth concrete have the ability to absorb and desorb moisture with the variation of surrounding conditions and thus they can be used to reduce the extreme values of humidity levels in indoor climates (Rode et al., 2005).

Our assessment carried out here concerns sorption isotherms. Water content is plotted as function of relative humidity. The moisture or water content (w) is calculated as follows:

$$w = \frac{m - m_0}{m_0} \quad (2-34)$$

where m and m_0 are the mass of the tested specimen and the mass of the specimen at dry conditions, respectively.

This assessment is important as it examines the influence of NS replacement by RS and clay content on water content variations in earth concrete as RH changes. In addition, the parameters A and B (in equations 2-11 and 2-12) can be determined for modeling purposes. To determine the sorption isotherms (or the hygroscopic sorption properties of the four mixtures), tests took place in a climatic chamber based on ISO12571 (ISO 12571, 2013). The isotherm curve would have one of the forms in figure 2.18.

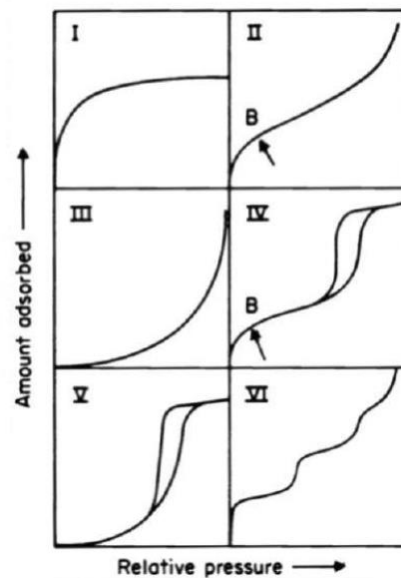


Figure 2.18: Different forms of isotherm curves

Three specimens (almost 10 g each) were considered for each material. Figure 2.19 below shows specimens in the climate chamber.



Figure 2.19: Specimens in the climate chamber

- Density and porosity

Apparent density, ρ , and porosity, \emptyset , were obtained experimentally at the age of 28 days. Specimens of 10-30 g were put in an airtight bell jar for 24 hours under a pressure of 60 mbars. Equations 2-35 and 2-36 state the corresponding equations where m_{sat} is mass saturated specimen, m_{dry} is the dry mass, ρ_w is the water density and m_{sat}^{imm} is the mass of a saturated specimen immersed in water.

$$\rho = \frac{m_{dry} * \rho_w}{m_{sat} - m_{sat}^{imm}} \quad (2-35)$$

$$\emptyset = \frac{m_{sat} - m_{dry}}{m_{sat} - m_{sat}^{imm}} \quad (2-36)$$

2.6 Results

2.6.1 Mechanical properties

Figure 2.20 shows the stress-strain curves of the different mixtures cured at RH=50% (the symbol -50 was added) and RH = 90% (those were presented in chapter 1) at the ages of 14, 28 and 90 days. Similarly as in chapter 1, the strain was calculated based on the loading plate displacement as the whole surfaces' strains exported directly from DIC did show the post-peak.

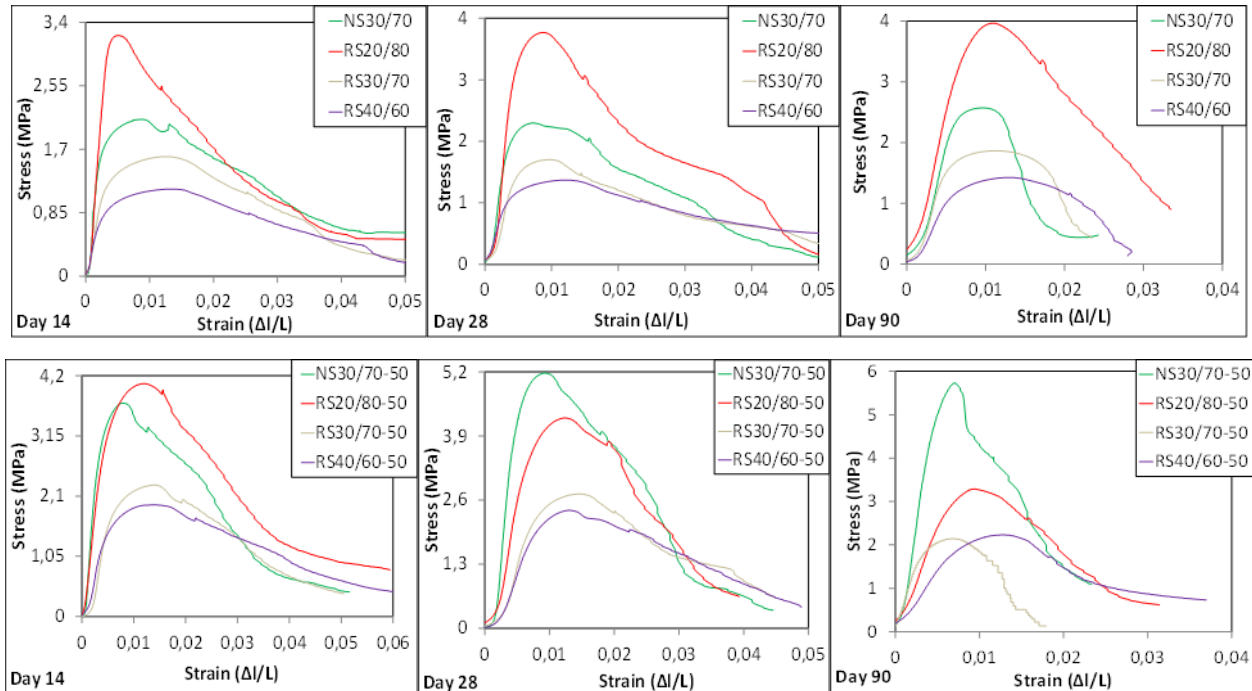


Figure 2.20: Stress-strain curves of all mixtures at the age of 14, 28 and 90 days

Figure 2.21 (a) shows that the compressive strength of the mixtures conserved at dried conditions revealed an increase in strength in all mixtures at the age of 14 and 28 days. This indicates that the suction effect phenomenon is the dominant phenomenon compared to shrinkage induced cracking phenomenon. In fact, the increase in the capillary pressure got the clay particles themselves or the clay particles with other ones closer. This justifies the lowest increase in compressive strength of RS20/80-50 as a result of drying as it had the least amount of clay. Similarly, this justifies the highest increase in compressive strength of RS40/60-50 as it possessed 40% of clay, more than any other RS mixture. On the other side, the increase in compressive strength in NS30/70-50 is much more remarkable than that of RS30/70-50. This indicates that the suction effect is more pronounced in the presence of NS, in addition to the modification of ITZ properties, and that more shrinkage induced cracks were generated in the RS mixture (RS30/70-50) curbing the effect of suction. NS30/70-50 still shows an increase in strength at curing age of 90 days indicating the continuous domination of suction effect. However, RS mixtures exhibited lower strength at 90 days in comparison to that obtained after 28 days of drying. This reflects the less domination of suction effect at later ages in RS mixtures and the more formation of shrinkage induced cracking with drying time.

To the contrary, the flexural strength of RS mixtures at the age of 28 days decreases at dried conditions with respect to specimens at wet conditions unlike that of the NS mixture (figure 2.21 (b)). On the other hand, the NS30/70-50 at dried condition showed increase in flexural strength. The difference in behavior of RS mixtures in compression and flexural tests may be attributed to RS-matrix interface.

Figure 2.21 (c) shows that the fracture energy decreases with age. This indicates that earth concrete behaves in a more brittle way with prolonged drying.

The pre-peak slope value (figure 2.21 (d)) - (calculated from specimen's whole surface (DIC-approach) as the loading plate approach exaggerates the strain values) - increases at RH=50% for all NS mixtures for all curing ages at lower rate. However, the slope increases slightly at the age of 14 days for all RS mixtures due to drying which may be due to the internal curing and decreases with an important rate at the age of 28 and 90 days. This may be due to porosity and the mixtures' components vulnerability to drying.

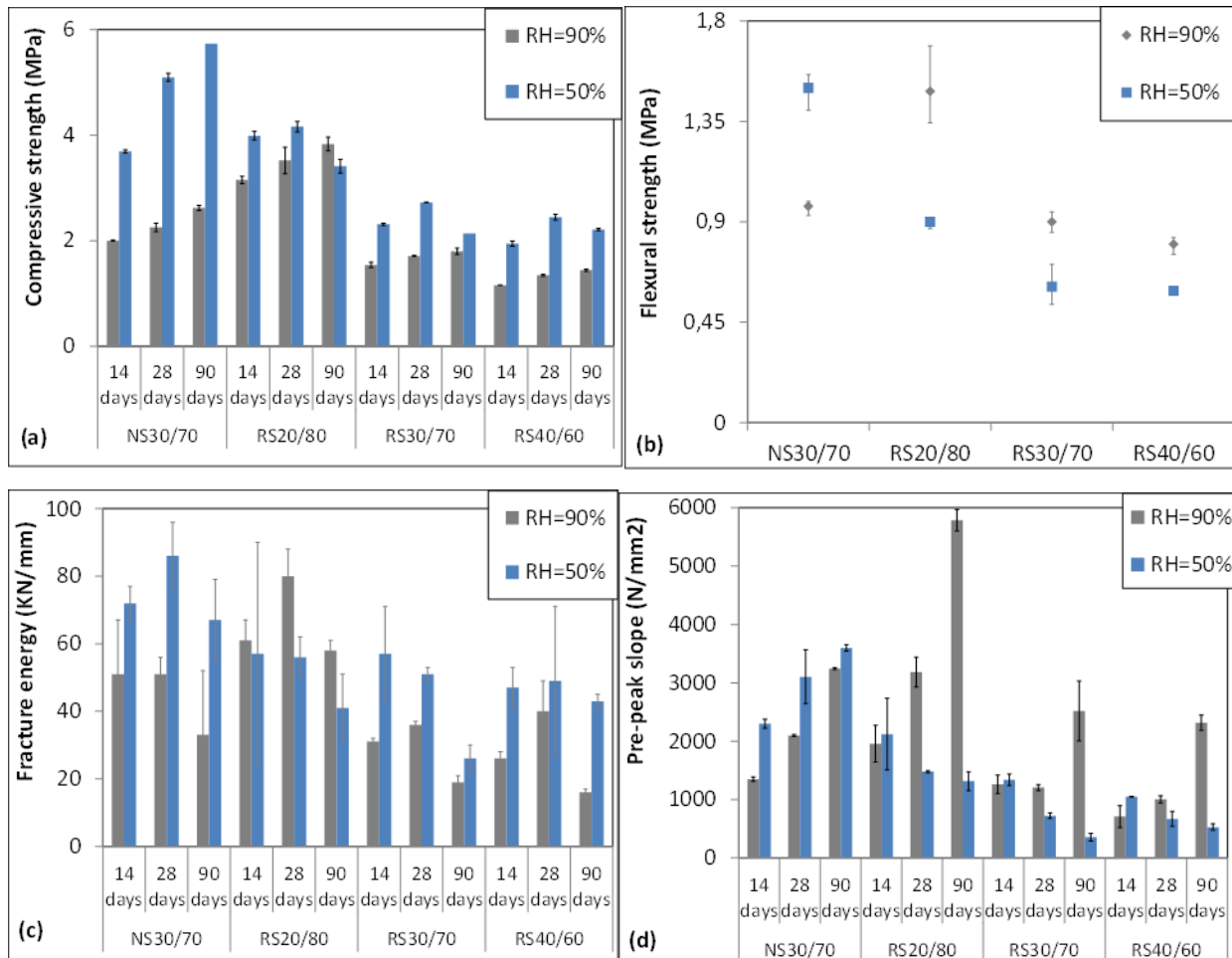


Figure 2.21: (a) compressive strength, (b) flexural strength, (c) fracture energy and (d) pre-peak slope of each mixture

2.6.2 Ultrasonic pulse velocity tests

Figure 2.22 (a) shows the UPV of each mixture at sealed and drying conditions. The UPV increases sharply in the first 14 days basically due to the reduction in porosity following the hydration reactions taking place. A slight increase continues until 28 days.

At 90 days, the velocity increases at wet curing condition while it decreases at dry curing one. In addition, at all ages, the UPV values at RH=90% are higher than those at RH=50%. In fact, UPV can be affected by the moisture degree of concrete and thus it would be higher at wet condition. It can be noticed that at day 28 of drying, NS30/70-50 reported the highest velocity after it was the second highest to show after that the lowest decrease at 90 days. In fact, at dry curing conditions, shrinkage induced cracking is formed. Knowing that cracks, pores and any other obstacles affect UPV, the higher UPV of NS30/70-50 at 90 days may be attributed to the less formation of these cracks in addition to higher porosity in RS mixtures.

The UPV is the parameter that provides information about the elastic response or modulus of elasticity of a mixture. The increase in the pre-peak slope value at RH=90% with age is proportional to the increase of UPV. However, at drying conditions, proportionality was not achieved in different occasions such as NS30/70-50 at 90 days. Thus a positive or negative change in the pre-peak slope value as a result of drying is not necessarily accompanied by a similar tendency in the UPV. It is worth to note that the UPV measurements are very sensitive to water content in earth concrete specimens.

The calculated pre-peak values don't represent the modulus of elasticity. In the lack of specific standards for the determination of the modulus of elasticity for certain material such as masonry, authors tend to apply the standards used in hardened concrete and stones that basically states the application of a few cycles of cyclic loading prior to the linear phase (Drougkas et al., 2016; Segura et al., 2018).

The determination of modulus of elasticity based on the ultrasonic pulse velocity is widely adopted according to equation 2-37.

$$V_L = \sqrt{\frac{E(1-\nu)}{\rho(1-2\nu)(1+\nu)}} \quad (2-37)$$

Here, the density, ρ , was calculated from equation 2-35. It is worth to note that same value was considered at 14 and 90 days (though porosity and density changes with curing age).

The values are in the table 2.2.

Mixture	NS30/70	RS20/80	RS30/70	RS40/60
Density (kg/m ³)	1350	1170	1015	1002

Table 2.2: Density values of each mixture

The Poisson's ratio, ν , was calculated by considering the lateral strain over the vertical strains where these strains are of the specimen surface exported directly from DIC. The results are presented in table 2.3. The Poisson's ratio values ranged here between 0.26 to 0.35. This is in agreement with past studies assessed ν in earthen materials (Bui et al., 2014). Moreover, the calculated E values that ranged between 4000 and 10000 MPa as shown in figure 2.22 (b) are in

agreement with a recent study that determined the E of different earth concrete mixtures of ultrasonic pulse velocity (Kanema et al., 2016).

Mixture	NS30/70			RS20/80			RS30/70			RS40/60		
Curing age (days)	14	28	90	14	28	90	14	28	90	14	28	90
N	0.27	0.30	0.30	0.33	0.3	0.27	0.35	0.32	0.26	0.3	0.35	0.31

Table 2.3: Poisson's ratio at different curing ages

This allowed the extraction of an equation that correlates the pre-peak slope values calculated from the stress-strain curves with the dynamic modulus of elasticity determined from UPV at sealed conditions. This would be applicable to different earth concrete mixtures. The equation is presented in figure 2.22 (b).

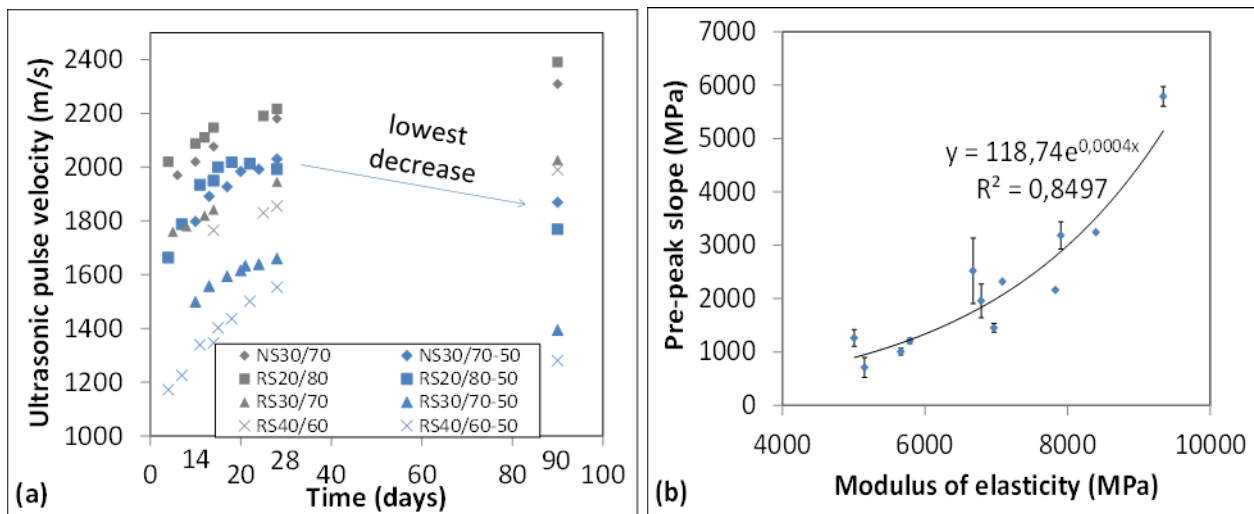


Figure 2.22: : (a) UPV at sealed and drying conditions in function of age; (b) Correlation between the pre-peak slope and modulus of elasticity at RH=90%

2.6.3 AE analysis

- Fracture behavior

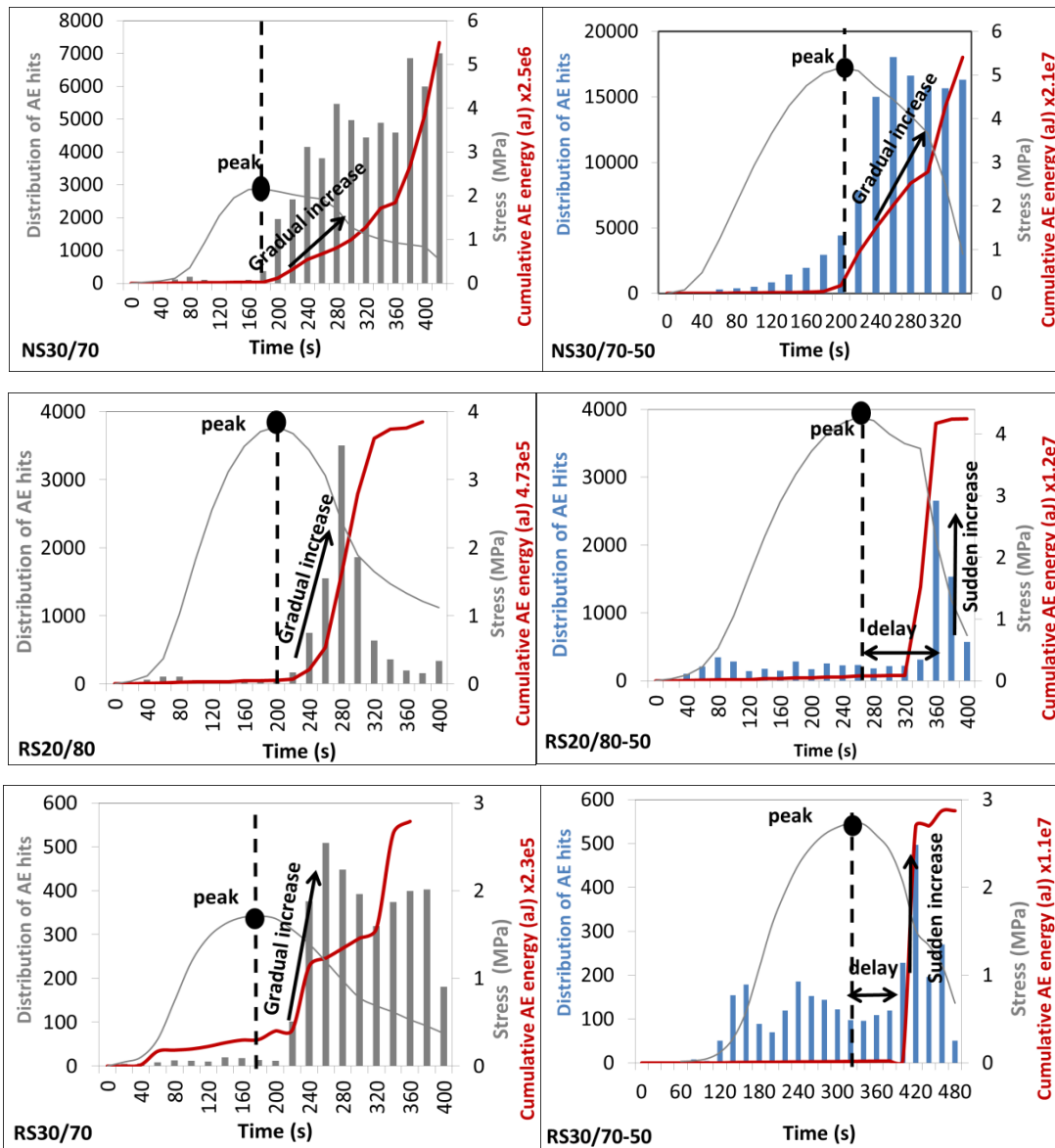
Figure 2.23 shows the correlation between stress and AE activity represented by distribution of AE hits and AE energy at 28 days at wet and dry curing conditions. The results reveal that at wet conditions, the AE hits gradually increase in the post peak phase. Such behaviour was accompanied by gradual increase in AE energy. This reflects the ductile behaviour experienced by the four mixtures.

At dry curing conditions, NS30/70-50 exhibited less gradual increase in AE hits and AE energy indicating a less ductile behaviour. On the other side, RS mixtures reported a delay in macro-crack formation to exhibit sudden failure after that indicating a brittle behaviour.

Figure 4 (c) showed that at 28 days, the fracture energy at dry curing conditions of NS30/70-50, RS30/70-50 and RS40/60-50 is higher than those at wet ones. This was reflected by higher AE.

However, it can be noticed that the AE energy increase in RS30/70-50 and RS40/60-50 due to drying is highly significant. In addition, though RS20/80-50 reported lower fracture energy than RS20/80 at 28 days (figure 4 (c)), the released AE energy of the former was much higher.

While fracture energy was calculated starting from the peak, this increase in AE energy cannot be attributed to the AE energy in the pre-peak phase because it's insignificant. This unsuccessful correlation between fracture energy and AE energy may be attributed to the sudden failure experienced by the mixtures. It can be noticed that the increase in AE energy occurred mainly at the moment of sudden failure of RS mixtures. Therefore it can be stated that delay in macro-crack formation followed by sudden failure can be a reason behind unsuccessful correlation between AE energy and fracture energy.



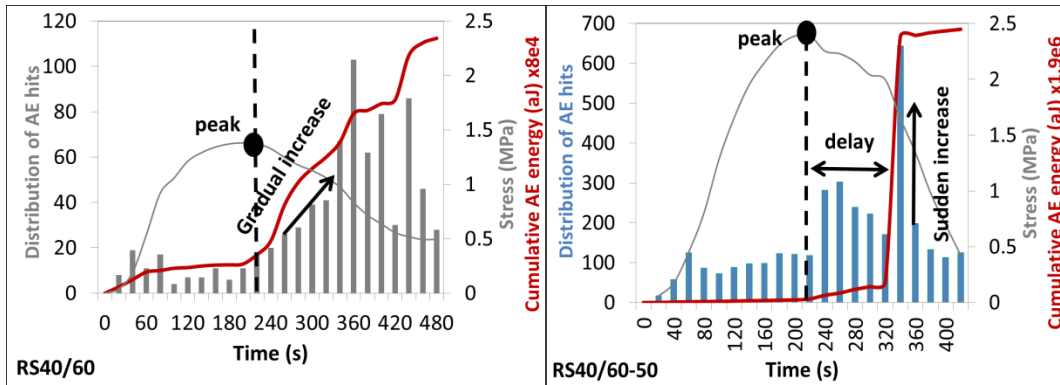


Figure 2.23: Correlation between stress and AE activity represented by distribution of AE hits and AE energy

- AE events localization and DIC

Figure 2.24 shows the AE events localization maps at 28 days of NS30/70 at RH=90% and RH=50%. For brevity, just those of NS30/70 and NS30/70-50 are presented. The AE events of each phase concerns only the phase itself (rather than accumulation of AE events). The first phase begins from the starting point of the curve and increases non-linearly to reach approximately a stress level of 20% of peak stress. As stated in chapter 1, this phase may be known to be the compaction phase (Sun et al., 2020). During this phase, no new cracks are formed. The axial compressive loading causes the closure of pre-existing cracks and pores in addition to friction. Compared to sealed specimens, the dried specimen reported an increase in the number of AE events.

During the linear phase (21-45%) –according to DIC-, the sealed specimens did not exhibit any single event whereas several events have reported in the dried one. This may point out that damage has started at earlier stress levels in the dried specimens. A similar trend was revealed in the phase that represent the stable growth of cracks (46-80% of stress level) and the phase of unstable growth of cracks (Wang et al., 2021; Zhao et al., 2020). It has been called the phase of non-stable growth of cracks due to the distribution of AE events. During these phases at dried conditions, the number of AE events increases reflecting the higher degree of damage taking place with the increase in stress level. A remarkable increase in the number of AE events was captured in the phase that directly precedes the peak (non-stable growth of cracks) due to the fact that this phase evidences microcracks' coalescence.

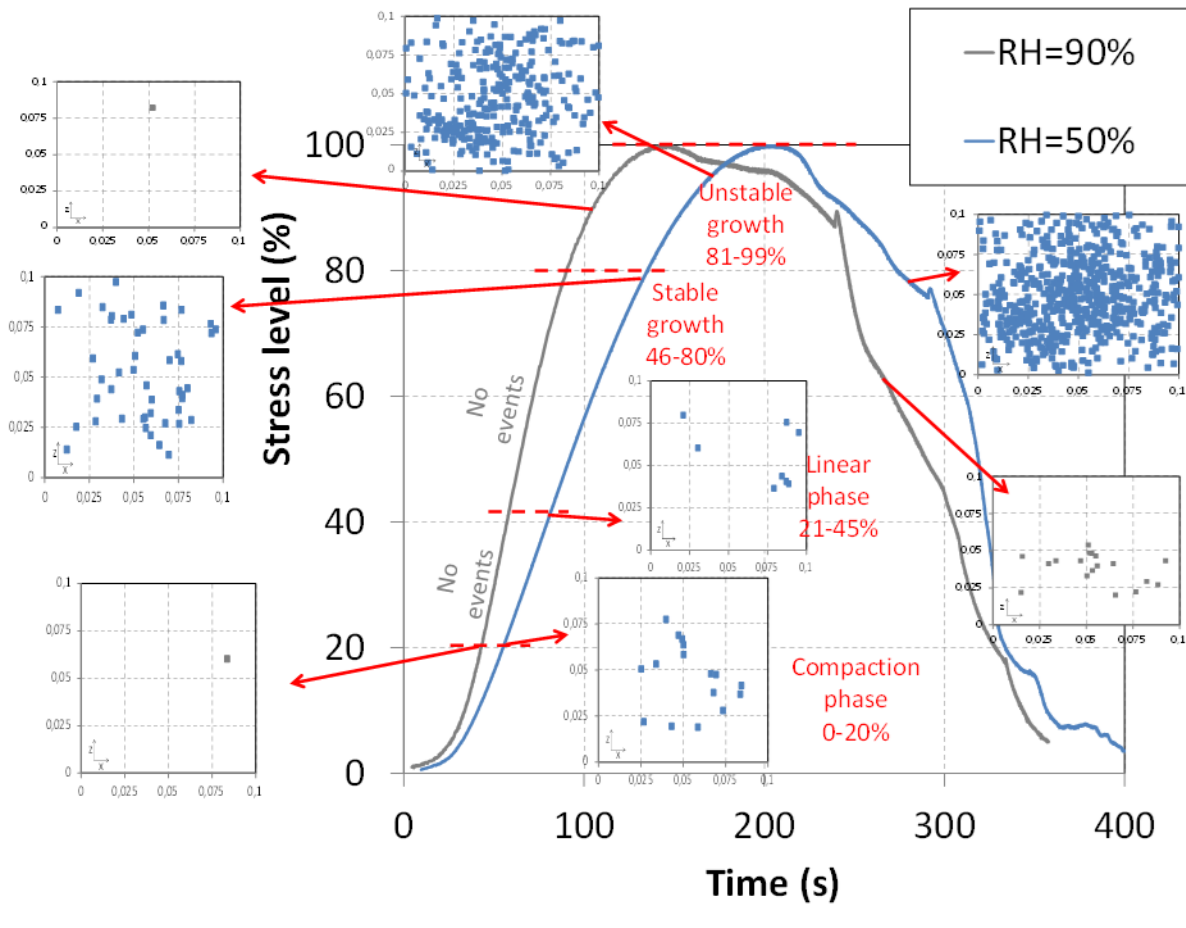


Figure 2.24: Localization of AE events (dimensions in meters) of NS30/70 at RH=90% and RH=50% with respect to different phases

Figure 2.25 shows the strain evolution (ϵ_{xx}) at the age of 28 days of each mixture at RH=90% at 80% of stress level, at peak and at stress level of 150% after the peak and for RH=50% at 40% and 60% stress levels in addition to the stress levels mentioned for RH=90%. While damage was basically not detected at stress level of 80% at RH=90%, it is present at RH=50% showing that the dried specimens are more vulnerable to generate cracks under mechanical loadings which can be attributed to pre-existing shrinkage induced cracking. At dried conditions, DIC results reveal that RS mixtures are more susceptible to cracking than the NS one.

A macrocrack comes after the phase of coalescence. The AE events are remarkably distributed all over the dried specimen at the end of the fracture process reflecting the spreading of cracks. The photos in figure 2.24 confirm with the AE events results where dried specimens are full of cracks particularly the RS mixtures –much more than NS one- reflecting their points of defects to develop cracks.

In fact, microcracks are initiated at the interfacial transition zone (ITZ) between the aggregate and the matrix (Golewski, 2018). The occurring of microcracks is governed by the extent of tensile stress and that of the bonding strength between the sand and the matrix (Li et al., 2017).

This zone serves as a bridge for stress transfer. It is believed that more defects exist in RS mixtures due to the presence of cracks and pores. These defects weaken the ITZs. In addition, Lee & Choi (2013) stated that recycled aggregate concrete failure may be due to the internal cracking in the recycled aggregate itself in addition to ITZ. By taking into consideration this aspect as well, this increases more the weak points and thus raises the possibility of micro-cracking initiation in RS mixtures. Drying, by its turn, causes points of defects or microcracks. A RS specimen that comprises this weak point as well (shrinkage induced cracking) would result in a higher degree of damage than NS specimen.

Eventually, still a general common type of failure is similar in all mixtures whether it is of a sealed condition or drying condition. Vertical cracks, theoretically speaking, are to be shaped when concrete is under compressive loading. Nevertheless, the loading plates restrict the specimen to expand laterally and accordingly a triaxial confined region is generated. Eventually, failure can be due to the effect of tension and shear.

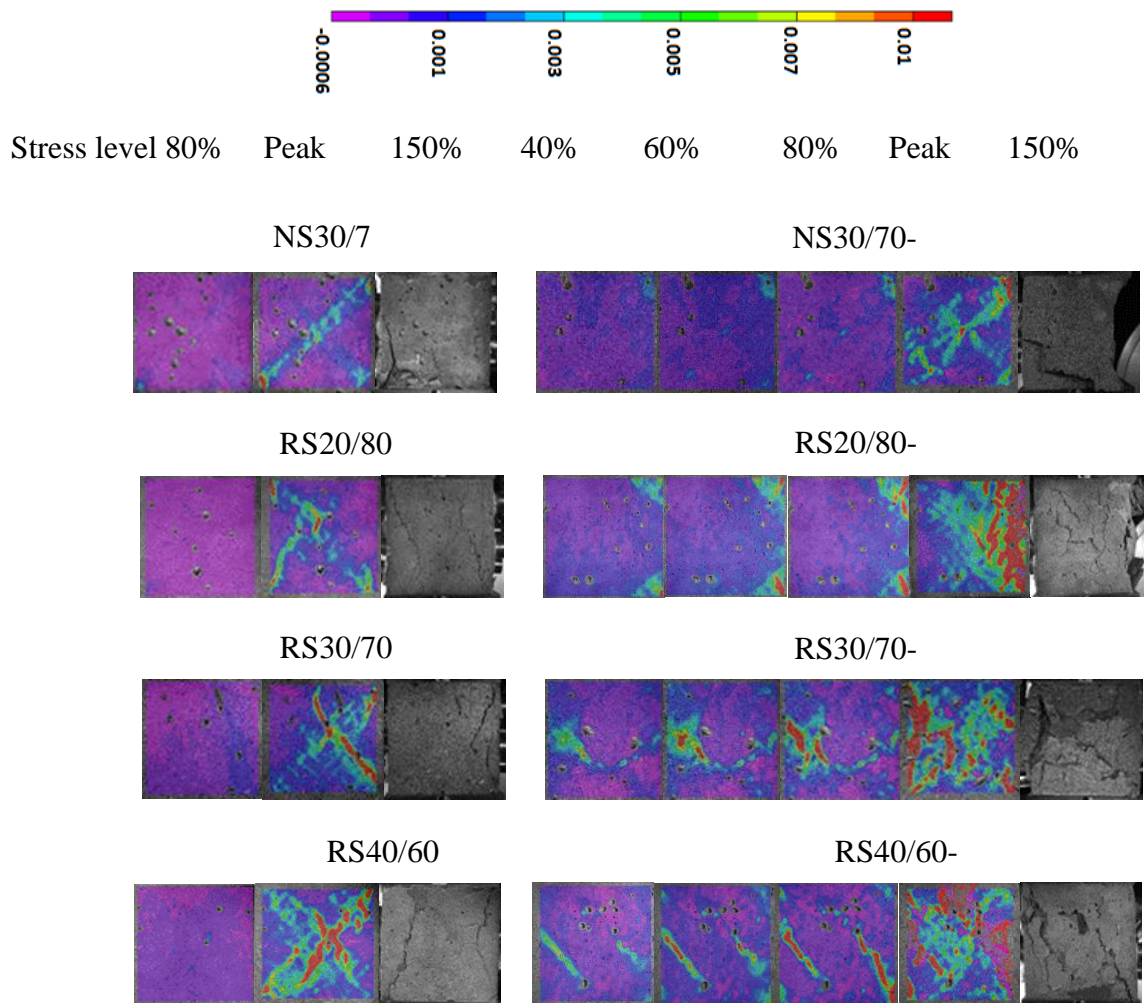


Figure 2.25: Strain evolution (ϵ_{xx}) of each mixture at 28 days at RH=90% and RH=50% at different stress levels

- AE peak frequency- AE energy

Figure 2.26 shows the correlation of peak frequency with cumulative AE hits (figure 2.26 (a)) and with AE energy (figure 2.26 (b)) for the four mixtures at dry curing condition. It may be worth to note here that the AE energy value represent the level where the AE activity were still significantly reported. The results in figure 8 shows that the AE signals are mainly of 101-150 KHz-peak frequency. In addition, they are distributed at lower AE peak frequency (51-100 KHz) in addition to other frequency bands.

It is agreed that the interpretation of AE signals based on the frequency characteristics can reflect the type of damage inside a material [34-36]. Past studies have alleged that low frequency AE signal represents the formation of macrocracks while those of high frequency correspond to microcracks generation. It can be noticed that 24% of the total hits of RS40/60-50 has 24% are of 51-100 KHz peak frequency signals. This percentage is more than any other mixture. By considering that 51-100 KHz is a low frequency band, it can be stated that RS40/60-50 has experienced more formation of major cracks than any other mixture. Eventually, RS40/60-50 may be more damaged than other mixtures. In addition, according to figure 8 (b), RS40/60-50 exhibited the lowest AE energy levels. This may indicate that the formation of crack requires less energy in RS40/60-50.

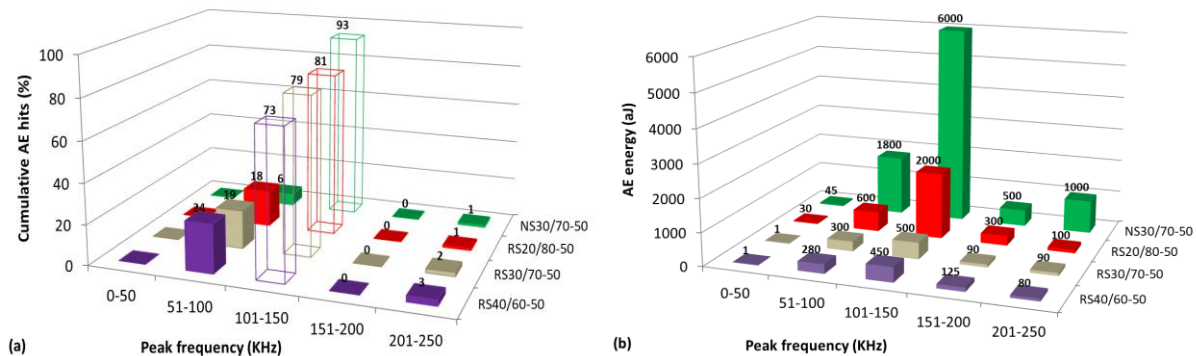


Figure 2.26: Correlation of cumulative AE hits (%) (a) and AE energy (aJ) (b) with peak frequency of each mixture at dry curing condition

2.6.4 Capillary rise

The capillarity of water due to surface tension is a common phenomenon in nature. It is associated to the water that exists at an elevation higher than the ground water level. As already stated, the water content affects the properties of earthen materials. In case of abnormal increase of water content, a collapse of earthen wall may occur (Traoré et al., 2021). The capillary rise tests were carried out at after 120 days of drying. Figure 2.26 shows the mass gain as function of time of each mixture. The mass gain is more important in RS mixtures and increases with the percentage of clay. RS40/60 gained the most compared to other mixtures in the first phase that corresponds to a high rate of mass gain. This trend continues during the second phase that

represents stabilization. Similarly, the coefficient of absorption reported the highest for RS40/60 particularly in the first phase indicating a higher sensitivity of RS40/60 to water.

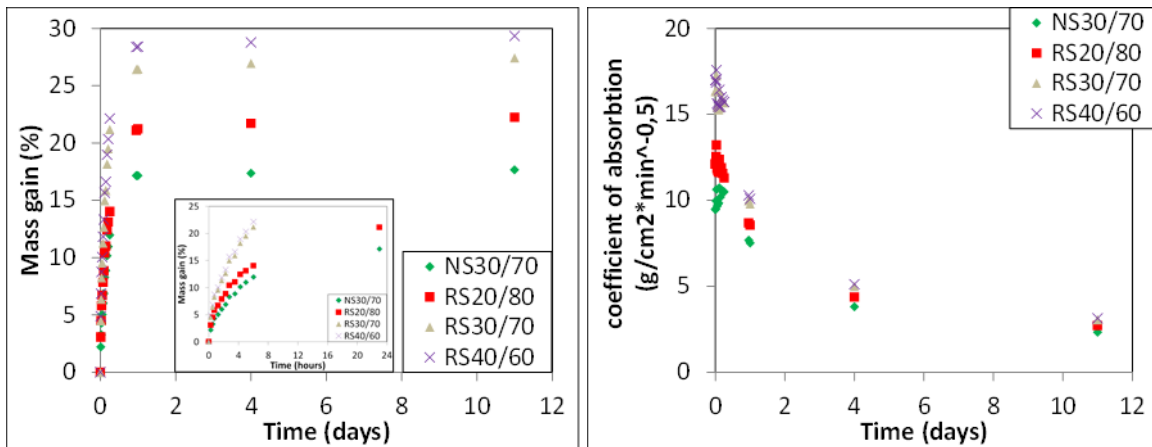


Figure 2.27: Mass gain and coefficient of absorption of each mixture due to capillary rise

2.6.5 Carbonation

The results of carbonation are present in figure 2.27. At wet curing conditions, specimens are not carbonated. At dry curing conditions, the depth of carbonation of NS30/70-50 is approximately equal to 2.5 cm and increases when NS is replaced by RS with RS30/70-50. However, the depth of carbonation of RS40/60-50 is very small in comparison which may be due to different porous network as a high content of clay is added.

This may indicate that carbonation may have contributed to strength development at drying curing conditions. Apart from this thesis, it would be interesting in the future to assess how much separately each of hydration, carbonation and suction effect contributed to strength development. In addition, shrinkage induced cracking should be taken into account. The use of those results for the evaluation of the carbon footprint would be also another important environmental insight of the mixtures that would be interesting to calculate.

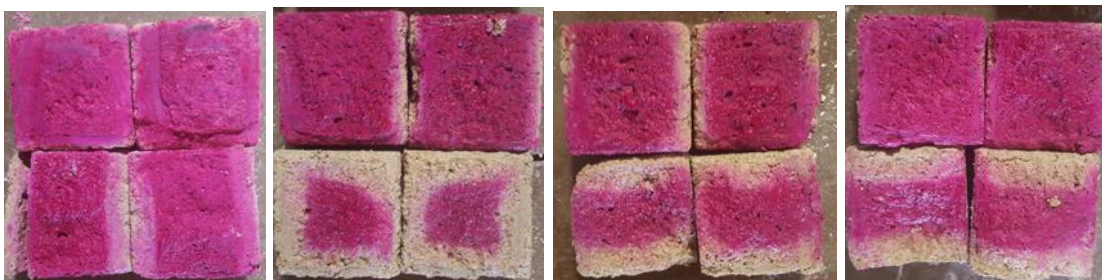


Figure 2.28: Carbonation at 120 days. From right to left: NS30/70, RS20/80, RS30/70 and RS40/60 where the upper and lower raw correspond to the specimens at wet and drying curing conditions, respectively.

2.6.6 Sorption isotherms

The results of earth concrete mixtures are presented in figure 2.28. Earth materials normally show S-shape. The first phase, until approximately 18% of RH, corresponds to the occurrence of single

layer of adsorbed molecules (until point B in figure 2.18). The linear section between 18% and 55% of RH points out to multiple layers of adsorbed water. A sharp increase is expected at RH levels higher than 80% indicating the thickness of layers and pore filling. The hygroscopic regime ends when the layers start to interconnect forming water meniscus which also represents the beginning of the capillary regime. Finally, supersaturation occurs.

According to the resulted curves, earth concrete mixtures are of type 2B of figure 2.18. In fact, clayey materials are known to exhibit this behavior with hysteresis loops (McGregor, 2014) that are more pronounced at higher relative humidities associated with the capillary condensation (the condensation of water vapor into liquid state).

The differences between RS mixtures can be attributed to the higher clay content that it is of fine particles and thus of large surface area. The latter permits the more adsorption of water molecules (Woodruff & Revil, 2011). However, as Arthur (Arthur, 2017) stated that clay mineralogy plays a role in moisture adsorption only starting from RH of 75%, it seems that clay in terms of its content at 30% and 40% also slightly affect the desorption and adsorption processes at 0-80% RH range. In addition, though differences were more remarkable at clay content of 20% at RH=80% during the desorption process; such difference was reduced as RH decreases. On the other side, NS30/70 showed the remarkable lowest water content than RS30/70 particularly and RS mixtures generally at different RHs.

The results show that the replacement of NS by RS has more effect on the sorption isotherms than clay content. Our assessment carried out on sorption isotherms reveals that a room or building made of NS earth concrete mixture is less sensitive to relative humidity variations and thus it is more capable of creating a better healthy environment to occupants than RS earth concrete mixture by regulating the hygric conditions.

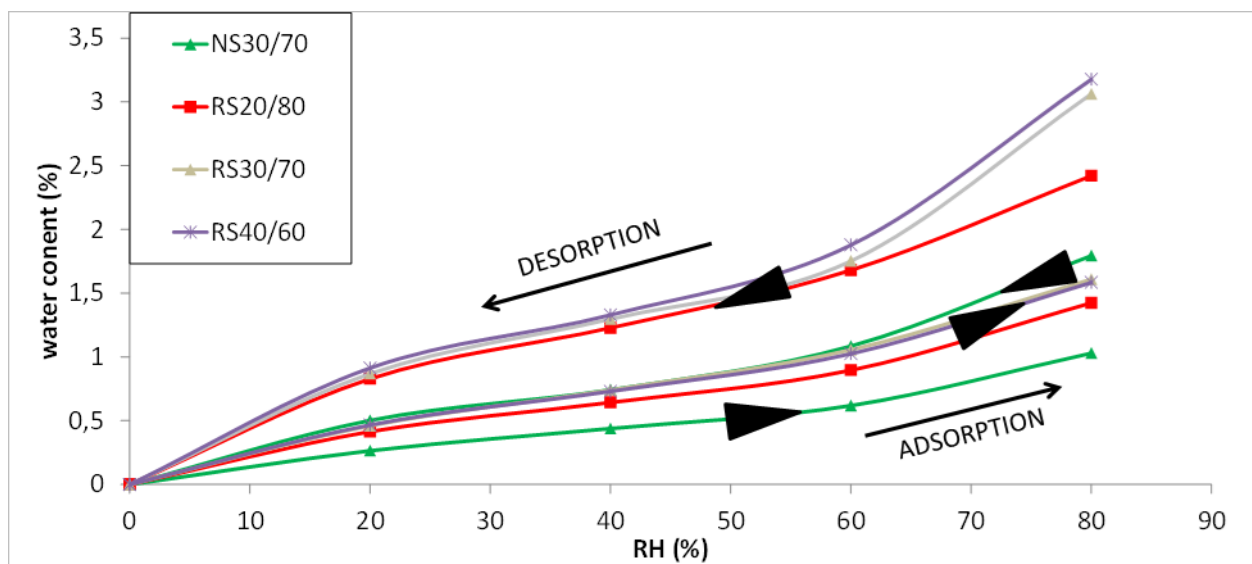


Figure 2.29: Equilibrium moisture content curves (sorption isotherms)

The parameters A and B (equation 2-11 and 2-12) were calculated using the least squares method. Those related to NS30/70 are presented in the table 2.5. The density values ρ_s were already presented in table 2.2. The porosity of each mixture based on equation 2-36 is present in table 2-4.

Mixture	NS30/70	RS20/80	RS30/70	RS40/60
Porosity	0.35	0.38	0.41	0.42

Table 2.4: Porosity of each mixture

The fitting S_1 is properly obtained when $A=0.44$ and $B=1.68E7$. Figure 2.29 shows the experimental and fitting curves related to all mixtures.

RH	w (equation 2-34)	P_c (Pa) (equation 2-9)	S_1 (%)(equation 2-8)	Fitting S_1 (%)(equation 2-12)
0.2	0.4	2.18E+08	1.5	1.3
0.4	0.6	1.24E+08	2.3	2.0
0.6	0.9	6.92E+07	3.3	3.3
0.8	1.4	3.02E+07	5.5	5.5

Table 2.5: Least square method for NS30/70

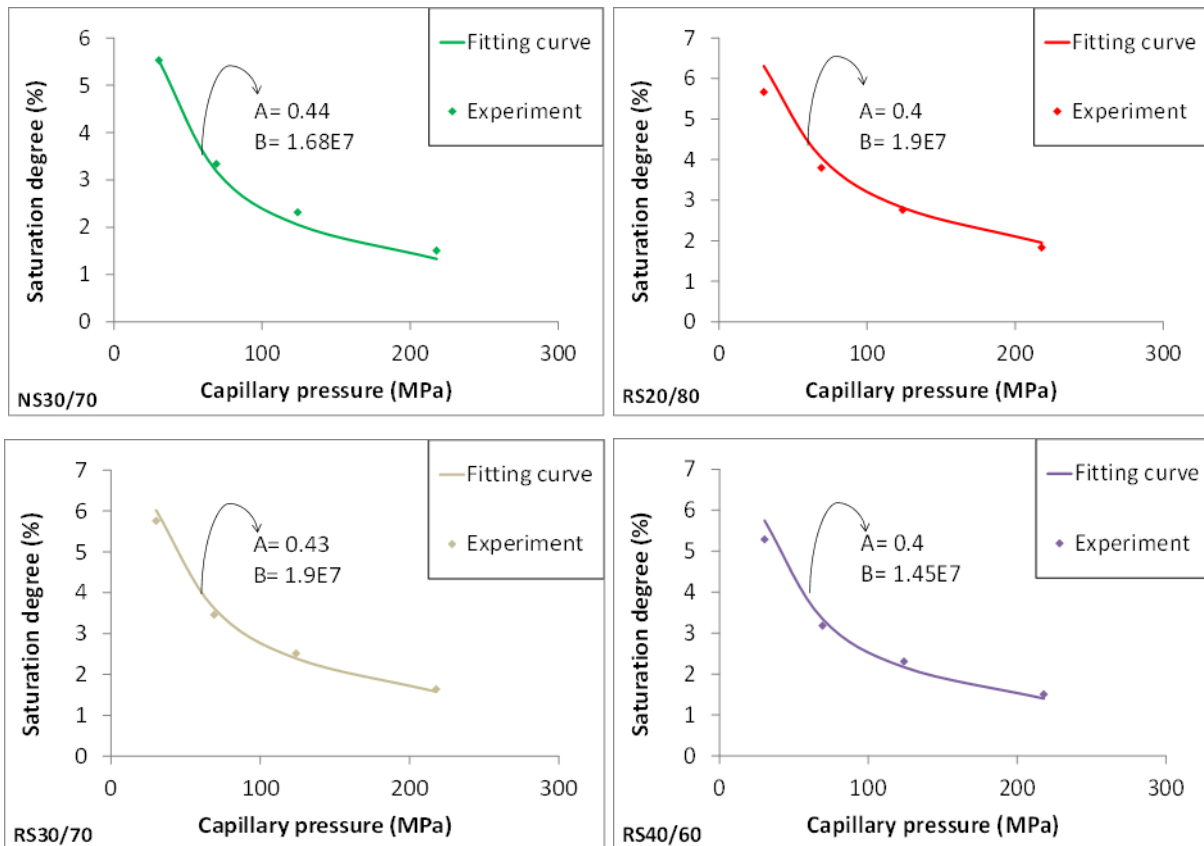


Figure 2.30: Fitting curves based on the least square method for all the mixtures

2.6.7 Shrinkage tests

In order to have a better understanding of the failure process of earth concrete specimens, shrinkage tests have been also conducted. Generally speaking, the higher drying shrinkage –and usually higher mass loss- and the lower tensile strength of a mixture, the more it is susceptible to develop cracks (Adams et al., 2016). Figure 2.30 shows the mass loss and the total shrinkage of each mixture. In addition, it displays the autogenous shrinkage of NS30/70 and RS30/70.

The autogenous shrinkage decreases when RS completely replaces NS. Indeed, this type of shrinkage tends to decrease with recycled aggregate remarkably (Abate et al., 2018; Nassar and Soroushian, 2013) due to the internal curing effect of recycled aggregate (or RS). The pre-absorbed water is released to compensate the self-desiccation occurring in the mixture (Mao et al., 2021). This means that the pre-saturation degree influences the autogenous shrinkage and that dry recycled aggregate may not effectively reduce this autogenous shrinkage. Yet the autogenous shrinkage is of low values and the drying shrinkage (total shrinkage-autogenous shrinkage) is the one that accounts for the most of the total shrinkage and accordingly the developed cracks.

The mass loss behavior in figure 2.30 can be divided into three phases in all specimens. A rapid mass loss was reported at the first days. Such phase is controlled by the ambient conditions and it continues as long as there is supply of water from inside the specimen. Once the water migrating from inside to the outside is not anymore enough to meet that evaporative demand, the second phase started and thus it would be characterized by a lower rate of drying compared to the first phase. The third phase is known to be of almost constant low evaporation rate (Tran et al., 2019).

The mass loss of NS30/70 and RS30/70 increases from almost 18% to 29% accompanied by a shrinkage increase from 2000 $\mu\text{m}/\text{m}$ to 4800 $\mu\text{m}/\text{m}$, respectively. For RS mixtures, shrinkage increases with clay content from almost 3000 $\mu\text{m}/\text{m}$ in the 20% clay mixture to 5500 $\mu\text{m}/\text{m}$ in the 40% clay mixture.

The mass loss values and accordingly the drying shrinkage ones reveal how much each component –based on its microstructure- permits the more or less migration of its water. The differences between NS30/70 and RS3/70 reveals to what extent the RS due to its porous state is vulnerable to drying shrinkage and similarly the comparison between RS mixtures shows the sensitivity of clay –being of fine particles- to drying shrinkage.

The already presented flexural strengths that have shown that NS30/70-50 is of highest strength and that RS40/60-50 and RS30/70-50 are of lowest strength in addition to these shrinkage results demonstrate that RS40/60-50 in addition to RS30/70-50 are more vulnerable to cracking than any other mixture.

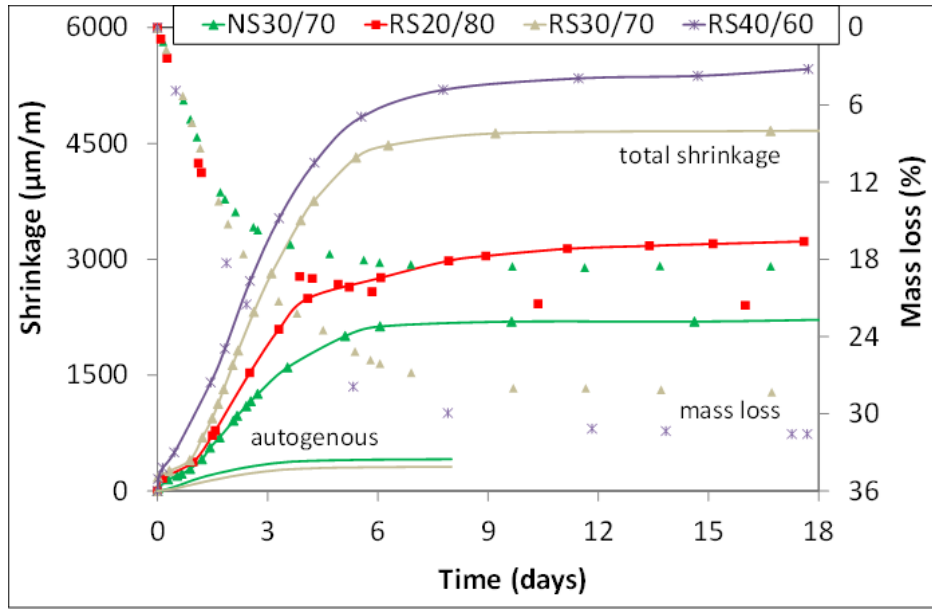


Figure 2.31: Mass loss, autogenous shrinkage and total shrinkage of different mixtures

For a better understanding of the effect of drying on the mechanical properties. The mass loss and shrinkage tests are simulated by considering a $\frac{1}{4}$ of a $4X4X16 \text{ cm}^3$ specimen in 2D where water migrates from one of the lateral sides. A similar approach was adopted for cubes as shown in figure 2.31.

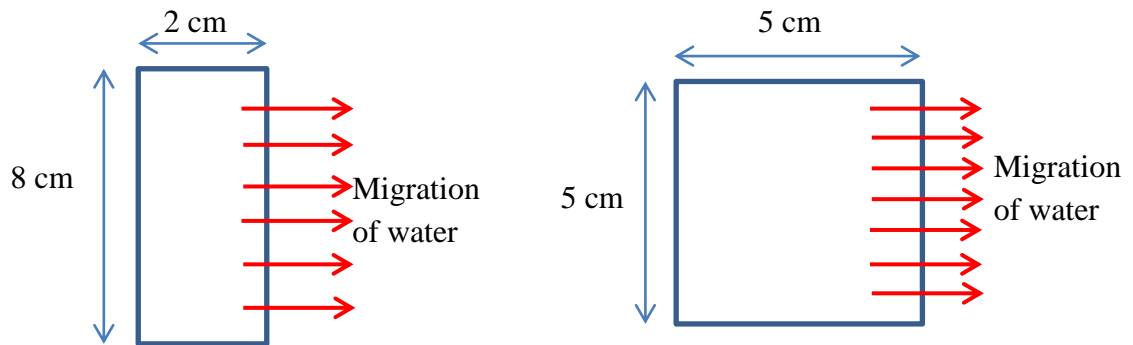


Figure 2.32: Geometry and boundary conditions for prisms (a) and cubes (b)

Table 2.6 shows the parameters adopted to reproduce the mass loss curves. The convection parameter h_0 was taken constant for all mixtures. The permeability was considered based on a past study carried out on earth concrete (Ngo, 2018) and then calibration was carried out.

Mixture	A	B	ϕ (%)	K (m^2)	q	RH _{ext} (%)	RH _{int} (%)	h_0
NS30/70	0.44	1.68E7	35	2.7E-15	4	50	98	2E4
RS20/80	0.4	1.9E7	37	2.77E-15	4	50	98	2E4
RS30/70	0.43	1.9E7	41	2.08E-15	4	50	98	2E4

RS40/60	0.44	1.8E7	42	2.4E-15	4	50	98	2E4
---------	------	-------	----	---------	---	----	----	-----

Table 2.6: Parameters used for simulation

The simulation of mass loss curves is shown in figure 2.32. The considered successful particularly the calculated porosity values permitted the successful reproduction of mass loss curves.

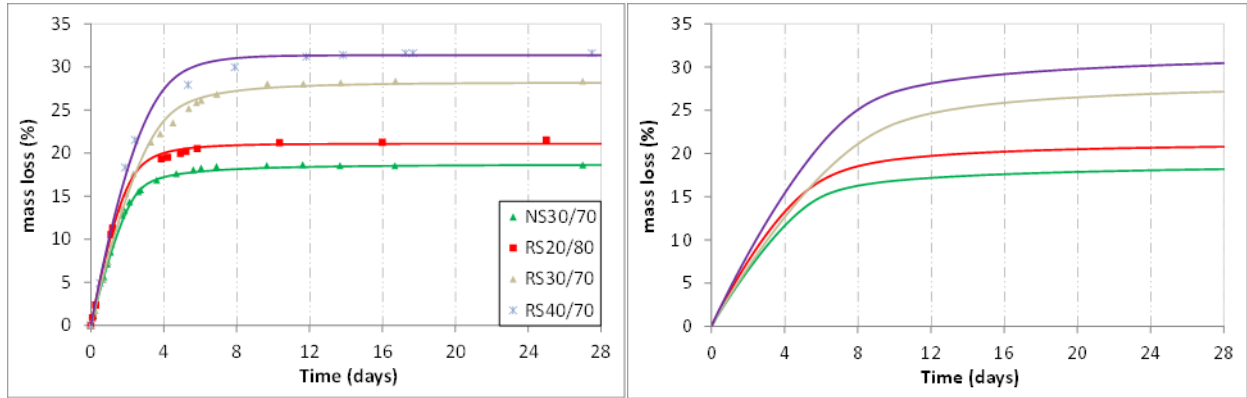


Figure 2.33: Reproduction of mass loss curves for prisms (a) and cubes (b)

In addition, the internal relative humidity (at core or center) for all mixtures at the age of 28 days is presented for the prisms and cubes (figure 2.33). An equilibrium is reached earlier in prisms than in cubes at this age. In fact, while the water required a maximum distance of 2 cm to reach the surface in prisms, it required a 5 cm distance in cubes. This was reflected by decrease in the rate of drying. For cubes specimens, the slight continuous increase or less stabilization in the mass loss curves at the end was reflected by internal higher relative humidity at 28 days.

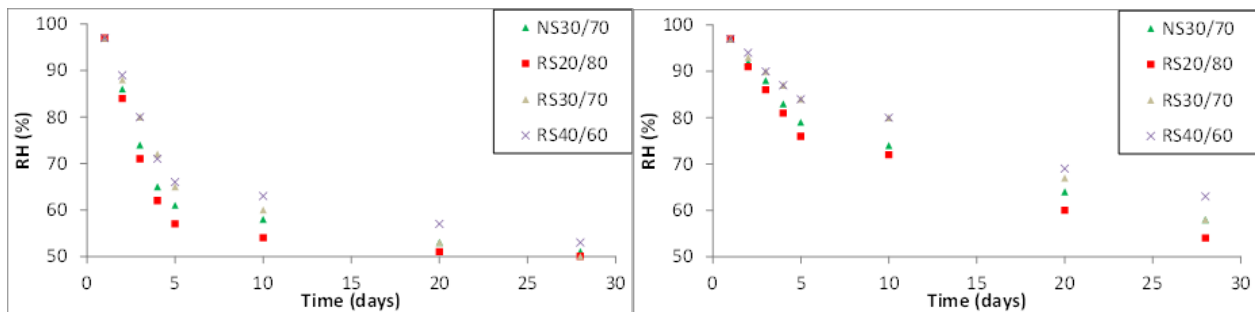


Figure 2.34: The evolution of internal RH in prisms (a) and cubes (b)

2.6.8 Modeling of drying shrinkage

The modeling of drying shrinkage is carried out in this section for NS30/70 and RS30/70 only as their autogenous shrinkage is known as was presented in chapter 2 part A. The modeling according to Granger is carried out (equation 2-15). Table 2.7 shows the parameters and figure 2.34 present the experimental and simulation curves for prisms and accordingly cubes. This part is linked with hygro-mechanical study in chapter 2 part B.

K	
NS30/70	7.6E-6
RS30/70	1.57E-5

Table 2.7: Granger's approach parameters

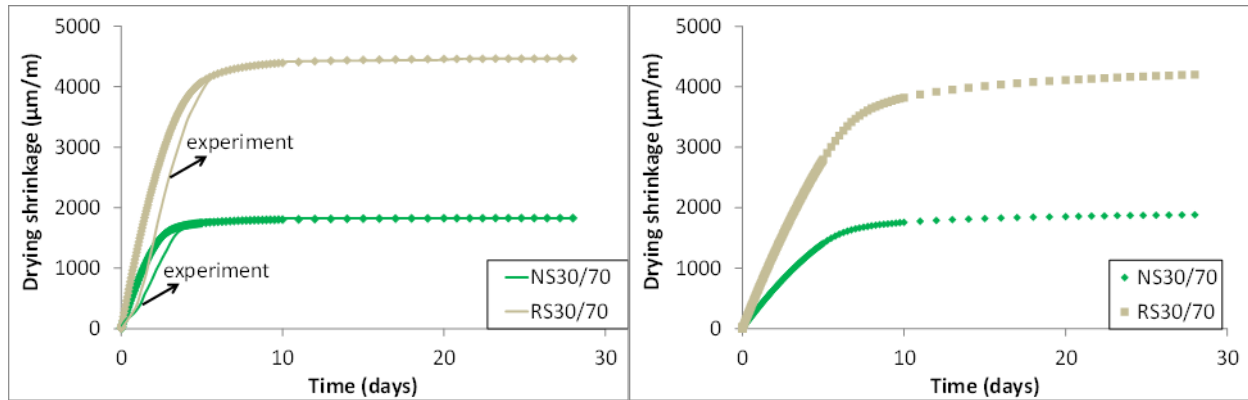


Figure 2.35: Simulation of drying shrinkage of prisms (left) and cubes (right)

Conclusions

Earth concrete mixtures were prepared with natural sand (NS) or recycled sand (RS) in addition to different amounts of kaolinite clay and conserved at relative humidity (RH) of 90% and 50% for 14, 28 and 90 days. The specimens were subjected to uniaxial compression tests. Several conclusions have been drawn:

- The dominancy of capillary suction effect declines with prolonged drying due to the more formation of shrinkage induced cracking.
- The pre-peak slope values are proportional to the ultrasonic pulse velocity values for specimens at sealed conditions. Eventually, an equation correlating the slope with modulus of elasticity has been proposed. On the other side, it seems that concerning drying, the decrease or increase in the slope value is governed by the vulnerability of the mixtures' components to drying.
- The fracture energy decreases with age at wet and dried conditions.
- The number of AE events increases in dried specimens throughout the whole testing process phases.
- The AE activity in the pre-peak phase can be used as a sign for strength development from one side and generation of shrinkage induced cracking from other side.
- Drying leads to the formation of random cracks all over the specimen.
- The replacement of NS by RS influences the sorption isotherm more than the clay content.
- The equilibrium state of RH is reached faster in prisms than in cubes.

<u>Chapter 3 Part A. Earth concrete under cyclic loadings: Stress-strain curves and acoustic emission damage assessment</u>	82
<u>3.1 Quasi-brittle materials under cyclic loadings</u>	82
<u>3.2 AE damage assessment</u>	84
<u>3.2.1 Kaiser Effect</u>	84
<u>3.2.2 Damage assessment</u>	87
<u>3.2.3 Shortcomings</u>	87
<u>3.3 Experimental program</u>	88
<u>3.3.1 Materials, preliminary test and mix design</u>	88
<u>3.3.2 Test procedure</u>	88
<u>3.4 Results</u>	89
<u>3.4.1 Stress-strain curves</u>	89
<u>3.5 Damage assessment by means of AE</u>	91
<u>3.5.1 Load ratio (LR) – Kaiser Effect</u>	91
<u>3.5.2 Calm ratio</u>	93
<u>3.5.3 Damage classification</u>	94
<u>3.6 Kaiser Effect by means of DIC</u>	95
<u>Conclusions</u>	99

Chapter 3 Part A. Earth concrete under cyclic loadings: Stress-strain curves and acoustic emission damage assessment

During its service, a structure is prone to cyclic loadings. Generally speaking, these loadings may be of wind, earthquake (Dang et al., 2018), oceanic loads (Ye & Jeng, 2012), drilling, blasting, mining (Attewell & Farmer, 1973; Zhang et al., 2020) and live loads variation sources (Mojsilović, 2020). For repeated mechanical loading, the stress-strain exhibit hysteresis loops. Assessments are basically proposed based on the features of such loops. More research is required to assess the behavior of other quasi-brittle materials under cyclic loading such as earth concrete.

The monitoring of a structure condition subjected to loading is mandatory. The consideration of AE technique is agreed to yield satisfactory results. Under loading-unloading cycles, the study of Kaiser Effect is a widely spread approach for damage assessment. This phenomenon states that if a material got loaded, unloaded and then reloaded, acoustic activity will not be generated until the previous maximum load (PML) or stress (PMS) is surpassed or exceeded. In a material that generally attains Kaiser Effect, the ‘stress memory’ gives the opportunity to engineers to determine the stresses experienced in the past of a certain structure. On the other side, the non-fulfillment of Kaiser Effect is a sign of damage occurrence before the previous maximum load. The damage assessment based on Kaiser Effect has yielded the Load ratio and Calm ratio indices (Burd and Kishen, 2021). Both indices together form a qualification scheme that characterizes the degree of damage in a material subjected to cyclic loadings into minor, intermediate and heavy levels.

In the following chapter, it is aimed to assess the pre-peak phase of different earth concrete mixtures. In addition, damage assessment is carried out based on AE technique. Finally, the possibility to examine Kaiser Effect by means of digital image correlation (DIC) is verified.

3.1 Quasi-brittle materials under cyclic loadings

The mechanism of concrete deterioration or damage under compressive stresses is still accompanied with ambiguity. Moreover, for repeated loads, damage accumulation is not well understood (Breccolotti et al., 2015). Different theories have been considered. The envelope concept (Sinha et al., 1964) is a general approach which states that regardless of the load pattern, all the stress-strain curves would lie within this envelope. This means that unloading and reloading paths do not exceed the envelope curve. The concept of common point was introduced reflecting the change of slope in the loading path (Karsan & Jirsa, 1969).

For repeated mechanical loading, the stress-strain shows hysteresis loops and failure can take place before the equivalent strength revealed for monotonic loading. It has been noticed in the literature that classical concrete under cyclic loadings concerns mainly the post peak phase with a probable consideration of a loop in the non-linear phase. This is due to the fact that this material exhibits elastic deformation at early stress levels. On the other side, the carrying out of cyclic

loading at early stress levels in certain materials such as masonry is more common as it exhibits inelastic deformations in the linear phase. Figure 3.1 shows a typical response of masonry subjected to semi-cyclic compression loadings.

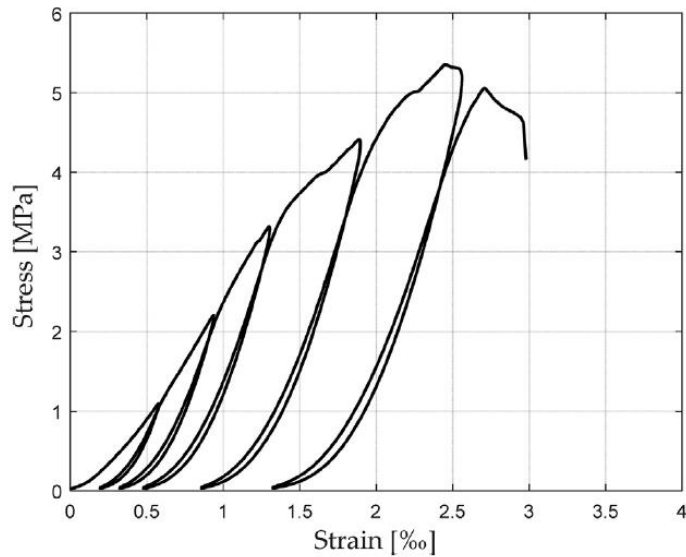


Figure 3.1: A typical response of masonry subjected to cyclic compression loadings (Mojsilović, 2020).

Assessments are basically carried out based on the features of the loops i.e. residual strain ϵ_{rp} , unloading strain ϵ_u , reloading point ϵ_r , the secant elastic modulus E_s and the common point (Chen et al., 2019). The unloading point is the maximum point reached before the descending branch of a loop. On the other side, the residual point or strain is the intersection point between the x-axis and the unloading curve. The secant modulus corresponds to the slope between the residual strain and unloading strain points. Figure 3.2 shows also, in addition to the common point which is the intersection point between the loading and reloading curves at the top side, the reloading point which is defined as the end point of the reloading curve.

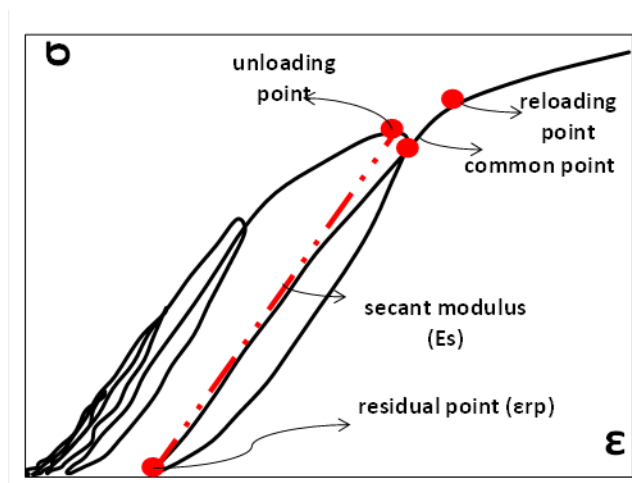


Figure 3.2: Key features of earth concrete under cyclic loadings:

3.2 AE damage assessment

3.2.1 Kaiser Effect

It is stated that the most important value of the work done by the Joseph Kaiser can be found on page 27 of his dissertation (Tensi, 2004):

'By a new reloading (of the tensile specimen) only few jumps occurred (in the photograph of the CRT) until the loading reached the former highest level of 50 kilograms and immediately the impact of the effects (acoustic emission AE) could be observed with the former vehemence'

Kaiser stated in the summary of his dissertation:

'One important result of this testing method developed is the fact that the ex-post statements can be made about the maximum of load, which the material has endured before, without destroying the probe. Also the knowledge of the stress that had laid on the material and not the stress, which exists at the moment'

Kaiser Effect is probably the most well-known approach to reproduce information and acquire knowledge on the stresses experienced in the past (known as memorized stress) by a certain structure. In his work, Joseph Kaiser carried out his experiments on small specimens of wood, sandstone and metals. Studies after than examined Kaiser Effect on concrete, rocks...

- The onset of AE

It is said that Kaiser Effect is satisfied when no AE activity is captured before the previous maximum stress (PMS) is attained. In fact, the best scenario is zero AE activity before the PMS is reached. Nevertheless, AE activity is more likely to be captured basically due to frictional movement along exiting cracks. In case of AE detection before PMS, this signifies that damage has occurred.

Thus, the task is to estimate the actual onset of AE activity. This onset which is related to damage rather than friction. Different approaches have been proposed. Cumulative number of hits versus stress is one of these ideas as shown in figure 3.3 where σ_m is the peak stress. Later studies replaced the cumulative hits by hit rate which can be the number of AE signals received per second or per 1 MPa increase. Bilinear regression has been applied as well. Moreover, the hit rate may be replaced by its square aiming to a sharper inflection (Hardy et al., 1989).

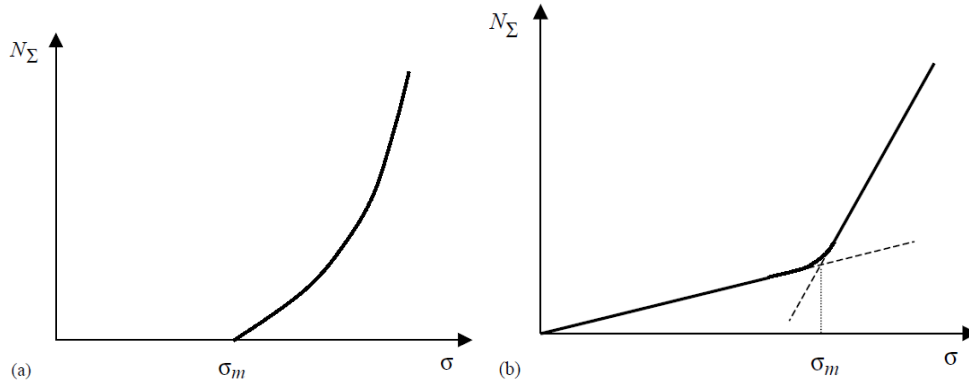


Figure 3.3: Cumulative number of AE hits versus stress in case of (a) zero AE activity and (b) AE activity at low stress level (Lavrov, 2003)

Momayez et al. (1992) proposed the calculation of the maximum curvature of cumulative AE hits versus stress. This approach states that such value of stress corresponds to the targeted stress. Other approaches were proposed in the past by Yoshikawa & Mogi (Yoshikawa and Mogi, 1989; Yoshikawa, & Mogi, 1981). Their method requires the applying of a preloading cycle followed by two reloading cycles of the same maximum stress and higher than the preloading stress (σ_m). Then, the hit rate versus stress is plotted and the moment where the two curves of the two reloading cycles separate corresponds to the preloading maximum stress (σ_m). Figure 3.4 clarifies this.

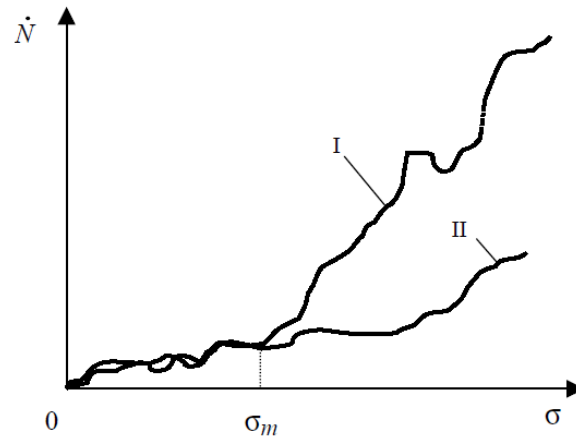


Figure 3.4: AE hit rate versus stress of the two reloading cycles (Yoshikawa & Mogi, 1989; Yoshikawa, & Mogi, 1981)

Recent studies in the literature considered ‘a least of 10 events per 10 seconds’ as the onset of AE activity (Shetty et al., 2019) and the cumulative number signal strength versus time (Xargay et al., 2020).

- Felicity ratio (FR)

Kaiser Effect is linked to the Felicity Ratio (FR) and it takes place by the determination of the latter. The Felicity Ratio is the stress at onset of AE to the previous maximum stress. A value of 1 or more of the Felicity Ratio (FR) indicates that Kaiser Effect is attained. On the other hand, a value less than 1 reveals that damage has occurred before reaching the level of the previous maximum stress.

$$FR = \frac{\text{onset of AE}}{\text{previous maximum stress (PMS)}} \quad (3-1)$$

- Loading rate

Regarding concrete, Vidya Sagar et al. (2015) and Wu et al., (2008) stated that the loading rate has no effect on Kaiser Effect in concrete. Regarding rocks, Zhang et al. (2021) revealed that the loading rate has as well no effect on Kaiser Effect in limestone but the stresses corresponding to Kaiser Effect significantly increase with loading rate for gritstone, sandstone and mudstone. In fact, the studies carried out on the effect of loading rate on Kaiser Effect in concrete are limited compared to that in rocks where it is assessed frequently (Meng et al., 2019). In all cases, if the loading rate is not a parameter to be assessed, keeping it constant would be the best option.

- Load ratio (LR) and calm ratio (CR)

The Kaiser Effect and Felicity Ratio have resulted in the damage indices load ratio (LR) and calm ratio (CR). It is worth to note that these damage indices were originally linked with reinforced concrete beams. Later on, they have been applied on specimens under cyclic compression loadings (Shetty et al., 2019).

LR -as FR- is the ratio of onset of AE to the previous maximum load. It is expressed as follows:

$$LR = \frac{\text{onset of AE}}{\text{previous maximum load (PML)}} \quad (3-2)$$

LR is an indication of structural integrity and a damage indicator. It is linked with the formation of new cracks and not necessarily cracks width development. Being linked with the occurring of damage, LR tends to decrease in case of damage accumulation and stays constant when no damage is reported.

CR is the ratio of cumulative AE activity during the unloading process to the AE activity during the whole cycle. It is expressed as follows:

$$CR = \frac{\text{Cumulative AE activity during unloading}}{\text{Cumulative AE activity during the whole cycle}} \quad (3-3)$$

The term AE activity in equation 3-3 is linked traditionally with hits. The cumulative number of signal strength has been considered as well rather than that of hits as signal strength indirectly expresses the amplitude and duration of the hit giving it its actual magnitude (Colombo et al., 2005).

CR examines the unloading phase. Such process would be basically complex as it comprises the closure of cracks and friction. When originally proposed in 2002 (Ohtsu et al., 2002), the CR was considered as the total AE activity during unloading to the total AE activity during the whole cycle of loading-unloading. Later studies have assigned the denominator to the loading phase only (Colombo et al., 2005; LIU & Ziehl, 2009; Vidya Sagar et al., 2015). In statistically stable structures, the AE activity is rarely captured in the unloading phase (ISO 16837, 2019). This means that –unlike the load ratio- the smaller is CR, the more stable is a structure.

3.2.2 Damage assessment

The LR concerns the assessment of the reloading phase and the CR investigates the unloading phase. Thus, both together are considered complementary. Eventually, a diagram that combines both ratios together was resulted. The both indices together form a qualification scheme that characterizes the degree of damage in a material subjected to cyclic loadings into minor, intermediate and heavy levels (Ohtsu, 2010). Figure 3.5 shows the scheme.

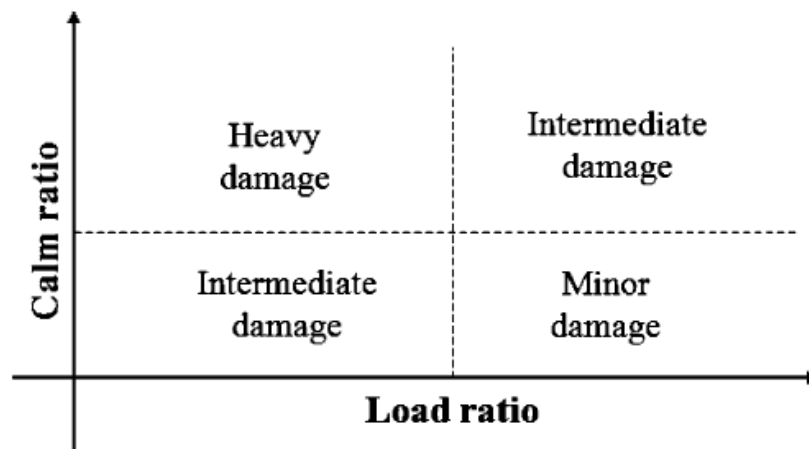


Figure 3.5: Damage classification based on the two ratios

3.2.3 Shortcomings

A known shortcoming is related to the damage assessment presented above. Such assessment lacks damage indices thresholds or boundary limits. In fact, the thresholds -the dash lines seen in figure 3.5- are often proposed by authors depending on the outcome of the LR and CR indices.

This is due to the fact that the indices are influenced by specimen size, test conditions, instruments and other parameters. Basically it can be said that the reference thresholds are 0.9 and 0.05 for LR and CR, respectively and changes are made according to results. This shortcoming requires the carrying out of more experiments, particularly in case of new materials such as earth concrete.

3.3 Experimental program

3.3.1 Materials, preliminary test and mix design

The same procedure stated in chapters 1 and 2 are considered here. The RS was pre-saturated at 80% 24 hours prior to mixing. Table 3.1 shows the mix design of each mixture.

Components (kg/m ³)	Clay (C)	Sand (S)	Cement	W_{eff}	Superplasticizers
NS30/70	440	1026	132	140	1.32
RS20/80	271	1084	110	167	1.32
RS30/70	366	855	110	177	1.32
RS40/60	460	690	103	187	1.32

Table 3.1: Mix design of each mix

3.3.2 Test procedure

- Cyclic compressive tests

10x10x10 cm³ cubes were casted for all mixtures. Demolding was done 3 days after casting and specimens were cured at RH of 90% and 50%. Compressive tests were carried out at the age of 28 days after casting. An electro-mechanical machine with a capacity of 100 kN was used. The velocity adopted was approximately 0.4 mm/min. Cycles at 20%, 40%, 60% and 80% of the maximum load were performed in the pre-peak phase under load control based on the monotonic tests. The unloading phases were under load control also and were targeted to stop at 200 N in all cycles.

- Strain measurement

As stated in the previous two chapters, several approaches were carried out to obtain strains: tracking the displacement of markers fixed on the loading plates, measuring press displacement (the strains are then obtained by dividing displacement over length) and measuring the deformation directly on the specimen's surface. Figure 3.6 shows the stress-strain curves of RS20/80-50 obtained by the three approaches. It can be noticed that the strain values obtained from DIC are lower than those obtained from the loading plate and press. In addition, though the loading plate pre-peak slope is greater than the press one, their residual strains are almost the same. In the following study, the strains of the whole surface exported directly from DIC (named DIC) have been considered.

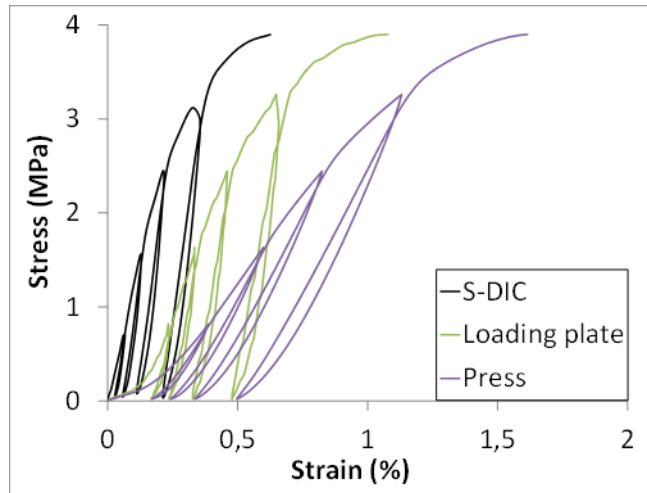


Figure 3.6: Stress-strain curves of RS20/80-50 obtained with different methods

3.4 Results

3.4.1 Stress-strain curves

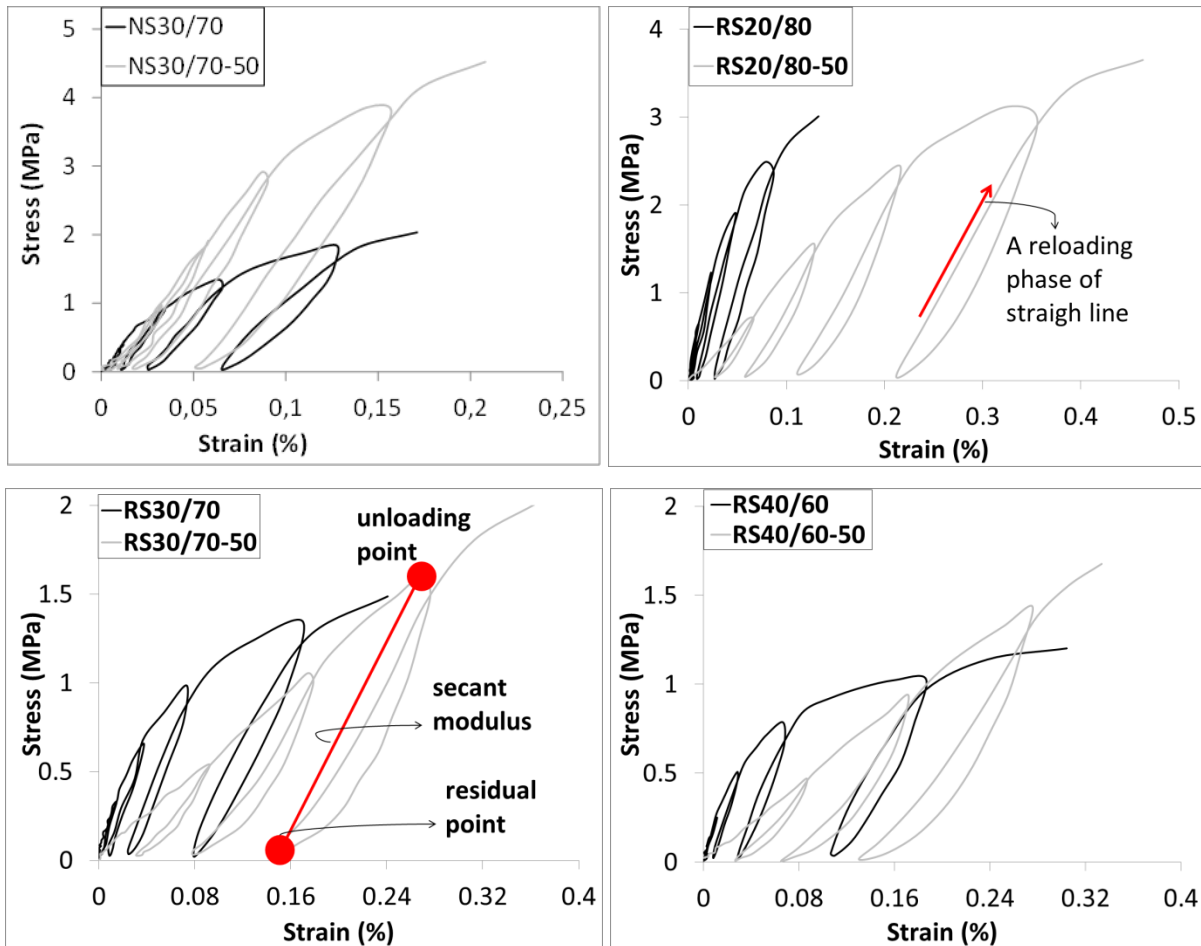


Figure 3.7: Stress-strain curves of the different mixtures

- Exhibition of loops

The strain values in figure 3.7 were obtained directly from the DIC. It can be seen that the fourth cycle of RS30/70-50 and RS40/60-50 are not displayed. In fact, the images' analysis by two-dimensional software requires the specimen to be flat, planer to the imaging center and at a constant distance perpendicular to the visual sensor during the whole experiment. Thus, this may indicate that RS30/70-50 and RS40/60-50 have reported a higher degree of damage which has led to the unsuccessful capture of strains at stress level of 80%.

- Residual strain

Figures 3.8 (a) shows for each cycle the residual strain at RH=90% and RH=50%. The results are presented as function of the maximum load (P/P_{max}). At wet conditions, the residual strains increase with clay content. In addition, the replacement of NS by RS exhibited increase in the residual strains. Lam & Teng (2009) stated that concrete strength is the only parameter governing the residual strains. Others attributed such strains to be led by confinement (Ozbakkaloglu & Akin, 2012). In this work, RS20/80 showed the highest strength and it exhibited the lowest residual strains and vice-versa for RS40/60. In absence of confinement, it can be stated that the residual strains at wet conditions may be governed by strength and that the higher the strength, the smaller the residual strains are. It may be worth to note that the low compressive strengths among the four mixtures contributed to not reveal great differences in the residual plastic strains (Li et al., 2019). At dried conditions, the residual strains decrease in the NS mixture and increase remarkably in the RS ones. This may be attributed to the vulnerability of RS to drying due the higher porosity and shrinkage induced cracking.

- Secant modulus

The secant modulus of each cycle at both curing conditions is shown in figure 3.8 (b). At wet conditions, RS20/80, the mixture of highest strength, reported the highest secant slope among the other mixtures at the four cycles followed by the NS30/70. The secant slope of RS30/70 and RS40/70 are of lower values. Due to drying, the secant slope increases in the NS mixtures (except at the first cycle 20% which can be attributed to the existence of compaction phase -that comes before the linear phase- at such stress level (Zhao et al., 2020)) and decreases in the RS mixtures. As for its effect on residual strains, this may be attributed to the vulnerability of RS to drying.

- Forms of loops

Fractional expressions for unloading and combination of straight lines and quadratic or cubic functions for reloading phases have been proposed in the literature as forms of loops (Hutagi et al., 2020). An almost straight line in the pre-peak reloading lines and a shift to a more complexity in the post-peak reloading lines have been observed with masonry under cyclic loadings (Naraine and Sinha, 1989; Segura et al., 2018). For the mixtures in the following study, it can be noticed that at RH=90%, the loops of the four mixtures are of similar form. At such RH, the unloading and reloading phases are basically of opposite arcs. At RH=50%, an obvious change can be

noticed particularly for the two mixtures of lowest strength, RS30/70-50 and RS40/60-50. At such RH, the reloading phase of these two mixtures is of acute curve and it is in a reverse direction of the arc at RH=90%. This tendency seems to reduce with higher strength and higher secant modulus to form almost a reloading path of straight line as clarified by a red arrow in figure 3.7. The results permit to state a general conclusion that earth concrete loop is of two simple opposite arcs at wet conditions regardless of the mixture's components. Due to drying, the reloading curve of low strength mixtures is in the form of an acute arc.

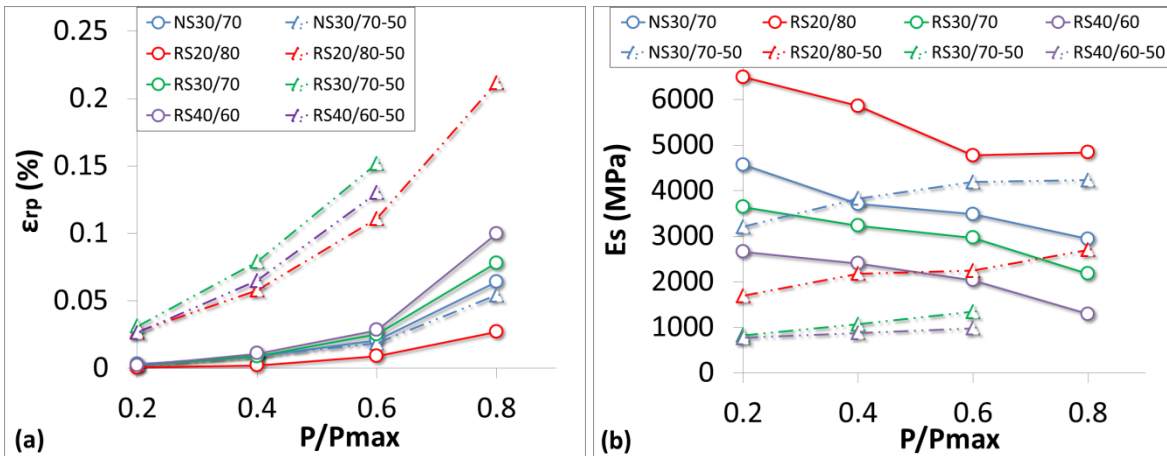


Figure 3.8: Residual strains at RH=90% and RH=50% (a) and the secant slope of each mixture (b)

3.5 Damage assessment by means of AE

The damage indices in the following study are with respect to the maximum load (P/P_{max}).

3.5.1 Load ratio (LR) – Kaiser Effect

As stated before, Kaiser Effect is satisfied when no AE activity is captured before the previous maximum stress (PMS) is attained. If AE activity was detected before PMS, Kaiser Effect is not fulfilled. The assessment of Kaiser Effect is linked to the Felicity Ratio (FR) and it takes place by the determination of the latter. The Felicity Ratio is the stress at onset of AE to the previous maximum stress. A value of 1 or more of the Felicity Ratio (FR) indicates that Kaiser Effect is attained. On the other hand, a value less than 1 reveals that damage has occurred before reaching the level of the previous maximum stress. The Kaiser Effect and Felicity Ratio have resulted in the damage indices load ratio (LR) and calm ratio (CR).

LR -as FR- is the ratio of onset of AE to the previous maximum load. Section 3.2.1 mentioned different approaches that were proposed in the past to recognize properly the onset of AE activity. The determination of the ‘onset of AE’ is subjective as it may yield different results among researchers and the methods adopted. In addition, not all approaches are applicable i.e. a specimen may not generate 10 events in a time interval of 10 seconds. Therefore, it seems essential to address explicitly the considered method. In this work, the breaking point of the ‘cumulative signal strength vs time’ is considered as the onset of AE activity. Figure 3.9 shows

the onset of AE at each cycle of NS30/70. Figure 3.10 demonstrates the four cycles together highlighting the onset of AE.

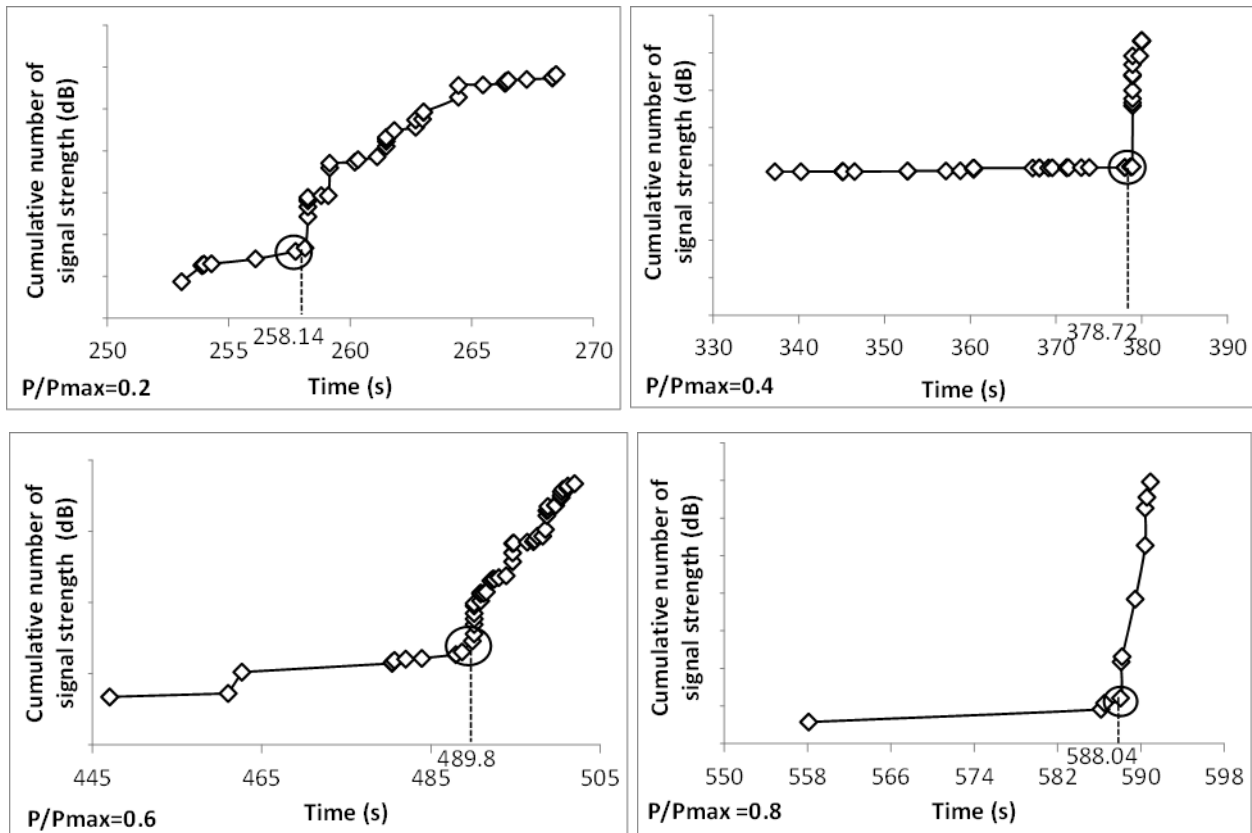


Figure 3.9: Onset of AE in NS30/70 at each cycle

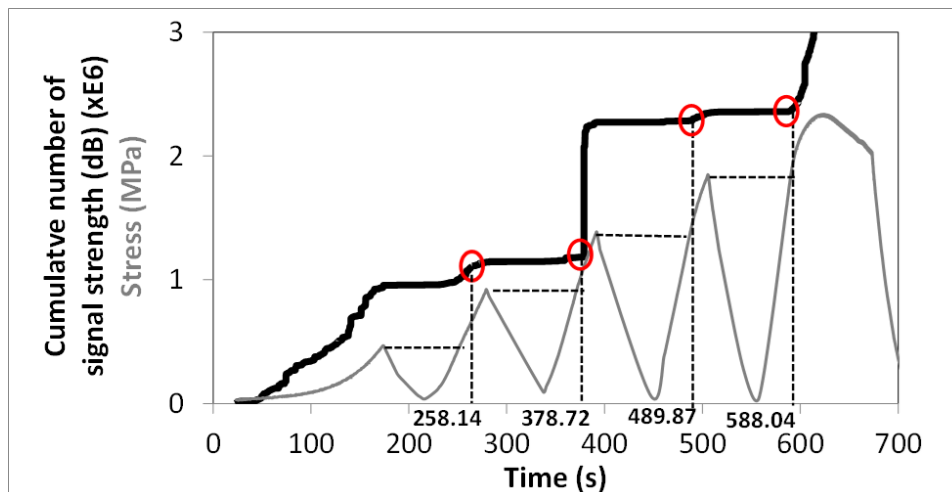


Figure 3.10: Correlation of stress and cumulative number of signal strength as function of time of NS30/70

Figure 3.11 shows the LR of each mixture at its wet and dried states. Being linked to the occurring of damage, LR tends to decrease in case of damage accumulation and stays constant when no damage is reported.

All LR at all cycles reveal a value more than 1 at RH=90%. Thus, Kaiser Effect is satisfied at all cycles. Therefore, it can be stated, that earth concrete at wet conditions exhibits the attainment of Kaiser Effect at all cycles and that the rate of damage of earth concrete mixtures at RH = 90% under cyclic loadings is small as the reduction in LR is not remarkable. Regarding the different earth concrete mixtures, a slight effect of NS replacement by RS or the increase in clay content has been observed.

The load ratios (LRs) of all mixtures are lower at dried conditions compared to their behavior at wet conditions. Kaiser Effect is achieved only at P/Pmax of 0.2 in dried specimens. The decline in LR is more significant for a stress level higher than 40%. As LR is the assessment of damage occurring with respect to the PML which is the same for all mixtures, a lower LR means that cracks were formed or damage occurred at earlier stress level. Thus, mixtures at dried conditions are more vulnerable to cracking. RS40/60-50 displayed the lowest LR and thus it can be said that it is more prone to damage than any other mixture.

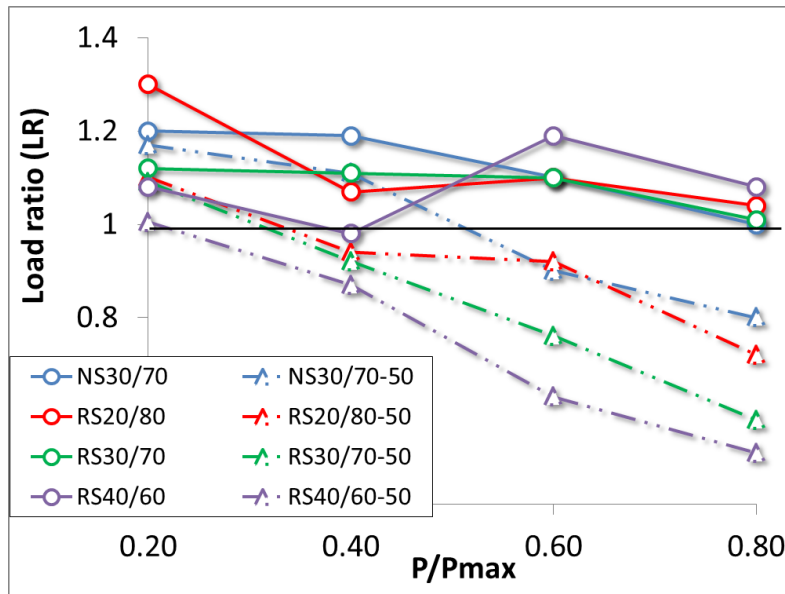


Figure 3.11: Load ratios of each mixture at RH=90% and RH=50%

3.5.2 Calm ratio

The previous section discussed the load ratio that investigates the reloading phase. The following damage index calm ratio (CR) examines the unloading phase. As stated, such process would be basically complex as it comprises the closure of cracks and friction. Based on what is said previously in section 3.2.1 about the original equation of CR and the modifications in the denominator later on, in the following work, it is decided to stay on the original equation. Regarding the AE activity, it is decided to consider it as the number of hits.

Figure 3.12 shows the CR of each mixture at both cured conditions. Though it is a complex phase that combines different processes, CR has been considered a sign of crack width development (Xargay et al., 2020). Basically, the general increase in CR values with increasing loading levels would not contradict this concept. At wet conditions, a fluctuation of CR values can be noticed. This does not permit the explicit assessment of RS or clay influence. At dried conditions, CR increases with loading level and is higher than that obtained at RH=90%. RS40/60-50 exhibited the highest CR values pointing out to its vulnerability to crack openings growth more than any other mixture.

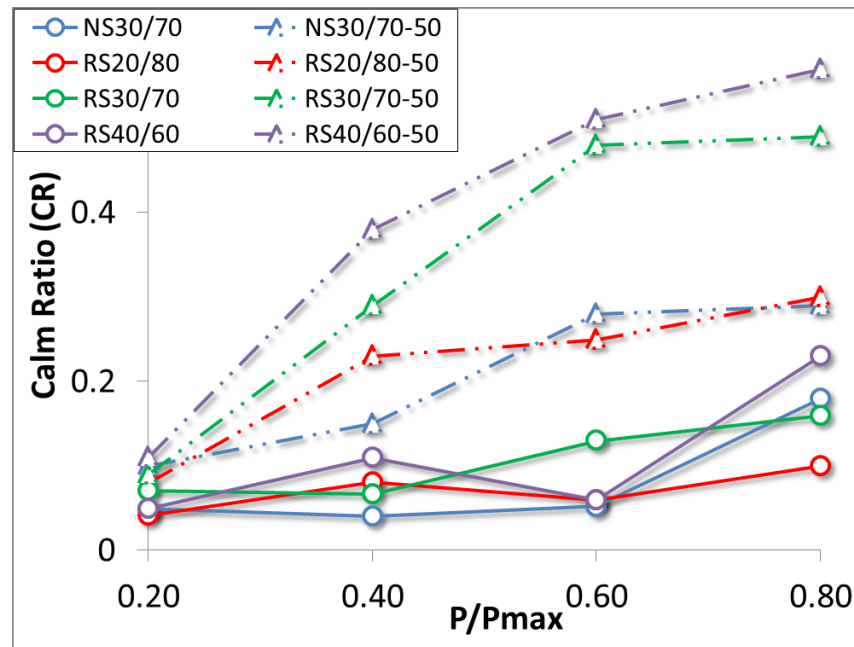


Figure 3.12: Calm ratios of each mixture at RH=90% and RH=50%

3.5.3 Damage classification

The LR concerns the assessment of damage in the reloading phase and the CR investigates the unloading phase. Thus, both together are considered complementary. A diagram that combines both ratios together was resulted. The diagram classifies damage into three levels: 1- minor, 2- intermediate and 3- heavy.

The considered threshold values differ from material to another and from type of loading to another. Yet a threshold of 0.9 for LR has been adopted by many past studies. According to the results of the following study on earth concrete, a value of 0.9 of LR seems applicable and hence it is adopted. In preference to one threshold CR for the material itself regardless of the curing condition, a CR value of 0.2 is considered. Therefore, the adopted boundary limits for LR and CR are 0.9 and 0.2, respectively. Note that the CR values ranged at $P/PMS = 0.2$ between 0.04-0.11 at wet condition and 0.08-0.11 at drying conditions.

Figure 3.13 shows the damage classification diagrams where each mixture is represented by four points where each point corresponds to a loading level. The four mixtures at wet curing condition exhibited a minor damage during the four cycles except RS40/60 that reported an intermediate damage during the fourth cycle. At dry curing condition, damage increases with loading level. NS30/70-50 is of minor damage level until the second cycle (P/PMS=0.4). On the other side, the RS mixtures seems to be more affected by drying at lower stress levels as an intermediate damage after the first cycle was reported. RS30/70-50 and RS40/60-50 revealed heavy damage starting from third cycle (P/PMS=0.6) and RS20/80-50 exhibited this level of damage at P/PMS=0.8 only.

Before any damage classification, the analysis carried out previously in the two sections 3.3.1 and 3.3.2 gives the readers enough knowledge that RS40/60-50 would be damaged more than any other mixture due to its highest clay content. This is revealed again in this section by means of damage classification. Clay, the finest particles in earth concrete, make a mixture more vulnerable to drying and more prone to generate shrinkage induced cracking (Fardoun, 2021; Fardoun et al., 2021; Huang et al., 2021; Y. Xie et al., 2021; Yazdandoust et Yasrobi, 2010; Youn & Tonon, 2010).

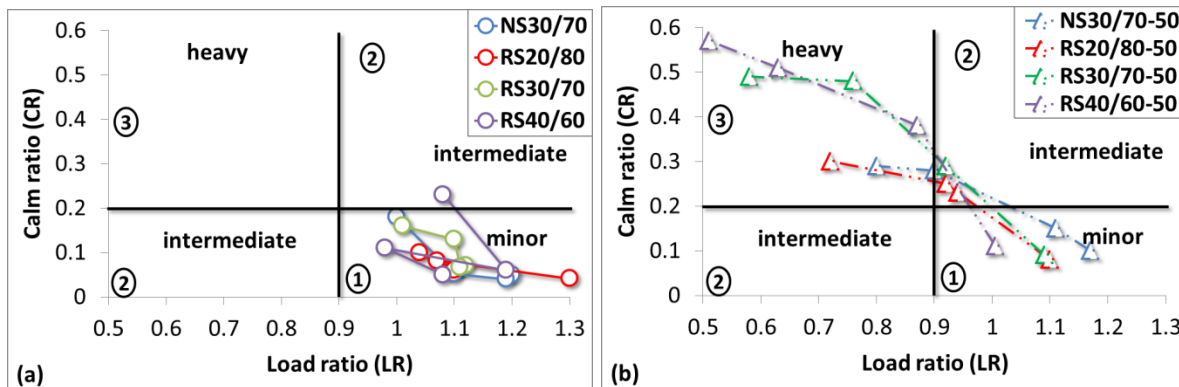


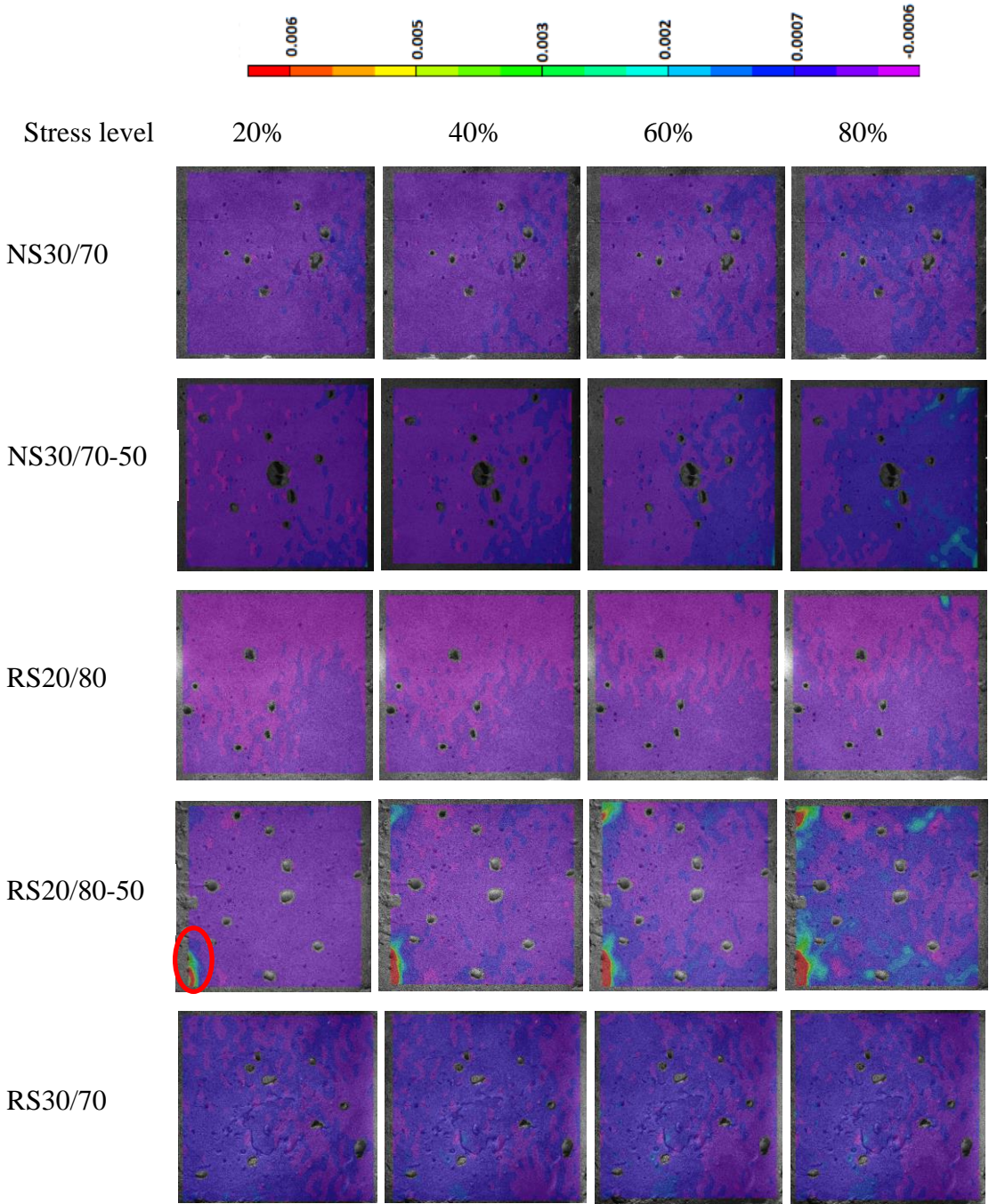
Figure 3.13: Load-Calm diagrams of each mixture

3.6 Kaiser Effect by means of DIC

Figure 3.14 shows the evolution of strain along x (ϵ_{xx}) of each mixture at both curing conditions at 20%, 40%, 60% and 80% of the maximal stress (unloading point). At RH=90%, no cracks were captured. On the other side, cracks were detected at RH=50%. While they were slightly formed in NS30/70-50 at stress level of 80%, they were clearly presented in the RS mixtures. This reflects the vulnerability of RS to drying.

As loading increases, cracks gradually develop and expand. Cracks at the stress level of 60% are more pronounced and larger compared to their previous state at the stress level of 40%. The stresses in the zones where micro-cracks have been formed will be released and redistributed to the next point of defect. At the stress level of 80%, coalescence of cracks can be noticed. Such union can be observed at the right side of RS30/70-50 specimen and at the top right side of RS40/60-50.

It can be observed that the expansion in the degree of damage from cycle to cycle is more pronounced in RS30/70-50 and RS40/60-50 demonstrating their vulnerability and weaknesses and thus showing successful correlation with AE results.



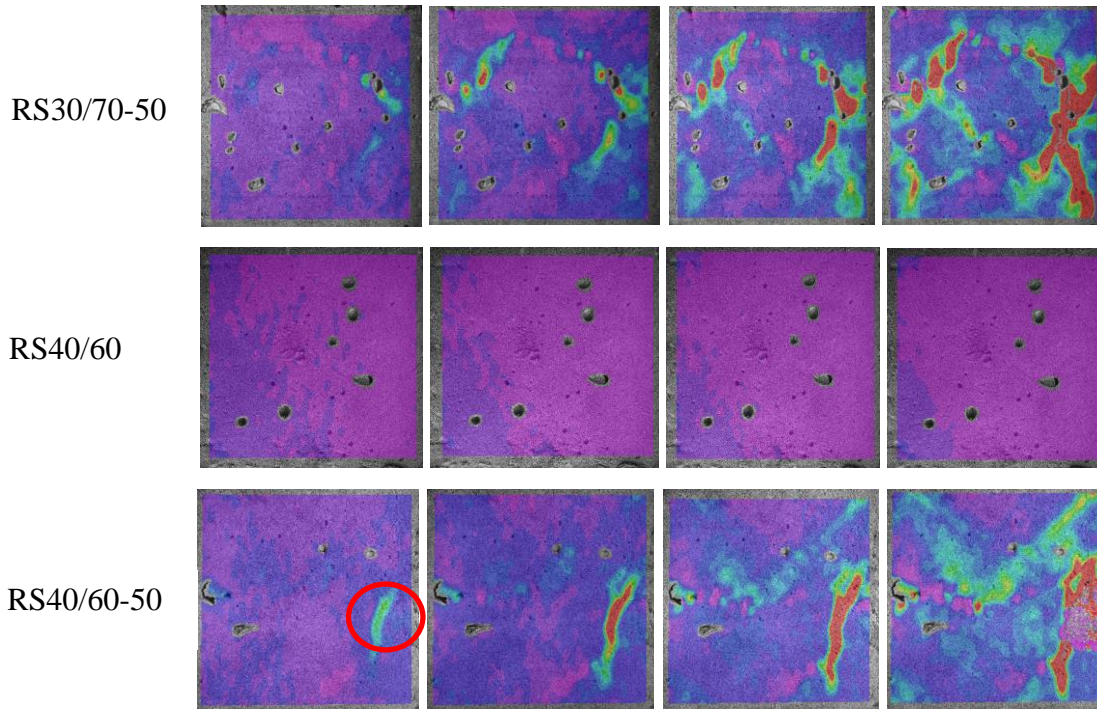


Figure 3.14: Evolution of strain (ϵ_{xx}) of each mixture at both curing conditions

It is aimed to examine the Kaiser Effect by means of DIC. To do so, the definition of Kaiser Effect is translated and applied on DIC. The attempt to verify Kaiser Effect by means of DIC is as follows: the crack mouth opening displacement (CMOD) of a certain crack at different peak stress levels is determined (it is named 'C20%' at stress level of 20%) and then it is compared to the CMOD of the last photo captured before reaching the previous maximum stress (PMS) during the reloading of the second cycle (this is named 'C20%+'). The bottom left crack of RS20/80-50 and the middle right crack of RS40/60-50 are adopted. A drawing clarifying the Kaiser Effect with DIC verification for at first cycle is shown in figure 3.15.

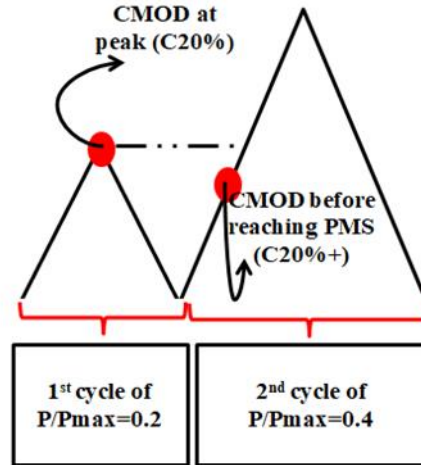


Figure 3.15: Attempt to verify Kaiser Effect

Figure 3.16 shows the CMOD of the considered cracks. The crack opening at a peak stress and its opening at the PMS in the subsequent cycle are different. An expansion can be seen at all occasions. The results in figure 3.11 have shown that the Kaiser Effect at RH=50% was achieved at $P/P_{max} = 0.2$ in all mixtures. Thus, though development in crack width has occurred, Kaiser Effect was attained. Therefore, it can be stated that Kaiser Effect is not necessarily affected by an evolution in crack opening. As known, Kaiser Effect and load ratio are linked to the damage occurrence. Therefore, this term ‘damage occurrence’ indicates the formation of new cracks and not necessarily the development of crack opening.

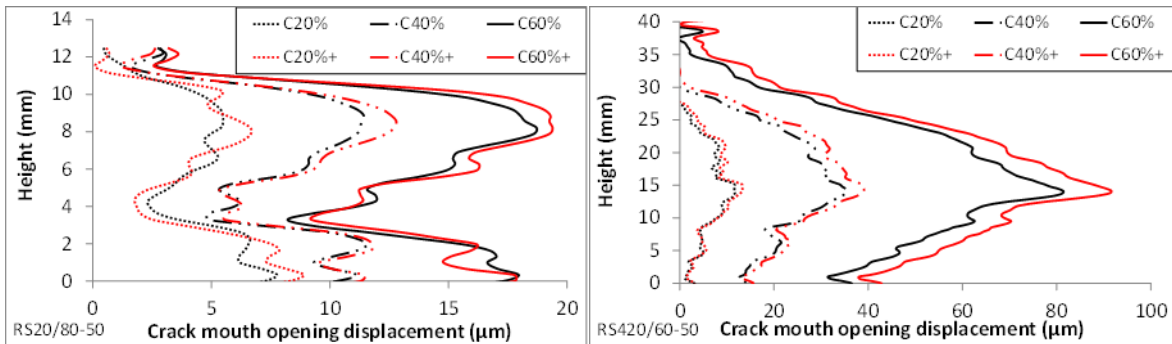
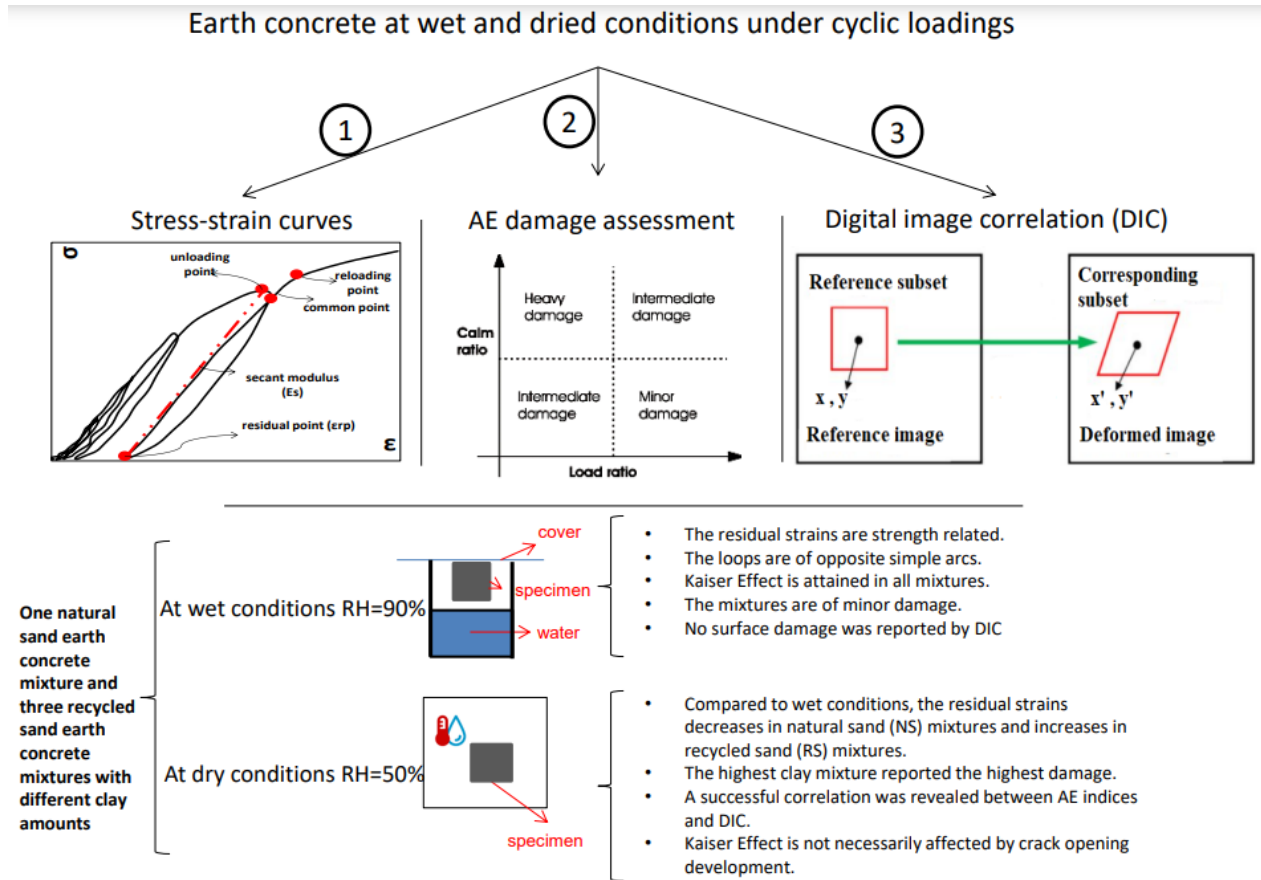


Figure 3.16: CMOD at different stress levels in RS20/80-50 and RS40/60-50

Conclusions



<u>Chapter 3 Part B. Hygro-mechanical modeling of natural and recycled earth concrete mixtures</u>	101
<u>3.7 Damage mechanics</u>	101
<u>3.7.1 Damage variable concept</u>	101
<u>3.7.2 Uniaxial damage: the classical theory</u>	102
<u>3.7.3 Mazars isotropic damage model</u>	105
<u>3.7.4 The unilateral effect</u>	106
<u>3.7.5 Plasticity</u>	107
<u>3.7.6 Localizing problem</u>	107
<u>3.7.7 Fichant isotropic damage model</u>	108
<u>3.7.8 Spatial variability</u>	109
<u>3.8 Application on earth concrete</u>	110
<u>3.8.1 Elastic and fracture parameters</u>	110
<u>3.8.2 Application on earth concrete at macroscale</u>	110
<u>3.9 Results</u>	111
<u>3.9.1 Monotonic curves</u>	111
<u>3.9.2 Damage field as function of stress level</u>	112
<u>3.10 Shrinkage induced cracking</u>	115
<u>Conclusions</u> 115	

Chapter 3 Part B. Hygro-mechanical modeling of natural and recycled earth concrete mixtures

As soil dries, it shrinks. Shrinkage may get restrained leading to the development of internal tensile stresses. If these stresses exceed the tensile strength of soil, microcracks are generated. In earth concrete, the restriction may be due to soil heterogeneity; in particular the fine-grained soils, and to non-uniform water distribution. In addition, in the case of earth concrete load bearing walls, the external restraint (frictional boundary condition) may be also responsible for shrinkage induced cracking. Such cracks are known as boundary cracks (Levatti et al., 2019). In the following chapter, a hygro-mechanical modeling is carried out.

3.7 Damage mechanics

3.7.1 Damage variable concept

Defined first by Kachanov (Kachanov, 1958) as one dimensional, several studies have been developed after that and were characterized by a tensor of second order (Ortiz, 1985) or fourth rank (Carol et al., 1994). This is based on the fact that the material becomes anisotropy as damage develops. In a simplest case, the damage variable is a scalar function.

Considering isotropic damage, the damage variable is considered as a surface density of intersections of cracks and cavities with any plane of \vec{n} orientation in the body. In figure 3.17, δS_D represents the area of defects in the considered plane and δS characterizes the area of the section of a finite volume element. Then, the damage variable is expressed as follows (Kachanov, 1958).

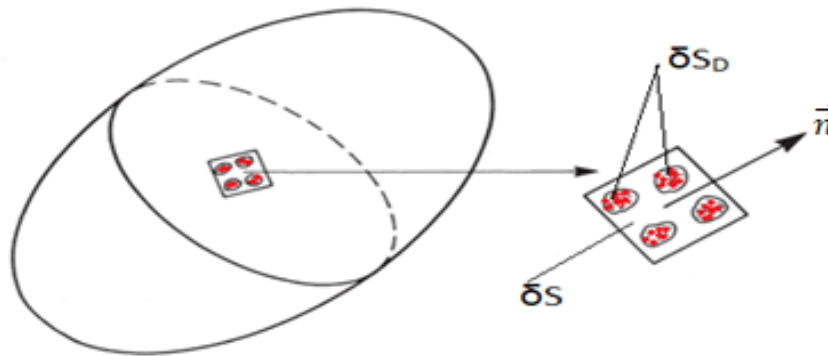


Figure 3.17: Definition of damage

$$d = \frac{\delta S_D}{\delta S} \quad (3-4)$$

The scalar d , that depends on the growth of the defects. It is equivalent to a value ranging from 0 to 1. A value of 0 corresponds to an undamaged material; a value of 1 is linked to a completely damaged material.

3.7.2 Uniaxial damage: the classical theory

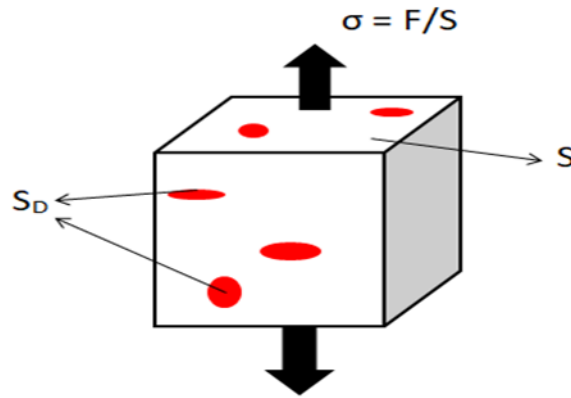


Figure 3.18: Element of damaged material subjected to tensile force F

Figure 3.18 represents a damaged material subjected to tensile force F . S_D represents the area of defects. Thus, the damage variable in the above one dimensional experiment is written as:

$$d = \frac{S_D}{S} \quad (3-5)$$

In order to precise the damage constitutive equations, Rabotnov (1969) proposed the effective stress. It is the stress to the area that effectively (area with no damage) supports the load. Hence, according to figure 2.35, ' $S - S_D$ ' displays the effective area.

$$\tilde{\sigma} = \frac{F}{S - S_D} = \frac{F}{S(1 - \frac{S_D}{S})} = \frac{\sigma}{1 - d} \quad (3-6)$$

According to uniaxial Hook's law:

$$\tilde{\sigma} = E \varepsilon \quad (3-7)$$

where E represents the elastic modulus of the undamaged material.

Thus, the total stress would be as follows:

$$\sigma = (1 - d)E \varepsilon \quad (3-8)$$

The damage evolution law is considered between the damage variable d and ε :

$$d = g(\varepsilon) \quad (3-9)$$

The case above represents the monotonous loading regime. However, in unloading and reloading phases, the damage variable kept its maximum value reached before. Hence, a variable \hat{k} is introduced which describes the maximum value of strain reached in the material before the current time t : $\hat{k}(t) = \max \varepsilon(T)$ for $T \leq t$. Then, equation 2-43 is reformed as follows:

$$d = g(\hat{k}) \quad (3-10)$$

Equation 2-44 is applicable for any type of loading regime. The damage evolution law is commonly represented as well in a limit state function as follows (Kondo et al., 2007):

$$f(\varepsilon, \hat{k}) = \varepsilon - \hat{k} \quad (3-11)$$

Knowing the classical Kuhn-Tucker condition:

$$f \leq 0; \quad \dot{\hat{k}} \geq 0; \quad \dot{\hat{k}}f = 0 \quad (3-12)$$

The first condition designates that ε cannot be greater than \hat{k} . The second condition indicates \hat{k} cannot decrease. In addition, \hat{k} can increase only if the current value of the strain (at time t) is equal to \hat{k} .

The complete response of the damaged material is shown in figure 3.19.

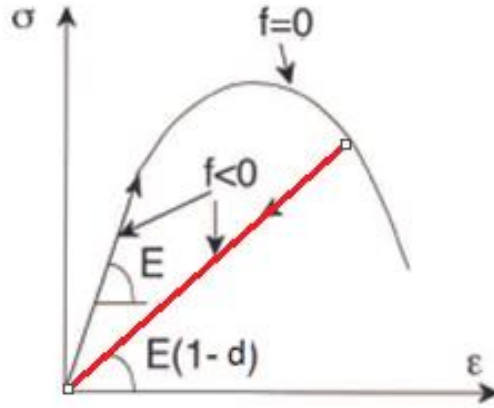


Figure 3.19: Complete response of the damaged material

Lemaitre and Chaboche (1978) gave a straightforward 3D extension of the previous theory. C_{ijkl} was introduced as a tensor of elasticity of the damaged material. C_{ijkl}^0 represents the elastic stiffness of the undamaged material.

$$C_{ijkl} = (1 - d)C_{ijkl}^0 \quad (3-13)$$

where the effective stress is described as:

$$\tilde{\sigma}_{ij} = C_{ijkl}^0 \varepsilon_{kl} \quad (3-14)$$

and the uniaxial stress-strain constitutive law takes the following form:

$$\sigma_{ij} = (1 - d)\tilde{\sigma}_{ij} = (1 - d)C_{ijkl}^0 \varepsilon_{kl} \quad (3-15)$$

The principle of equivalence strain (ε_{eq}) assumes that the various behaviors (elastic, plastic...) are affected by the same way by the damage. The generalization of equation 2-45 implies:

$$f(\varepsilon, \dot{\varepsilon}) = \varepsilon_{eq}(\varepsilon) - \dot{\varepsilon} \quad (3-16)$$

where ε_{eq} is a norm of ε to be chosen that quantifies the local deformation state in the material.

A simple option can be as follows:

$$\varepsilon_{eq} = \sqrt{(\varepsilon : \varepsilon)} \quad (3-17)$$

3.7.3 Mazars isotropic damage model

Equation 2-51 implies a symmetric elastic domain in tension and compression. However materials such as concrete (ceramics, rocks...) often display a dissymmetric damage surface where the yield value in tension being several times less than in compression.

To overcome this shortcoming, Mazars (1984) introduced d_t and d_c as two damage parameters. The first is devoted to damage under tension while the second is associated to the compression mechanism. The aforementioned parameters are evaluated from two evolution functions, g_t and g_c , assumed to be both dependent on a unique definition of the equivalent strain (ε_{eq}):

$$\varepsilon_{eq} = \sqrt{\sum_{i=1}^3 \langle \varepsilon_i \rangle^2} \quad (3-18)$$

where $\langle . \rangle$ is the Macaulay bracket and ε_i are the principal strains. $\langle \varepsilon_i \rangle$ represents the positive side of ε_i of the strain tensor.

This constitutive model aims to capture the response of materials exposed to loading paths in which extension of the materials exist. Hence, the evolution of damage depends on the amount of extension the material is undergoing during loading.

For a loading path of tension and compression, the damage variable is split into two parts:

$$d = \alpha_t d_t + \alpha_c d_c \quad (3-19)$$

where d_c and d_t represents the damage variables in compression and tension respectively. α_t and α_c characterize the weighting coefficients and they are as follows (Pijaudier-Cabot and Mazars, 2001):

$$\alpha_t = \sum_{i=1}^3 \left[\frac{\langle \varepsilon_i^t \rangle \langle \varepsilon_i \rangle}{\varepsilon_{eq}^2} \right]^\beta$$

$$\alpha_c = \sum_{i=1}^3 \left[\frac{\langle \varepsilon_i^c \rangle \langle \varepsilon_i \rangle}{\varepsilon_{eq}^2} \right]^\beta \quad (3-20)$$

For uniaxial compression test, $\alpha_c = 1$ and $\alpha_t = 0$ and in uniaxial tensile $\alpha_t = 1$ and $\alpha_c = 0$. Therefore, the damage variables d_c and d_t can be acquired separately from uniaxial tests. Pijaudier-Cabot & Mazars (2001) reported the evolution of damage in an integrated form as function of the variable \hat{k} :

$$d_t = 1 - \frac{\bar{k}_0 (1 - A_t)}{\bar{k}} - \frac{A_t}{\exp[B_t (\bar{k} - \bar{k}_0)]}$$

$$d_c = 1 - \frac{\bar{k}_0 (1 - A_c)}{\bar{k}} - \frac{A_c}{\exp[B_c (\bar{k} - \bar{k}_0)]} \quad (3-21)$$

noting that $\bar{k}_0 = \frac{f_t}{E}$ is the initial threshold of damage where E is the modulus of elasticity of the undamaged material and f_t is the tensile strength.

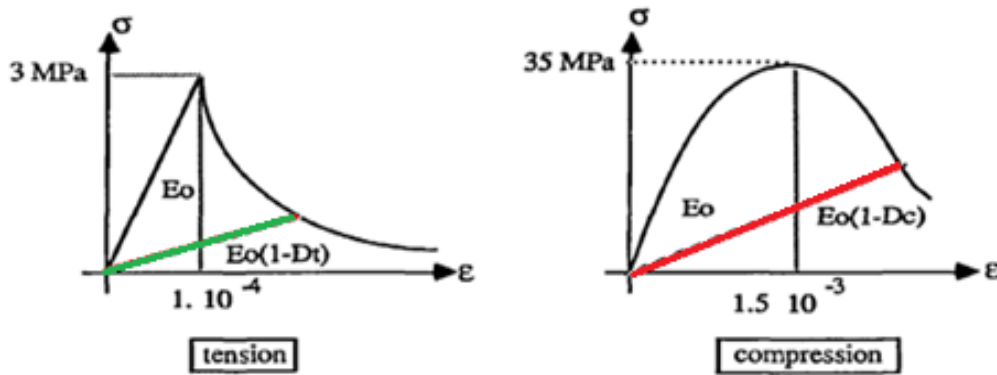


Figure 3.20: The damage theory: stress-strain for uniaxial loading

3.7.4 The unilateral effect

When a concrete specimen is loaded in tension, until reaching the softening regime, and then loaded in compression, there is a gradual restoration of stiffness. Several techniques (as in equation 2-53) were developed before that have taken this effect into account (Ju, 1989 ; La Borderie, 1991 ; Lee & Fenves, 1998) . The last one is presented below:

The damage variable in traction is multiplied by a parameter s which translates the transfer from tension to compression

$$(1 - D_{ii}) = 1 - (1 - D_C)(1 - s(\tilde{\sigma})D_t^{ii}) \quad (3-22)$$

The parameter 's' can be written under the form:

$$s(\tilde{\sigma}) = s_0 + (1 - s_0) r(\tilde{\sigma}) \quad (3-23)$$

where $r(\tilde{\sigma})$ is as follows:

$$r(\tilde{\sigma}) = \begin{cases} (\sum_{i=1}^3 \tilde{\sigma}_{ii})^+ \\ (\sum_{i=1}^3 |\tilde{\sigma}_{ii}|) \end{cases} \quad (3-24)$$

3.7.5 Plasticity

3.7.5.1 Von Mises Criterion

We are presenting here the Von Mises Criterion. Mathematically, the Von Mises yield criterion is stated as follows:

$$J_2 = k^2 \quad (3-25)$$

where J_2 is the second deviatoric stress invariant in which the yielding of the material begins when this parameter reaches a critical value. k is the yield stress of the material in pure shear.

The threshold area of plasticity is expressed:

$$f = \sigma_{eq} - w(k) - w_0 \quad (3-26)$$

where σ_{eq} is the Von Mises stress (or equivalent stress) and $w(k)$ is the hardening function of effective plastic deformation (k) being initially 0.

3.7.6 Localizing problem

As concrete exhibits a softening behavior, localization of strains and damage occur. The application of this phase by finite element programs forms difficulties. Due to the negative slope in stress-strain curve (softening phase), the strain-softening damage tends to localize in a zero volume, leading to structural failure with zero dissipated energy which is physically unrealistic (Pijaudier-Cabot & Bažant, 1987).

The problem is related to the finite element approximation. The result is a localization of the deformations in a band whose thickness is directly controlled by the size of the finite elements. The size of the localization area decreases with the refinement of the mesh and is also sensitive to the orientation of the elements.

3.7.6.1 The integral non-local

The internal length (it controls the size of the region in which damage may localize) is incorporated in a modification of the variable which controls damage growth. This approach is based on the averaging of some variables, in order to regularize the responses of the local model.

$$\bar{\varepsilon}(x) = \frac{1}{V_r(x)} \int_{\Omega} \psi(x-s) \tilde{\varepsilon}(s) ds \quad (3-27)$$

where Ω is the volume of the structure and $V_r(x)$ is representative volume at point x . The weight function is represented as $\psi(x-s)$:

$$\psi(x-s) = \exp\left(-\frac{4\|x-s\|^2}{l_c^2}\right) \quad (3-28)$$

where l_c is the internal length. However, dependency on mesh will occur when the finite element is greater than the internal length.

3.7.6.2 Energy regularization

This type of regularization demands the presence of a direct relation between the fracture energy and the law controlling the softening. The relation is generally obtained on one-dimensional case and thus in non-uniaxial case, overestimation or underestimation of dissipated energy would happen.

3.7.7 Fichant isotropic damage model

Fichant's damage model has been adopted in the following. This model is implemented in the finite element software Cast3m. It is based on the relationship between effective stress and total stress as presented in the previous section. It is an extension of Mazars model taking into account the unilateral effect and plasticity.

The softening phase is designated by B_t and it is expressed as follows:

$$B_t = \frac{f_t h}{G_t - 0.5 \varepsilon_{d0} h f_t} \quad (3-29)$$

where ε_{d0} is the k_0 in Mazars model and f_t , G_t , h and ε_{d0} are the tensile strength, fracture energy and the characteristics element length respectively based on energy localization.

To take into account the unilateral effect, a multiple factor is generally introduced. In this model, it is represented by the factor α which is a material parameter linked to damage in the compressive state.

$$d_t = (1-d) + (1-d)^\alpha \quad (3-30)$$

The Nadai yield function is a combination of two Drucker-Prager functions (F_t and F_c) with the same hardening evolution. It is adopted for plasticity. Drucker-Prager criterion represents a modification to Von Mises by adding the first invariant of the stress tensor I_1 . The expression is as follows:

$$F_i = \alpha_i J_2(\tilde{\sigma}_{ij}) + \beta_i I_1(\tilde{\sigma}_{ij}) - w(p) - w_0 \quad (3-31)$$

Where I_1 is the first invariant of the effective stress, J_2 the second invariant of the second deviatoric effective stress and $\tilde{\sigma}_{ij}$ is stress tensor.

The non-linear evolution of the plastic internal variable is replaced by a linear one:

$$w = p * q + w_0 \quad (3-32)$$

Where p is the plastic strains and q is a model parameter and w_0 concerns the elastic domain.

The evolution of plastic deformation is also given as follows (Aissaoui, 2018):

$$\dot{\varepsilon}^p = \frac{E}{E + \frac{q}{\frac{dF_i}{d\tilde{\sigma}_{ij}}}} \dot{\varepsilon} \Rightarrow \varepsilon^p = \frac{E}{E + \frac{q}{\frac{dF_i}{d\sigma}}} (\varepsilon - \varepsilon_{d0}) \quad (3-33)$$

Taking $\xi = \frac{E}{E + \frac{q}{\frac{dF_i}{d\sigma}}}$

The softening phase is then expressed as follows:

$$B_t (1 - \xi) = \frac{f_t h}{G_t - 0.5 \varepsilon_{d0} h f_t} \quad (3-34)$$

3.7.8 Spatial variability

A spatial variability has been considered for the mechanical properties using the Turning Bands Method that creates a spatially correlated random property field. Soil exhibits a strong nonlinear and heterogeneous behavior (Wang et al., 2019). Its parameters vary significantly within a minimal distance (Halder & Chakraborty, 2020). Soil's properties may display high variability resulting from many sources of uncertainties. The variability of a given uncertain parameter (modulus of elasticity, Poisson's ratio, undrained cohesion...) is measured by the coefficient of variability (COV). In order to model these parameters, the spatial variability has been taken into account, in advanced approaches, by considering the uncertain parameter as random fields (Abdel Massih, 2008). A method implemented in the finite element software Cast3m named The Turning Band Methods (TBM) displays the spatial variability feature. It is used in this study.

TBM generates realizations of isotropic Gaussian random fields by summing contributions from line processes (Matallah et al., 2009). Realizations of two or three-dimensional isotropic Gaussian random fields are determined according to the following expression:

$$Z(\vec{x}_n) = \frac{1}{\sqrt{L}} \sum_{k=1}^L Z_k(\xi_n, k) \quad (3-35)$$

$Z_k(\xi_n, k)$ is the value of one dimensional process at the point ξ_n, k . It is obtained by orthogonal projection of \vec{x}_n (the field point with n being the number of points) on to the line k .

$C_z(\vec{h})$, the three dimensional covariance, is fixed. $C_1(\vec{h})$, the one dimensional covariance, is to be simulated for each line as follows:

$$C_1(\vec{h}) = \frac{d}{dh} [hC_z(\vec{h})] \quad (3-36)$$

The three dimensional covariance has an isotropic exponential form:

$$C_z(h_{ij}) = s_d^2 \exp\left(-\frac{h_{ij}}{l}\right) \quad (3-37)$$

where s_d is the standard deviation, l the correlation length and h_{ij} is the coordinates of vector \vec{h} .

3.8 Application on earth concrete

3.8.1 Elastic and fracture parameters

The strain measurement approach that is based on adopting the strains of the whole specimen did not yield a post-peak phase. Furthermore, after the linear phase, the hardening phase is exaggerated. Therefore, it is decided to deal with the ‘loading plate’ approach that resulted in a full stress-strain curve and acceptable hardening phase. The compressive tests ($10 \times 10 \times 10 \text{ cm}^3$) done at 28 days are considered.

The parameters E, ν, G_t and f_t are considered based on the monotonic tests. The parameters of the four mixtures at 28 days are presented in table 3.4.

Mixture	E (MPa)	ν	f_t (MPa)	G_t (N/m ²)
NS30/70	786	0.3	0.045	45
RS20/80	875	0.3	0.07	80
RS30/70	421	0.32	0.031	35
RS40/60	369	0.35	0.027	34

Table 3.2: Elastic and fracture parameters of each mixture

3.8.2 Application on earth concrete at macroscale

Numerical simulations are conducted at a macroscale under plane stress condition. The boundary conditions are shown in the figure 3.21. An imposed displacement load is designed at the top. The corner point is restrained in X-direction while the bottom side is restrained in Y-direction.

Quadrilateral (QUA4) elements with four Gaussian points are considered. A mesh size of 0.4 cm is adopted. It properly fit with the experimental curve and requires reasonable time to be accomplished.

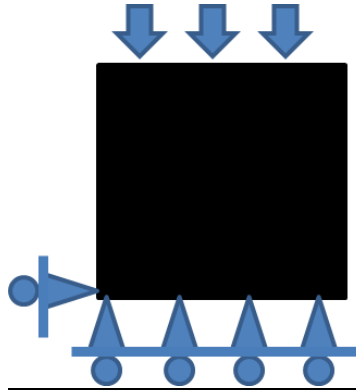
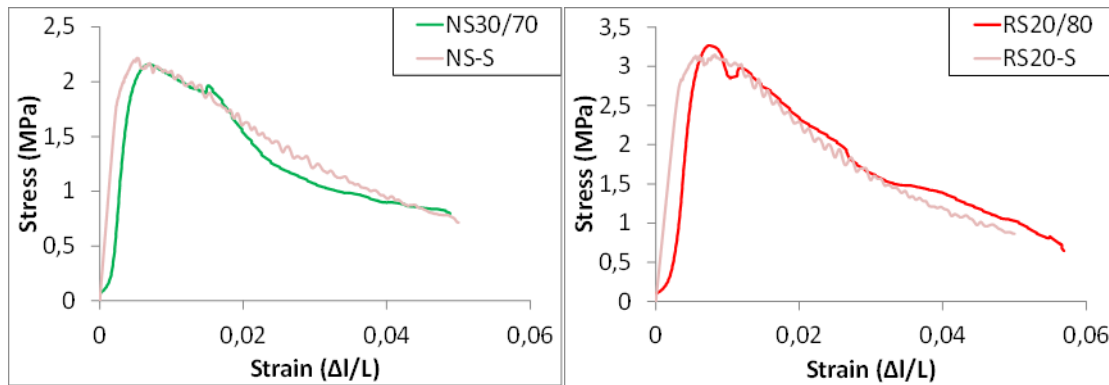


Figure 3.21: Boundary conditions

3.9 Results

3.9.1 Monotonic curves

Figure 3.22 shows the experimental and simulation curves of each mixture where the letter S corresponds for simulation. It can be stated that the model successfully reproduce the stress-strain curves (Fardoun et al., 2020).



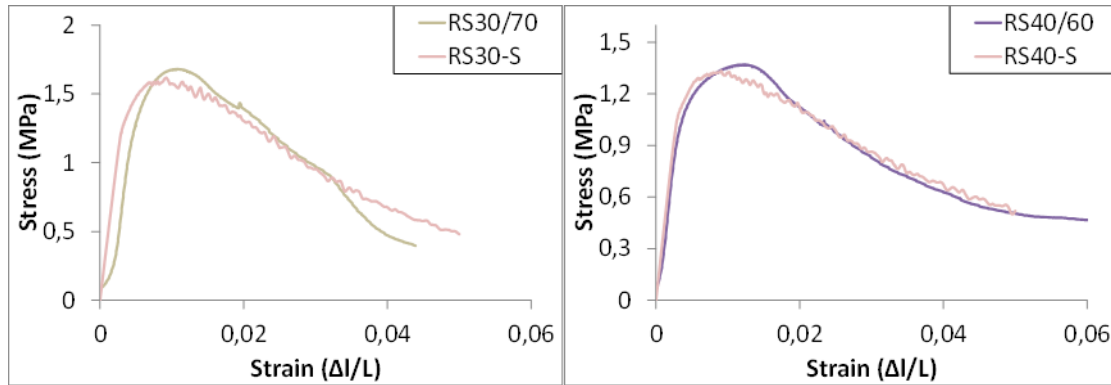


Figure 3.22: Comparison between the experimental and numerical stress-strain curves

3.9.2 Damage field as function of stress level

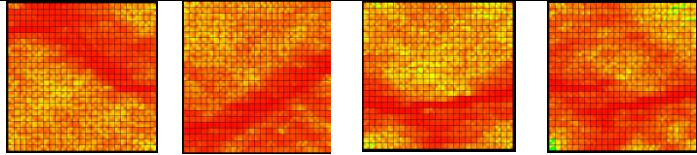
The correlation length (l) describes the distance over which properties have a tendency to be spatially correlated or linked to each other. It is known as well as the scale of fluctuation (Griffiths et al., 2011). A smaller value of correlation lengths indicates a higher randomness in the soil properties. Often, its value horizontally is greater than that vertically. However, in order to generate isotropic random fields, here, they are assumed to be equal. In geotechnical works, its value is taken with respect to the footing length (Bezih et al., 2015). In concrete, some authors have linked the correlation length to the maximum aggregate size in the mixture (Haidar et al., 2005; Matallah et al., 2009). Note that adopting a higher or smaller correlation length does not mean a different standard deviation (s_d) value of the property (Griffiths et al., 2011).

The coefficient of variation (COV) of uncertain soil parameter is the ratio of its standard deviation to its mean value. The COV of the internal friction angle, for example, may vary from 7% to 20%. For modulus of elasticity, studies have estimated a range of COV between 2% and 50% (Bezih et al., 2015). In fact, there is no information regarding the tensile strength.

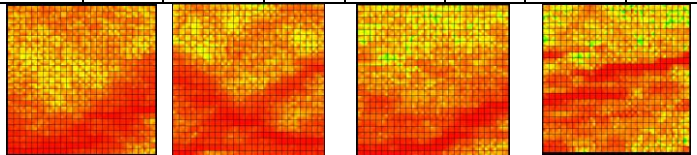
In the model adopted here, the modulus of elasticity and the tensile strength are the variable parameters. In our study, the value for correlation length is chosen to be for modulus of elasticity and tensile strength three times the maximum size of the sand particle size presented in the mix: $3 \times 4 \text{ mm} = 12 \text{ mm}$. Regarding standard deviation, different values are adopted. Table 3.5 shows the parameters and results.

The difference among the damage figures is that for standard deviation at a 30% value, the damage takes the form of a horizontal line which contradicts with the fact that vertical in addition to shear cracks are to be formed when concrete is under compressive loadings. Eventually, between the smallest values of 1% and 5%, it is decided to take the 5% where 1% requires much more time during modeling. In addition, this value is taken for E and f_t . Then, the values of correlation length and s_d for both parameters are 0.012m and 5%, respectively. It is worth to mention that s_d may have affected the peak stress at some occasions.

	D1		D2		D3		D4	
parameter	l (m)	S _d (%)						
E	0.012	5	0.012	10	0.012	20	0.012	30
f _t	0.012	1	0.012	1	0.012	1	0.012	1



	D5		D6		D7		D8	
parameter	l (m)	S _d (%)						
E	0.012	1	0.012	1	0.012	1	0.012	1
f _t	0.012	5	0.012	10	0.012	20	0.012	30



	D9		D10		D11		D12	
parameter	l (m)	S _d (%)						
E	0.012	5	0.012	10	0.012	20	0.012	30
f _t	0.012	5	0.012	10	0.012	20	0.012	30

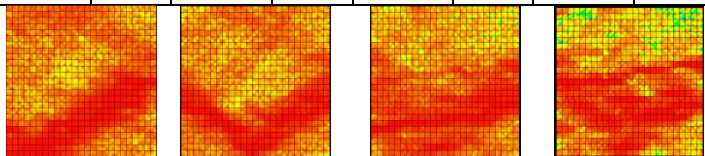


Table 3.3: Effect of standard deviation of E and f_t on damage filed

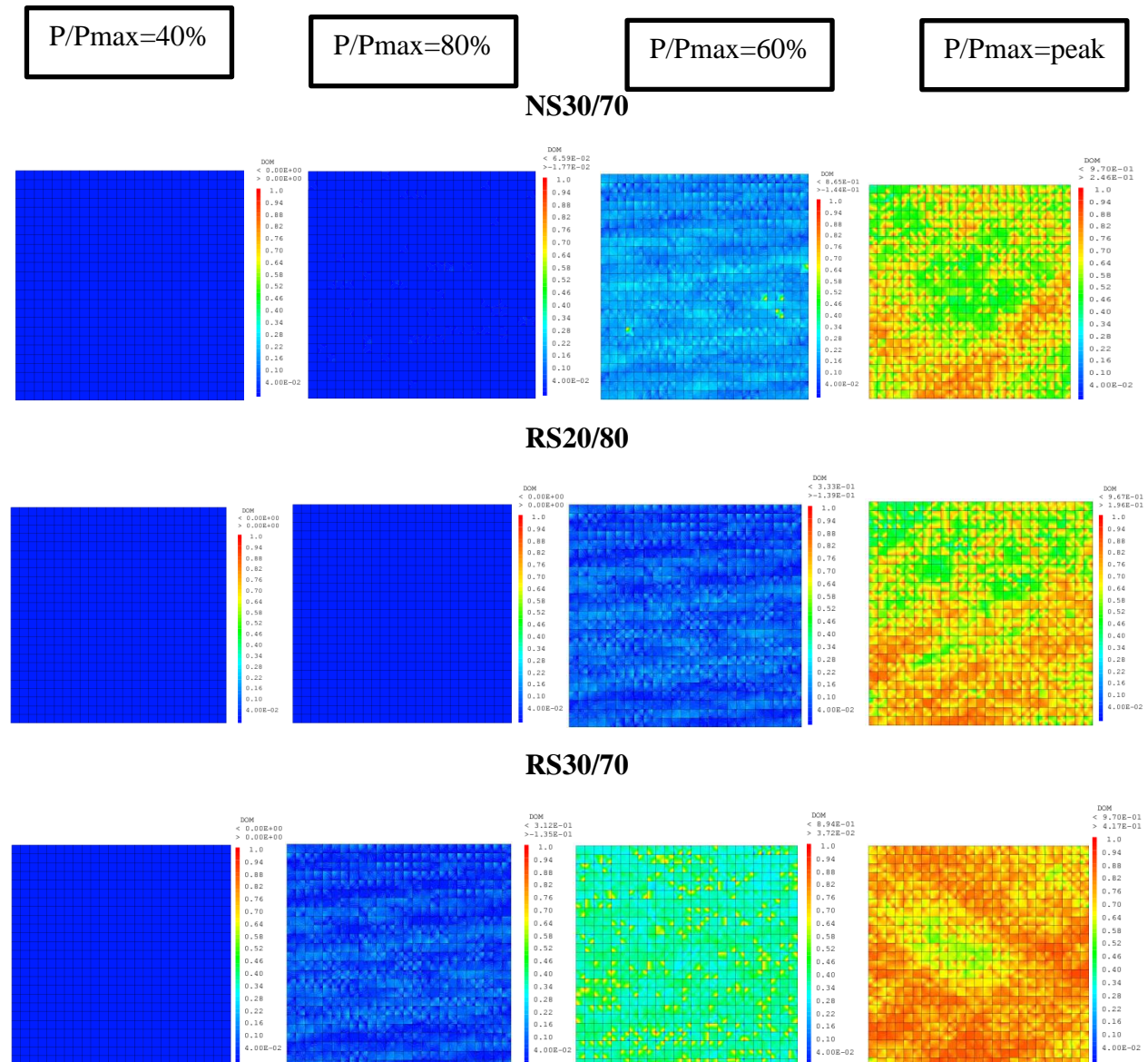
The damage field of each mixture at stress level of 40%, 60%, 80% and 100% (peak) are presented in figure 3.23. At stress level of 40%, all mixtures are zero damaged. At stress level of 60%, damage is detected from highest to lowest degree of damage in RS40/60, RS30/70 then slightly in NS30/70. RS20/80 did not exhibit any damage.

Two parameters govern cracks' initiation in damage models: tensile strength and modulus of elasticity. The higher the tensile strength and the lower the modulus of elasticity are, the later the damage is formed. RS20/80 is of higher tensile strength and higher modulus of elasticity than all

other mixtures. This may indicate that the value of tensile strength contributes more to crack formation than the modulus of elasticity.

This aspect revealed here that NS30/70 is –barely- more damaged at earlier stress level than RS20/80 contradicts with what has been stated in chapter 1 regarding the earlier generation of AE events in RS20/80. A mesoscale modeling approach would be beneficial to better assess this aspect.

The damage increases with stress level. At stress level of 80%, the damage is higher than that at 40% and 60%. At peak where macrocracks are formed, it can be noticed that cracks in RS mixtures are more distributed than NS mixture. Even RS20/80 that showed lower degree of damage at 60%, is now of more distributed damage than NS30/70. This can be attributed to the more points of defects RS possesses.



RS40/60

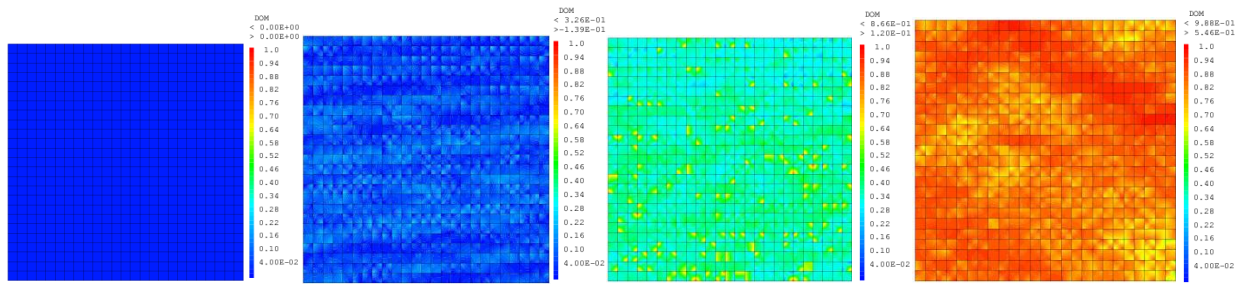


Figure 3.23: Damage field of each mixture at different curing condition

3.10 Shrinkage induced cracking

Cracking modeling is based on the mechanical properties of each mixture. The damage resulted due to drying shrinkage for NS30/70 and RS30/70 can be seen in figure 3.24. According to the results, both specimens possess shrinkage induced cracking. However, that of RS30/70 is much more pronounced.

Back to chapter 2, at 28 days, both specimens revealed increase in strength due to drying. Thus, though shrinkage induced cracking was formed, strength increases. This shows again that processes, capillary suction and shrinkage induced cracking, have taken place and that the former dominated over the other. The higher increase in strength for NS30/70 compared to RS30/70 can be attributed to higher degree of drying cracking reported in the latter.

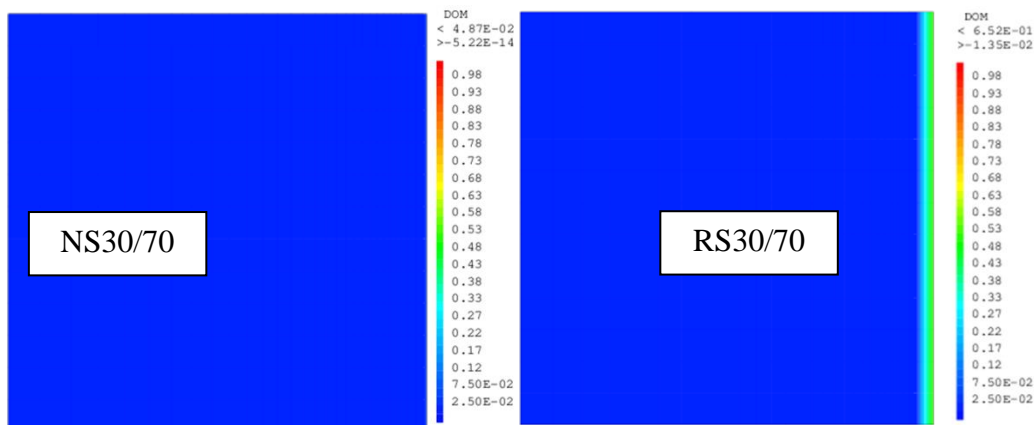


Figure 3.24: Shrinkage induced cracking on NS30/70 and RS30/70

Conclusions

First, in this sub-chapter, a reproduction of the monotonic tests at 28 days at wet conditions of the four earth concrete mixtures was carried out. It can be stated that:

- Fichant's damage model was capable of reproducing the stress-strain curves of earth concrete mixtures under monotonic compressive tests.

- RS20/80 showed the lowest degree of damage at stress levels before the peak which can be attributed due to its highest tensile strength.
- At peak, the propagation of damage was seen in RS mixtures. Therefore, the damage model was capable of reflecting the fact that RS mixtures are of more points of defects and thus they are more vulnerable for cracks' propagation.

In a second step, a hygro-mechanical modeling was carried out by examining the shrinkage induced cracking in NS30/70 and RS30/70. It can be stated that:

- Though both specimens revealed increase in strength due to drying as was displayed in chapter 2, shrinkage induced cracking was generated. Therefore, suction effect and shrinkage induced cracking have taken place. Nevertheless, the former was dominant
- The drying crack in RS30/70 was more important than that formed at the surface of NS30/70. Thus, the higher increase in strength of NS30/70 can be attributed to its less sensitivity to drying and accordingly to the less formation of drying cracks.

<u>Chapter 4 Long-term deformations of earth concrete</u>	119
<u>4.1 Shrinkage</u>	120
<u>4.1.1 Capillary pressure:</u>	120
<u>4.1.2 Disjoining pressure:</u>	121
<u>4.1.3 Surface tension:</u>	121
<u>4.1.4 Interlayer water theory:</u>	121
<u>4.1.5 Dominant mechanism</u>	121
<u>4.1.6 Elastic or viscoelastic response</u>	122
<u>4.2 Creep</u>	122
<u>4.2.1 Creep mechanisms in soils</u>	122
<u>4.2.2 Creep mechanisms in concrete</u>	123
<u>4.2.3 Drying creep as structural effect</u>	124
<u>4.3 Effect of recycled concrete aggregate (RCA) on long-term deformations</u> ...	124
<u>4.3.1 Effect of RCA on total shrinkage and total deformations</u>	125
<u>4.3.2 Effect of RCA on autogenous shrinkage and basic creep</u>	127
<u>4.3.3 Effect of aggregate size on shrinkage and creep</u>	127
<u>4.3.4 Effect of temperature (T) and relative humidity (RH)</u>	128
<u>4.4 Experimental program</u>	130
<u>4.4.1 Materials</u>	130
<u>4.4.2 Experimental procedure</u>	130
<u>4.5 Results</u>	132
<u>4.5.1 Long-term deformations</u>	132
<u>4.5.2 Shrinkage</u>	132
<u>4.5.3 Creep</u>	133
<u>4.5.4 Strength development due to long-term deformations</u>	136
<u>4.5.5 Reference specimens</u>	137
<u>4.5.6 AS specimens</u>	137
<u>4.5.7 BC specimens</u>	137
<u>4.5.8 DS specimens</u>	138
<u>4.5.9 DC specimens</u>	138
<u>4.6 Acoustic emission (AE) analysis</u>	139
<u>4.6.1 Distribution of AE hits</u>	139
	117

[Conclusions](#)..... 141

Chapter 4 Long-term deformations of earth concrete

Structures are subjected to different mechanical loading in addition to temperature and humidity variations during their life time (Fardoun, 2021; Fardoun et al., 2021). These loads cause long-term deformations which are of high importance in earth concrete due particularly to the latter's fine particles; principally clay.

The total strain at time t of a concrete element subjected to a constant stress can be defined as the sum of several strains:

$$\varepsilon_t = \varepsilon_{EL}(t) + \varepsilon_C(t) + \varepsilon_S(t) + \varepsilon_{th}(t) \quad (4-1)$$

Where $\varepsilon_{EL}(t)$ is the instantaneous strain, $\varepsilon_C(t)$ the creep strain, $\varepsilon_S(t)$ the shrinkage strain, and $\varepsilon_{th}(t)$ the thermal strain.

The knowledge of each of these components is necessary to assess the long-term total strain of concrete members.

Figure 4.1 (a) shows the evolution of strains versus time where shrinkage represents autogenous and drying shrinkage and total creep corresponds to basic creep and drying creep in addition to the elastic strain. Figure 4.1 (b) shows the creep strains as function of time. Three stages can be resulted depending on the stress level.

- Primary phase: It is characterized by a negative acceleration and a stabilization of deformation at a stress threshold around 45% of peak stress in ordinary concrete (Saliba, 2012).
- Secondary phase: The acceleration becomes almost zero with a constant evolution deformation. In case of ordinary concrete, this phase is known to be valid until 75% of peak stress (45%-75% of peak stress) (Saliba, 2012).
- Tertiary phase: It is characterized by positive acceleration and strong interaction between damage and the progression of deformations (Saliba, 2012). The rapid growth of cracks causes sudden failure.

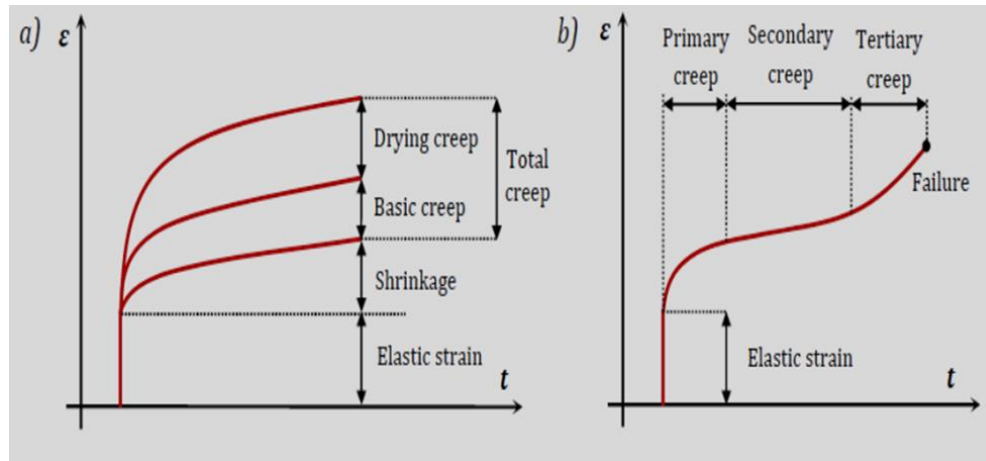


Figure 4.1: time-dependent strains with time (a) strain versus time under creep test (b) (Neville et al., 1983)

In the following chapter, the long term deformations of NS mixture NS30/70 and RS mixture RS30/70 were studied. Their impact on the mechanical properties was also assessed. In the coming pages, the physical origins of shrinkage and creep in addition to the past studies related to the effect of recycled aggregate on these two phenomena are first exposed. Then, the materials and experimental procedure are presented. Finally, results are displayed and analyzed.

4.1 Shrinkage

Shrinkage is represented by autogenous and drying shrinkage. Autogenous shrinkage is the time dependent strain of a non-loaded specimen exchanging no water with the outside (or in other words at sealed conditions). The reduction in volume here is due to chemical shrinkage and self-desiccation (Tang et al., 2021). The former from one side represents the absolute reduction of concrete internal volume as the reactants are greater in volume than the products while the latter from other side represents the gradual consumption of water in pores. This type of shrinkage has been generally ignored before as it is relatively small. It has gained attention with high and ultra-high performance concrete as they are designed to be with low water content (or low water to cement ratio). On the other hand, drying shrinkage is the time dependent strain difference between a non-loaded specimen exchanging water with the outside (at drying conditions) and the autogenous shrinkage. The reduction in volume here is due to drying.

Physical origin

The four discussed mechanisms behind shrinkage are the capillary tension, disjoining pressure, surface tension and interlayer water theory.

4.1.1 Capillary pressure:

The decrease in relative humidity due to hydration (autogenous shrinkage) or due to drying (drying shrinkage) induces a decrease in the pressure of the liquid water. As water is consumed, the gaseous volume increases and thus more menisci (water/gas interface) are formed and

accordingly capillary forces (tension) are created. This causes the contraction of the solid skeleton (compression) and eventually shrinkage.

4.1.2 Disjoining pressure:

This mechanism concerns the interaction between very two close solid surfaces (Hua et al., 1995). In case of increase in RH, the water between the two solids increase the separation distance between the two solids. The disjoining pressure is the force required to maintain the separation between these two solids (Godin et al., 2012). Mathematically speaking, this pressure exerted by two solids reaches its maximum at saturated state.

4.1.3 Surface tension:

It is linked to the C-S-H gel particles. The surface energy of these particles creates surface tensile stresses from one side and compressive stresses within the solid. Unlike adsorption that decreases the surface tensions, desorption leads to increase of the surface tension and thus the solid skeleton undergoes compression (Hua et al., 1995). Accordingly, shrinkage occurs.

4.1.4 Interlayer water theory:

In cement, it concerns the C-S-H gel which is the dominant hydration product of Portland cement. A possibility of water migration from the interstitial space of C-S-H can take place causing volume shrinkage (Tang et al., 2021). In clays, the term interlayer water is referred to the water present between sheets (tetrahedral sheet (T) and octahedral sheet (O), TOT...) (Glaus et al., 2007). The theory's occurrence has been linked to low RHs in the former (Tang et al., 2021) and to high temperature in the later (Le et al., 2012; Zheng et al., 2010).

4.1.5 Dominant mechanism

Knowing that the autogenous shrinkage takes place generally in an internal environment of RH above 70%, this may allow the ignoring of the disjoining pressure that is believed to be constant above RH of 80% (Ferraris, 1986). Similarly, this may permit not to take into account the surface tension theory that requires an RH less than 40%. In the same way, the interlayer water theory is lunched at RH less than 11%. Regarding the latter in clay, it was stated that the complete remove of interlayer water in montmorillonite requires temperature in excess of 100°C (Le et al., 2012). Therefore, this justifies adopting the capillary pressure as the main driving force that leads to autogenous shrinkage. It may be worth to note that the meniscus is no longer stable below RH of 40-50% and thus the capillary forces would not exist anymore. However, this does not contradict with required environment of autogenous shrinkage. Regarding drying shrinkage, the capillary pressure forces are considered alone as the driving force of volume change by scholars in case of ambient environment (RH not less than 50% and of temperature around 22 °C).

4.1.6 Elastic or viscoelastic response

Different studies have considered the two types of shrinkage as an elastic response to the capillary forces due to the self-desiccation for autogenous shrinkage and to drying for drying shrinkage from one side (Di Bella et al., 2017; Wu et al., 2017; Zhang et al., 2012) and a viscoelastic response to the capillary effect (Luan & Ishida, 2013).

It was reported that considering the former (elastic response) yield lower values lower than the measured ones (Li et al., 2020). On the other hand, the second approach, which is known as creep model, was said to give a better prediction. This has been attributed to the creep properties in the cement based materials. For example, one of the models which is based on the concept of activation energy (Lu, 2019), considers the total autogenous shrinkage of a cement paste as an elastic part and creep part.

Apart from the cement paste in which its constituents exhibit creep properties and in which it is an earth concrete component, clay and soil are of similar feature as going to be presented in the coming section.

4.2 Creep

4.2.1 Creep mechanisms in soils

Time dependent settlements in soils are referred to two processes or components that may be called the components of compression:

-Primary consolidation: It concerns the change in volume due to the dissipation of free water (known as pore water) under applied stress (Chen et al., 2021).

-Creep or so-called secondary compression: It is the deformation under a constant effective stress (Le et al., 2012). It is mainly due to the viscous behavior of solid skeleton (Chen et al., 2021).

Creep can be due to the following (Le et al., 2012):

- Breakdown of interparticle bond: the applied stress makes water move out. This decreases the voids and increases soil-solid contact. Between these solids and particularly clay particles, bonds of different types exist (hydrogen bonds, primary valence bonds, van der Waals forces ...). The increase in particles contact leads to an increase in the effective stresses. These stresses may lead to breakdown of bonds. In addition to the occurrence of rearrangement of soil particles due to the flow out of water, due to the breakage of bonds, more rearrangement occurs. Eventually, creep takes place. The creep as a result of breakdown of interparticle bond was proposed, explained or mentioned previously in different studies (Gibson & Lo, 1961; Mesri & Godlewski, 1977; Taylor & Merchant, 1940).
- Jumping of molecule bonds: based on the theory of rate process, it is said that under constant stress, the flow unit –movement of atoms and molecules- to a new equilibrium

position causes creep (Murayama, 1963). Regarding clays, the process of movement concerns the oxygen atoms. This is related to the theory of rate process as the movement of ion requires the breakage of bonds with the surrounded molecules where such breakdown of bonds requires activation energy. Creep deformations are based on the activation energy and the number of inter-particle bonding.

- Sliding among particles: the applied stress can cause slipping between soil grains causing creep (Grim, 1962). Gupta (1964), in the same way, attributed creep to sliding movement of clay particles. As stated, bonds exist between solids and primary consolidation increases friction. Deformation depends basically on three factors which are the sliding force, the sliding velocity and the friction ratio between the tangential force and the normal force.
- Water flow in a double pore system: the microstructure units of a clay structure, which are a multiple of single particles connected with each other by binds and interparticle forces, are known as clusters and peds or flocs. At such level, the pores are micropores. The accumulation of several microstructure units forms the macrostructure (often described as continuous solid skeleton and large pores). At such level, the pores are macropores. Creep is a result of water transfer from micropores to macropores under a pressure. Such transfer or flow causes deformation at the microstructural level such as clay clusters. The secondary compression –which is the deformation under constant effective stress- is attributed to this loss in water at the microstructural level.
- Structural viscosity: in clays, the term structural viscosity is attributed to the plastic structural resistance within clay structure to compression as a result of the double layer (the layer of anions and cations on clay particle surface) surrounding the clay particle. It is stated that the flow of viscous water may be responsible for creep compression (Le et al., 2012).

4.2.2 Creep mechanisms in concrete

The creep theories applied on concrete such as consolidation, seepage, bond breakage and others are originally linked to soil and clay. Furthermore, they are all interconnected and involve water movement. As there is a viscous behavior that concerns clay and soil, approaches were proposed in concrete as well to reflect the viscous behavior of cement paste. The viscoelastic response of C-S-H has been attributed to take place during the motion of C-S-H globules that is accompanied by water layer movement and bond breakages and the formation of new bonds (Alizadeh et al., 2010). The solidification theory by Bazant, that attributed creep to the viscoelastic hydration products (C-S-H) whereas the aging was linked with their volume growth on solidification, did not give a good prediction for the total creep (basic and drying). Accordingly, the microprestress was produced to eventually propose the microprestress-solidification theory. The latter gave satisfactory prediction of creep with and without simultaneous drying of concrete. Finally, the extended microprestress-solidification theory (XMPS) was advised to overcome certain

limitations in the microprestress-solidification theory. XMPS revealed that the viscosity of creep is significantly reduced by the existence of water layer between the planer walls of C-S-H. In addition, as the water layer moves, the effective viscosity of slip between the solid surfaces decreases (Rahimi-Agham et al., 2018; Sinko et al., 2018).

4.2.3 Drying creep as structural effect

The summation of autogenous shrinkage, drying shrinkage and basic creep yields strain less than a loaded specimen subjected to drying simultaneously. This excess of strain is known as drying creep strain or Picket effect. Water migration processes (as mentioned above regarding XMPS theory) amplifies the creep process and thus it may be –partially- behind the drying creep strain. In addition, the increase of material stiffness due to hydration may contribute to this. These are known as intrinsic effect. On the other side, other sources of structural origin (structural effect) can contribute to this excess in strain : (1) stress-induced cracking, (2) tensile strain softening due to progressive cracking, and (3) irreversibility of unloading contraction after tensile strain softening. Among these three sources, the first which is known as microcracking effect is the most important one (Bazant & Chern, 1985). As the specimen dries (drying shrinkage specimen), it shrinks. Shrinkage may get restrained to form drying cracks at the surface (chapter 2). The formed microcracks will not fully close and thus irreversible deformations are present. This deformation reduces the shrinkage of the specimen.

On the other side, when a loaded drying specimen is assessed, there will be basically no microcracking or closure of cracks on the planes normal to the direction of compression. The shrinkage of this specimen will not be reduced in the same manner as a non-loaded drying specimen and thus an extra strain (drying creep) is reported.

4.3 Effect of recycled concrete aggregate (RCA) on long-term deformations

In the following section, several studies that comprise shrinkage and creep together or only creep are displayed. Before such approach, it is worth to define the general creep properties found in the literature:

- Total load-induced strain: Total change in length per unit length measured in a concrete under a sustained load applied at age t_0 at uniform temperature (t_0 represents the start of loading or time of zero value).
- Initial strain: Elastic or instantaneous strain
- Creep strain: Time-dependent strain recorded after the initial strain
- Creep coefficient: Ratio of creep strain to initial strain
- Compliance: Total load induced strain at age t per unit stress caused by a unit uniaxial sustained load applied since loading age t_0
- Specific creep: Creep strain per unit stress

4.3.1 Effect of RCA on total shrinkage and total deformations

Domingo-Cabo et al. (2009) assessed the effect of replacement of coarse natural concrete aggregate (NCA) by 0%, 20%, 50% and 100% of coarse RCA on shrinkage and creep. Figure 4.2 shows shrinkage and creep results. The decrease in shrinkage values at 70-84 days was accompanied by an increase in the relative humidity as presented in the authors' study. Eventually, as the % of coarse RCA increases, the total shrinkage and total deformations (resulted from loaded drying specimen or drying creep specimen) values increase. At 100% replacement, shrinkage and creep increase by 70% and 50% respectively.

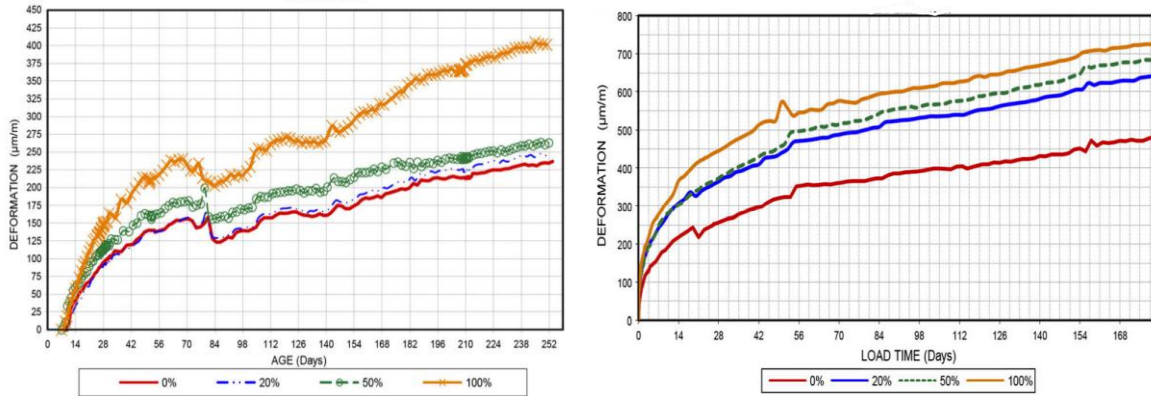


Figure 4.2: Effect of RCA replacement on shrinkage and creep evolution with age (Domingo-Cabo et al., 2009)

Geng et al. (2019) examined the specific creep of different mixtures. Those made with coarse NCA and 100% of coarse RCA are presented. The results in figure 4.3 show that natural aggregate concrete (NAC) exhibited a form of stabilization before recycled aggregate concrete (RAC). With a 100% replacement, the creep increases by 50%.

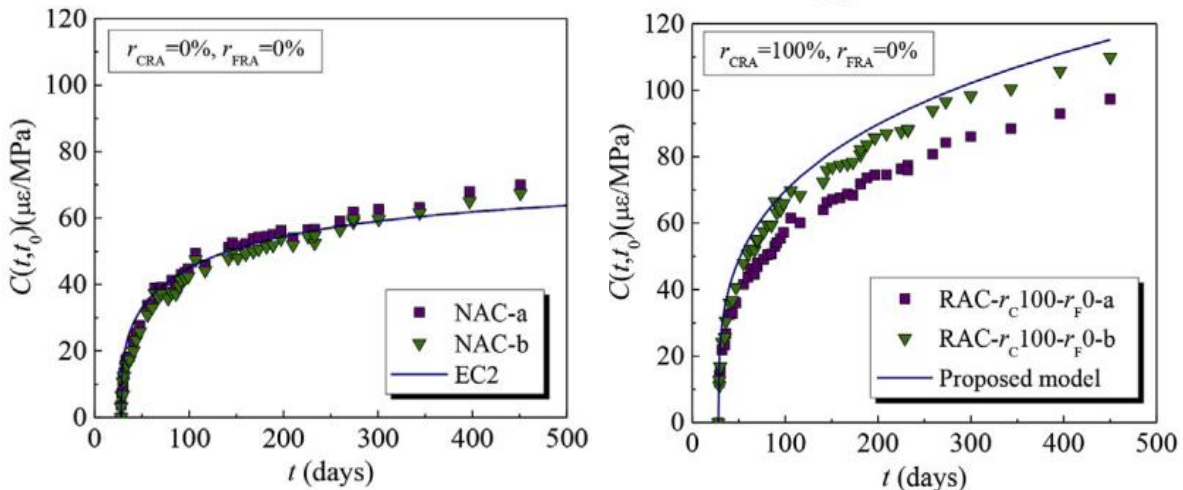


Figure 4.3: Specific creep from left to right of NAC and RAC (Geng et al., 2019)

All studies have reported that the increase in total shrinkage is accompanied by an increase in total deformations (Gayarre et al., 2019). A higher drying shrinkage or shrinkage in RAC is attributed to the following:

- Porosity and water absorption (Bravo et al., 2018; Pan et al., 2017). The porosity of the adhered mortar is correlated to drying shrinkage. Very often, higher water absorption of RA requires additional water to compensate the loss in workability. This increases the migration of water to the outside increasing the drying shrinkage.
- Pore size distribution: As stated in the physical origin of drying shrinkage above, this phenomenon is related to capillary pressure where it is high for smaller pores.
- Elastic modulus. The general low elastic modulus of RCA contributes to a lower elastic modulus of RAC. A lower modulus of elasticity reduces the restraint provided by the aggregate and thus it increases the drying shrinkage (Silva et al., 2015).
- RCA Source. It was found that lower water to binder ratio, lower porosity and high modulus of elasticity of the parent concrete reduces drying shrinkage. These facts have been stated above. In fact, the parent concrete is a part of the RAC and thus its better properties affects the overall influence.
- Particle size (Zhen Li et al., 2020). Discussed in section 3.3.

These factors are similarly linked to total deformations. Lye et al. (2016) carried out a review and found that most of the studies attributed the higher creep in RAC to the low properties of adhered mortar, high porosity and low elastic modulus. Geng et al. (2019) carried out scanning electron microscope (SEM) to show that RAC is of higher porosity as shown in figure 4.4 to thus justify its higher creep deformations.

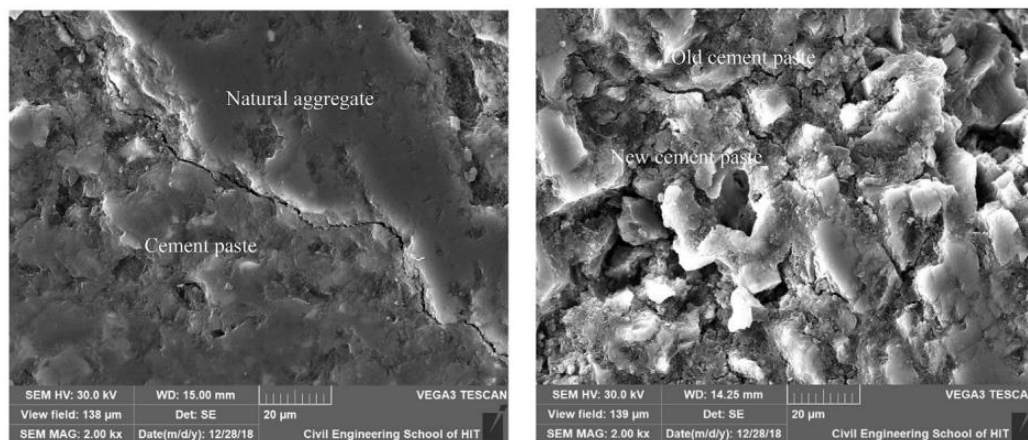


Figure 4.4: From left to right: SEM of (a) NAC and (b) RAC (Geng et al., 2019)

In this section, we have shown that the trend of total shrinkage and total deformations values are proportional. In addition, both increases with the RCA replacement level. Furthermore, both phenomena are being justified similarly.

4.3.2 Effect of RCA on autogenous shrinkage and basic creep

The autogenous shrinkage and basic creep are both considered at sealed conditions. It has been reported that RA reduces autogenous shrinkage. This was attributed to the internal curing effect of RA. More water will flow out of the RCA to compensate the water loss due to self-desiccation and thus basically the higher the saturation degree of RCA is, the more the autogenous shrinkage is reduced. Studies have found that a dry RCA cannot effectively reduce the autogenous shrinkage (Mao et al., 2021). The latter, even if additional water was added to the mixture, may be attributed to the absorption process that will take place by RCA.

Regarding basic creep, it is said that the lower the evaporable water content, the lower the basic creep (Acker and Ulm, 2001). This would basically intersect with the relation of autogenous shrinkage with water. On the other side, Fan et al. (2020) reported an increase of basic creep with RCA replacement as shown in figure 4.5 below. In Fan's study, additional water was added due to the absorption capacity of RCA rather than previous pre-saturation. It is important to note that most studies considered the assessment of total deformations rather than an individual assessment of each type, i.e. basic creep and drying creep. More work is required on the influence of RCA on basic creep (Tošić et al., 2019).

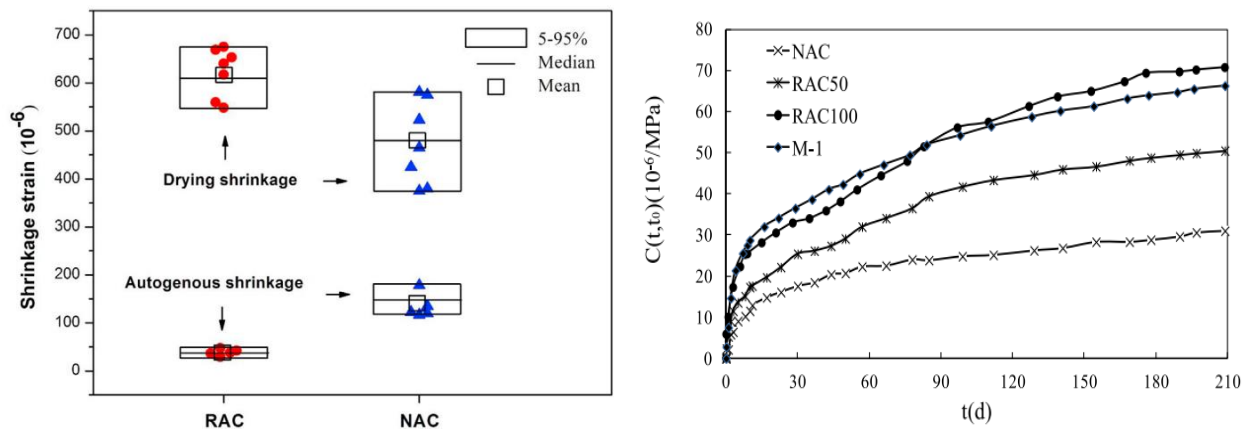


Figure 4.5: Effect of RCA on autogenous and drying shrinkage (a) (left) (Mao et al., 2021) and Effect of RCA on basic creep (Fan et al., 2020) (b) (right).

4.3.3 Effect of aggregate size on shrinkage and creep

RCA has a curing effect and it is able to release water to compensate the water loss due to cement hydration. Light weight aggregate (LWA) is of similar feature but with higher curing effect and thus it reduces the autogenous shrinkage more than RCA. This is attributed to LWA higher porosity and pore structure than RCA (Liu and al., 2019). On the other side, though fine RCA is usually more porous than coarse RCA, it was stated that autogenous shrinkage is more reduced with coarse RCA. Zhang and al. (2020) reported a decrease by 60% and 18% of autogenous shrinkage with 100% of coarse RCA and 100% of fine RCA, respectively. The author as well

stated that the incorporation of fine and coarse RCA together is the best effective option. It is believed that such approach optimize the pore size distribution and enhance the internal curing.

Regarding the drying shrinkage, a review carried out by Mao (Mao et al., 2021) showed that a concrete with 100% fine RCA from one side or 100% coarse RCA from other side increases drying shrinkage by 17.4%-61.5% and 20.5%-76.9, respectively. Based on these numbers, coarse RCA leads to higher drying shrinkage. Nevertheless, it is important to note that the volume of coarse aggregates in concrete accounts more to the total volume of concrete than fine aggregates (coarse aggregate corresponds to almost 70% of total volume of concrete).

Concerning creep, Krajcinovic and Lemaitre (1987) reported a 36% increase for concrete with 100% fine RCA. Such percentage of increase is not high compared to a 60% increase in creep on average for coarse RCA. Cartuxo et al. (2015) reported a 60%-150% increase in creep strains compared to the control natural mixture.

Geng et al. (2019) stated a complete replacement of coarse NCA with coarse RCA boosts creep by 53%. On the other side, a complete replacement of fine NCA by fine RCA increases creep by 34%. The lowest increase was revealed in the mixture that combines both 100% of fine and coarse RCA. The author attributed the latter to the ability of fine RCA to absorb water.

4.3.4 Effect of temperature (T) and relative humidity (RH)

Nastic et al. (2019) assessed subjected prim specimens to shrinkage tests at different environment conditions as shown in figure 4.6.

- Environment A: RH=10% and T=40°C
- Environment B: RH=10% and T=ambient temperature
- Environment C: Ambient environment

Generally speaking, the ambient RH and T are around 50% and 20°C, respectively. The results are presented below. The results show that the specimens of environment A which is of lowest RH and highest T has almost reached stabilization at 100 days. Such stabilization was not achieved for the specimens of environment B as the temperature was lower. The same aspect was reported in environment C at ambient environment.

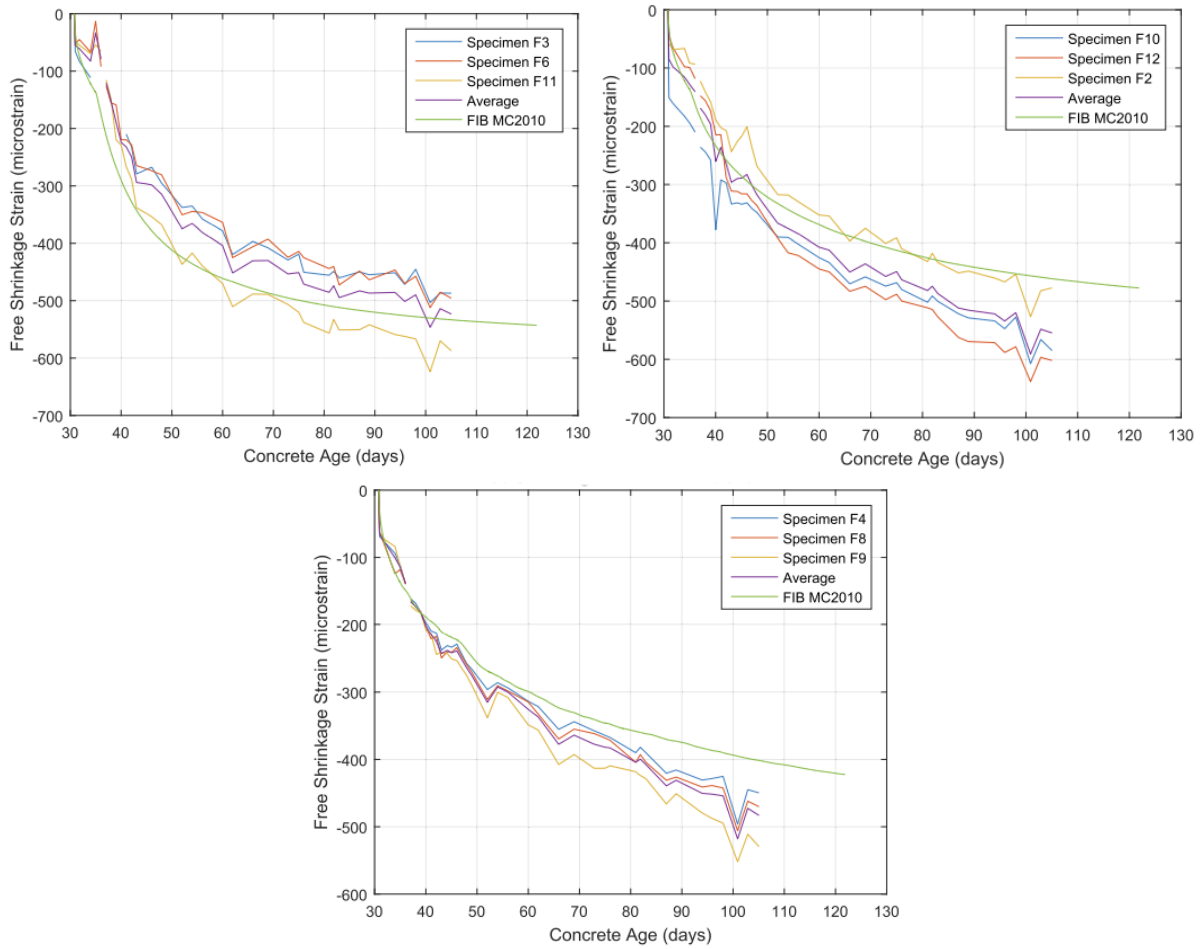


Figure 4.6: The free shrinkage strains of different sepcimens at different environment conditions (from left to right: Environments A, B and C)

Chen & Sorelli (2021) examined the effect of relative humidity (internal) and porosity of special concrete on creep properties. 1.4 nm tobermorite and jennite, which have been considered as natural analogs to the layered structure of calcium silicate hydrates (C-S-H) in the microstructure, were prepared. Figure 4.7 below shows that the creep rate increases with RH. This ensures the important role of water on their creep mechanisms.

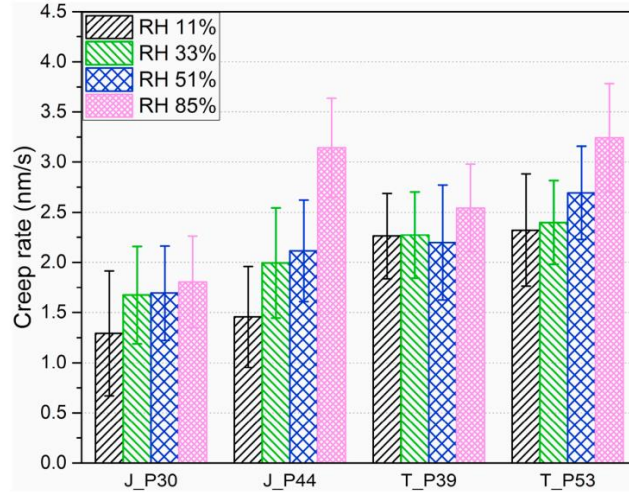


Figure 4.7: Effect of RH on creep rate

4.4 Experimental program

4.4.1 Materials

NS30/70 and RS30/70 are used. Cylinders of size $\text{Ø}11 \times 22 \text{ cm}^3$ are adopted. Specimens were conserved first in a climate controlled chamber at a relative humidity of 50 % and a temperature of 20°C with no exchange of water.

Components (kg/m^3)	Clay (C)	Sand	Cement	W_{eff}	Superplasticizers
NS mixture	440	1026	132	140	1.32
RS mixture	366	855	110	177	1.32

Table 4.1: Mix design of each mixture

4.4.2 Experimental procedure

Autogenous and drying shrinkage and creep tests were conducted at the age of 28 days outdoor and monitored for two months. For basic creep and autogenous shrinkage tests, the exchange of moisture is prevented by a double layer of self-adhesive aluminium paper. Basic and drying creep tests were conducted using electromechanical machine at a loading rate of 70% of the maximum load that was previously measured at the age of 28 days. It is aimed from this loading rate to avoid the tertiary phase. Two rings were fixed on the specimens with three screws and three LVDT sensors were placed at 120° as shown in figure 4.8. The relative displacement between the two sections is measured on a base of 80 mm at the central zone and the mean value was considered. A ball joint was designed to compensate any defects and avoid bending due to defects in the geometry of mechanical parts and the cylinder. The longitudinal deformation due to shrinkage was measured using LVDT sensors.



Figure 4.8: Autogenous shrinkage, drying shrinkage, basic creep and drying creep tests

After the long-term tests, the cylinders were subjected to uniaxial compressive tests using the electromechanical machine used on cubes in the previous experiments mentioned in the past chapters. Three LVDT sensors were set to measure the displacement with accuracy $3 \mu\text{m}$. In addition, the tests were monitored in parallel by means of acoustic emission technique using 8 piezoelectric sensors. Three sensors were put above the first ring, another three between the two rings and two below the second ring as shown in figure 4.9. The amplitude threshold was taken at 30 dB.

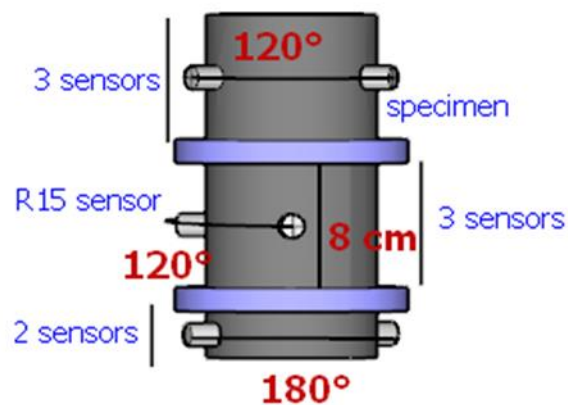


Figure 4.9: AE sensors positions

4.5 Results

4.5.1 Long-term deformations

4.5.2 Shrinkage

Figure 4.10 shows the results of mass loss of NS30/70 and RS30/70 done on cylinders. In addition, it shows the autogenous shrinkage and total shrinkage of NS30/70 and RS30/70 done on cylinders and named respectively NS and RS and the total shrinkage on 4x4x16 cm³ prisms and named respectively NS-P and RS-P (subjected to drying at RH=50% as was shown in chapter 2).

A rapid mass loss was reported at the first days. Such phase is controlled by the ambient conditions and it continues as long as there is supply of water from inside the specimen. This was accompanied by a low rate of shrinkage. Once the water migrating from inside to the outside is not anymore enough to meet that evaporative demand, the second phase started and thus it would be characterized by a lower rate of drying compared to the first phase. This phase is accompanied with high shrinkage rate. The third phase is known to be of almost constant low evaporation and drying shrinkage rates (Tran et al., 2019). In the following study, the complete replacement of NS by RS following a pre-saturation of 80 % reported a 54% decrease in the autogenous shrinkage of earth concrete.

The higher porosity and pre-saturation of RS and lower modulus of elasticity (figure 4.16) contribute to a higher drying shrinkage. The results reveal that RS permits the more migration of its water than NS. Regarding autogenous shrinkage, the higher shrinkage of NS shows that the pre-saturation of RS reduces such shrinkage as the loss of water due to self-desiccation is compensated. In the following study, the complete replacement of NS by RS was reflected by a 77% drying shrinkage increase from 2313 $\mu\text{m}/\text{m}$ to 4095 $\mu\text{m}/\text{m}$.

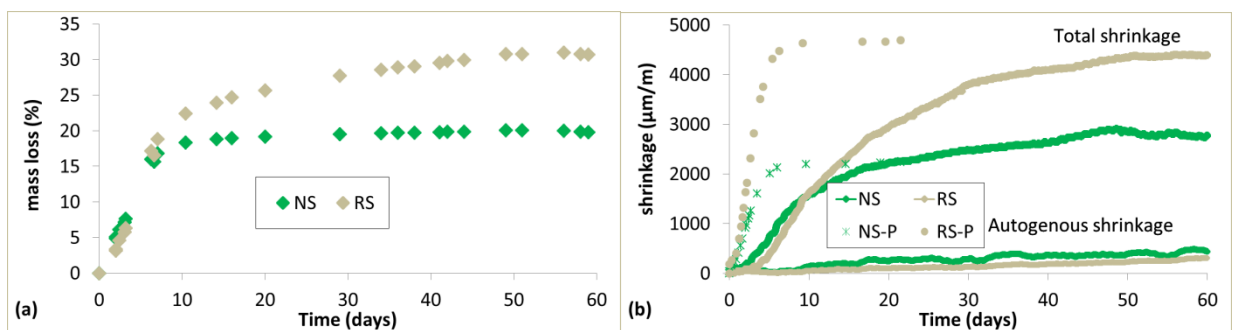


Figure 4.10: Mass loss (a) and autogenous shrinkage and total shrinkage of cylinders (NS and RS) and prisms (NS-P and RS-P) (b)

Though the shrinkage measurements started at day 3 on prisms while at day 28 on cylinders, the values were close (figure 4.10 (b)). This can be due to the prevention of water migration to the outside of the specimens for both cases regardless of the length of the initial curing period. The

rate of drying is faster in prisms and accordingly they reached the stabilization period in a shorter time. This can be attributed to the smaller size of prisms and thus a shorter distance was required for water to migrate outside the specimen from one side and to the weathering environment where prisms were put at a constant RH of 50% while the cylinders were kept in an environment of variable RH that was mostly above 50% as shown in figure 4.11 (a).

Figure 4.11 (a) shows the drying shrinkage (total shrinkage – autogenous shrinkage) as function of relative humidity and temperature. Basically, the temperature values did not show great differences throughout the test while the RH values did. As highlighted by arrows a decrease in RH was accompanied by increase in shrinkage and an increase was reflected by decrease in shrinkage or swelling.

Figure 4.11 (b) shows drying shrinkage as function mass loss. The high mass loss values in first phase were accompanied by low drying shrinkage rate. It has been stated that the migration of free water during this period does not induce shrinkage. However, the linear relation obtained between the mass loss and shrinkage on small specimens may contradict this hypothesis (Benboudjema et al., 2005). On the other side, hydration taking place, micro cracks in addition to wall effect due to formwork may be behind this aspect (Samouh et al., 2017). As highlighted by circle, the rate of shrinkage (in addition to mass loss rate as shown in figure 4.10 (a)) is higher in the NS mixture which may be attributed to a different porosity network. It can be noticed that the phases are longer in RS mixture which may be attributed to the fact that water in RS mixture is not only migrated locally as for NS mixture; but from the RS itself due to pre-saturation.

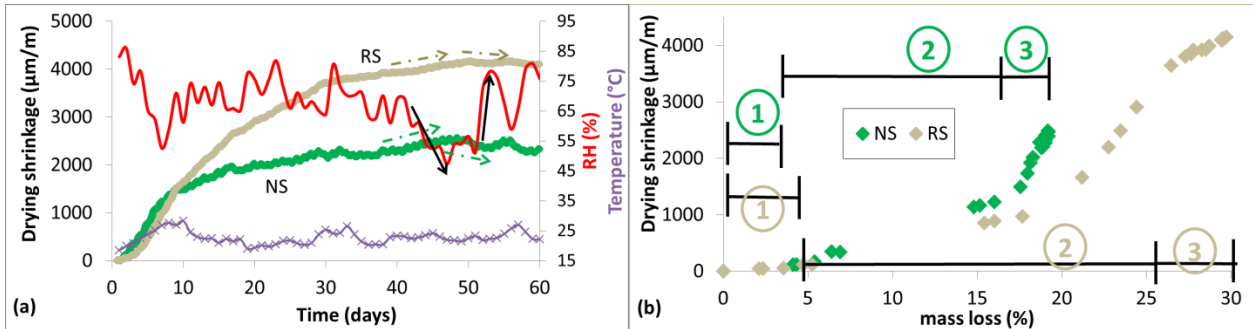


Figure 4.11: Drying shrinkage as function of RH and temperature (a) and Drying shrinkage as function of mass loss

4.5.3 Creep

The basic creep is presented in figure 4.12 for both mixtures after subtracting the instantaneous strains and autogenous shrinkage. The total deformations are also presented after subtracting the elastic strains.

Knowing that a loaded drying specimen test yields total deformations in addition to elastic strains, the extended strain $\varepsilon_{ex}(t)$ is expressed as follows:

$$\varepsilon_{ex}(t) = \varepsilon_{EL}(t) + \varepsilon_{TLTD}(t) + \alpha \cdot \Delta T(t) \quad (4-2)$$

where $\Delta T(t)$ temperature variation over a period of time and α is a variable. However, as shown in figure 4.11, temperature did not exhibit great differences and thus it was not taken into account (Domingo-Cabo et al., 2009).

The results show that RS did not reduce basic creep strains. Thus, the results are contrary to autogenous shrinkage. Knowing that pre-saturation was carried out to RS in our study while additional water was added rather than pre-saturation in other study (Fan et al., 2020), and both studies reported an increase of basic creep, this can indicate that basic creep increase with RCA regardless of the way adopted for RS saturation.

Akono et al. (2021) stated higher basic creep deformations tendencies in RAC as well. It was found that higher creep deformations are observed at low-density C-S-H, then at high-density C-S-H and that the hard grains hardly creep. In their study, the hard grains corresponded to almost 45% and 26% of the microstructure of NAC and RAC, respectively. This permits to state that the lower basic creep in NS mixture in this study may be attributed to the presence of more quantity of hard grains in its microstructure compared to RS mixture.

Furthermore, as creep can be caused by the transfer of water from the micropores to the macropores under a pressure, and as RS comprises more water than NS and different porosity distribution, more water may have been transferred to the larger pores due to the applied stress causing more of creep strain.

In the following study, the complete replacement of NS by RS in earth concrete reported a 121% increase of total long-term deformations from 3085 to 6829 $\mu\text{m}/\text{m}$. Regarding basic creep, it increases by 12% from 445 to 500 $\mu\text{m}/\text{m}$ as RS replaces NS. On the other side, knowing that RS specimen is of lower strength than NS specimen, it may be worth to state that the basic creep per unit stress as shown in figure 4.12 (b) increases by 128% from 327 to 746 $\mu\text{m}/\text{m.MPa}$. For a better verification of the effect of RS on basic creep, the basic creep deformations per stress or compliance are calculated to show an increase by more than 100%.

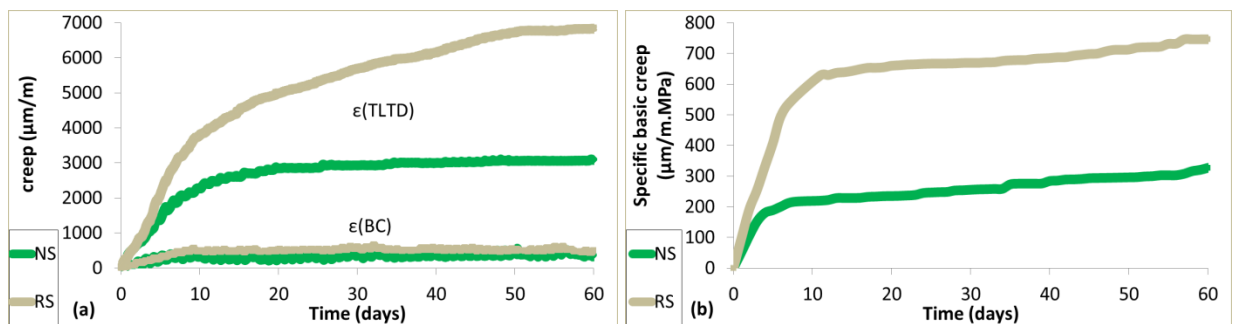


Figure 4.12: Basic creep strains of NS and RS mixtures (a) and basic creep strain per stress (b)

Figure 4.13 shows the strain summation $\varepsilon_s(t)$ of the individual strains from one side (basic cree, drying shrinkage and autogenous shrinkage -without elastic strain for a better verification of

$\varepsilon_{DC}(t)$ -) and $\varepsilon_{TLTD}(t)$ related to DC specimen from other side. As already verified, $\varepsilon_{BC}(t)$, $\varepsilon_{DS}(t)$ and total $\varepsilon_{TLTD}(t)$ increase while $\varepsilon_{AS}(t)$ decreases when RS replaces NS.

The total deformations increase with RS confirming with the studies in the literature. As said before, the increase in total shrinkage is accompanied by increase in total deformations resulted from drying creep specimen. In addition, both are being justified by the same aspects by scholars (porosity, water absorption...).

The difference between summation strains and strains from drying creep specimen represents the drying creep $\varepsilon_{DC}(t)$ or Picket's effect. The drying creep in the RS mixture is much higher than that in the NS mixture. In fact, it is negligible in the latter. Regardless of the microstructural variations, we would like to highlight the microcracking effect. In fact, the RS drying specimen is more vulnerable to drying cracks than NS drying specimen. The formed microcracks will not fully close and thus irreversible deformations are resulted. This deformation reduces the shrinkage of the specimen and thus this shrinkage does not represent the true one. As more cracks would be formed in the RS specimen, its true shrinkage is more reduced than the NS specimen. The structural desiccation creep effect is linked to a reduction in microcracks generated by desiccation. Indeed, the application of a uniform compressive stress on a specimen subjected to drying generates a less pronounced cracking than that of an unloaded specimen. This leads to an additional strain due to the decrease of cracking effect. When a loaded drying specimen is assessed, there will be basically no microcracking (or closure of cracks will take place) on the planes normal to the direction of compression. Logically speaking, as more cracks would be formed on a non-loaded drying RS specimen, compressive will be preventing the formation (or closing) of more cracks in RS than NS and eventually a higher extra strain (drying creep) is reported in the RS mixture due microcracking effect.

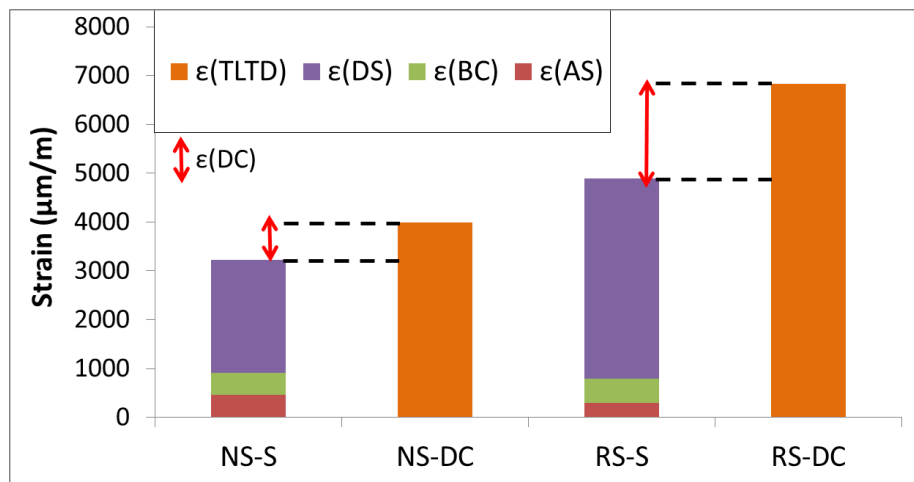


Figure 4.13: Evaluation of drying creep for NS and RS

4.5.4 Strength development due to long-term deformations

Specimens monitored for long deformation tests were subjected to compressive tests after 60 days.

The specimens subjected to the durability tests were subjected to compressive tests after 60 days. The stress-strain curves are presented below in 4.14. Besides, a specimen at the end of the compressive test is displayed. It may be worth to state again that DC corresponds to drying creep specimen, DS for drying shrinkage, BC for basic creep, AS for autogenous shrinkage and ref for reference.

Figure 4.15 shows the compressive strength of each specimen in addition to the compressive strength of the reference (NS-ref and RS-ref) specimens at 28 days. Figure 4.16 shows those of the modulus of elasticity.

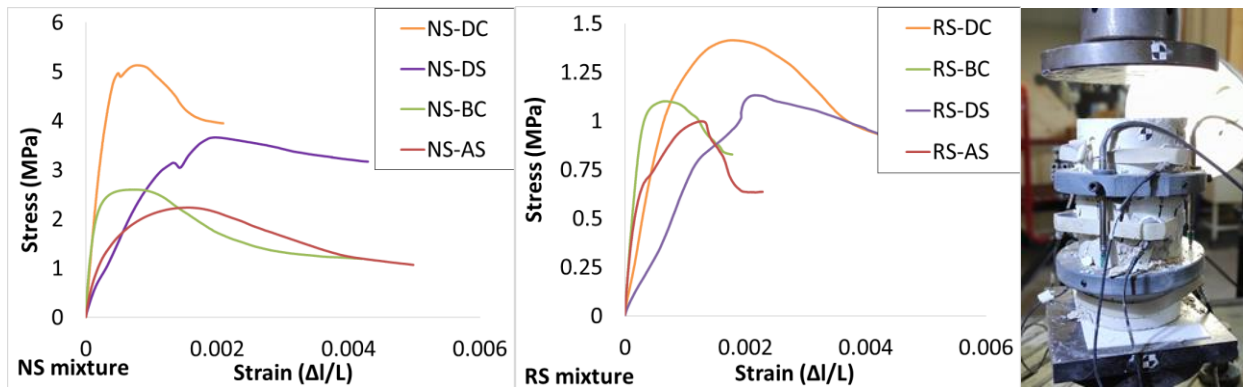


Figure 4.14: Stress-strain curves of each specimen

In both mixtures -NS and RS- the compressive strength follows the same trend. The reference mixture reported the lowest strength. This was followed by the AS specimen, BC specimen, DS specimen and finally DC specimen.

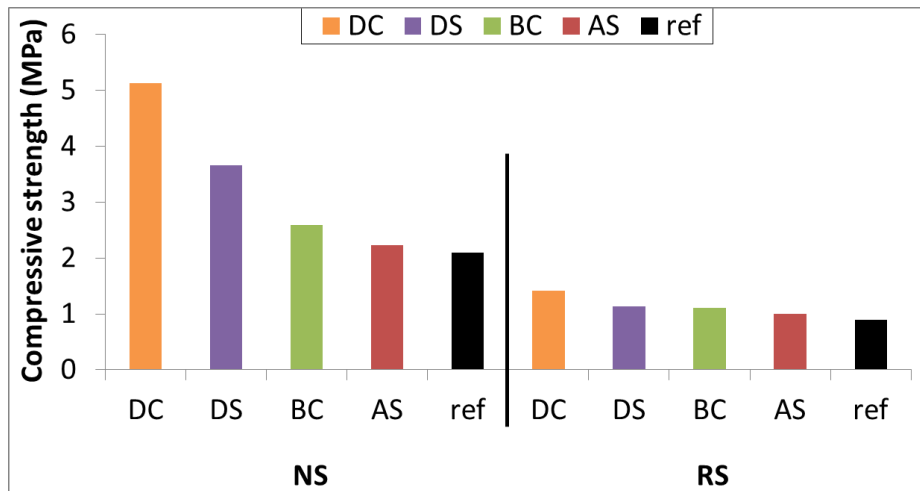


Figure 4.15: Compressive strength of each mixture

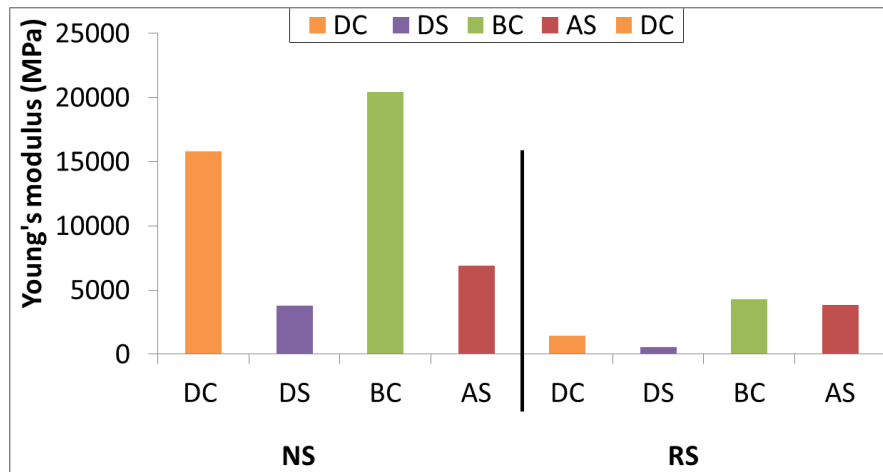


Figure 4.16: Young's modulus of each mixture

4.5.5 Reference specimens

Starting by the reference specimens, NS reported higher strength than RS. This is in agreement with the theoretical trend that declares degradation in the mechanical properties when RS replaces NS. This has been attributed to the bad state of RS or recycled aggregate in general that comprises cracks and pores. The loss in strength in this study can be attributed the higher porosity in addition to the increase in the initial water content represented pre-saturation of RS.

4.5.6 AS specimens

Compared to the reference, the AS specimen is of higher strength. While the reference tests were conducted at the age of 28 days, the compressive tests on AS specimens were carried out at the age of 60 days. Therefore, the increase in strength can be attributed to the increase in the curing age period and thus better hydration. The strength of NS and RS specimens increases by 11% and 6%, respectively. Thus, the specimen that exhibited lower autogenous shrinkage exhibited higher increase in strength.

4.5.7 BC specimens

The BC specimens are of higher strength than AS shrinkage specimen. The difference between these two specimens is the external load and thus such increase in strength has to be linked to such stress. The increase in strength can be attributed to consolidation and its consequences that involve water movement. Indeed, the applied load induces free water to flow and eventually rearrangement of soil particles takes place. This increases the solid-solid contacts at different positions and decreases the voids in the soil (Le et al., 2012) . This improvement in stiffening contributes to strength.

BC specimens reported a 16% and 10% increase in strength in NS and RS compared to AS specimen, respectively. This may be attributed to the higher porosity of RS. As more voids and

pores exist in the RS mixture, the resulted solid-solid contacts will be less important than the NS mixture.

4.5.8 DS specimens

The strength of DS specimens is higher than that of AS specimen. The difference between the specimens is the drying process and thus it should be attributed to it. Due to the difference in relative humidity between the external and internal environments, the water migrates outside the specimen. As stated previously in chapter 2, the compressive strength may increase or decrease as a result of water transfer from inside the specimen to outside. The increase in strength is due to the increase in capillary pressure and disjoining pressure which leads to stiffening effect (Yurtdas et al., 2004).

The increase in strength due to drying shows that the suction effect is the dominant phenomenon over the shrinkage induced cracking one. Compared to AS specimen, the increase in the NS and RS specimens reached 63% and 13%, respectively. This can be attributed again to the porous state of the RS mixture in addition to the more shrinkage induced cracking in the RS mixture that has curbed the effect of suction.

Compared to AS specimen, DS revealed more increase in strength than the BC one. As the strength development of both, DS and BC specimens, involves water movement, where the former is due to drying while the latter is due to external load, the higher increase of strength in DS specimen may be attributed to the complete loss of water particles in the DS specimen and that led to the more of solid-solid contacts.

4.5.9 DC specimens

The strength due to drying creep (DC) reported the highest value. With respect to AS specimen, strength of DC specimen increases by 129% and 42% of NS and RS, respectively. The extended microprestress-solidification (XMPS) theory was successful in taking the drying creep into account. It concerns the water layer movement between the C-S-H walls. Nevertheless, regardless of the intrinsic effect, the structural effect has to be highlighted. We stated before that the extra strain reported due to drying creep tests may be due to the less existence of drying cracks and particularly to those who are on the planes normal to the compressive loading direction. Therefore, the increase in strength can be attributed to the better health condition of the specimen. In the same way, the strength development in NS is more than RS which can be attributed to the more existence of drying cracks in RS mixture at positions not affected by the compressive loadings.

As compressive strength, the Young's modulus decreases with RS. On the other side, the latter does not follow the same trend of the former. First, BC specimen reported the highest value. Second, it can be noticed that DC and BC specimens are of higher Young's modulus than DS and AS specimens, respectively. Thus, the loaded specimen is of higher Young's modulus than the unloaded specimen at same curing condition. Third, it can be noticed the Young's modulus of DS

for both specimens exhibited the lowest value which may be due to shrinkage induced cracking. The lower elasticity of drying creep specimen compared to basic creep specimen may ensure this deduction.

4.6 Acoustic emission (AE) analysis

4.6.1 Distribution of AE hits

Figure 4.17 shows the correlation between stress and distribution of AE hits as function of strain. In the following analysis, we are interested in the pre-peak phase.

First of all, the AE activity in RS specimens is lower than that NS ones. This can be attributed to the lower strength of the former in addition to the pre-saturation of its RS and the lower ITZ properties.

The remarkable number of AE activity at the beginning of all mixtures can be attributed to the compaction taking place due to initial loadings. This phase evidences the closure of cracks and pores without the formation of new cracks.

It can be seen that BC specimens exhibited lower AE activity in the pre-peak phase than the AS specimens. This can be attributed to different aspects:

- The decrease in the Young's modulus in AS specimens will accommodate more stress buildup before cracking occurs. This stress buildup will be accompanied by more AE signals.
- The strength increase in the BC specimens will be reflected by lower pre-peak AE activity (Fardoun et al. 2022).
- The compaction phase exhibited lower AE in the specimen that was previously loaded during the durability tests (BC specimen). Thus, such pre-loading acted as pre-compaction process.
- The higher peak strain in the AS specimens will be most probably accompanied by more AE activity.

These four factors were valid between NS-DS and NS-T from one side and between RS-DS and RS-T from other side. Nevertheless, it was to a lower extent in RS specimens which can be attributed the less significant variations in strength and Young's modulus in the latter.

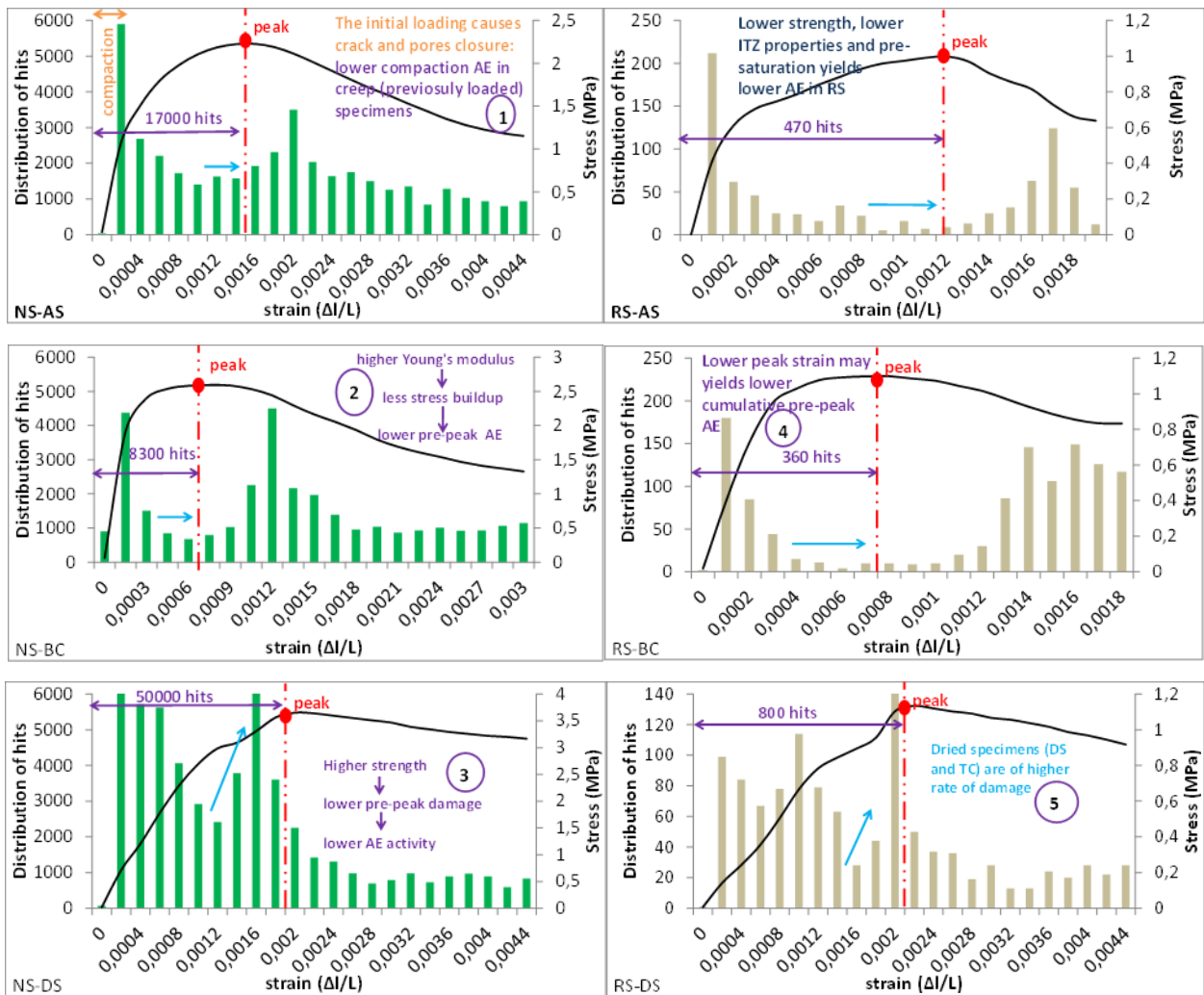
DS and DC specimens reported the highest AE activity. This may indicate that AE reflected successfully:

- the suction effect where the particles got closer to each other and thus higher friction takes place upon loading.
- the shrinkage induced cracking where friction along already existing drying cracks can take place upon loading.

This resulted friction based on the two processes will be accompanied by AE activity during the application of external stress.

Furthermore, increase in the rate of AE activity can be noticed for DS and DC specimens before the peak. This may point out that these specimens exhibited higher rate of damage (as shown in sky blue arrows) than the sealed specimens (AS and BC). This may indicate higher vulnerability to crack formation and propagation in dried specimens.

DC specimen reported lower pre-peak AE activity than DS specimen due to the aforementioned aspects (higher strength, higher Young's modulus, lower peak strain, previously loaded specimen).



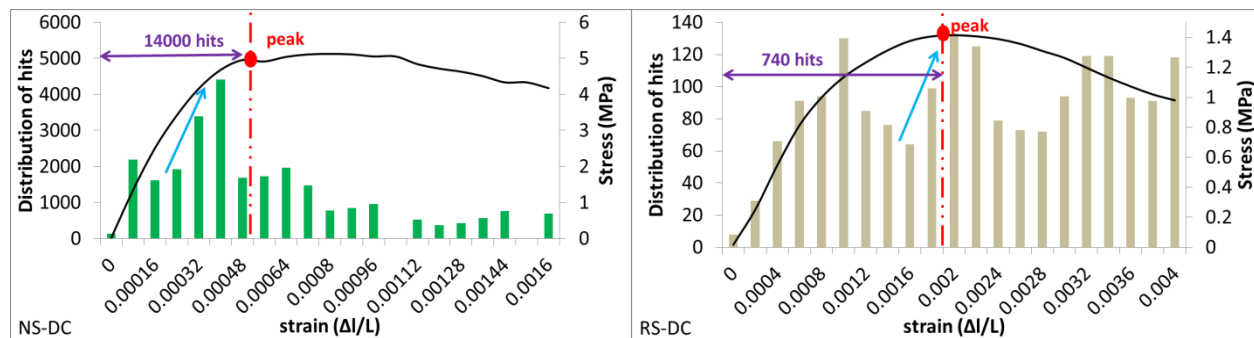


Figure 4.17: Correlation between the stress-strain curves and distribution of AE hits

Conclusions

Structures are subjected to different loadings in addition to temperature and relative humidity variations during their life time. These loads cause long-term deformations which are of high importance in earth concrete due particularly to the latter's fine particles, principally clay. The long-term or time-dependent deformations are: autogenous shrinkage, drying shrinkage, basic creep and drying creep.

In this chapter, compressive creep tests were conducted on cylindrical ($\text{Ø}11 \times 22 \text{ cm}^3$) earth concrete mixtures prepared with natural sand (NS) and recycled sand (RS) mixed to 30 % of kaolinite clay and 9% of cement by mass of solid components. Specimens were conserved first in a climate controlled chamber at a relative humidity of 50 % and a temperature of 20°C with no exchange of water. Shrinkage and creep tests were then conducted at the age of 28 days outdoor and monitored for two months. After the long-term tests, the cylinders were subjected to compressive stress. These tests were monitored in parallel with acoustic emission technique.

The results revealed that when RS replaces NS, the autogenous shrinkage decreases while drying shrinkage, basic creep and drying creep increase. The results also showed that compared to the reference mixture, the compressive strength of both NS and RS mixtures reported a strength increase from least to most as follows: reference < autogenous shrinkage < basic creep < drying shrinkage < drying creep specimen. In addition, NS specimens reported higher strength development than RS ones except for the autogenous shrinkage specimen. On the other hand, the Young's modulus of the drying shrinkage specimen exhibited the lowest value in NS and RS which can be attributed to shrinkage induced cracking. Regarding AE activity, the results showed that their generation is influenced by compressive strength, Young's modulus, the drying process, specimen health condition, peak strain and whether the specimen was previously loaded during the durability tests or not. In addition, NS mixtures reported AE signals of higher peak frequency than RS mixture.

General Conclusions and Perspectives

Ecological construction materials are being proposed aiming to curb the use of classical concrete or at least to reduce its unwanted impacts. The construction with earth or soil is gaining a renewed interest. Beyond the different traditional techniques adopted, studies and applications are being carried out recently on a new earth material known as earth concrete. This one is designed to be pourable. Being able to achieve a construction material that combines earth and recycled sand (RS) would be a real turning point in the sustainable construction field (Fardoun, 2021; Fardoun et al., 2021, 2021; Fardoun et al., 2020). The following thesis aimed to assess the effect of different amounts of clay and RS on the mechanical properties and durability. The work considered four mixtures. A mixture that comprised of an artificial soil with 30 % of clay and 70% of NS –NS30/70- and three others constituted of RS and 20%, 30% and 40% of clay named respectively: RS20/80, RS30/70 and RS40/60

In chapter 1, the specimens at wet conditions were subjected to monotonic compressive tests at different curing ages. The compressive tests were monitored in parallel with acoustic emission (AE) technique and digital image correlation (DIC). The compressive strength and the fracture energy decreases when RS replaces NS and with clay content. On the other side, the fracture toughness increases with RS and clay content. According to the results, a good correlation has been observed between AE energy and fracture energy at short term curing ages. However, the higher degree of brittleness at 90 days of NS30/70 and RS20/80 yielded unsuccessful AE energy-fracture energy correlation. The fracture process has been distinguished by different phases as follows: compaction, linear, stable growth –of cracks-, stable growth and softening. RS mixtures generate more AE events in the compaction phase than NS mixture due to the pre-existing pores and cracks. In addition, RS mixtures exhibited AE events at earlier stress levels which may indicate an earlier initiation of cracks. All phases reported higher shear AE hits and shear AE energy except the unstable growth phase which directly comes before the peak reported higher tensile AE hits and remarkable increase in AE energy and thus it can be considered as a future potential failure. Furthermore, shear cracks are dominant in the post-peak region of earth concrete mixtures and thus they are more responsible for the final collapse. Regarding AE and DIC, the correlation between AE events and DIC under compressive loadings seems applicable in case of consecutive high energized AE events generation.

Chapter 2 assessed numerically and experimentally the water transfer due to drying and the damage of earth concrete mixtures at RH=90% and RH=50%. The mechanical behavior of the earth concrete mixtures at wet and dried conditions was examined. In addition to AE and DIC assessments in this chapter, ultrasonic pulse velocity test was adopted for specimens at wet (RH=90%) and dried conditions (RH=50%). Moreover, mass loss shrinkage and capillary tests were conducted to better understand the fracture behavior. The results showed that the dominance of capillary suction effect declines with prolonged drying due to the more formation

of shrinkage induced cracking. Moreover, the results revealed that the pre-peak slope values are proportional to the ultrasonic pulse velocity values for specimens at sealed conditions. Eventually, an equation correlating the slope with modulus of elasticity has been proposed. On the other side, it seems that concerning drying, the decrease or increase in the slope value is governed by the vulnerability of the mixtures' components to drying. In this chapter, the results exhibited that drying leads to the formation of random cracks all over the specimen and this was accompanied by increase in the AE activity and events. Furthermore, it is important to state that the results revealed that the AE activity in the pre-peak phase can be used as a sign for strength development from one side and generation of shrinkage induced cracking from other side. Moreover, in this chapter the hygric properties were assessed.

Chapter 3 part A examines the specimens under cyclic loadings at the same curing conditions mentioned above. The stress-strain curves were assessed and AE damage assessment was carried out. For the first part, the results revealed that the residual strains in earth concrete at wet conditions are strength related. Such strains increase with clay content and when RS replaces NS. At RH=50%, the residual strains of NS30/70 decreases and those of RS mixtures increases highlighting the vulnerability of RS to drying. Similarly, the secant slope increases in the NS mixture and decreases in the RS mixtures due to drying. An earth concrete loop is of two simple opposite arcs at wet conditions regardless of the mixture's components. Due to drying, the reloading curve of low strength mixtures is in the form of an acute arc. Concerning AE, the attainment of Kaiser Effect at wet conditions reflected the low damage rate of earth concrete mixtures under cyclic loading. Moreover, the damage indices and the damage classification diagram indicated that the RS mixture with highest clay amount at dried conditions is more vulnerable to damage than any other mixture. A good correlation was revealed between the AE indices and the DIC that showed crack propagation at low loading levels at RH=50%. Finally, the DIC has shown that Kaiser Effect and load ratio are not necessarily affected by the evolution of crack opening. Chapter 3 Part B is completely numerical. It reproduced the stress-strain at wet conditions curves by means of Fichant's damage model and assessed the damage field of each mixture. The model was capable of reflecting the fact that RS mixtures are more vulnerable to crack propagation. In addition, the shrinkage induced cracking due to drying was examined on the NS earth concrete and RS earth concrete mixtures. Though both reported strength increase due to drying, drying cracks were present in both mixtures. This showed that both suction effect and shrinkage induced cracking phenomena took place where the former was dominant. The shrinkage induced cracking was more important in the RS mixture leading to its lower strength development than the NS mixture.

Chapter 4 investigates the effect of RS on the long-term deformations (cylindrical NS30/70 and RS30/70 specimens were put outdoors for two months) and the effect of these deformations on strength development in addition to Young's modulus (pre-peak slope). The results revealed that when recycled aggregate or RS replaces natural aggregate or NS, the autogenous shrinkage decreases (with pre-saturated RS) while the basic creep, drying shrinkage and drying creep

increases. Due to these long-term deformations, the compressive strength increases in all specimens where the TC specimen reported the highest. The order is as follows: AS<BC<AS<TC. In all these specimens NS reported higher strength development except for the AS one. Regarding the Young's modulus, compared to the reference mixture, it decreases in all the specimens. Between the four specimens, DS reported the lowest value which can be attributed to drying cracks. Regarding AE activity, the results showed that their generation is influenced by compressive strength, Young's modulus, the drying process, specimen health condition, peak strain and whether the specimen was previously loaded during the durability tests or not. In addition, NS mixtures reported AE signals of higher peak frequency than RS mixture.

It is worth to note that additional work and more investigation are required. The author would like to highlight the following points:

- Improvement of the formulation methodology in order to adapt it to the nature of the RS and clay soil to obtain consistent results in terms of quality.
- Reduction in the quantity of cement by replacing it with coagulants to have a more ecological earth concrete.
- Study of hygrothermal comfort and fire resistance of these materials.
- Study of carbonation evolution and its effect on mechanical properties.
- Evaluation of life cycle assessment / carbon footprint.
- Thermo-hydro-mechanical modeling.

Mohr–Coulomb theory is adopted to describe the response of soils. It would be better to take it into account.

References

- Abate, S.Y., Song, K.-I., Song, J.-K., Lee, B.Y., Kim, H.-K., 2018. Internal curing effect of raw and carbonated recycled aggregate on the properties of high-strength slag-cement mortar. *Construction and Building Materials* 165, 64–71. <https://doi.org/10.1016/j.conbuildmat.2018.01.035>
- Acker, P., Ulm, F.-J., 2001. Creep and shrinkage of concrete: physical origins and practical measurements. *Nuclear Engineering and Design* 203, 143–158. [https://doi.org/10.1016/S0029-5493\(00\)00304-6](https://doi.org/10.1016/S0029-5493(00)00304-6)
- Adams, M.P., Fu, T., Cabrera, A.G., Morales, M., Ideker, J.H., Isgor, O.B., 2016. Cracking susceptibility of concrete made with coarse recycled concrete aggregates. *Construction and Building Materials* 102, 802–810. <https://doi.org/10.1016/j.conbuildmat.2015.11.022>
- Aggelis, D.G., 2011. Classification of cracking mode in concrete by acoustic emission parameters. *Mechanics Research Communications* 38, 153–157. <https://doi.org/10.1016/j.mechrescom.2011.03.007>
- Aissaoui, N., 2018. Apport de la modélisation mésoscopique dans la prédiction de la fissuration des structures en béton: Aspects énergétiques et effets d'échelle. Université Aboubakr Belkaïd, Tlemcen.
- Akono, A.-T., Chen, J., Zhan, M., Shah, S.P., 2021. Basic creep and fracture response of fine recycled aggregate concrete. *Construction and Building Materials* 266, 121107. <https://doi.org/10.1016/j.conbuildmat.2020.121107>
- Albrecht, B.A., Benson, C.H., 2001. Effect of desiccation on compacted natural clays. *ASCE, J. of Geotech. And Geoenviron. Engrg.*
- Aldahdooh, M.A.A., Muhamad Bunnori, N., 2013. Crack classification in reinforced concrete beams with varying thicknesses by mean of acoustic emission signal features. *Construction and Building Materials* 45, 282–288. <https://doi.org/10.1016/j.conbuildmat.2013.03.090>
- Alizadeh, R., Beaudoin, J.J., Raki, L., 2010. Viscoelastic nature of calcium silicate hydrate. *Cement and Concrete Composites* 32, 369–376. <https://doi.org/10.1016/j.cemconcomp.2010.02.008>
- Arrigoni, A., Beckett, C.T.S., Ciancio, D., Pelosato, R., Dotelli, G., Grillet, A.-C., 2018. Rammed Earth incorporating Recycled Concrete Aggregate: a sustainable, resistant and breathable construction solution. *Resources, Conservation and Recycling* 137, 11–20. <https://doi.org/10.1016/j.resconrec.2018.05.025>
- Arrigoni, A., Grillet, A.-C., Pelosato, R., Dotelli, G., Beckett, C.T.S., Woloszyn, M., Ciancio, D., 2017. Reduction of rammed earth's hygroscopic performance under stabilisation: an experimental investigation. *Building and Environment* 115, 358–367. <https://doi.org/10.1016/j.buildenv.2017.01.034>
- Arthur, E., 2017. Rapid estimation of cation exchange capacity from soil water content: Cation exchange capacity from soil water content. *Eur J Soil Sci* 68, 365–373. <https://doi.org/10.1111/ejss.12418>
- Atkins, P.W., De Paula, J., 2006. *Physical chemistry*. Oxford University Press, Oxford.
- Attewell, P.B., Farmer, I.W., 1973. Fatigue behaviour of rock. *International Journal of Rock Mechanics and Mining Sciences & Geomechanics Abstracts* 10, 1–9. [https://doi.org/10.1016/0148-9062\(73\)90055-7](https://doi.org/10.1016/0148-9062(73)90055-7)
- Avrami, E., Guillaud, H., Hardy, M., 2008. *Terra Literature Review An Overview of Research in Earthen Architecture Conservation*. The Getty Conservation Institute, Los Angeles, USA.
- Bazant, Z.P., Chern, J.C., 1985. Concrete creep at variable humidity: constitutive law and mechanism. *Materials and Structures* 18, 1–20. <https://doi.org/10.1007/BF02473360>
- Beattie, A., 2013. *Acoustic Emission Non-Destructive Testing of Structures Using Source Location Techniques*. California.
- Beckett, C., 2011. *The Role of Material Structure in Compacted Earthen Building Materials: Implications for Design and Construction*. Durham University, United Kingdom.
- Beckett, C., Augarde, C., 2012. The Effect of Relative Humidity and Temperature on the Unconfined Compressive Strength of Rammed Earth, in: Mancuso, C., Jommi, C., D'Onza, F. (Eds.), *Unsaturated Soils: Research and Applications*. Springer Berlin Heidelberg, Berlin, Heidelberg, pp. 287–292. https://doi.org/10.1007/978-3-642-31116-1_39
- Bell, F.G., 1996. Lime stabilization of clay minerals and soils. *Engineering Geology* 42, 223–237. [https://doi.org/10.1016/0013-7952\(96\)00028-2](https://doi.org/10.1016/0013-7952(96)00028-2)
- Benboudjema, F., Meftah, F., Torrenti, J.M., 2005. Interaction between drying, shrinkage, creep and cracking phenomena in concrete. *Engineering Structures* 27, 239–250. <https://doi.org/10.1016/j.engstruct.2004.09.012>

- Bravo, M., de Brito, J., Evangelista, L., Pacheco, J., 2018. Durability and shrinkage of concrete with CDW as recycled aggregates: Benefits from superplasticizer's incorporation and influence of CDW composition. *Construction and Building Materials* 168, 818–830. <https://doi.org/10.1016/j.conbuildmat.2018.02.176>
- Breccolotti, M., Bonfigli, M.F., D'Alessandro, A., Materazzi, A.L., 2015. Constitutive modeling of plain concrete subjected to cyclic uniaxial compressive loading. *Construction and Building Materials* 94, 172–180. <https://doi.org/10.1016/j.conbuildmat.2015.06.067>
- Bruno, A., 2016. Hygro-mechanical characterisation of hypercompacted earth for building construction. Université de Pau et des Pays de l'Adour.
- Bui, Q.-B., Morel, J.-C., Hans, S., Walker, P., 2014. Effect of moisture content on the mechanical characteristics of rammed earth. *Construction and Building Materials* 54, 163–169. <https://doi.org/10.1016/j.conbuildmat.2013.12.067>
- Burud, N.B., Kishen, J.M.C., 2021. Response based damage assessment using acoustic emission energy for plain concrete. *Construction and Building Materials* 269, 121241. <https://doi.org/10.1016/j.conbuildmat.2020.121241>
- Carette, J., Soleilhet, F., Benboudjema, F., Ma, X., Nahas, G., Abahri, K., Darquennes, A., Bennacer, R., 2020. Identifying the mechanisms of concrete drying: An experimental-numerical approach. *Construction and Building Materials* 230, 117001. <https://doi.org/10.1016/j.conbuildmat.2019.117001>
- Cartuxo, F., de Brito, J., Evangelista, L., Jiménez, J.R., Ledesma, E.F., 2015. Rheological behaviour of concrete made with fine recycled concrete aggregates – Influence of the superplasticizer. *Construction and Building Materials* 89, 36–47. <https://doi.org/10.1016/j.conbuildmat.2015.03.119>
- Chen, Y., Xu, L., Xuan, W., Zhou, Z., 2019. Experimental study on four-point cyclic bending behaviours of concrete with high density polyethylene granules. *Construction and Building Materials* 201, 691–701. <https://doi.org/10.1016/j.conbuildmat.2018.12.191>
- Chen, Z., Sorelli, L., 2021. Effect of relative humidity and porosity on the logarithmic creep of the layered C–S–H minerals tobermorite and jennite. *Cement and Concrete Composites* 116, 103872. <https://doi.org/10.1016/j.cemconcomp.2020.103872>
- Chen, Z.-J., Feng, W.-Q., Yin, J.-H., 2021. A new simplified method for calculating short-term and long-term consolidation settlements of multi-layered soils considering creep limit. *Computers and Geotechnics* 138, 104324. <https://doi.org/10.1016/j.compgeo.2021.104324>
- Chinh Ngo, D., 2018. Développement d'un nouveau éco-béton à base de sol et fibres végétales : étude du comportement mécanique et de durabilité. Université de Bordeaux.
- Colombo, S., Forde, M.C., Main, I.G., Shigeishi, M., 2005. Predicting the ultimate bending capacity of concrete beams from the “relaxation ratio” analysis of AE signals. *Construction and Building Materials* 19, 746–754. <https://doi.org/10.1016/j.conbuildmat.2005.06.004>
- Corte, A., Higashi, A., 1960. Experimental research on desiccation cracks in soil (No. Report No. 66).
- Dang, W., Konietzky, H., Chang, L., Frühwirt, T., 2018. Velocity-frequency-amplitude-dependent frictional resistance of planar joints under dynamic normal load (DNL) conditions. *Tunnelling and Underground Space Technology* 79, 27–34. <https://doi.org/10.1016/j.tust.2018.04.038>
- Di Bella, C., Wyrzykowski, M., Lura, P., 2017. Evaluation of the ultimate drying shrinkage of cement-based mortars with poroelastic models. *Mater Struct* 50, 52. <https://doi.org/10.1617/s11527-016-0870-0>
- Dierks, K., Ziegert, C., 2002. Neue Untersuchungen zum Materialverhalten von Stampflehm.
- Domingo-Cabo, A., Lázaro, C., López-Gayarre, F., Serrano-López, M.A., Serna, P., Castaño-Tabares, J.O., 2009. Creep and shrinkage of recycled aggregate concrete. *Construction and Building Materials* 23, 2545–2553. <https://doi.org/10.1016/j.conbuildmat.2009.02.018>
- Drougkas, A., Roca, P., Molins, C., 2016. Compressive strength and elasticity of pure lime mortar masonry. *Mater Struct* 49, 983–999. <https://doi.org/10.1617/s11527-015-0553-2>
- Du, K., Li, X., Tao, M., Wang, S., 2020. Experimental study on acoustic emission (AE) characteristics and crack classification during rock fracture in several basic lab tests. *International Journal of Rock Mechanics and Mining Sciences* 133, 104411. <https://doi.org/10.1016/j.ijrmms.2020.104411>
- Estabragh, A.R., Khatibi, M., Javadi, A.A., 2018. Effect of cement on mechanical behavior of soil contaminated with monoethylene glycol (MEG). *ACI Materials Journal*.
- Fan, Y., Niu, H., Zhang, X., 2020. Impact of the properties of old mortar on creep prediction model of recycled aggregate concrete. *Construction and Building Materials* 239, 117772. <https://doi.org/10.1016/j.conbuildmat.2019.117772>
- Fang, H.Y., 1997. Introduction to Environmental Geotechnology. *New Directions in Civil Engineering*.

- Fardoun, H., Saliba, J., Saiyouri, N. Evolution of acoustic emission activity throughout fine recycled aggregate earth concrete under compressive tests, *Theoretical and Applied Fracture Mechanics* (2022) 103365. <https://doi.org/10.1016/j.tafmec.2022.103365>
- Fardoun, H., 2021. Evaluating the drying effect on the behavior of earth concrete using acoustic emission technique. *Academic Journal of Civil Engineering* 38, 163–166.
- Fardoun, H., Saliba, J., Saiyouri, N., 2021a. Monitoring the effect of age and drying on the fracture behavior of earth concrete. *Academic Journal of Civil Engineering* 39, 1–4. <https://doi.org/10.26168/AJCE.39.1.1>
- Fardoun, H., Saliba, J., Saiyouri, N., 2021b. An attempt to estimate the fulfillment of Kaiser Effect in earth concrete mixtures. *Academic Journal of Civil Engineering* 39, 116–119. <https://doi.org/10.26168/AJCE.39.1.26>
- Fardoun, H., Saliba, J., Saiyouri, N., 2020. Finite Element Modeling of the Mechanical Behavior of Earth Concrete.
- Fardoun, H., Saliba, J., Saiyouri, N., 2020. Finite Element Modeling of the Mechanical Behavior of Earth Concrete. *Academic Journal of Civil Engineering* 38, 117–120. <https://doi.org/10.26168/AJCE.38.1.28>
- Ferraris, C.F., 1986. Mécánisme du retrait de la p&e de ciment durcie. Ecole polytechnique fkdCrale de lausanne.
- Fisher, R.A., 1926. On the capillary forces in an ideal soil; correction of formulae given by WB Haines. *The Journal of Agricultural Science* 16.
- Folliard, K., Smith, C., Sellers, G., Brown, M., Breen, J., 2003. Evaluation of Alternative Materials to Control Drying Shrinkage Cracking in Concrete Bridge Decks (No. FHWA/TX-04/0-4098-4).
- Gao, J., Geng, Y., Li, S., Chen, X., Shi, D., Zhou, P., Zhou, Z., Wu, Z., 2021. Effect of silane emulsion on waterproofing and Anti-icing performance of foamed concrete. *Construction and Building Materials* 301, 124082. <https://doi.org/10.1016/j.conbuildmat.2021.124082>
- García-González, J., Rodríguez-Robles, D., Juan-Valdés, A., Morán-del Pozo, J., Guerra-Romero, M., 2014. Pre-Saturation Technique of the Recycled Aggregates: Solution to the Water Absorption Drawback in the Recycled Concrete Manufacture. *Materials* 7, 6224–6236. <https://doi.org/10.3390/ma7096224>
- Gayarre, F.L., González, J.S., Pérez, C.L.-C., Serrano López, M.A., Ros, P.S., Martínez-Barrera, G., 2019. Shrinkage and creep in structural concrete with recycled brick aggregates. *Construction and Building Materials* 228, 116750. <https://doi.org/10.1016/j.conbuildmat.2019.116750>
- Geng, Y., Zhao, M., Yang, H., Wang, Y., 2019. Creep model of concrete with recycled coarse and fine aggregates that accounts for creep development trend difference between recycled and natural aggregate concrete. *Cement and Concrete Composites* 103, 303–317. <https://doi.org/10.1016/j.cemconcomp.2019.05.013>
- Gens, A., 2010. Soil–environment interactions in geotechnical engineering. *Géotechnique* 60, 3–74. <https://doi.org/10.1680/geot.9.P.109>
- Gibson, R.E., Lo, K.Y., 1961. A theory of soils exhibiting secondary compression. *Acta Polytechnica Scandinavica* 1–15.
- Glaus, M., Baeyens, B., BRADBURY, B., Jakob, A., Van loon, L., Yaroshcuk, A., 2007. Diffusion of ²²Na and ⁸⁵Sr in Montmorillonite: Evidence of Interlayer Diffusion Being the Dominant Pathway at High Compaction. *Environ. Sci. Technol.*
- Godin, B., Toutitou, E., Krishnan, R., Heller, M.J., Green, N.G., Nili, H., Bakewell, D.J., Xu, D., Subramanian, A., Dong, L., Nelson, B.J., Zhang, Y., Berger, R., Butt, H.-J., Kim, S.H., Lafitte, N., Haddab, Y., Gorrec, Y., Kumemura, M., Jalabert, L., Yamahata, C., Chaillet, N., Collard, D., Fujita, H., Qi, Y., Nayak, A.P., Islam, M.S., Logeeswaran, V.J., Bordonaro, G.J., Gubala, V., Nowotny, T., Varona, P., 2012. Disjoining Pressure and Capillary Adhesion, in: Bhushan, B. (Ed.), *Encyclopedia of Nanotechnology*. Springer Netherlands, Dordrecht, pp. 572–577. https://doi.org/10.1007/978-90-481-9751-4_212
- Golewski, G.L., 2018. An assessment of microcracks in the Interfacial Transition Zone of durable concrete composites with fly ash additives. *Composite Structures* 200, 515–520. <https://doi.org/10.1016/j.compstruct.2018.05.144>
- González-Fonteboa, B., Martínez-Abella, F., 2005. Recycled Aggregates Concrete: Aggregate and Mix Properties. *Materiales de Construcción*.
- Grim, R., 1962. *Applied clay mineralogy*, McGraw-Hill Book. ed, International Series in the Earth Sciences. New York ; Toronto.
- Gupta, B., 1964. Creep of saturated soil at different temperatures. The University of British Columbia.
- Haines, W., 1923. The volume-changes associated with variations of water content in soil. *J. of Agricultural science*.
- Han, Q.-H., Yang, G., Xu, J., 2018. Experimental study on the relationship between acoustic emission energy and fracture energy of crumb rubber concrete. *Struct Control Health Monit* 25, e2240. <https://doi.org/10.1002/stc.2240>

- Hardy, Jr.H., Zhang, D., Zelanko, J.C., 1989. Recent studies of the Kaiser effect in geologic materials, materials. In: Proceedings of the Fourth Conference. AE/MA in Geologic Structures and Materials, Clausthal-Zellerfeld: Trans Tech Publications.
- Ho, L.S., Nakarai, K., Ogawa, Y., Sasaki, T., Morioka, M., 2017. Strength development of cement-treated soils: Effects of water content, carbonation, and pozzolanic reaction under drying curing condition. *Construction and Building Materials* 134, 703–712. <https://doi.org/10.1016/j.conbuildmat.2016.12.065>
- Horpibulsuk, S., Katkan, W., Sirilerdwattana, W., Rachan, R., 2006. Strength Development in Cement Stabilized Low Plasticity and Coarse Grained Soils: Laboratory and Field Study. *Soils and Foundations* 46, 351–366. <https://doi.org/10.3208/sandf.46.351>
- Houben, H., Guillaud, H., 1994. Earth construction: a comprehensive guide, Earth construction series. Intermediate Technology Publ, London.
- Hua, C., Acker, P., Ehrlicher, A., 1995. Analyses and models of the autogenous shrinkage of hardening cement paste. *Cement and Concrete Research* 25, 1457–1468. [https://doi.org/10.1016/0008-8846\(95\)00140-8](https://doi.org/10.1016/0008-8846(95)00140-8)
- Huang, S., He, Y., Liu, X., Xin, Z., 2021. Experimental investigation of the influence of dry-wet, freeze-thaw and water immersion treatments on the mechanical strength of the clay-bearing green sandstone. *International Journal of Rock Mechanics and Mining Sciences* 138, 104613. <https://doi.org/10.1016/j.ijrmms.2021.104613>
- Hutagi, A., Khadiranaikar, R.B., Zende, A.A., 2020. Behavior of geopolymer concrete under cyclic loading. *Construction and Building Materials* 246, 118430. <https://doi.org/10.1016/j.conbuildmat.2020.118430>
- ISO 16837, 2019. Non-destructive testing - Acoustic emission testing - Test method for damage qualification of reinforced concrete beams.
- ISO 12571 (2013) Hygrothermal performance of building materials and products — Determination of hygroscopic sorption properties.
- Jacquin, P.A., Augarde, C.E., Legrand, L., 2008. Unsaturated characteristics of rammed earth. In First European Conference on Unsaturated Soils 417–422.
- Kanema, J.M., Eid, J., Taibi, S., 2016. Shrinkage of earth concrete amended with recycled aggregates and superplasticizer: Impact on mechanical properties and cracks. *Materials & Design* 109, 378–389. <https://doi.org/10.1016/j.matdes.2016.07.025>
- Karsan, I.D., Jirsa, J.O., 1969. Behavior of Concrete Under Compressive Loadings. *J. Struct. Div.* 95, 2543–2564. <https://doi.org/10.1061/JSDEAG.0002424>
- Kavak, A., Baykal, G., 2012. Long-term behavior of lime-stabilized kaolinite clay. *Environ Earth Sci* 66, 1943–1955. <https://doi.org/10.1007/s12665-011-1419-8>
- Kianimehr, M., Shourijeh, P.T., Binesh, S.M., Mohammadinia, A., Arulrajah, A., 2019. Utilization of recycled concrete aggregates for light-stabilization of clay soils. *Construction and Building Materials* 227, 116792. <https://doi.org/10.1016/j.conbuildmat.2019.116792>
- Kouta, N., 2020. Comportement mécanique et caractérisation : durabilité de nouveaux matériaux a base d'argile. UNIVERSITÉ DE BORDEAUX, Bordeaux.
- Krajcinovic, D., Lemaitre, J. (Eds.), 1987. Continuum Damage Mechanics Theory and Application. Springer Vienna, Vienna. <https://doi.org/10.1007/978-3-7091-2806-0>
- Lam, L., Teng, J.G., 2009. Stress–strain model for FRP-confined concrete under cyclic axial compression. *Engineering Structures* 31, 308–321. <https://doi.org/10.1016/j.engstruct.2008.08.014>
- Lavrov, A., 2003. The Kaiser effect in rocks: principles and stress estimation techniques. *International Journal of Rock Mechanics and Mining Sciences* 40, 151–171. [https://doi.org/10.1016/S1365-1609\(02\)00138-7](https://doi.org/10.1016/S1365-1609(02)00138-7)
- Le, H.-B., Bui, Q.-B., 2020. Recycled aggregate concretes – A state-of-the-art from the microstructure to the structural performance. *Construction and Building Materials* 257, 119522. <https://doi.org/10.1016/j.conbuildmat.2020.119522>
- Le, T.M., Fatahi, B., Khabbaz, H., 2012. Viscous Behaviour of Soft Clay and Inducing Factors. *Geotech Geol Eng* 30, 1069–1083. <https://doi.org/10.1007/s10706-012-9535-0>
- Lee, G.C., Choi, H.B., 2013. Study on interfacial transition zone properties of recycled aggregate by micro-hardness test. *Construction and Building Materials* 40, 455–460. <https://doi.org/10.1016/j.conbuildmat.2012.09.114>
- Lemaire, K., Deneele, D., Bonnet, S., Legret, M., 2013. Effects of lime and cement treatment on the physicochemical, microstructural and mechanical characteristics of a plastic silt. *Engineering Geology* 166, 255–261. <https://doi.org/10.1016/j.enggeo.2013.09.012>

- Levatti, H.U., Prat, P.C., Ledesma, A., 2019. Numerical and experimental study of initiation and propagation of desiccation cracks in clayey soils. *Computers and Geotechnics* 105, 155–167. <https://doi.org/10.1016/j.compgeo.2018.09.015>
- Li, P., Sui, L., Xing, F., Zhou, Y., 2019. Static and cyclic response of low-strength recycled aggregate concrete strengthened using fiber-reinforced polymer. *Composites Part B: Engineering* 160, 37–49. <https://doi.org/10.1016/j.compositesb.2018.10.002>
- Li, W., Long, C., Tam, V.W.Y., Poon, C.-S., Hui Duan, W., 2017. Effects of nano-particles on failure process and microstructural properties of recycled aggregate concrete. *Construction and Building Materials* 142, 42–50. <https://doi.org/10.1016/j.conbuildmat.2017.03.051>
- Li, Zhen, Liu, J., Xiao, J., Zhong, P., 2020. Internal curing effect of saturated recycled fine aggregates in early-age mortar. *Cement and Concrete Composites* 108, 103444. <https://doi.org/10.1016/j.cemconcomp.2019.103444>
- Li, Zhenming, Zhang, S., Liang, X., Ye, G., 2020. Cracking potential of alkali-activated slag and fly ash concrete subjected to restrained autogenous shrinkage. *Cement and Concrete Composites* 114, 103767. <https://doi.org/10.1016/j.cemconcomp.2020.103767>
- Liu, J., Shi, C., Farzadnia, N., Ma, X., 2019. Effects of pretreated fine lightweight aggregate on shrinkage and pore structure of ultra-high strength concrete. *Construction and Building Materials* 204, 276–287. <https://doi.org/10.1016/j.conbuildmat.2019.01.205>
- LIU, Z., Ziehl, P.H., 2009. Evaluation of Reinforced Concrete Beam Specimens with Acoustic Emission and Cyclic Load Test Methods. *ACI Structural Journal* 106.
- Lorenzo, G., Bergado, D.T., 2006. Fundamental characteristics of cement-admixed clay in deep mixing. *Journal of Materials in Civil Engineering*.
- Lorenzo, G.A., Bergado, D.T., 2004. Fundamental Parameters of Cement-Admixed Clay—New Approach. *J. Geotech. Geoenviron. Eng.* 130, 1042–1050. [https://doi.org/10.1061/\(ASCE\)1090-0241\(2004\)130:10\(1042\)](https://doi.org/10.1061/(ASCE)1090-0241(2004)130:10(1042))
- Lu, T., 2019. Autogenous shrinkage of early age cement paste and mortar. Delft University of Technology. <https://doi.org/10.4233/UUID:E06BD615-7FC4-481B-A334-37627F142E3D>
- Luan, Y., Ishida, T., 2013. Enhanced Shrinkage Model Based on Early Age Hydration and Moisture Status in Pore Structure. *ACT* 11, 360–373. <https://doi.org/10.3151/jact.11.360>
- Lye, C.-Q., Dhir, R.K., Ghataora, G.S., Li, H., 2016. Creep strain of recycled aggregate concrete. *Construction and Building Materials* 102, 244–259. <https://doi.org/10.1016/j.conbuildmat.2015.10.181>
- Ma, C., Chen, B., Chen, L., 2016. Variables controlling strength development of self-compacting earth-based construction. *Construction and Building Materials* 123, 336–345. <https://doi.org/10.1016/j.conbuildmat.2016.07.017>
- Maniatidis, V., Walker, P., 2003. A Review of Rammed Earth Construction. University of Bath.
- Mao, Y., Liu, J., Shi, C., 2021. Autogenous shrinkage and drying shrinkage of recycled aggregate concrete: A review. *Journal of Cleaner Production* 295, 126435. <https://doi.org/10.1016/j.jclepro.2021.126435>
- Meng, Q., Chen, Y., Zhang, M., Han, L., Pu, H., Liu, J., 2019. On the Kaiser Effect of Rock under Cyclic Loading and Unloading Conditions: Insights from Acoustic Emission Monitoring. *Energies* 12, 3255. <https://doi.org/10.3390/en12173255>
- Meng, T., Wei, H., Yang, X., Zhang, B., Zhang, Y., Zhang, C., 2021. Effect of Mixed Recycled Aggregate on the Mechanical Strength and Microstructure of Concrete under Different Water Cement Ratios. *Materials* 14, 2631. <https://doi.org/10.3390/ma14102631>
- Mesri, G., Godlewski, P.M., 1977. Time- and Stress-Compressibility Interrelationship. *J. Geotech. Engrg. Div.* 103, 417–430. <https://doi.org/10.1061/AJGEB6.0000421>
- Miccoli, L., Müller, U., Fontana, P., 2014. Mechanical behaviour of earthen materials: A comparison between earth block masonry, rammed earth and cob. *Construction and Building Materials* 61, 327–339. <https://doi.org/10.1016/j.conbuildmat.2014.03.009>
- Mojsilović, N., 2020. Masonry subjected to semi-cyclic compression: Inelastic response modelling. *Construction and Building Materials* 263, 120147. <https://doi.org/10.1016/j.conbuildmat.2020.120147>
- Momayez, M., Hassani, M., Hardy, H., Jr. HR, 1992. Maximum curvature method: a technique to estimate kaiser-effect load from acoustic emission data. *Journal Acoust Emission*.
- Murayama, S., 1963. Rheological Properties of Clay. *Journal of the Society of Materials Science, Japan* 12, 72–78. <https://doi.org/10.2472/jsms.12.72>
- Nakamura, H., Nanri, T., Miura, T., Roy, S., 2018. Experimental investigation of compressive strength and compressive fracture energy of longitudinally cracked concrete. *Cement and Concrete Composites* 93, 1–18. <https://doi.org/10.1016/j.cemconcomp.2018.06.015>

- NAM, N., 2016. Valorisation de fines et granulats issus de bétons recyclés comme matériaux cimentaires. L'université Toulouse 3 Paul Sabatier.
- Naraine, K., Sinha, S.N., 1989. Loading and unloading stress-strain curves for brick masonry. *J. Struct. Eng.* 115, 2631–2644.
- Nassar, R.-U.-D., Soroushian, P., 2013. Use of milled waste glass in recycled aggregate concrete. *Proceedings of the Institution of Civil Engineers - Construction Materials* 166, 304–315. <https://doi.org/10.1680/coma.11.00059>
- Nastic, M., Bentz, E.C., Kwon, O.-S., Papanikolaou, V., Tchner, J., 2019. Shrinkage and creep strains of concrete exposed to low relative humidity and high temperature environments. *Nuclear Engineering and Design* 352, 110154. <https://doi.org/10.1016/j.nucengdes.2019.110154>
- Neville, A.M., Dilger, W.H., Brooks, J.J., 1983. *Creep of plain and structural concrete*. Construction Press, London ; New York.
- NF (French Standards), 1992. Reconnaissance and testing - Particle size analysis - Sedimentation method (No. NF P94-057).
- Ngo, D.C., Saliba, J., Saiyouri, N., Sbartaï, Z.M., 2020. Design of a soil concrete as a new building material – Effect of clay and hemp proportions. *Journal of Building Engineering* 32, 101553. <https://doi.org/10.1016/j.job.2020.101553>
- Ohno, K., Ohtsu, M., 2010. Crack classification in concrete based on acoustic emission. *Construction and Building Materials* 24, 2339–2346. <https://doi.org/10.1016/j.conbuildmat.2010.05.004>
- Ohtsu, M., 2010. Recommendation of RILEM TC 212-ACD: acoustic emission and related NDE techniques for crack detection and damage evaluation in concrete*: Test method for damage qualification of reinforced concrete beams by acoustic emission. *Mater Struct* 43, 1183–1186. <https://doi.org/10.1617/s11527-010-9639-z>
- Ohtsu, M., Isoda, T., Tomoda, Y., 2007. Acoustic emission techniques standardized for concrete structure. *J acoust emiss.*
- Ohtsu, M., Uchida, M., Okamoto, T., Yuyama, S., 2002. Damage assessment of reinforced concrete beams qualified by acoustic emission. *Aci Structural Journal* 99, 411–417.
- Ozbakkaloglu, T., Akin, E., 2012. Behavior of FRP-Confined Normal- and High-Strength Concrete under Cyclic Axial Compression. *J. Compos. Constr.* 16, 451–463. [https://doi.org/10.1061/\(ASCE\)CC.1943-5614.0000273](https://doi.org/10.1061/(ASCE)CC.1943-5614.0000273)
- Ozbek, M., Rixen, D.J., Erne, O., Sanow, G., 2010. Feasibility of monitoring large wind turbines using photogrammetry. *Energy* 35, 4802–4811. <https://doi.org/10.1016/j.energy.2010.09.008>
- Pan, B., Wu, D., Yu, L., 2012. Optimization of a three-dimensional digital image correlation system for deformation measurements in extreme environments. *Appl. Opt.* 51, 4409. <https://doi.org/10.1364/AO.51.004409>
- Pan, G., Zhan, M., Fu, M., Wang, Y., Lu, X., 2017. Effect of CO₂ curing on demolition recycled fine aggregates enhanced by calcium hydroxide pre-soaking. *Construction and Building Materials* 154, 810–818. <https://doi.org/10.1016/j.conbuildmat.2017.07.079>
- Park, P., Kent, D.C., Sampson, R.A., 1972. **REINFORCED CONCRETE MEMBERS WITH CYCLIC LOADING**. American Society of Civil Engineers.
- Poon, C.S., Shui, Z.H., Lam, L., Fok, H., Kou, S.C., 2004. Influence of moisture states of natural and recycled aggregates on the slump and compressive strength of concrete. *Cement and Concrete Research* 34, 31–36. [https://doi.org/10.1016/S0008-8846\(03\)00186-8](https://doi.org/10.1016/S0008-8846(03)00186-8)
- Poozesh, P., Sabato, A., Sarrafi, A., Niezrecki, C., Avitabile, P., Yarala, R., 2020. Multicamera measurement system to evaluate the dynamic response of utility-scale wind turbine blades. *Wind Energy* 23, 1619–1639. <https://doi.org/10.1002/we.2505>
- Quattrone, M., Cazacliu, B., Angulo, S.C., Hamard, E., Cothenet, A., 2016. Measuring the water absorption of recycled aggregates, what is the best practice for concrete production? *Construction and Building Materials* 123, 690–703. <https://doi.org/10.1016/j.conbuildmat.2016.07.019>
- RAHIMI-AGHAM, S., Bazant, Z.P., Cusatis, G., 2018. Extended Microprestress-Solidification Theory (XMPS) for Long-Term Creep and Diffusion Size Effect in Concrete at Variable Environment (No. 18– 04/33788r). Northwestern University, USA.
- Ramaroson, V.H., Becquer, T., Sá, S.O., Razafimahatratra, H., Delarivière, J.L., Blavet, D., Vendrame, P.R.S., Rabeharisoa, L., Rakotondrazafy, A.F.M., 2018. Mineralogical analysis of ferralitic soils in Madagascar using NIR spectroscopy. *CATENA* 168, 102–109. <https://doi.org/10.1016/j.catena.2017.07.016>

- Rode, C., Peuhkuri, R.H., Mortensen, L.H., Hansen, K.K., Time, B., Gustavsen, A., Ojanen, T., 2005. Moisture Buffering of Building Materials (No. R-127). University of Denmark, Denmark.
- Sagar, R.V., Srivastava, J., Singh, R.K., 2018. A probabilistic analysis of acoustic emission events and associated energy release during formation of shear and tensile cracks in cementitious materials under uniaxial compression. *Journal of Building Engineering* 20, 647–662. <https://doi.org/10.1016/j.jobe.2018.09.006>
- Sagasta, F., Zitto, M.E., Piotrkowski, R., Benavent-Climent, A., Suarez, E., Gallego, A., 2018. Acoustic emission energy b -value for local damage evaluation in reinforced concrete structures subjected to seismic loadings. *Mechanical Systems and Signal Processing* 102, 262–277. <https://doi.org/10.1016/j.ymsp.2017.09.022>
- Saliba, J., 2012. APPORT DE L'ÉMISSION ACOUSTIQUE DANS LA COMPRÉHENSION ET LA MODÉLISATION DU COUPLAGE FLUAGE-ENDOMMAGEMENT DU BÉTON. l'École Centrale de Nantes.
- Samouh, H., Rozière, E., Loukili, A., 2017. The differential drying shrinkage effect on the concrete surface damage: Experimental and numerical study. *Cement and Concrete Research* 102, 212–224. <https://doi.org/10.1016/j.cemconres.2017.09.016>
- Sariosseiri, F., Muhunthan, B., 2009. Effect of cement treatment on geotechnical properties of some Washington State soils. *Engineering Geology* 104, 119–125. <https://doi.org/10.1016/j.enggeo.2008.09.003>
- Schouenborg, B., Aurstad, J., Hagnestål, L., Petursson, P., Winblad, J., 2004. Test methods adapted for alternative and recycled, porous aggregate materials Part 3 - Water absorption. Nordic Innovation Centre, Oslo, Norway.
- Segura, J., Pelà, L., Roca, P., 2018. Monotonic and cyclic testing of clay brick and lime mortar masonry in compression. *Construction and Building Materials* 193, 453–466. <https://doi.org/10.1016/j.conbuildmat.2018.10.198>
- Shetty, N., Livitsanos, G., Van Roy, N., Aggelis, D.G., Van Hemelrijck, D., Wevers, M., Verstrynge, E., 2019. Quantification of progressive structural integrity loss in masonry with Acoustic Emission-based damage classification. *Construction and Building Materials* 194, 192–204. <https://doi.org/10.1016/j.conbuildmat.2018.10.215>
- Silva, R.V., de Brito, J., Dhir, R.K., 2015. Prediction of the shrinkage behavior of recycled aggregate concrete: A review. *Construction and Building Materials* 77, 327–339. <https://doi.org/10.1016/j.conbuildmat.2014.12.102>
- Sinha, B., Gefstle, K., Tulin, L., 1964. Stress-Strain Relations for Concrete Under Cyclic Loading. *JP* 61. <https://doi.org/10.14359/7775>
- Sinko, R., Bažant, Z.P., Keten, S., 2018. A nanoscale perspective on the effects of transverse microprestress on drying creep of nanoporous solids. *Proc. R. Soc. A* 474, 20170570. <https://doi.org/10.1098/rspa.2017.0570>
- Standard AFNOR, 1995. Reconnaissance and testing - Size identification -Wet sieving method (No. XP P94-041).
- Sun, X., Li, X., Zheng, B., He, J., Mao, T., 2020. Study on the progressive fracturing in soil and rock mixture under uniaxial compression conditions by CT scanning. *Engineering Geology* 279, 105884. <https://doi.org/10.1016/j.enggeo.2020.105884>
- Tang, S., Huang, D., He, Z., 2021. A review of autogenous shrinkage models of concrete. *Journal of Building Engineering* 44, 103412. <https://doi.org/10.1016/j.jobe.2021.103412>
- Taylor, D.W., Merchant, W., 1940. A Theory of Clay Consolidation Accounting for Secondary Compression. *Journal of Mathematics and Physics* 19, 167–185. <https://doi.org/10.1002/sapm1940191167>
- TENSI, H., 2004. THE KAISER-EFFECT AND ITS SCIENTIFIC BACKGROUND. *J. Acoustic Emission*.
- Tošić, N., de la Fuente, A., Marinković, S., 2019. Creep of recycled aggregate concrete: Experimental database and creep prediction model according to the fib Model Code 2010. *Construction and Building Materials* 195, 590–599. <https://doi.org/10.1016/j.conbuildmat.2018.11.048>
- Trabelsi, H., Jamei, M., Zenzri, H., Olivella, S., 2012. Crack patterns in clayey soils: Experiments and modeling: CRACK PATTERNS IN CLAYEY SOILS: EXPERIMENTS AND MODELLING. *Int. J. Numer. Anal. Meth. Geomech.* 36, 1410–1433. <https://doi.org/10.1002/nag.1060>
- Tran, D.K., Ralaizafisolariovony, N., Charlier, R., Mercatoris, B., Léonard, A., Toye, D., Degré, A., 2019. Studying the effect of desiccation cracking on the evaporation process of a Luvisol – From a small-scale experimental and numerical approach. *Soil and Tillage Research* 193, 142–152. <https://doi.org/10.1016/j.still.2019.05.018>
- Ulloa, V., Taengua, E., Pelufo, M., Domingo, A., Serna, P., 2013. New Views on Effect of Recycled Aggregates on Concrete Compressive Strength. *ACI Materials Journal*.
- Van Damme, H., Houben, H., 2018. Earth concrete. Stabilization revisited. *Cement and Concrete Research* 114, 90–102. <https://doi.org/10.1016/j.cemconres.2017.02.035>

- Vidya Sagar, R., Raghu Prasad, B.K., Singh, R.K., 2015. Kaiser effect observation in reinforced concrete structures and its use for damage assessment. *Archives of Civil and Mechanical Engineering* 15, 548–557. <https://doi.org/10.1016/j.acme.2014.05.004>
- Wang, J., Fu, J., Song, W., Zhang, Y., Wu, S., 2021. Acoustic emission characteristics and damage evolution process of layered cemented tailings backfill under uniaxial compression. *Construction and Building Materials* 295, 123663. <https://doi.org/10.1016/j.conbuildmat.2021.123663>
- Wang, R., Yu, N., Li, Y., 2020. Methods for improving the microstructure of recycled concrete aggregate: A review. *Construction and Building Materials* 242, 118164. <https://doi.org/10.1016/j.conbuildmat.2020.118164>
- Watanabe, T., Nishibata, S., Hashimoto, C., Ohtsu, M., 2007. Compressive failure in concrete of recycled aggregate by acoustic emission. *Construction and Building Materials* 21, 470–476. <https://doi.org/10.1016/j.conbuildmat.2006.04.002>
- Woodruff, W.F., Revil, A., 2011. CEC-normalized clay-water sorption isotherm: CLAY-WATER SORPTION ISOTHERM. *Water Resour. Res.* 47. <https://doi.org/10.1029/2011WR010919>
- Wu, F., Li, G., Li, H.-N., Jia, J.-Q., 2013. Strength and stress–strain characteristics of traditional adobe block and masonry. *Mater Struct* 46, 1449–1457. <https://doi.org/10.1617/s11527-012-9987-y>
- Wu, L., Farzadnia, N., Shi, C., Zhang, Z., Wang, H., 2017. Autogenous shrinkage of high performance concrete: A review. *Construction and Building Materials* 149, 62–75. <https://doi.org/10.1016/j.conbuildmat.2017.05.064>
- Wu, S., Zhang, S., Shen, D., 2008. Experimental study on Kaiser effect of acoustic emission in concrete under uniaxial tension loading. *Tumu Gongcheng Xuebao/China Civil Engineering Journal*.
- Wu, Y., Li, S., Wang, D., Zhao, G., 2019. Damage monitoring of masonry structure under in-situ uniaxial compression test using acoustic emission parameters. *Construction and Building Materials* 215, 812–822. <https://doi.org/10.1016/j.conbuildmat.2019.04.192>
- Xargay, H., Ripani, M., Folino, P., Núñez, N., Caggiano, A., 2020. Acoustic emission and damage evolution in steel fiber-reinforced concrete beams under cyclic loading 274. <https://doi.org/10.1016/j.conbuildmat.2020.121831>
- Xian, X., Zhang, D., Lin, H., Shao, Y., 2022. Ambient pressure carbonation curing of reinforced concrete for CO₂ utilization and corrosion resistance. *Journal of CO₂ Utilization* 56, 101861. <https://doi.org/10.1016/j.jcou.2021.101861>
- Xie, C., Yuan, L., Zhao, M., Jia, Y., 2020. Study on failure mechanism of porous concrete based on acoustic emission and discrete element method. *Construction and Building Materials* 235, 117409. <https://doi.org/10.1016/j.conbuildmat.2019.117409>
- Xie, Y., Zhang, B., Liu, B., Zeng, Z., Zhang, Y., Zheng, Y., 2021. Shrinkage cracking and strength deterioration of red clay under cyclic drying and wetting. *Alexandria Engineering Journal* S1110016821005275. <https://doi.org/10.1016/j.aej.2021.08.011>
- Yang, K., Chung, H., Ashour, A., 2008. Influence of Type and Replacement Level of Recycled Aggregates on Concrete Properties. *ACI Materials Journal*.
- Yazdandoust, F., Yasrobi, S.S., 2010. Effect of cyclic wetting and drying on swelling behavior of polymer-stabilized expansive clays. *Applied Clay Science* 50, 461–468. <https://doi.org/10.1016/j.clay.2010.09.006>
- Ye, J.H., Jeng, D.-S., 2012. Response of Porous Seabed to Nature Loadings: Waves and Currents. *J. Eng. Mech.* 138, 601–613. [https://doi.org/10.1061/\(ASCE\)EM.1943-7889.0000356](https://doi.org/10.1061/(ASCE)EM.1943-7889.0000356)
- Yoshikawa, S., Mogi, K., 1989. Experimental studies on the effect of stress history on acoustic emission activity — a possibility for estimation of rock stress. *Journal of acoustic emission*.
- Yoshikawa, S., Mogi, K., 1981. A NEW METHOD FOR ESTIMATION OF THE CRUSTAL STRESS FROM CORED ROCK SAMPLES: LABORATORY STUDY IN THE CASE OF UNIAXIAL COMPRESSION. *Tectonophysics* 74.
- Youn, H., Tonon, F., 2010. Effect of air-drying duration on the engineering properties of four clay-bearing rocks in Texas. *Engineering Geology* 115, 58–67. <https://doi.org/10.1016/j.enggeo.2010.06.012>
- Yurtdas, I., Burlion, N., Skoczylas, F., 2004. Experimental characterisation of the drying effect on uniaxial mechanical behaviour of mortar. *Mat. Struct.* 37, 170–176. <https://doi.org/10.1007/BF02481616>
- Zhang, C., Hu, M., Dong, L., Gebremariam, A., Miranda-Xicotencatl, B., Di Maio, F., Tukker, A., 2019. Eco-efficiency assessment of technological innovations in high-grade concrete recycling. *Resources, Conservation and Recycling* 149, 649–663. <https://doi.org/10.1016/j.resconrec.2019.06.023>
- Zhang, H., Wang, Y.-Y., Lehman, D.E., Geng, Y., 2020. Autogenous-shrinkage model for concrete with coarse and fine recycled aggregate. *Cement and Concrete Composites* 111, 103600. <https://doi.org/10.1016/j.cemconcomp.2020.103600>

- Zhang, J., Hou, D., Han, Y., 2012. Micromechanical modeling on autogenous and drying shrinkages of concrete. *Construction and Building Materials* 29, 230–240. <https://doi.org/10.1016/j.conbuildmat.2011.09.022>
- Zhang, L.W., Sojobi, A.O., Kodur, V.K.R., Liew, K.M., 2019. Effective utilization and recycling of mixed recycled aggregates for a greener environment. *Journal of Cleaner Production* 236, 117600. <https://doi.org/10.1016/j.jclepro.2019.07.075>
- Zhang, M., Dou, L., Konietzky, H., Song, Z., Huang, S., 2020. Cyclic fatigue characteristics of strong burst-prone coal: Experimental insights from energy dissipation, hysteresis and micro-seismicity. *International Journal of Fatigue* 133, 105429. <https://doi.org/10.1016/j.ijfatigue.2019.105429>
- Zhang, Y., Okere, C.J., Su, G., 2021. Effect of loading rates on accurate in-situ stress determination in different lithologies via Kaiser effect. *Arab J Geosci* 14, 1304. <https://doi.org/10.1007/s12517-021-07674-3>
- Zhao, K., Yang, D., Gong, C., Zhuo, Y., Wang, X., Zhong, W., 2020. Evaluation of internal microcrack evolution in red sandstone based on time–frequency domain characteristics of acoustic emission signals. *Construction and Building Materials* 260, 120435. <https://doi.org/10.1016/j.conbuildmat.2020.120435>
- Zhao, Z., Remond, S., Damidot, D., Xu, W., 2015. Influence of fine recycled concrete aggregates on the properties of mortars. *Construction and Building Materials* 81, 179–186. <https://doi.org/10.1016/j.conbuildmat.2015.02.037>
- Zheng, Y., Zaoui, A., Shahrour, I., 2010. Evolution of the interlayer space of hydrated montmorillonite as a function of temperature. *American Mineralogist* 95, 1493–1499. <https://doi.org/10.2138/am.2010.3541>